UNIVERSITÀ DEGLI STUDI DI PADOVA
Dipartimento di Fisica e Astronomia “Galileo Galilei”

SCUOLA DI DOTTORATO DI RICERCA IN ASTRONOMIA
CICLO XXIX

Observation of extrasolar planets at various ages

Direttore della scuola: Ch.mo Prof. Giampaolo Piotto
Supervisore: Dr. Raffaele Gratton
Co-supervisore: Dr. Silvano Desidera
Co-supervisore: Dr. Riccardo Claudi

Dottorando: Elena Sissa

Sommario

La ricerca e la caratterizzazione dei pianeti extrasolari è uno dei maggiori campi di ricerca dell'astronomia attuale, con lo scopo ultimo di capire i meccanismi di formazione e di evoluzione dei sistemi planetari, le condizioni che permettono la formazione di ambienti adatti alla vita, e di trovare le prove di vita extra-solare. Negli ultimi decenni, la ricerca dei pianeti extrasolari ha visto un rapido aumento di interesse, e sono state cosí sviluppate nuove metodologie di ricerca. Ognuna di esse ha aspetti positivi e negativi per lo studio dell'architettura dei sistemi extrasolari e la caratterizzazione dei pianeti. Le stelle e il loro entourage planetario si formano e crescono assieme, per lo meno nella maggioranza dei casi, legate dal disco circumstellare. Al momento manca una teoria universale che possa descrivere tutti i processi che accadono tra le fasi del collasso della nube protostellare e la stabilizzazione finale del sistema. I metodi indiretti sono molto utili per studiare le zone interne dei sistemi più evoluti, nei quali il contributo del disco protoplanetario è trascurabile. Dall'altro lato, la tecnica dell'imaging diretto con strumenti ad alto contrasto offre la possibilità di studiare le prime fasi della formazione planetaria, non accessibili con altri metodi indiretti, e gioca un ruolo fondamentale per le attuali teorie di formazione planetaria.

Questa tesi si focalizza sulle capacità dell'imaging diretto ottenuto con SPHERE, il nuovo strumento ad alto contrasto del VLT, nel rivelare pianeti in diversi stadi della loro evoluzione, e presenta uno studio complementare di sistemi vecchi basato sulle osservazioni delle velocità radiali con SARG, il vecchio spettrografo echelle del TNG.

Il Capitolo 1 introduce brevemente le teorie di formazione ed evoluzione dei pianeti con i più importanti metodi di ricerca.

Il Capitolo 2 descrive SPHERE, lo strumento usato per la maggior parte dei risultati presentati in questa tesi.

Nel Capitolo 3 presento il caso di quattro oggetti giovani. Ho sfruttato il canale visibile di SPHERE per studiare i jet di Z CMa, e il canale nel vicino infrarosso per HD 100546 e T Cha, cercando segnali della presenza di pianeti. Allo stesso tempo, ho potuto studiare in dettaglio il disco circumstellare di HD 100546 in un intervallo spettrale relativamente ampio: nella sezione ad esso dedicata mosta che le strutture più brillanti del sistema suggeriscono la presenza di almeno tre regioni vuote nelle zone interne del disco, assieme ad altre strutture, come ad esempio bracci a spirale. Ho anche rilevato la presenza di una sorgente diffusa nella posizione attesa per il potenziale pianeta b (Quanz et al. 2015; Currie et al. 2015), ma la natura di questa emissione è, tuttavia, ancora sconosciuta. Infine, LkCa 15 è stato studiato sia nel canale visibile che in quello del vicino infrarosso di SPHERE.

Nel Capitolo 4 presento lo studio dei segni distintivi di accrescimento in un gruppo di oggetti. L'accrescimento di GQ Lup b è stato osservato sia in H_α che il Pa_β, sfruttando tutti e tre i sottosistemi di SPHERE.

Due sistemi i cui dintorni sono già stati ripuliti dal gas e dalla polvere sono presentati nel Capitolo 5: HIP 80591 e HIP 65426. In quest'ultimo, ho scoperto che uno dei candidati compagni aveva un'alta probabilità di essere legato alla stella a causa della sua posizione e delle sue caratteristiche spettrali. Queste conclusioni sono state poi confermate da un'analisi approfondita e da ulteriori osservazioni che hanno dimostrato che quel compagno, HD 65426 b, è un pianeta gioviano caldo con massa compresa tra 6 e 12 M_J.

Nel Capitolo 6, studio l'attività cromosferica in stelle binarie vecchie allo scopo di identificare un segnale nelle velocità radiali nascosto dallo spostamento Doppler indotto dall'attività. Ho scoperto che $\Delta H\alpha$, un indice basato sulla riga H_α, è un buon indicatore dell'attività stellare

quando l'indice $\log R'_{HK}$ non è disponibile e puó essere anche usato per derivare l'età delle stelle nel caso siano più giorvani di 1.5 Gyr. Inoltre, HD 76037 B mostra una variazione elevata delle velocità radiali che puo' essere spiegata con la presenza di un compagno di piccola massa (Sissa et al. 2016).
Infine, nel Capitolo 7 fornisco le conclusioni del lavoro ed espongo sviluppi futuri.
Le appendici sono dedicate agli aspetti più tecnici del mio lavoro, che sono stati necessari per migliorare le capacità dello strumento e la riduzione dei dati, e per definire al meglio i set-up necessari allo strumento per raggiungere i differenti scopi scientifici.

Abstract

The search and characterization of extrasolar planets is one of the main topics of current astronomy, with the ultimate goals of understanding the formation and evolution of planetary systems, the general conditions for the formation of life-friendly environments, and possibly detecting signature of extra-solar life. In the last decades the research of extrasolar planets underwent a steep increase of interest and different methods of detection were developed. Each of them has its own merit and lack in studying the extrasolar system architecture and the characteristics of extrasolar planets. Stars and their planetary entourage form and grow together, at least in most cases, tied by the circumstellar disk. A unique theory that can describe all the processes that happen between the protostellar cloud collapse and the final system stabilization is not available at the moment. Indirect methods are very useful to study more evolved systems, where the protoplanetary disk contribution is negligible, in their innermost regions. On the other hand, direct imaging with high-contrast instruments offers the possibility to study the early phases of the planet formation, that are not accessible to other indirect methods of planets detection, and plays a key role in current planet formation theories.

This thesis focuses on the capabilities of direct imaging with SPHERE, the new high-contrast imager of VLT, in detecting planets at different stages of their evolution, coupled with radial velocities observations of old systems obtained from SARG, the old TNG echelle spectrograph.

Chapter 1 briefly introduces the planet formation and evolution theories with the most important exoplanets research methods.

Chapter 2 describes the SPHERE instrument used for the majority of the results presented in this thesis.

In Chapter 3 I present the case of four young objects. I exploit the SPHERE visible channel to study Z CMa jets, and the near-IR channel for HD 100546 and T Cha, looking for the presence of planets. At the same time, I was able to study in detail the circumplanetary disk of HD 100546 in a quite wide spectral range: in the dedicated Section I show that the system brightest structures suggest the presence of at least three gaps in the inner regions of the disk, coupled with other structures, such as spiral arms. I detected a diffuse source at the location of the claimed planet HD 100546 b (Quanz et al. 2015; Currie et al. 2015), but the nature of this emission is, however, still unknown. Lastly, LkCa15 was studied both in the visible and in the near-IR of SPHERE.

In Chapter 4 I present the study of the accretion signature in a few objects. GQ Lup b accretion was observed both in H_α and in Pa_β, exploiting all three SPHERE subsystems.

Two systems that have already cleaned out their surroundings from gas and dust are presented in Chapter 5: HIP 80591 and HD 65426. In the latter, I first found out that one companion candidate had high probability to be bound to the star due to its position and it spectral features. These findings were later confirmed by a deeper analysis and follow up observations that demonstrate HD 65426 b, the companion I studied, is a warm Jupiter-like planet with mass between 6 and 12 M_J.

In Chapter 6, I study the chromospheric activity in older binary stars in order to detect a radial velocity signal hidden by the Doppler shift induced by the activity. I found out that $\Delta H\alpha$, an index based on the H_α line, is a good indicator of the star activity when the $\log R'_{HK}$ index is not available and can be used also to infer stellar ages in case of stars younger then 1.5 Gyr. Moreover, HD 76073 B shows a high radial velocities scatter that can be explained by the presence of a low-mass companion (Sissa et al. 2016).

Finally, in Chapter 7 I give the conclusions and explain future prospects.
Appendixes are dedicated to the more technical aspects of my work, that were needed to improve instrument capabilities and data reduction, and to better defining the instrument set-ups needed to achieve different scientific aims.

Contents

List of Figures

List of Tables

Chapter 1

Introduction

The search and characterization of extrasolar planets is one of the main topics of current astronomy, with the ultimate goal of understanding the general conditions for the formation of life-friendly environments and possibly detecting signatures of extra-solar life. About 3500 extrasolar planets have been discovered in the last twenty years. The discovered planets display a wide diversity both in physical parameters (mass, radius, etc.) and in the architecture of the systems where they are located. Even after accounting for the substantial biases present in the population of discovered planets, current results challenge models for planet formation. The evolution of the individual planets is still to be properly understood. Since the evolution of planets and planetary systems mainly occur during their infancy, the most crucial observations concern very young planets or even those that are still forming within the disks that surround very young stars. Like in other areas of extra-solar planet research, a substantial improvement is expected in the next decade, thanks to a number of new instruments that are available since few years (ALMA and high contrast imagers on large telescopes such as GPI and SPHERE) or soon will be available (JWST).

1.1 Planet formation and evolution theories

The discovery of these last twenty years demonstrate that planets are common, with a significant fraction of the stars hosting planetary systems. In Figure 1.1, the detected planets can be subdivided into three different groups: Hot Jupiters (masses similar to Jupiter and $P < 10$ days), super-Earths or Neptunes ($M_p \sim 10\ M_\oplus$ and $P < 100$ days), and gas and ice giants (with super jovian masses and $P \sim 1000$ days). However, this distribution in masses and periods is strongly biased by the detection methods as will be described in following Sections. The observed systems show a wide variety, from that similar to Solar System to alien systems such as those hosting Hot Jupiters. Planets are found both close and very far from the hosting stars with a wide range of masses. Likely planets might form through different mechanisms. Construction of a unified picture defies current understanding of planet formation and evolution. The conceptual basis of the modern theories of planet formation reside in the nebular hypothesis developed independently by Kant and Laplace in the second half of the eighteenth century to describe the Solar System formation: planets are thought to form from the same material of their star, and evolve with it and its circumstellar (or protoplanetary) disk (Fig. 1.2).

Stars form generally in groups inside a common molecular cloud. Each star originates when

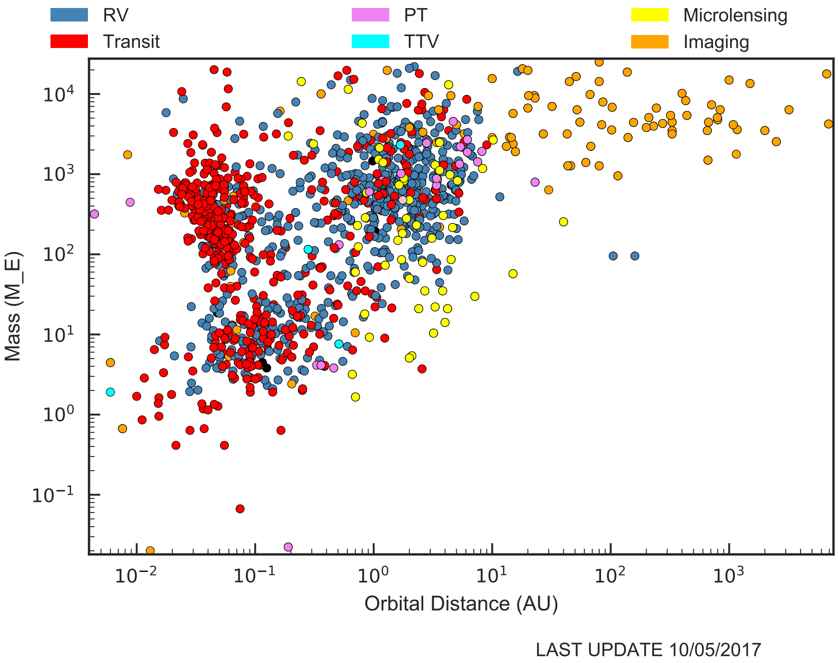

Figure 1.1: Approximate masses and orbital distances of known planets, based on a May 2017 query of the `exoplanets.eu` encyclopedia. For Doppler discovered planets, the plotted mass is infact $M_\mathrm{p} \sin i$. For imaging planets, the plotted mass is based on theoretical models relating the planet's age, luminosity, and mass. With microlensing, the planet-to-star mass ratio is determined more directly than the planet mass. For microlensing and imaged planets, the plotted orbital distance is really the sky-projected orbital distance. For transiting planets, those with unknown mass are missing. For timing planets, many are dubious cases of circumbinary planets around evolved stars.

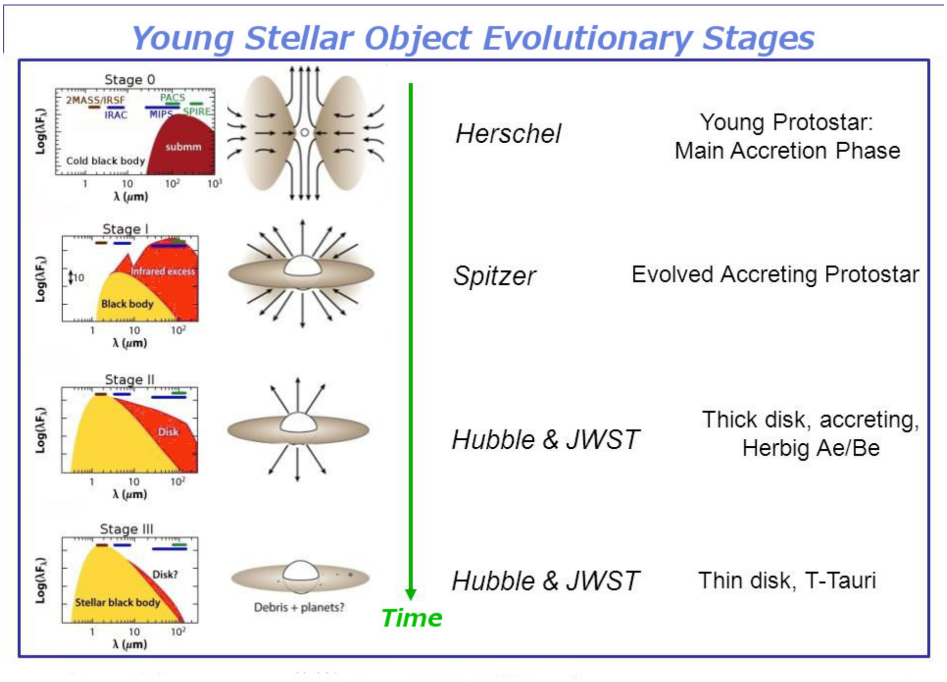

Figure 1.2: Scheme for star-planet systems formation. For each phase, the expected SED, its schematic representation and the observabilities (by space instruments) are provided.

the cloud starts to collapse locally under its own gravity. In the central region, the seed of what will be the star starts to form a hot core. This young protostar grows rapidly in mass due to the gravitational collapse. The central region of the system appears heavily obscured by the infalling envelope and emits in the sub-millimetre regime.

As the nebula radius decreases, the conservation of the angular momentum makes the nebula rotation to increase, and in the central region the gas cannot flow directly to the protostar but is forced to orbit around it in its equatorial plane, forming a disk that feeds the accreting central core. The angular momentum is also dissipated trough two bipolar outflows (or jets) along the star rotational axis. In this phase, the envelope disappears and the accreting protostar ignites the hydrogen in its core: the star and its disk become observable, mostly in the IR light.

Accretion of gas onto the star continues, while the disk realizes the conditions for planets formation. In this phase planets embryos are deeply embedded in the disk.

As they grow accreting material from the disk, protoplanets clean their surroundings and become more luminous. Moreover, they interact with the gas and the dust perturbing the disk: they are thought to be the origin of disks spiral arms and cavities. This makes their observation more favourable. The disk structure starts to evolve from a continuous primordial disk towards a more segregated structure called transition disk: they are identified by gaps and holes in the innermost regions.

The presence of planets, the photoevaporation by UV-radiation from the central star and nearby stars, the still ongoing accretion onto the central star and other mechanisms remove the gas from the disk. The dust and larger solids still orbiting the star (a young or a main-sequence star) results in a so called debris disk that can be detected thanks to its thermal

emission in the IR. They are thought to be the analogues of the Solar System asteroids belts and exozodiacal dust. Direct imaging of these objects revealed sharp edges, gaps, warps, spirals, rings and other asymmetries (see e.g. Wyatt 2008; Wyatt et al. 2015; Lagrange et al. 2008), footprint of the presence of planets.
Due to the collisions, dust grains will disgregate and, when their dimension is of the order of sub-micrometer, radiative pressure from the hot star will remove them.
In evolved systems, in which most of the disk is dissipated, thermal emission is still significant at younger ages and/or for the most massive objects, though reflected light is the dominant emission component for all cold planets (T$<$ 300 K) from the visual to near-IR spectral region. That allows the detection of extrasolar planets at wide separation through direct imaging technique. Also scattered light can be used, since the reflected radiation is generally polarized and the degree of polarization may be particularly high at short wavelengths ($< 1\ \mu m$) due to Rayleigh scattering by molecules and scattering by haze particles in planetary atmospheres. On the other hand, the presence of companions orbiting the stars at short separations ($< 5\ au$) can be retrieved using the so called indirect methods, exploiting the perturbation of some stellar parameters due to the presence of the planets.

Two different scenarios have been proposed to describe how planets form in the disk. In the first (Disk Instability: Cameron 1978; Boss 1997) massive planets form directly from the mainly gaseous circumstellar disk as a consequence of the instabilities that may be present in such a disk. Instabilities are most likely to appear in massive disks and they typically occur on large scales. While it is not entirely clear if disks are massive enough for planet formation through this mechanism, once instabilities arise, planet formation should be very fast producing massive planets without any solid core. Disk instability might then be implied in the formation of rather massive planets at large separations from the star. The second mechanism (Core Accretion: Mizuno 1980; Pollack et al. 1996) is more complex, requiring several steps. The starting point is the presence of dust that should deposit toward the mid-plane of the disk on a short timescale. Due to the very low relative velocities, dust grains are expected to often stick when collide and then grow in size. While the early growth is quite slow, it becomes much faster when the bodies become larger than about 1 km because of the funneling effect due to their gravity. In a timescale of the order of 1 Myr, these solid bodies should grow to $\sim$1000 km sized objects (planetesimals). Further interaction of the planetesimals may then give raise to planet cores that might become massive enough for a runaway accretion of the gas. Core accretion may then form both rocky planets and gas giants, as observed in the Solar System. A general difficulty of this model is the timescale for the planet core formation (a few million years) that is similar to the lifetime of gaseous disks. This creates a bottleneck for the formation of gas giants (Mordasini et al. 2008) that is efficient only in the intermediate part of the disk: at short separation, ices (an essential ingredient of the cores) sublimate due to the strong radiation field, while at large separations the timescale for core formation becomes too long. In addition, the efficiency of formation of gas giants should depend on the amount of dust initially present, which on turn depends on the metallicity and mass of the star. Various migration mechanisms (Lin & Papaloizou 1979; Lubow & Ida 2010) due to interaction of the planet with the disk shorten the timescale related to core accretion and may cause a wide variety of architectures. In all these scenarios, an accretion disk should form during the early phases of formation of gas giants. The main sources of energy for massive planets are gravitational contraction and differentiation: in both cases the planet starts with a relatively high luminosity but rapidly cools down and fades (Baraffe et al. 2003). Direct

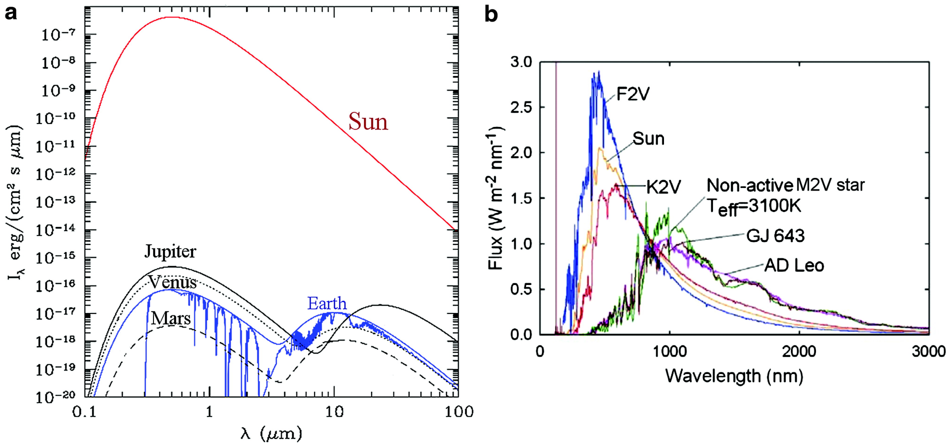

Figure 1.3: (a) Smithsonian Astrophysical Observatory model of our Solar System (assumed here to be blackbodies with Earth spectrum shown). (b) Spectra of different host stars (Segura et al. 2005). From Kaltenegger et al. (2010)

detection of planets is then much easier for young and massive planets.

In addition, massive planets ($M_*/M_P < 100$) close to small mass stars – that is systems with rather low mass ratios – might possibly form through fragmentation of the protostellar cloud, with the same mechanism usually considered for the formation of binary stars. Planetary systems formed in this way might have very large separations and very eccentric orbits, in analogy with the binary systems.

1.2 Direct imaging

Planets orbiting stars in the solar neighbourhood are expected to be bright enough to be observed through Direct Imaging (DI). This means that we can detect radiation reflected by the planet and the circumplanetary disk, if any, and their thermal emission. Reflected flux depends on the host star brightness, the distance of the planet to the star and planetary albedo, and is dominant in the visible spectral range; thermal emission depends on the planetary temperature and reveals itself mainly in the IR, where stellar flux is highly depleted with respect to the visible, as shown in Fig. 1.3 in the case of planets of our Solar System seen by a hypothetical observer located 10 pc away. In this case the visible contrast in flux is of the order of 10^{-10}, the infrared one is three orders of magnitude less demanding. DI is the easiest technique that allows to have information about the colors and the spectrum of the planets, with clues on their atmosphere, by using a spectrometer or an integral field spectrograph to image the planets at different wavelengths. Since planets are faint, this method can provide informations only on planets similar to massive gaseous objects in the Solar System, and can even probe their atmosphere. Moreover, in the last decades, planets and planetary systems were accessible to observations mostly as the final outcomes of the planet formation process and only some hints of the structure of protoplanetary disk can be retrieved by spectroscopy or direct imaging. The new high-contrast imagers also aim to detect planet formation as it happens inside the circumstellar disk, and the interaction between the planets and the disk; that is to observe the first phases of the planetary systems evolution, that are not accessible to the indirect methods due to the presence of the disk and also study the morphology and the composition of the disk. Direct images of the birth of planets and their evolution and interaction within the disk may play a key role for understanding the different planets formations processes.

Detection of planets through direct imaging is extremely difficult, due to the high contrast (typically $> 10^{-5}$) and low separation (typically less than $1''$), and only a few tens of planets were discovered with this method up to date. A combination of techniques is required to achieve their detection: extreme Adaptive Optics, coronagraphy, and differential imaging. Even when these techniques are combined, achieving the required high contrast remains very challenging and only the very tip of the planet brightness distribution can be explored with current high-contrast imagers.

1.2.1 Extreme Adaptive Optics

The idea of the Adaptive Optics (AO) is to limit the impact of the atmosphere on the target light. The atmosphere is a turbulent ambient formed by, as a first approximation, layers of bubbles with different characteristic size, r_0, called Fried parameter. The wavefront is coherent inside them but is modified at their surface. Different bubbles have different refraction coefficients and shapes, so that the wavefront entering the telescope pupil is no more flat, but deformed and tilted: light rays, that arrives from an infinite distance and therefore parallel at the top of the atmosphere, are tilted several times in the last few kilometers of their travel from the star to the telescope. These bubbles act like telescope pupils: this implies a loss in angular resolution of the telescope, smearing and blurring of the differential image. If D is the telescope pupil diameter, the theoretical angular resolution which corresponds to

$$\theta_{diff} = 1.22\frac{\lambda}{D}[\text{rad}] \tag{1.1}$$

drops to $\theta_0 = 1.22\lambda/r_0$ due to the turbulence. Assuming a telescope of the 8-meter class observing in the near infrared at 1μm, its theoretical angular resolution is of the order of 30 mas, but in the case of a $r_0 = 10$ cm, it will provide an angular resolution of $2.5''$. Another important parameter for AO is the coherence time, defined as $\tau_0 \propto r_0/v_\text{w}$ with v_w being the average wind speed. It describes the interval during which the wavefront entering the pupil can be considered as constant, and therefore provides a requirement to the temporal working capabilities of the AO. Characteristic values of τ_0 in a good astronomical site are of the order of a few milliseconds at visible wavelengths. The mutual interferences of the corrugated wavefront due to the turbulent atmosphere and the telescope/systems surfaces generates the so called speckle pattern.

An AO system aims to provide diffraction-limited images removing the noise pattern introduced by the atmosphere. To do this, incoming stellar light is partially corrected for larger movements with a tip/tilt mirror and a DM corrects for higher order perturbations in a close loop regime (Fig. 1.4). The efficiency of an AO system is measured by the Strehl ratio (SR), e.g. the ratio of the peak intensity of the PSF image measured in the detector to the theoretical peak of the diffraction limited PSF: a perfectly flat wavefront that impact the detector has SR=1, while a typical AO instrument provides SR 0.2-0.6 in the NIR (Y-K bands)[1]. Extreme

---

[1] Since the index of refraction (related to tilts of the wavefront) depends on the wavelength, the wavefront corrugation expressed in wavelengths units strongly depends on wavelength. For this reason, the SR generally

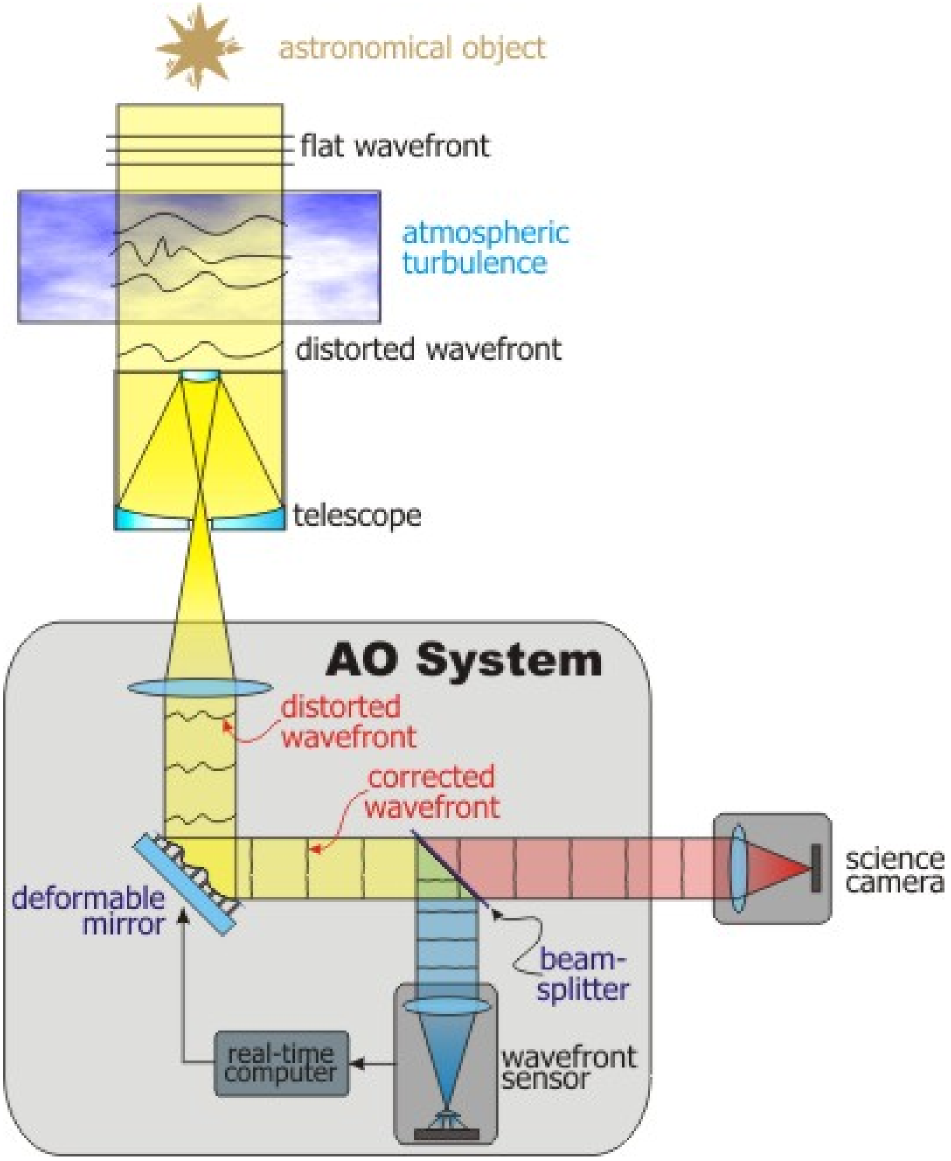

Figure 1.4: Cartoon of the AO concept. Flat stellar wavefronts before the atmosphere are distorted by the atmosphere before entering the telescope. The AO system (grey area) sends part of the light to the WFS that regulates in a close loop configuration the DM. Corrected wavefronts are the send to the scientific camera.

adaptive optics (ExAO) systems are new generations of AO instruments developed mostly for the high contrast imagers. These systems aim to fully correct both atmospheric perturbation and instrumental aberrations within the isoplanatic angle, providing a Strehl ratio that can reach $SR = 0.9$ in the H-band on bright stars. The AO can correct the wavefront till a separation defined as the outer working angle: this is defined by spatial frequency of actuator (a quantity that should be compared with the Fried radius) in the DM and the telescope diameter.

1.2.2 Coronagraphy

Another important element to reach high contrast performances is the coronagraph, an occulting disk often located in the focal plane of the telescope, that blocks the light coming in the center of the field of view. Originally invented to study the Sun corona (Lyot 1939), the technique is now widely used in stellar observations. In the field of extrasolar planets, the AO systems corrects the incoming wavefront reconstructing the Airy pattern and the coronagraph suppresses its diffraction peak aiming to detect in the stellar halo the glare of extrasolar planets that are orders of magnitudes fainter.

More complex coronagraphs were designed to improve the performances of the systems (see e.g. Guyon et al. 2006, for a deeper description), albeit some of them mostly evolved from Lyot's original device. These latter are defined as Apodized Pupil Lyot Coronagraph (APLC, Soummer et al. 2003) and use more optical elements to remove, in addition to the star light, the diffraction pattern introduced after the focal plane by the occulting mask: an apodizer located in a pupil plane upstream the mask limits the diffraction of the light, radially modifying its transmission, and a Lyot stop, located after the focal plane, attenuates the diffracted light. The shape of this element is similar to the entrance pupil to ensure the maximum suppression of the light.

1.2.3 Differential imaging

Differential imaging is a high-contrast imaging technique that aims to reduce quasi-static speckle pattern due to AO residual aberrations. If the instrument optical system does not change during the whole exposure, then the speckle pattern due to it would not be modified. Due to its origin, this noise pattern is, indeed, almost fixed with the system pupil: actually, variations of temperature, wind speed and telescope pointing always introduce a deformation of the speckle pattern and create the quasi-static speckle pattern. Speckles appear as spots, with a dimension of λ/D, that is of the same order of a real point source and therefore, looking at one single exposure, they can be confused with a faint companion. Removing this pattern yields a better contrast, and allows the detection of fainter nearby companions.

The Angular Differential Imaging

The basic idea of the Angular Differential Imaging (ADI) is to estimate the speckle pattern with a reference PSF observation, and remove it from the scientific images. To avoid real sources to be confused with speckle, ADI technique needs to acquire several images with different field of view positions; the simplest way is to use an azimuthal mounting telescope and observe in pupil stabilized mode (switching the derotator off): the quasi-static speckle

---

decreases with decreasing wavelength.

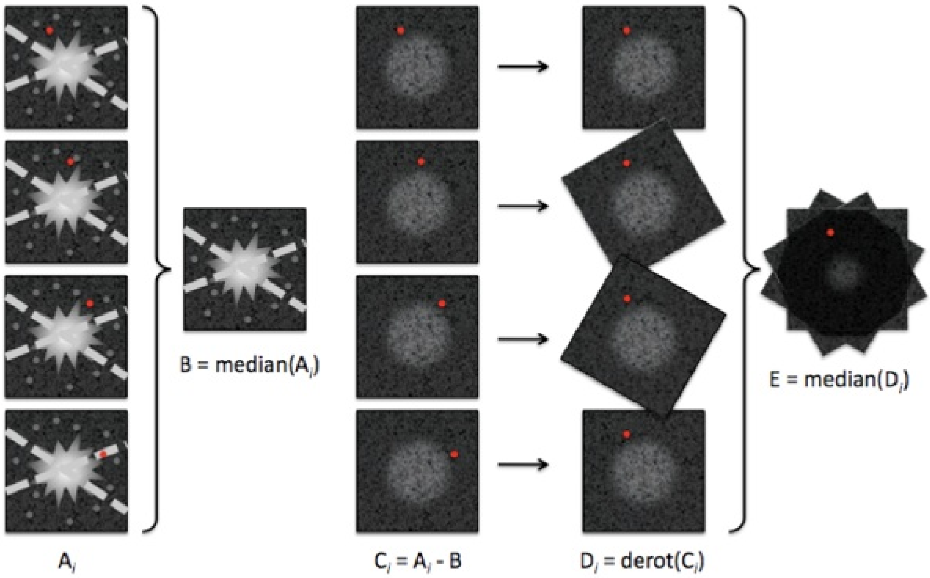

Figure 1.5: Diagram explaining how the ADI works (from C. Thalmann).

pattern stays fixed with respect to the detector because the telescope and the instrument optics are kept aligned, while the field rotates with respect to the instruments. In this case, it is possible to distinguish real objects, that moves from one frame to the other, from these speckles. A median over time would capture the quasi-static speckle pattern that can be removed from each frame, but not the real object. Finally, frames can be rotated to follow the field rotation and stacked to produce an image quite clean from these speckles. For a sequence $A_i(t_i, \theta_i)$ composed of frames imaged at the median exposure time t_i at which the FoV rotation is θ_i, the final image is then

$$E = \text{median}(\text{derot}(A_i - B, \theta_i - \theta_0)) \tag{1.2}$$

A schematic description is in Fig. 1.5.
This technique was first introduced by Marois et al. (2006) for HST observations, and then several algorithms were developed also to exploit it for ground-based observations. Two methods can be used to define and subtract the PSF (B): this can be defined as the median of all the initial frames (not derotated) or can be retrieved from a few dedicated no-coronagraphic observations of a reference star acquired as close in time as possible with the same set up (Reference Differential Imaging, RDI). Also a combination of these is possible.

The Simultaneous Differential Imaging

The Simultaneous Differential Imaging technique (SDI, Racine et al. 1999) exploits the wavelength dependence of the speckle pattern: the diffraction of the light makes speckle moving radially with the wavelength. On the contrary, planets lie in the same position at each wavelength, because their light is not masked by the coronagraph and therefore not diffracted. Two coronagraphic images taken simultaneously at two close wavelength λ_0 and λ_1, can be used to remove stellar halo and speckle pattern: in this case the two images have a similar PSF and the same speckle pattern homothetically scaled. Rescaling radially the two

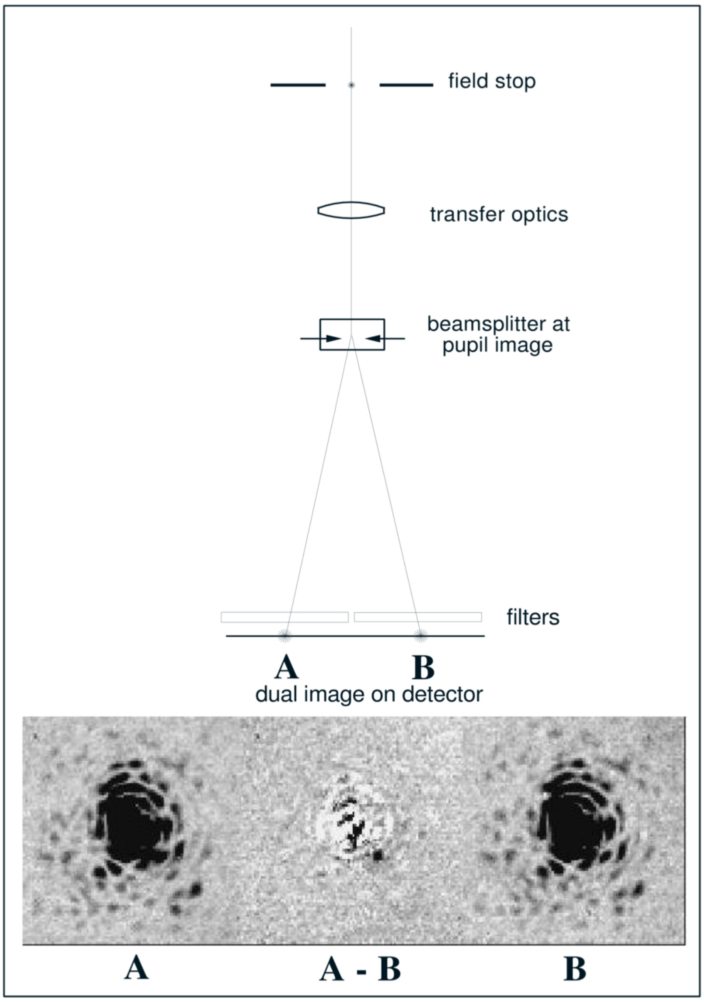

Figure 1.6: Top: Scheme of a dual band imager. Bottom: resulting images (A and B), and their subtraction (from Racine et al. 1999).

image to a common wavelength and subtracting them, the speckle-pattern is then defined (Fig. 1.6), while the presence of a planet in the field will be indicated by a dark and a bright radially close structures. The two figures can also be rescaled in flux according to the two filters. This technique requires Dual Band Imaging (DBI), that is a system in which the coronagrafic AO corrected light enters a beam splitter and is sent to two different narrow band filters. Moreover, this technique can be used to disentangle a planet, that shows strong molecular absorptions, from a star, that has a flat spectrum. To do this, the two filters are selected to be inside and outside the absorption band, as in the case of GJ758 (in Fig.1.7). Simultaneous Differential Imaging produces a gain of about one or two magnitudes.

Spectral Deconvolution

An extension of the SDI method was suggested by several authors (see e.g. Sparks & Ford 2002; Fusco et al. 2005; Berton et al. 2006; Thatte et al. 2007). They showed that the spectral information available in an integral field spectrograph (IFS) datacube can be used to identify scattered stellar light and remove it from the datacube, e.g. use the IFS as a multi-wavelengths SDI. This implies a better identification of the planets and the possibility to extract their spectrum with an enhanced SNR. In a IFS datacube, each frame is a monochromatic image of the instrument FoV. Therefore, has a speckle pattern that changes regularly with wavelength. The Spectra Deconvolution (SD) removes the speckles by spatially rescaling each individual monochromatic images, proportionally to its wavelength. The speckle spectra for each pixel may now be well represented by a low order polynomial function in the direction of the dispersion. Simultaneously, the rescaling makes the planets moving with the wavelength and appear as a bump in the spectra, that cannot be represented by the low order polynomial and therefore is not subtracted. Removing this smooth pattern and rescaling back each monochromatic image will improve the speckle subtraction and the contrast limits. However, Thatte et al. (2007) demonstrated that this method is not working for separation smaller than the bifurcation radius. If a planet, which image extends up to $2\theta_{diff}$ for each wavelength, is located at the distance r from the star, and is observed at wavelength from λ_1 to λ_2, then its movement in the rescaled datacube is defined by:

$$\Delta r = r - r\frac{\lambda_1}{\lambda_2} = r\frac{\Delta\lambda}{\lambda_2}. \tag{1.3}$$

Since the dimension of the companion in the rescaled datacube is constant, the bifurcation point at wavelength λ is then defined as:

$$r = 2\epsilon \times 1.22\frac{\lambda}{D}\frac{\lambda_1}{\Delta\lambda} \tag{1.4}$$

where ϵ is a suitable parameter related to the "inclination" of the planet spectrum within the datacube in the rescaled images. If ϵ is greater than 1, SD can remove speckle signal for separation larger then the bifurcation point.

Polarimetry

For objects having polarized signal, the strongest method for the speckle subtraction is perhaps the dual-mode polarimetry (Kuhn et al. 2001; Perrin et al. 2004; Oppenheimer et al. 2008). It exploits the fact that starlight is, in general, weakly polarized and aims to remove

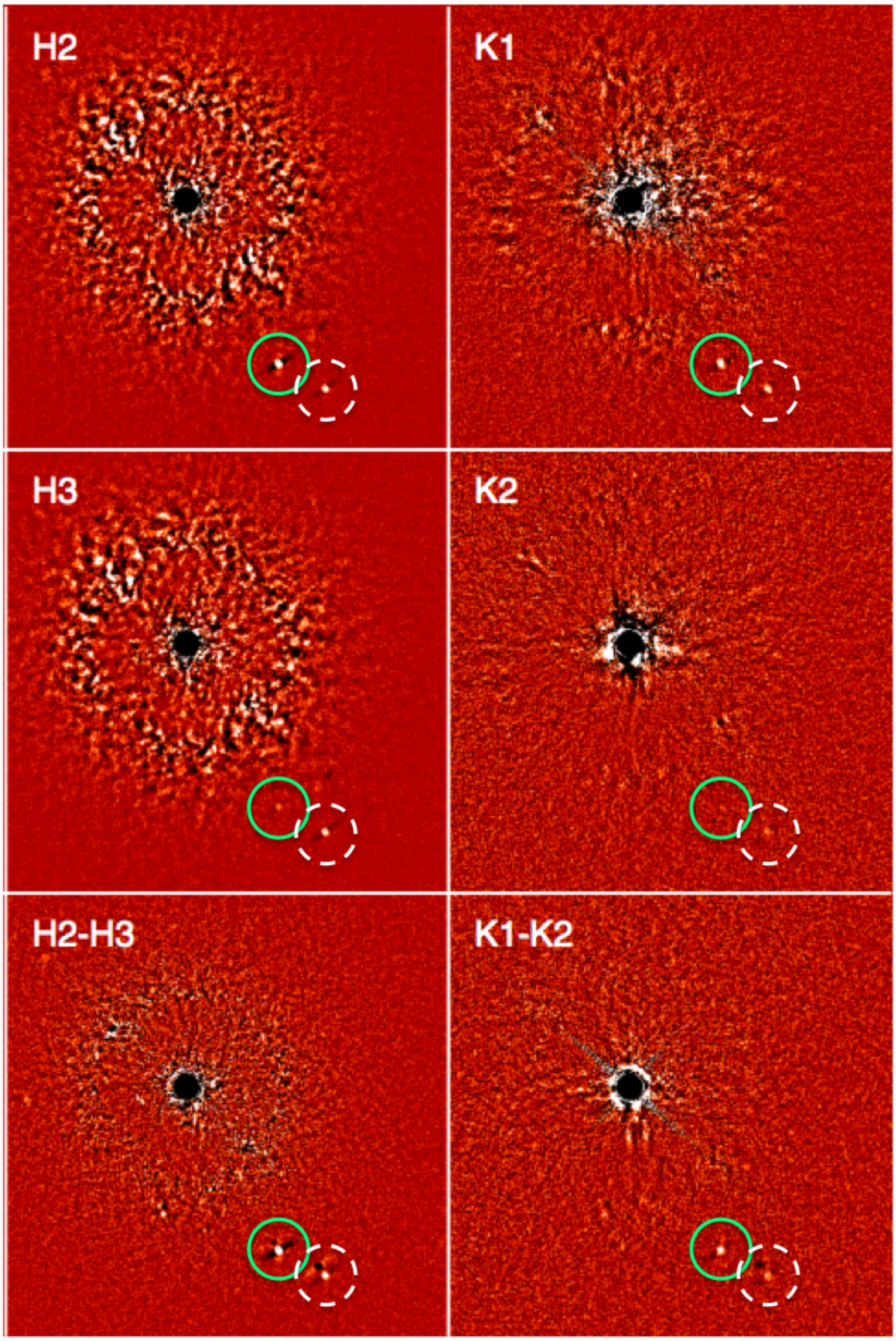

Figure 1.7: Images of GJ 758 after ADI and SDI prcessing in IRDIS DBI filters H2H3 and K1K2. A late T-dwarf, GJ758B (green circle) and a background star (white dotted circle) are visible. In the bottom row, the difference image: the methan absorption of the brown dwarf is clear in the H3 band, where the flux of GJ758B is lower, while the background star appear as a dark area plus a bright peak. Edited from Vigan et al. (2016).

speckles almost completely subtracting two images with perpendicular polarization. In this case, the light coming from an object or material (planet or disk) around a star that exhibits large fractional polarization remains on the image. In the case of extrasolar planets, they can reflect stellar light, that is polarized by the planet atmosphere with a typically high scattering polarization ($> 10\%$) for large apparent separations (e.g., Seager et al. 2000; Stam et al. 2004; Schmid et al. 2006a).

All these concepts are implemented in the various sub systems of the SPHERE intruments at VLT, that will be presented in Chapter 2.

1.3 Detecting planets with indirect methods

Since 1995, year in which the first extrasolar planet around a solar type star was discovered around 51 Pegasi (Mayor & Queloz 1995), a few indirect techniques were developed to detect this kind of objects. The so called indirect methods exploit the effects caused by the planet on the host star, such as radial velocity measurements, flux monitoring, astrometry variation measurement, and microlensing campaign. All these techniques have some limitations that entail their sensitivity in different zones of the planetary systems and provide different but complementary informations about the planets.

1.3.1 The Radial Velocity technique

Radial Velocity (RV) technique gave the first hints of extrasolar planet discoveries (Campbell et al. 1988; Latham et al. 1989; Hatzes & Cochran 1993) and was used to reveal the first extrasolar planet (Mayor & Queloz 1995). This technique looks for the variations of the radial velocity of the star, that can be interpreted as the motion of the star with respect to the system barycenter due to the presence of a massive companion. This variation is periodic and can be described as:

$$V(t) = K\left[\cos\left(\nu + \omega\right) + e\cos\omega\right]; \tag{1.5}$$

where the amplitude of radial velocity variations K is

$$K = \left(\frac{2\pi G}{P}\right)^{\frac{1}{3}} \cdot \frac{M_p \sin i}{(Mp + M*)^{\frac{2}{3}}} \cdot \frac{1}{(1-e^2)^{\frac{1}{2}}}. \tag{1.6}$$

In these equations ν is the orbits true anomaly, ω is the argument of periastron, P is the period of the planetary orbit, i is the inclination angle between the normal to the orbital plane and the line of sight, M_p and M_* are the mass of the planet and of the star, respectively, e is the eccentricity of the orbit and G is the gravitational constant. A Jupiter analogue orbiting around a solar mass star at an orbital distance of 5.2 AU will induce a 11.2 m/s reflex motion with a period of 12 years, whereas an Earth-like planet at 1 AU would cause a reflex motion on the host star of 10 cm/s. The currently available technology allows to reach an RV precision of 0.5-1.0 m/s, with e.g. the High Resolution Echelle Spectrometer (HIRES) installed at Keck Observatory, and the two twin High Accuracy Radial velocity Planet Searchers (HARPS and HARPS North) mounted at NTT in La Silla and TNG in La Palma, respectively. These performances imply that it is possible to detect massive planets (from SuperEarths to $20M_J$) close to their stars (up to 10 AU). However, the variation of the stellar radial velocity can also be caused by other factors, such as instrument instability, or stellar noise. The RV signal due to stellar activity is the greatest obstacle in finding planets exploiting the Doppler shift of the lines. This activity jitter could be relevant in the visible spectral range (up to 40 m/s) when observing solar-type stars (F, G and K spectral types), but it is reduced at the near-Infrared wavelengths, where stellar cool spots, hot faculae and plages have a lower contrast with respect to the stellar integrated flux (Desort et al. 2007). The simultaneous or quasi-simultaneous measurements of RV and of indicators linked to stellar activity (chromospheric emission, photometric variability, line profile indicators ...) can help to disentangle the origin of the observed RV variations (Queloz et al. 2001; Meunier et al. 2017). For this reason, and thanks to the increasing interest in finding rocky planets orbiting around M dwarfs, new IR spectrographs are being developed. GIANO, a new Near Infrared High Resolution Spectrograph, is mounted at TNG. This instrument can now also work in parallel with HARPS-N, helping to disentangle real planet-induced signal from the RV jitter related to stellar activity.

The Radial Velocity precision depends not only on the properties of the spectrograph but also on the properties of the star. Good RV precision allows to study cool stars of spectral types later than F6, while with poor RV precision can be achieved for cool stars of spectral type earlier than F6. This is due to the few spectral lines (high effective temperatures) and high rotation rates typical of early-type stars have and has the consequence that 98% of known exoplanets discovered with RV are found around stars with spectral types later than F6. In addition, since stellar activity is a function of the stellar age, planet detection from RV becomes very difficult around young stars, due to the large stellar noise.

1.3.2 Astrometry

Similar to the RV, the astrometry method aims to observe the motion of the stellar position on the sky plane due to the gravitational interaction with a companion, around the system barycentre. This method originates from the characterization of astrometric binary stars systems, but needs more accurate measurements, coupled with a long baseline of observations.

No planets detected with this technique are confirmed at this time, but promising results on low-mass companion s(e. g. Muterspaugh et al. 2010; Sahlmann et al. 2013), together with the new Gaia mission capabilities, are expected to allow the detection of several thousands of extrasolar planets (Sahlmann 2016) in the next decade.

1.3.3 Transits and timing variation techniques

The Transits (T) method is the most productive method so far in detecting extrasolar planets. It was proposed for the fist time in 1952 by Struve, ~ 50 year before the technology needed to detect transits was developed. The basic idea is that, if the orbital planes of extrasolar planets are randomly oriented in space, some of them lie on, or close to, the observer line of sight and therefore during each orbit the planet will transit the stellar disk and the star will occult it, like it happens for Venus and Mercury on the Sun as seen from the Earth. This corresponds to an integrated star+planet flux variation during the whole orbit as shown in Fig. 1.8: as planet revolves around the star, its disk is partially illuminated in the observer direction and present phases. During the occultation, only stellar light is visible, while during the transits the planet will hide a small portion of the stellar disk. In this configuration, stellar light passing across the planets atmosphere is reprocessed: this allows to characterize

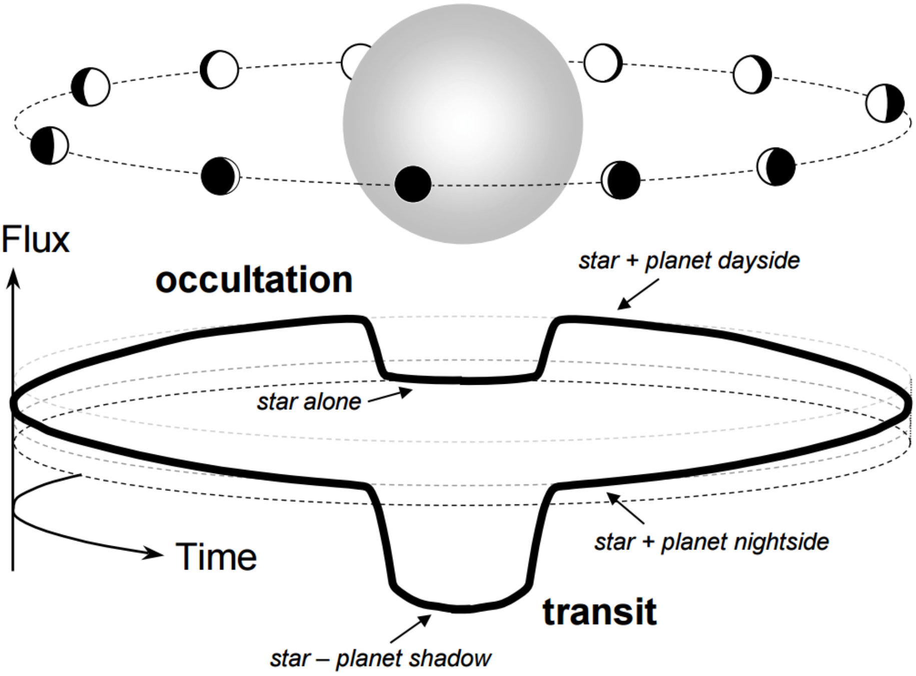

Figure 1.8: Top: geometry of the transit with planet different phases. Bottom: the flux variation as a function of the system geometry.

planets atmosphere (Transmission spectroscopy, Brown 2001).
The light curve of a transit give us a huge quantity of informations. The period of the transit, P, is directly dependent on the orbit semi-major axis, a_p, through Kepler's third law:

$$a_p^3 = \frac{GM_* P^2}{4\pi^2} \tag{1.7}$$

assuming that the planetary mass is negligible with respect to stellar mass. The depth of the flux depletion $\frac{\Delta F}{F}$ is directly related to the planet over star radii ratio

$$\frac{\Delta F}{F} = \left(\frac{R_p}{R_*}\right)^2, \tag{1.8}$$

and coupled with the transit duration T and the time between the fist and the last contact τ gives information on the inclination of the orbits:

$$b \approx 1 - \frac{R_p}{R_*}\frac{T}{\tau} \quad b = a_p \frac{\cos i}{R_*}. \tag{1.9}$$

Given the stellar mass and radius, the transit method gives the planet radius.
However, this simple picture of one planet transiting one star does not correspond to the common geometry of extrasolar systems detected with T method: the *Kepler* mission has demonstrated that the probability of detecting multiple planetary system is high. It is then possible to exploit both the transit timing variation (TTV) and the transit duration variation (TDV) techniques: the presence of additional bodies in the system can perturb the planet

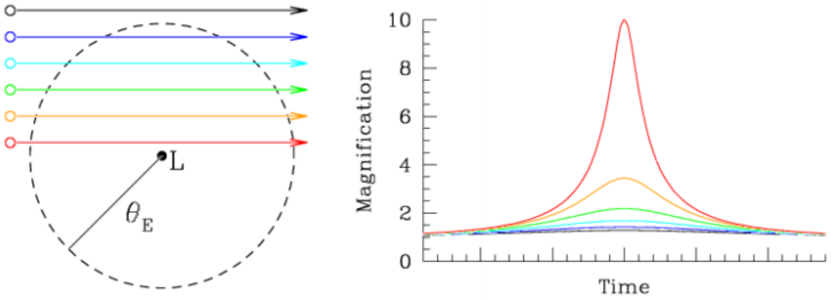

Figure 1.9: The microlensing occurs inside the Einstein radius θ_E of the source L. Different impact parameters (left) correspond to different magnification of the signal (right).

orbit and causes a delay between consecutive transits and alter the transit duration.
All these techniques are prone to false alarms and false positives. These latter consists of tansit-like events caused by phenomena other then planetary transit, such as stellar chromospheric activity, grazing binaries, low-stellar mass object transiting the star or blended eclipsing binaries.
Even if transits are intrinsically rare (the probability of observing an Earth transiting a Sun is only 0.46%, and drops down to 0.09% in the case of a Jupiter), current photometric surveys dedicated to exoplanets research scan million of stars with a photometric precision better than 1% using arrays of relatively small telescope from ground (OGLE, TrES, WASP, HATNet ...) or from space (Corot, Kepler and, in the future, TESS, Plato 2.0). The determination of planetary radius from T and of planetary mass by either RV monitoring or TTV enables the determination of planet density and so insights in the planet interiors. Furthermore, the transit geometry is of special interest for atmospheric characterization, providing complementary information to those obtained from spatially resolved planets with the direct imaging technique, even if the two class of object are, till now, separate.

1.3.4 Microlensing

The gravitational microlensing is a product of the General Relativity: the light from a distant source is deviated by the presence of a massive object (the lens) along its path to the observer and results in distorted unresolved images of the source and flux magnification. This happens when the background star, located at the distance d_S, enters the Einstein radius θ_E of the lens, defined as:

$$\theta_E = \sqrt{\frac{4GM_*}{c^2 d_{rel}}} \tag{1.10}$$

where $1/d_{rel}$ is the lens-source relative parallax, $d_{rel}^{-1} = d_L^{-1} - d_S^{-1}$ with d_L being the distance of the lens. The magnification effect increases opposite to the impact parameter of the background star motion with respect to the lens, as shown in Fig. 1.9.

If the lens consists of two bodies, the magnification pattern is more complex and can be used to retrieve information about the lens-system geometry. In the simplest case of a star hosting one planet, the magnification pattern can show a main peak corresponding to light crossing close to the star and a second one when the light is perturbed by the planet (Fig. 1.10), but

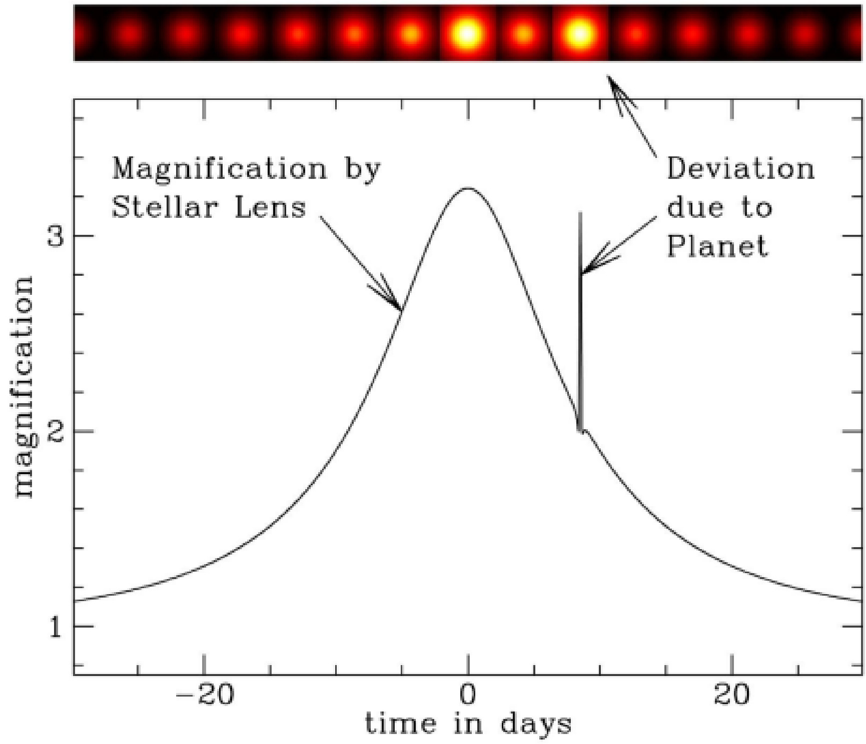

Figure 1.10: Cartoon of a magnification event due to the presence of a planet orbiting the star.

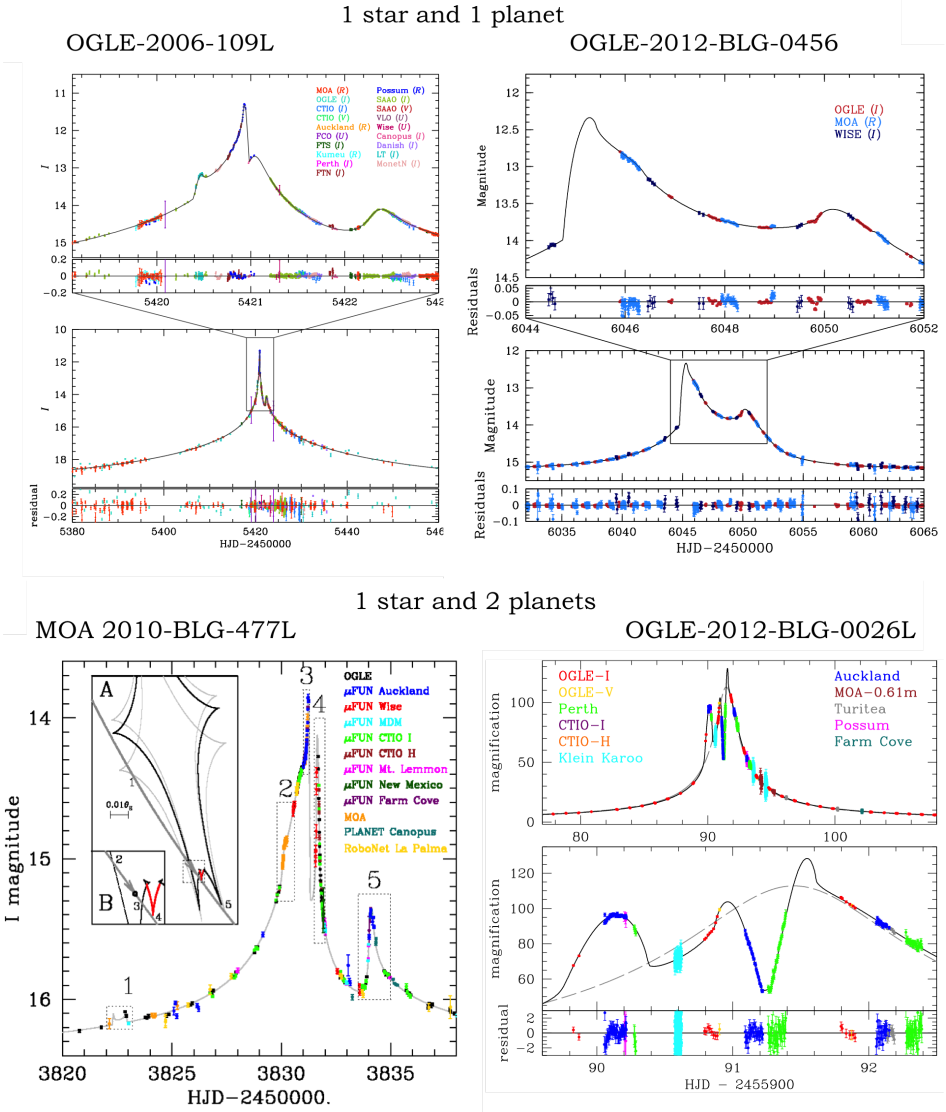

Figure 1.11: Top:complex magnification curves due to the presence of a massive planet clos to stars OGLE-2006-109L (Bachelet et al. 2012) and OGLE-2012-BLG-0456 (Henderson et al. 2014) Bottom: more complex magnification curve due to the presence of two planets around the star. The two multiple systems known trough microlensing, OGLE-2006-109L (Gaudi et al. 2008) and OGLE-2012-BLG-0026L(Beaulieu et al. 2016).

more complex curves are also possible as shown in Fig. 1.11. Microlensing are unique events that cannot be predicted except for some special cases (such as for Proxima Centauri in 2016, Sahu et al. 2014) and therefore it is extraordinarily difficult and inefficient to discover planets. Moreover, system parameters have to be found with a complex modelling of the light curve. However, this method permits to detect very low-mass planets on large orbit, accessing a parameter space that is difficult to reach with other methods. With the aim of monitoring microlensing events (that normally take more than 20 days), several dedicated telescopes were located around the world surveying hundreds of fields, mostly in the Galaxy bulge. The two principal collaborations are OGLE, observing from Las Campanas, and MOA from New Zeland. In the future, a new generation of wide-field instruments incuding the Large Synoptic Survey Telescope (LSST) from the ground, and the Wide-Field Infrared Survey Telescope (WFIRST) from the space, will enlarge the sky coverage and improve the detection limit down to Earth-mass planets.

Chapter 2

SPHERE

SPHERE (Spectro-Polarimetric High-contrast Exoplanet REsearch) is a second generation instrument of the VLT, offered to the whole ESO community. SPHERE goal is to detect planets by direct imaging; it allows to reach a contrast of better than 10^{-5} at a separation of a few tenths of an arcsecond. With such performances, SPHERE is expected to detect several tens of objects in total for a survey over a few hundread targets[1], with separations of 5-50 AU from the star and younger than $2 \times 10^8 yr$. SPHERE allows mapping the outer regions of several planetary systems and to characterize in detail several young planets. SPHERE was built by a large consortium of eleven institutes in five European countries and ESO. It involves institutes in France (IPAG, LAM, LESIA, ONERA and Nice Observatory), Italy (INAF), Germany (MPIA), Switzerland (ETH Zürich and Obs. Geneva) and Netherland (ASTRON). The PI of the project is J.L. Beuzit (IPAG). INAF has a strong (about 20%) participation, and is responsible for the Integral Field Spectrograph (IFS, Claudi et al. 2008) and Instrument Control Software (INS, Baruffolo et al. 2010). In exchange of the in-kind and manpower contributions for the construction of the instrument, the SPHERE Consortium has received a total of 260 nights of Guaranteed Time Observations (GTO) to be spent in five years (2015-2019). The Consortium agreed to use these nights for four science programs, mostly devoted ($\sim$ 200 nights) to a large survey on a sample of about 400 young stars called SHINE (SpHere INfrared survey for Exoplanets). Other two programs consist of observations of circumstellar disks and their characterization ($\sim$ 20 nights) and to planets in reflected light and visible ($\sim$ 20 nights).

Besides imaging of exoplanets and companions around stars, SPHERE can provide competitive or unprecedented results in other research fields. The Other Science GTO program ($\sim$ 12 nights) cover related astrophysical fields such as brown dwarfs and planet formation and Solar System Objects (asteroids) but also stars (evolved stars, stellar jets, planetary nebulae, binaries, starburst regions, etc.)

2.1 SPHERE Science Case

The direct detection and spectral characterization of extrasolar planets is one of the most exciting but also one of the most challenging areas in modern astronomy. The prime objective of SPHERE is the discovery and study of new extrasolar giant planets orbiting nearby stars by direct imaging of their circumstellar environment. The challenge consists in the very large

---

[1] From Sphere Science Case.

contrast between the host star and the planet, larger than 12.5 magnitudes (or 10^5 in flux ratio), at very small angular separations from the star, typically inside the seeing halo (few arcsec at most). The whole design of such an instrument is therefore optimized towards reaching the highest contrast in a limited field of view and at short distances from the central star (Mouillet et al. 2002).
While radial velocities and transits are the best technique currently available to study the inner side of the planet distribution, direct imaging technique based on high-resolution and high contrast imaging like that provided by SPHERE is expected to be the most efficient to discover planets in the outer regions of planetary systems and provide properties of these young planets in the expected peak region of gas giant formation. Both evolved and young planetary systems will be detected, respectively through their reflected light and through the intrinsic planet emission. These two classes of planets are characterized by different observable and intrinsic properties. The transition from one class to the other depends on several factors and cannot be defined quantitatively: age of the system, mass of the planet, albedo, orbital separation, and luminosity of the parent star (both absolute and apparent) contribute to the final planet emission.

Self luminous planets: young planets are self-luminous and their luminosity depends on age, mass and on their atmosphere composition. The peak of their emission lies in the near infrared between 1.05 and 2.1μm according to their effective temperature. In this case, the star/planet contrast does not depend on the distance between them and can be studied using IR differential imaging and integral field spectroscopy;

Reflected-light planets: planets shining by reflecting stellar light might be detected in polarimetry. Those planets are normally old, their intrinsic flux is low and emit mainly reflected stellar light. Their luminosity, therefore, strongly depend on the distance between the star and the planet and on the planet atmospheric albedo and polarization level that constraint the reflective property. The reflected light is smaller in the near infrared (because the star flux and planetary albedo drop) and thus the optimal wavelength domain for such systems is the I band. Moreover, the polarization is expected to be large in these old planets (Stam et al. 2004, 2006; Buenzli & Schmid 2009) and does not depend on the distance between the star and the planet.

SPHERE will help to determine the frequency of giant planets in wide orbits ($> 5 - 10$ AU) observing a few hundred of stars, investigate the impact of stellar mass on the frequency and characteristics of planetary companions over the range 0.5 to 3.0 $M_\odot$ and will therefore contribute in testing several aspects of the planet formation models. Moreover, SPHERE can contribute to the study of the architecture of planetary systems (multiplicity and dynamical interactions), of extrasolar planets in binaries and clusters, of the Brown Dwarfs and infer the relation of planets with circumstellar disks. All these purposes call for some scientific requirements. First of all, SPHERE provides a high monocromatic contrast to detect planets around stars. This implies a powerful AO system that includes either a larger number of actuators or a shorter timescale for instrument response, or both, but also a brighter limiting magnitude. In order to confirm the proper motion of detected planets, SPHERE astrometric accuracy is of the order of a few milliarcseconds (mas). SPHERE offers a combination of spectroscopic and dual band photometric modes to study planetary spectra. Simultaneous observation of several monochromatic images con be used to reduced the impact of the speckles (Sparks & Ford 2002): the separation of speckles from the star increases with wavelength and

their intensity decreases, while the separation of a planet (or a companion, more in general) is constant. Furthermore, planets and the host stars have different spectral features, such as the presence of a molecular band, that can be used to this purpose. While an integral field spectrograph for planet imaging is conceptually challenging and can only provide a limited field of view, it is widely recognized as a potentially extremely useful science module for a planet-searching instrument. The reasons for this are two-fold: firstly the IFS can be build with virtually zero differential aberrations, and secondly the multiple spectral channels allow for better correction of speckle chromaticity and even data analysis strategies that do not rely on the presence of a-priori assumed features in the planet's spectrum. Finally, polarimetry is useful for observations of extra-solar planets and circumstellar disk because the stellar light is essentially unpolarized while it becomes polarized when scattered by molecules and other constituents in the planetary atmosphere (Schmid et al. 2006b). This polarization could be detected when the planet is seen under suitable angles, e.g. near quadrature, when the maximum of polarization occurs in a direction close to the line of sight. The polarization is expected to be particularly high at short wavelengths $< 1\mu m$ due to Rayleigh scattering by atoms and molecules and scattering by aerosol particles in planetary atmospheres and by dust grains in circumstellar disk. Polarization measurements can provide diagnostics on atmosphere structure and composition taking advantage of multiple scattering properties that decreases the observed degree of polarization.
SPHERE main technical requirements can be summarized as follows:

- high contrast imaging able to detect a planets ~ 15 magnitude fainter than its host star at $0.5''$. This implies to detect 0.5 M_J at 10 Myr and 115 M_J at 10 Gyr;
- access to very small angular separations ($0.1''$ to $0.3''$) from host star;
- access to an extended wavelength range wide enough to allow the characterization of the objects at resolving power ~ 30.

With these capabilities, SPHERE is also a direct competitor of space telescopes in the study of protoplanetary disks. The capacity to detect so faint a surface brightness and the PSF stability provided by SPHERE allow the study of fine details in the variations of the brightness profiles in the disks as a function of radius. Asymmetries can be revealed, either tracing the presence of nearby stellar companions, or suggesting the presence of large bodies, possibly planets, embedded within the disk. A systematic exploration of planets candidates and an extensive study of the link between planets at wide separations and debris disks would enable a better understanding of the planet formation process.
Finally, the SPHERE instrument is also able to address important scientific questions related to a wide range of astrophysical targets: evolved stars, Novae, Asteroids, OB stars binaries, Active massive stars etc.

2.2 The SPHERE design

SPHERE is composed of four subsystems (Fig. 2.1):

1. the Common Path and Infrastructure (CPI). It receives direct light from the telescope and supports the other three subsystems feeding them with an highly stabilized, AO corrected coronagraphic beam. It includes pupil stabilizing fore-optics (tip-tilt and

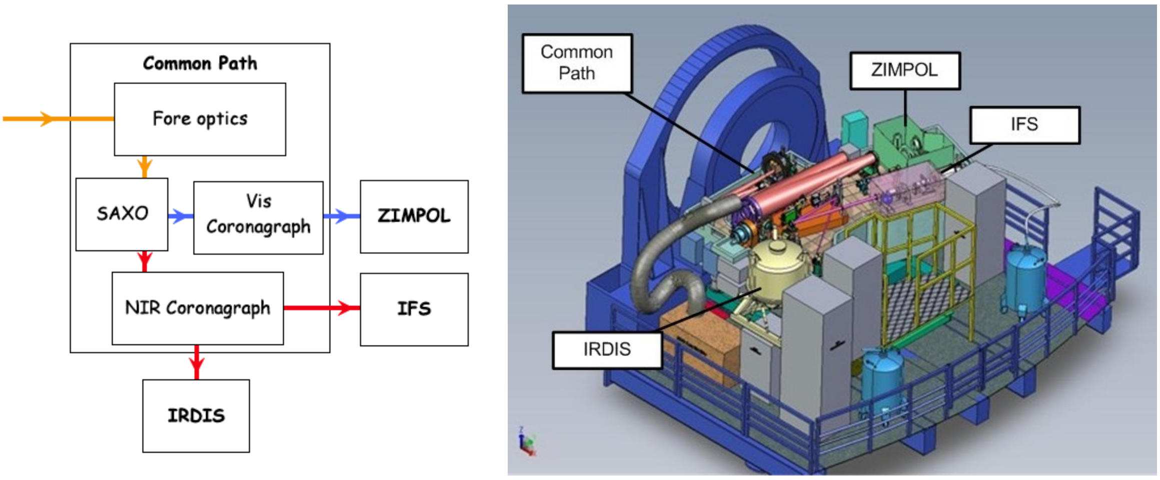

Figure 2.1: SPHERE subsystems (left) including the common path (CPI) with adaptive optics system SAXO and coronographic units, and sub-instruments IRDIS, IFS and ZIMPOL. Right: schematic view of the instrument on the UT3 Nasmyth platform. From SPHERE User Manual.

rotation), calibration units, the Sphere eXtreme Adaptive Optics (SAXO) system and the near-infrared and visible coronagraphs wheels;

2. the Zurich Imaging Polarimeter (ZIMPOL). This visible subsystem works in classical imaging and differential polarimetric imaging mode;
3. the Integral Field Spectrograph (IFS) produces spectra on each position of the whole FoV in near-IR.
4. the InfraRed Dual Imaging Spectrograph (IRDIS), that also works in the near-IR with a larger FoV than IFS and provides various observing modes: it provides classical imaging (CI), Dual band imaging (DBI), Dual Polarimetric Imaging (DPI) or Long Slit Spectroscopy (LSS);

All components of SPHERE allow complementary detection capabilities and characterization potential, in terms of field of view, contrast, and spectral domain.

2.2.1 CPI

CPI is the biggest SPHERE subsystem: it includes the main optical bench and guarantees a perfect alignment with the telescope focus (see Fig. 2.2). The hearth of the whole SPHERE is the adaptive optics system SAXO with its Deformable Mirror (DM), that corrects for the variable wave-front distortions due to the atmosphere turbulence and the static aberrations introduced by the instrument itself. SAXO includes a visual Shack-Hartmann wavefront sensor (WFS) connected to a tip-tilt mirror (ITTM) and the DM with 41×41 actuators. The SAXO system works nominally providing H-band Strehl ratio in excess of 92% for median seeing conditions ($0.8''$-$1.2''$) on a bright natural guide star with $R<9$. A general description of the system can be found in Fusco et al. (2006), while its performances are described in Petit et al. (2014) and Fusco et al. (2014). The light beam is sent from SAXO to the visual or to

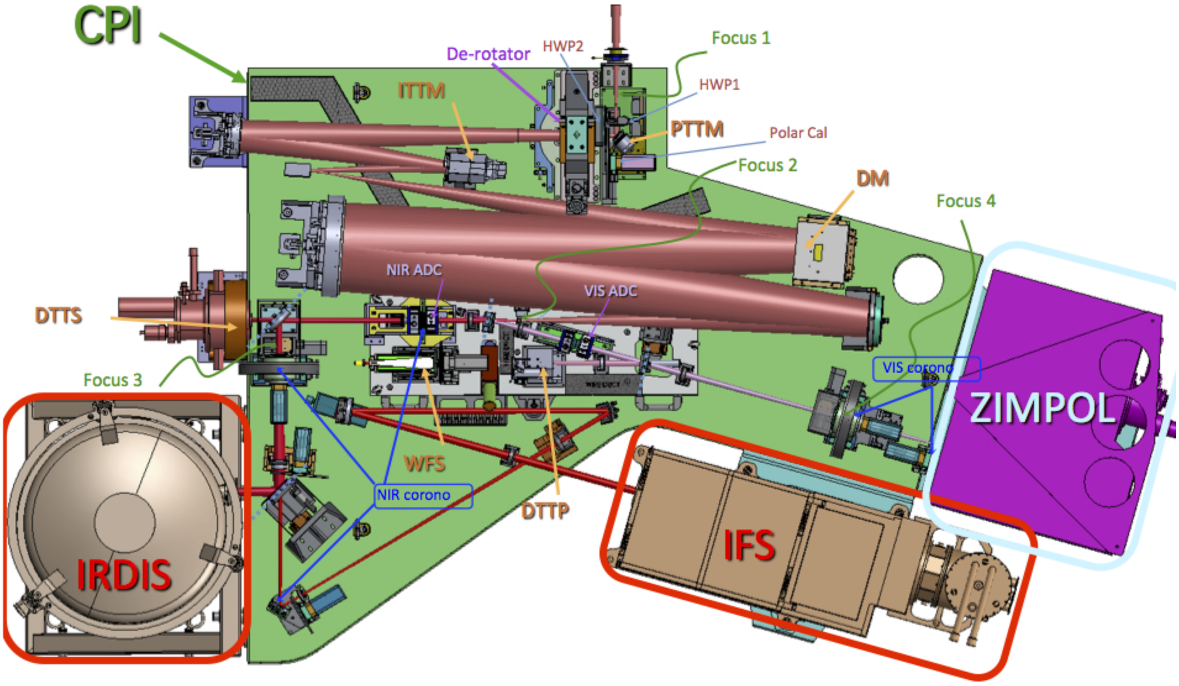

Figure 2.2: The common path optical beam on the main optical bench (green) feeding the other three subsystems: ZIMPOL (magenta), IFS (brown) and IRDIS (gray). From SPHERE User Manual.

the near-IR channel where the first element along both paths is a stellar coronagraph, which attenuates the central source light to avoid detector saturation and allow higher contrast performances; classical Lyot coronagraphs (CL) and four quadrant phase masks (4QPM) are available for both channels, whereas apodized Lyot coronagraphs (ALC) is available only in the near-IR .

2.2.2 ZIMPOL

ZIMPOL is a high contrast diffraction limited imaging polarimeter with very high sensitivity in the visual band. Its 3D model is in Fig. 2.3. The main observing mode for ZIMPOL is a relative polarization measurement of the immediate surroundings of the central stars, which is used as a (zero)-polarization reference to remove the polarization throughput of the instrument. It performs quasi-simultaneous Differential Polarization Imaging (DPI) exploiting fast (kHz) polarimetric modulation allowing to avoid atmospheric seeing variations effects. Fast modulation coupled with a on-chip-de-modulation by two CCDs constitute a new concept for imaging polarimetry: thanks to a beam-splitter that works as a polarization modulator, the two perpendicular polarizations are sent to two different CCDs and are then synchronized (Fig. 2.4). In these de-modulating CCDs every second row is masked so that photo-charges created in the unmasked row during one half of the modulation cycle are shifted to the next masked row, a temporary buffer storage, for the second half of the cycle and again back for the next modulation cycle. After more than a thousand of modulation cycles, the CCDs can be read out: two frames of opposite polarization states are stored in alternating pixel rows and the real polarization signal is the difference between these two frames while their sum is

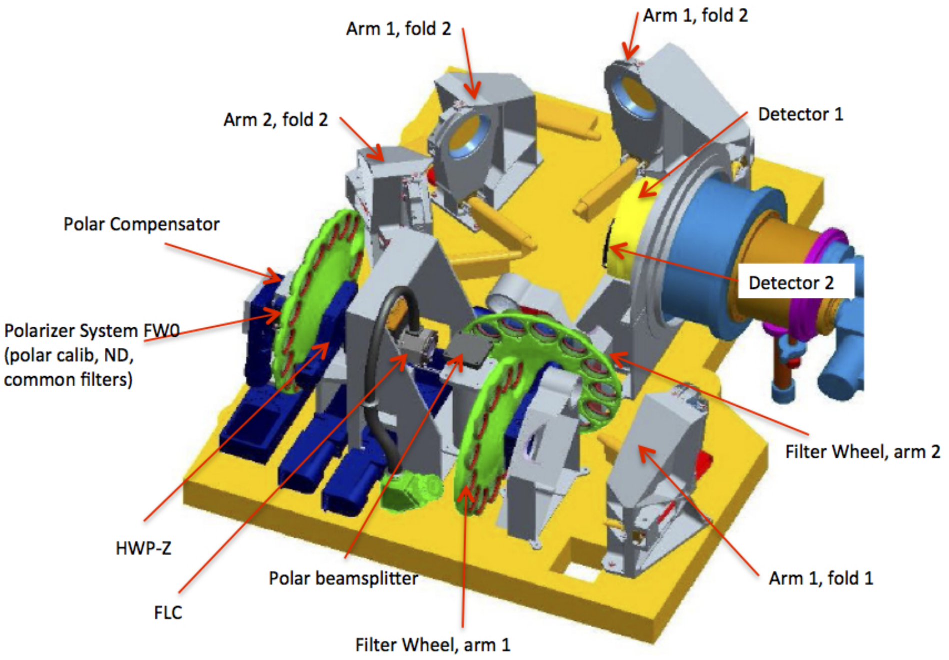

Figure 2.3: ZIMPOL hardware model. Some of its main elements are indicated: the polarization compensator, the Ferroelectric Liquid Crystal (FLC) modulator to the splitter, the filter wheels and the two adjacent detectors. From SPHERE User Manual.

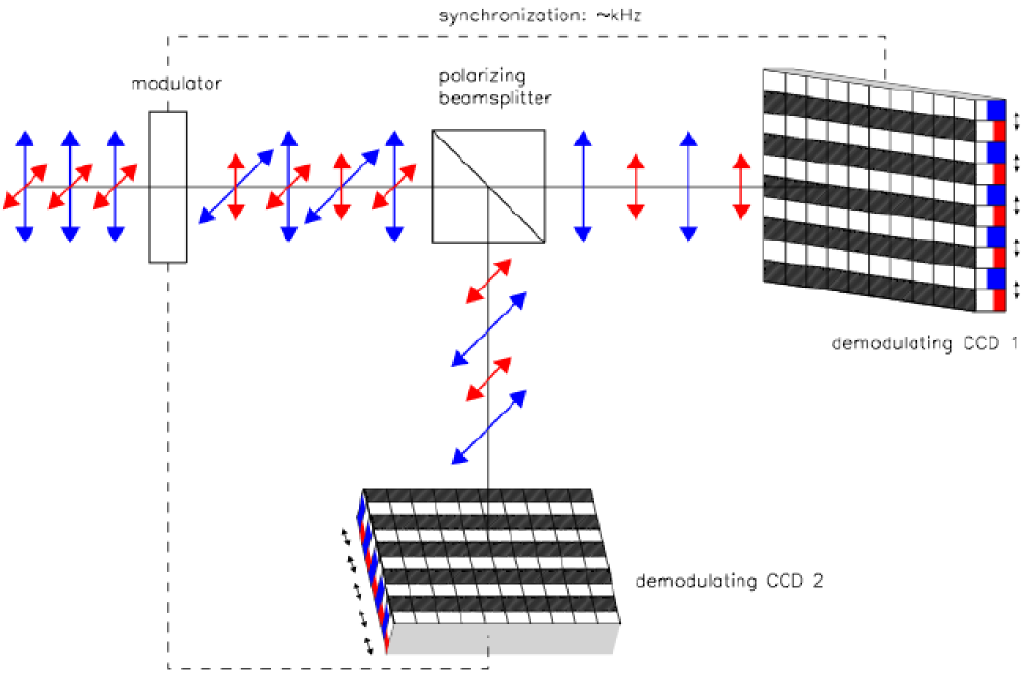

Figure 2.4: In ZIMPOL the polarized signal is modulated on CCD1 and CCD2 through a beam-splitter. The detectors are read after a charge shifting sequence that is synchronized to the polarization swap. From SPHERE User Manual.

proportional to the intensity. The main advantages of this technique are:

- both images are created quasi-simultaneously since the modulator is faster then the seeing variations;
- both images are recorded by the same pixels reducing significantly flat-fielding issues;
- differential effects due to the storage of two images in different buffer pixels can be compensated with a demodulation phase-switch between subsequent images;
- only very small differential aberrations appear between the two frames;
- the differential signal does not suffer from chromatic effects due to diffraction or speckle chromatism.

This technique also guarantees a low read out noise. Moreover, each ZIMPOL arm provides a full polarimetric measurement and the two arms can perform simultaneous polarimetry in the same or in two different filters. The instrument offers a wide selection of broadband and narrowband filters divided in three different filters wheels, one (FW0) upstream to the beam-splitter and one in each of the two cameras optical paths (FW1 and FW2). FW0 is common to the two CCDs and includes both filters and polarimetric components used to calibrate the intrinsic polarization of ZIMPOL, therefore the remaining filters located in this wheel can not be used for polarimetric imaging but only for imaging observing mode (see below). Some filter type are present in both FW1 and FW2 to perform an additional differential imaging while others are present only in one of them.

ZIMPOL can be used also as an imager, providing high contrast imaging in broad and narrow band filters and also DBI. Image quality is slightly ($\sim 10\%$) better than polarimetric observing modes.

ZIMPOL operates in the visible between 0.5 μm and 0.9μm, and is diffraction limited for $\lambda > 0.6\mu$m with a sampling of $(3.6\text{mas})^2$/pixel and a field of view of $3.5'' \times 3.5''$ with access to a total field of view of $8''$ diameter by an internal field selection mechanism. Both the pupil and the field stabilization are available for imaging observing mode, while in polarimetry only field stabilized or fixed derotator with stable and minimized instrumental polarization is possible. All the details about ZIMPOL observing modes and performances can be found in Thalmann et al. (2008). Additional technical descriptions of the instrument are in Gisler et al. (2004); Bazzon et al. (2012); Schmid et al. (2012); Roelfsema et al. (2014) and references therein.

2.2.3 IFS

The integral field spectrograph of SPHERE is based on a lenslet-based Integral Field Unit (IFU) called BIGRE (Antichi et al. 2009). It produces about 21000 spaxels and their spectra are aligned with the detector columns, covering an area of 5.1×41 pixel each. IFS was designed to work in two different wavelength ranges: 0.95 and 1.35 μm (YJ mode) with a spectral resolution of $R \sim 50$ or between 0.95 and 1.65 μm (YH mode) with R$\sim$ 30. IFS (Claudi et al. 2008) is able to Nyquist sample the whole field of view ($1.73''\times1.73''$, 7.46 mas/pixel) at 0.95μm. The purpose of this instrument is thus to realize diffraction limited integral field spectroscopy. To do this, the whole IFS system, which is downstream the entrance slits array, should only reimage and disperse these slits with the highest optical stability and a

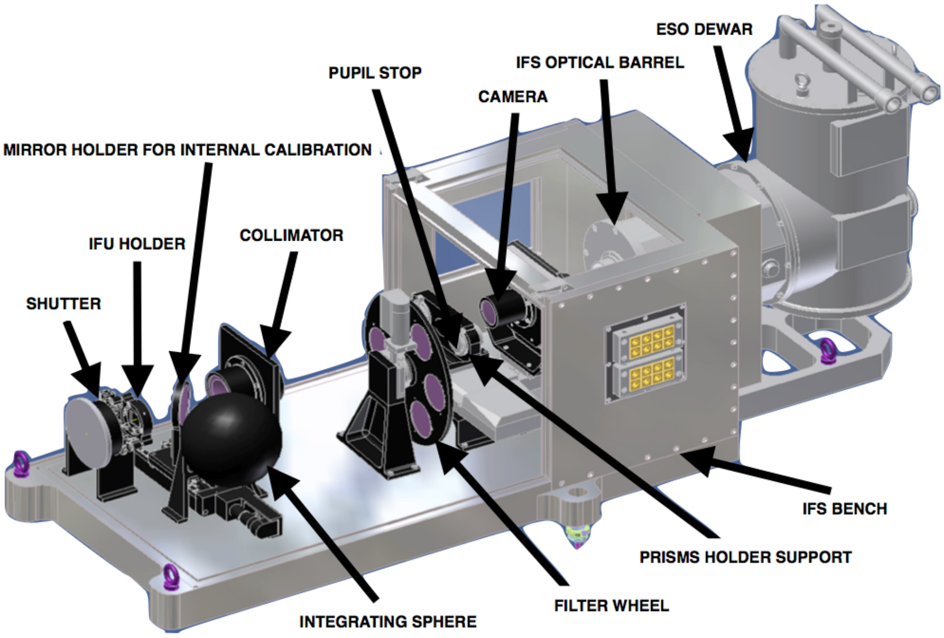

Figure 2.5: The IFS opto-mechanical concept. From SPHERE User Manual.

Observing modes	**DBI, DPI, CI**	**LSS**
Spectral range	0.95 – 2.32 μm: NB and BB filters	0.95 - 2.32 μm: R$\sim$ 50 0.95 - 1.65 μm: R$\sim$ 350
FOV	11” x 11”	11” slit
Coronagraph	None, or with classical or apodized pupil Lyot coronagraphs, 4QPM	Central blocking
Stabilization	Pupil- or Field-stabilized Field stabilized	
Sampling	(12.25mas)^2/pixel, Nyquist-sampled at 0.95 μm	

Table 2.1: IRDIS observing modes properties.

good optical quality. Finally a very peculiar characteristic of IFS is the possibility to derive accurate spectra using the spectrum subtraction technique (Thatte et al. 2007).
The optimized IFS optical design is a fully dioptric concept design, shaped by several optics located all along a unique optical axis. It includes the IFU, the collimator, a filter wheel with several neutral density filters, a prisms holder with the two different prisms, the camera, the detector and also a unit for internal calibration made of several light sources (Fig. 2.5).

2.2.4 IRDIS

The most versatile subsystem of SPHERE is IRDIS (Dohlen et al. 2008). It can work in a spectral range between 0.95 and 2.32 μm providing Dual Band Imaging (DBI, Vigan et al. 2010) Dual-Polarization imaging (DPI, Langlois et al. 2014), Classical Imaging (CI) or Long Slit Spectroscopy (LSS, Vigan et al. 2008). The image scale of 12.25 mas/pixel is consistent with Nyquist sampling at 0.95μm and the FOV is of $11'' \times 12.5''$. Two parallel images are

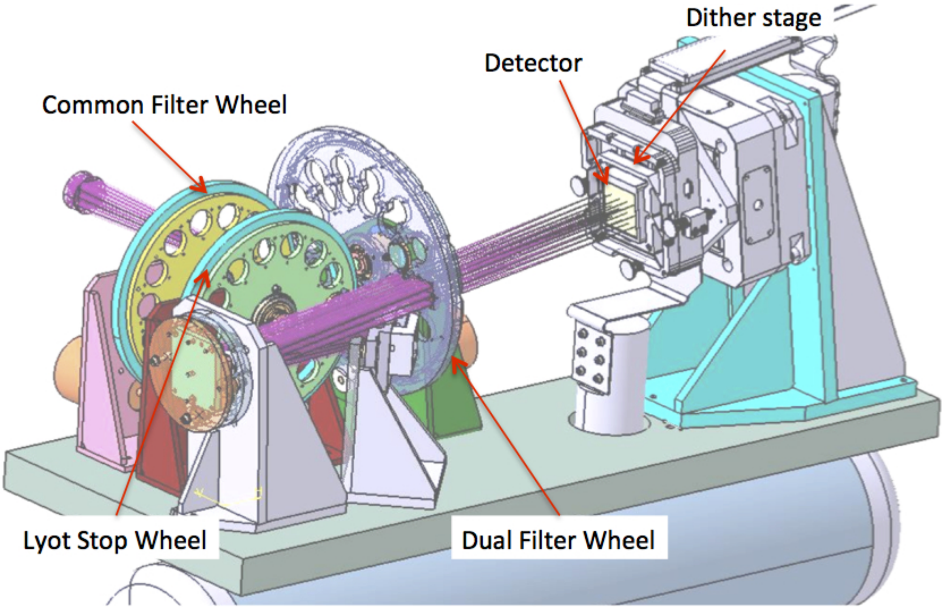

Figure 2.6: Inside view of the IRDIS cryostat. The CPI beam comes from the left, goes through the common filter and Lyot stop wheels, is split in two, then goes through the dual filter wheel before landing on the infrared detector. From SPHERE User Manual.

projected onto about half of the available area of the same 2kx2k detector. IRDIS optical path and mechanics are shown in Fig. 2.6 an different characteristics of the observing modes are summarized in Table 2.1. The main mode of IRDIS is the DBI mode, providing images in two neighboring spectral channels with minimized differential aberrations. In the CI mode, broad, medium and narrow-band filters are defined. LSS at resolving powers of 50 and 350 is provided exploiting a coronagraphic slit and also suitable dispersers. Finally a DPI mode is also offered; it uses polarizers providing images in the two polarization directions at the same time. The common filters wheel provides blocking filters, broadband and narrowband filters. The Lyot stop wheel includes Lyot stops for the coronagraphs of the CPI and the two LSS prisms. Finally the dual filter wheel holds a series of filter pairs corresponding to different spectral features in modelled exoplanet spectra, polarizers and a pupil-imaging lens for self calibration.

2.3 SHINE

The SPHERE Consortium designed a large survey targeting nearby young stars in order to contribute to planet formation theories, observing about several hundreds of young stars. The expected detections number of a few tens of planets or brown dwarfs formed in the disk, will allow a first statistical discussion of the planetary systems properties. It should then be possible to derive the distributions of planets parameters such as mass, semi-major axis and eccentricities as a function of stellar mass. This is the main purpose of SHINE, added together with a first-order planet characterization of the new discoveries and the characterization of planet-disk connection (working in parallel with the Disk program). SPHERE will be used in the IRDIFS mode, taking advantage of the complementary capabilities of IFS (in YJ bands)

Priority	Early-type	Solar and Low-mass
P0	special targets	
P1	20 MGs + 40 ScoCen	120 MGs + 20 Field
P2	20 Field + 40 ScoCen	140 Field
P3	20 Field + 40 ScoCen	140 Field
P4	20 Field + 40 ScoCen	140 Field
P5	Bad weather Backup or Filler	

Table 2.2: SHINE final targets distribution and their priorities.

and IRDIS (in H band) to enable planet detection and characterization in the inner regions or in the IRDIFS_EXT mode (IFS in YH and IRDIS covering K band).
For a few selected targets with known substellar companions, characterization observations (e.g., IRDIS Long-Slit Spectroscopy; Zimpol H_α imaging) will also be performed. The program includes also the search for H_α emission due to accretion onto very young substellar objects (Zhou et al. 2014). The availability of Paschen β from IFS spectra will allow further diagnostics of these phenomena.

2.3.1 Sample Definition

Stars in the SHINE survey were selected in order to satisfy the following criteria:

- Declination limits between -84 to +21
- Exclusion of spectroscopic and close visual binaries (projected separation $< 6''$).
- AO flux $>$ 5 e-/subpup/frame or $R < 11.5$
- Age $<$ 800 Myr
- Distance $<$ 100 pc except for members of the Scorpoin-Centaurus association
- $M_\star < 3M_\odot$

Among this star list, a sub sample composed of Sco Cen members was identified in order to have a homogeneous sub-sample of young stars.
Simulation of expected detections on the SHINE star list were then performed using QuickMESS code (Bonavita et al. 2013) to estimate the potential for planet detectability of each target, then a ranking was assigned.
The final SHINE target list is made up of 6 categories as described in Table 2.2. Groups from P1 to P4 contain mainly known members of nearby young moving groups (Beta Pic, Tucana, Columba, Carina, TW Hya, Argus, AB Dor) within 60 pc, the known members of the youngest groups (those listed above except AB Dor, which has a significantly older age) between 60 to 80 pc and the Sco-Cen stars (using the 50 AU outer cut-off), taking stars alternatively from the two list, sorted according to planet detection probabilities. A number of special targets (P0 sample) were identified due to their high scientific interest, such as the presence of already observed planets, a circumstellar disk, protoplanet candidate or a planet known from RV that should be detected with SPHERE. Finally, a sample of backup targets

(P5) to be observed in case of bad weather conditions or short time slot consists of stars with well known planets, stars with ranking just outside SHINE selection criteria in terms of age, distance, mass function value, on-sky calibrators, other stars with RV signatures etc.

2.3.2 Work organization

SHINE activities are assigned to four different Working Packages (WP) and to the Coordination group.

WP1: Targets & Preparatory observations works on the sample definition and on the collection of all the useful data for refinement of stellar parameters. It provides all the necessary informations for the observations and characterization of SHINE targets and propose observing strategy. It is in charge of the Target Database functionality;

WP2: Observations & Data analysis activities include the study of SPHERE calibration plan, the development of tools for observing preparation and data reduction, including science analysis routines and provides performances estimation. For each observing run, a small group of people in rotation (Data Reduction Team, DRT) curates the IRDIS and IFS data calibration, reduction and detected candidate companions characterisation up to the candidate photometry and astrometry determination and update the target database accordingly;

WP3: Planet Identification & Characterization is in charge of False Alarms Tools implementation and atmosphere and orbital characterization based on theoretical models and orbital fitting tools. It plans the strategy of second epoch observations and complementary observations with other instruments.

WP4: Statistical Analysis aims to the statistical characterization of the complete SHINE survey. It contributed to both the *a priori* sample definition and the *a posteriori* statistical characterization of the complete survey. It will use planet and brown dwarf populations synthesis and statistical tools.

As a member of this consortium, mainly in the WP2 sub-group, I was in charge of several activities: I performed 3 runs of observation (11.5 nights) with SPHERE@VLT. I also performed the first-look data reduction and analysis of several target observed with IFS and IRDIS simultaneously, such as HD 106906 (Lagrange et al. 2016), HD100453 (Benisty et al. 2017), RX J1615.3-3255 (de Boer et al. 2016), SAO 206462 (Maire et al. 2017), HIP 73145 (Feldt et al. 2017), HD 141569 (Perrot et al. 2016), HD 142527 (Claudi et al. in prep), HR 3549 Mesa et al. (2016). I then performed deeper analysis on the SHINE targets HD100546 (Garufi et al. 2016, Sissa et al. in prep), T Cha (Pohl et al. 2017), Proxima Cen (Mesa et al. 2017), LkCa 15 (Thalmann et al. 2016).
In order to handle ZIMPOL data, I contributed to the first ZIMPOL imaging technical analysis and to the development of the imaging data reduction procedure and scientific analysis techniques (Schmid et al. 2017) that were later used in Antoniucci et al. (2016).

Chapter 3

Planets embedded in disks

Recently developed high-resolution imaging instruments like SPHERE and GPI provide the excellent capability to directly obtain images of protoplanetary disks in scattered light and thermal emission. In principle, this makes possible to observe planets in their birthplace and understand their interaction with the disk: the planets and planetesimal systems seen orbiting around the main sequence stars are thought to be already in place during the protoplanetary disk phase, but obscured by the rest of the disk so that it is difficult to observe them. In addition, it is expected that circumstellar disks evolution and its dissipation have influences on the subsequent planetary system. On the other hand, forming planets can introduce disk chemistry alteration, a change of the dust-to-gas ratio, reduce gas reservoir, and affect disk geometry. In fact, the presence of the planets induce gravitational perturbation on the disk and it is thought to be the prime cause of carving spirals and opening gaps. Also migration mechanisms are important in this phase since they contribute to the system geometry. To understand the formation process of planets, we need to study the initial condition and evolution of circumstellar disks, and how the disk can be shaped by ongoing planet formation. Protoplanetary disks are found around young newly formed stars, such as T Tauri or Herbig Ae/Be stars, that can also show jets.
The properties of protoplanetary disks are mainly inferred from spectroscopic and direct imaging observations. At mid-infrared through millimeter wavelengths, they trace large, mm-sized grains located in the disk midplane. Optical and near-infrared scattered light observations probe (sub-)micron-sized dust grains in the upper disk surface layers (see e.g. Dullemond & Dominik 2004). Protoplanetary disks around Herbig Ae/Be stars are in general brighter and wider than their lower mass T Tauri star counterparts. In both cases, they are thought to be made of gas, mostly H_2, with a small fraction ($\sim 1\%$) of dust, so that they are optically thick for the star light: their temperature changes along the disk from 1000 K in the innermost regions, where hot compact rings are observed (such as in HD97048 van der Plas et al. (2009), HD100546 Brittain et al. (2013)) down to 30-10 K, in the most distant part, where the stellar light barely reaches the circumstellar material, and the disk is weakly illuminated by the star (see e.g. Dullemond & Monnier 2010). They can extend up to 1000 AU (Yorke & Bodenheimer 1999) and can appear both flat or flared (Garufi et al. 2017).

Till now, only a few young candidate planets have been observed with high-contrast imaging, embedded in the protoplanetary disk surronding a few young stars. The first one was HD 100546 b (Quanz et al. 2013), that was detected in the L' band with NACO and confirmed with second epochs observations and by Quanz et al. (2015), Currie et al. (2014c)

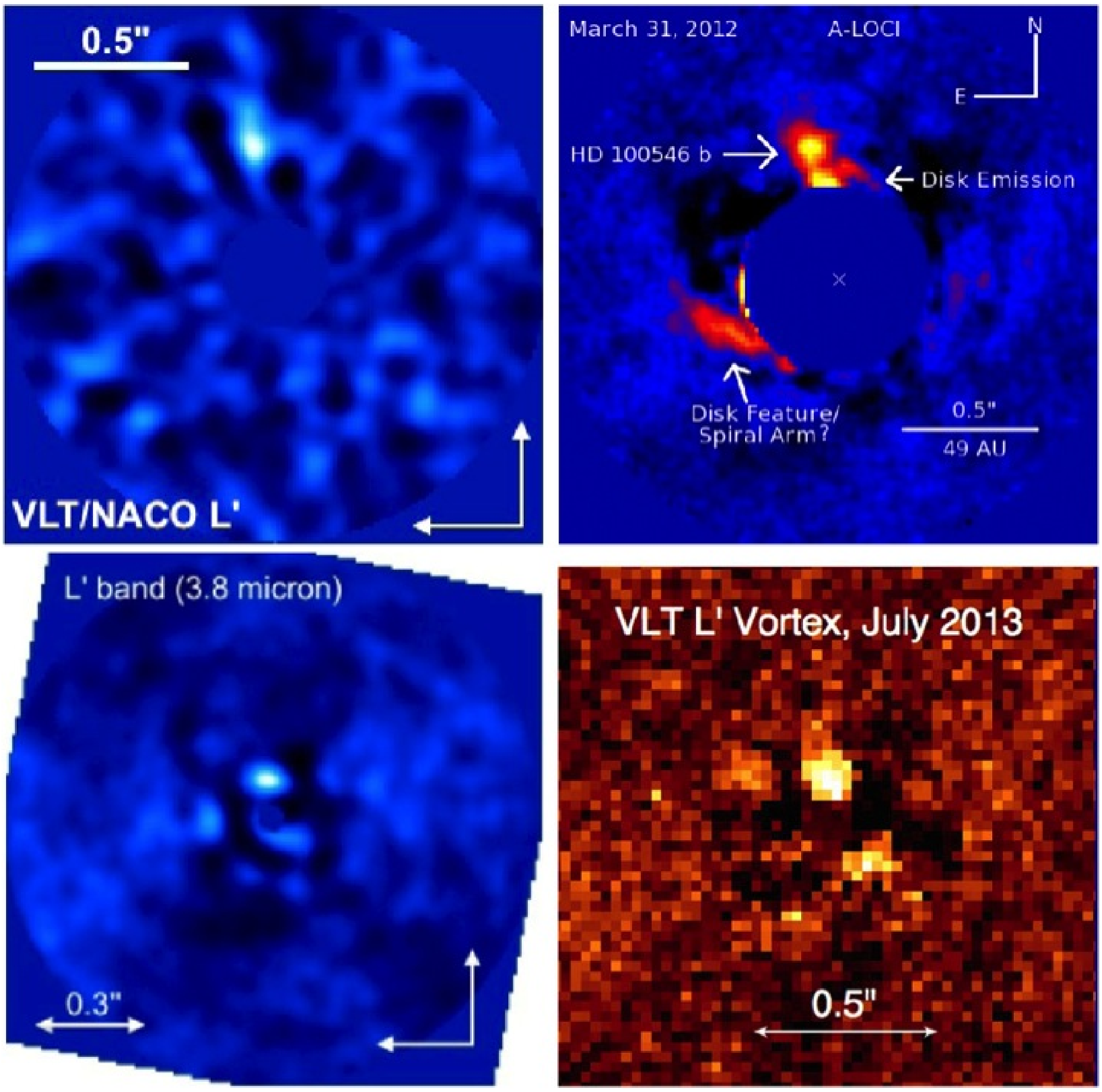

Figure 3.1: Top: Detection of HD 100546 b in NACO L' band (Quanz et al. 2013) and NICI L' band (Currie et al. 2014c). Bottom: Detection of HD 169142 candidate in NACO L' band (Reggiani et al. 2014) and simultaneously using the NACO annular groove phase mask vector vortex coronagraph (Biller et al. 2014).

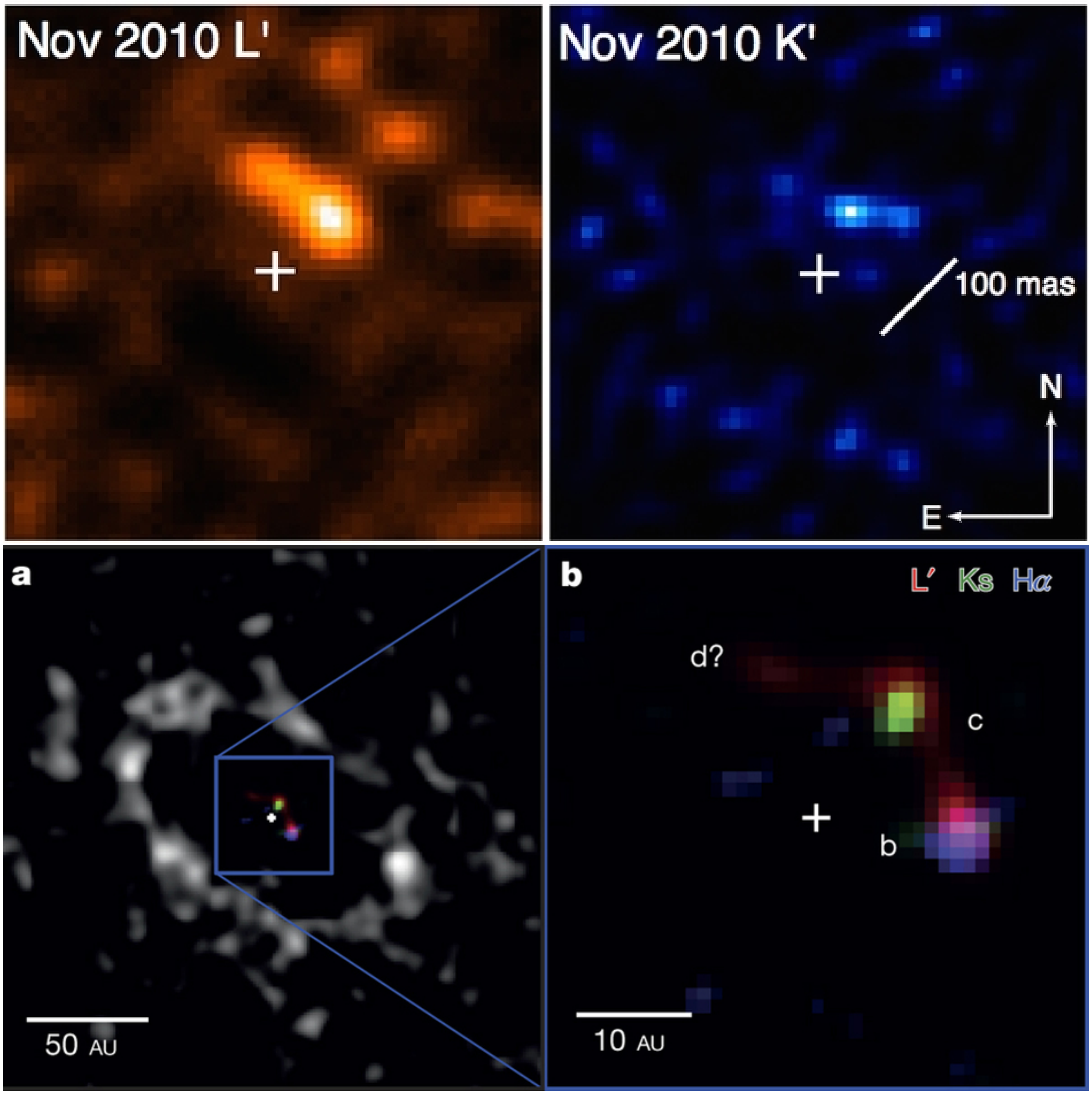

Figure 3.2: Detection of LkCa 15 b in L' and K_S band by Kraus & Ireland (2012) (top) and in H_α by Sallum et al. (2015b) (bottom).

and Currie et al. (2015). Another candidate companion was proposed to HD 169142 by two quasi-simultaneous works (Reggiani et al. 2014; Biller et al. 2014) based on NACO L' observations in standard coronagraphy and exploiting a vortex mask, respectively. Actually, for both these two systems, other observational techniques provided evidence for a second companion therefore, if confirmed, they would be the first two systems where the formation of multiple planets and their interactions with the disk can be studied directly. T Cha b was detected using sparse aperture marsking (SAM) technique by Huélamo et al. (2011) in the L' and K' broadband filters of NACO at VLT but following works (see e.g. Sallum et al. 2015a) did not confirm it. Exploiting non-redundant aperture marsking (NRM) technique, Kraus & Ireland (2012) detected LK Ca 15 b in the L' and K' broadband filters of NIRC2, the Keck-II AO facility, and later confirmed by Sallum et al. (2015b) with observations in the MagAO H_α filter and NRM in K_S and L' broadband at LBT that show the presence of two additional objects. However, detections of these objects at shorter wavelengths (J- and H-band) is still debated.

This Chapter presents my major contributions to the study of four systems in the early phases of their evolution using VLT/SPHERE. I'll start with the most massive and more distant object I studied, Z CMa: this is a binary system that was observed at H_α wavelengths, looking for the presence of two jets. For this object, no infrared image of the system was acquired since the two close massive stars present in the system prevented us to detect the circumstellar disk. ZIMPOL H_α mode was used within the Other Science Program to observe and study the jets in ZCMa (Antoniucci et al. 2016).
The study of HD 100546 system was the main activity of my work. This system has a key role in the planet formation context since it hosts a complex and wide disk, showing several asymmetrical structures, and footprints of two embedded forming planets. The main topic of my study was the detection and the characterization of the two proposed companions but I found out that the presence of the disk prevents their detection at near-IR wavelength. However, the HD 100546 SHINE campaign exploiting IFS and IRDIS provided new insight of the system, that were partially scooped by simultaneous papers based on GPI images (Rameau et al. 2017; Follette et al. 2017), SPHERE direct competitor. The difficulties I found detecting planets in the near infrared are also reported by other studies (such as for instance the cited paper by the GPI group) and on other targets (e.g. HD 169142, Ligi et al., submitted), and provide a caveat on the interpretation of data acquired at these wavelength for very young targets.
T Cha is a T Tauri star, surrounded by a transition disk. With the new SHINE observations I aimed to push down the detection limits for planets orbiting its star and characterize candidate companions, if any. Since there is no hint of companions in the field, my work, included in the paper Pohl et al. (2017), consisted on IFS and IRDIS data reduction, the detection/mass limits determination and the characterization of a background object, that was possible analysing archival data of NACO and HST.
Lastly, LkCa 15 is the only system where a candidate accreting protoplanetary object was observed embedded in the disk. I analysed both SHINE images and the ZIMPOL H_α images acquired during SPHERE Science Verification. Near-IR images could detect the disk but not the claimed candidate, whereas H_α images were found out to be of very poor quality. This activity contributed to the paper Thalmann et al. (2016).

SHINE observations can provide a limit to the mass of unseen companions, through the

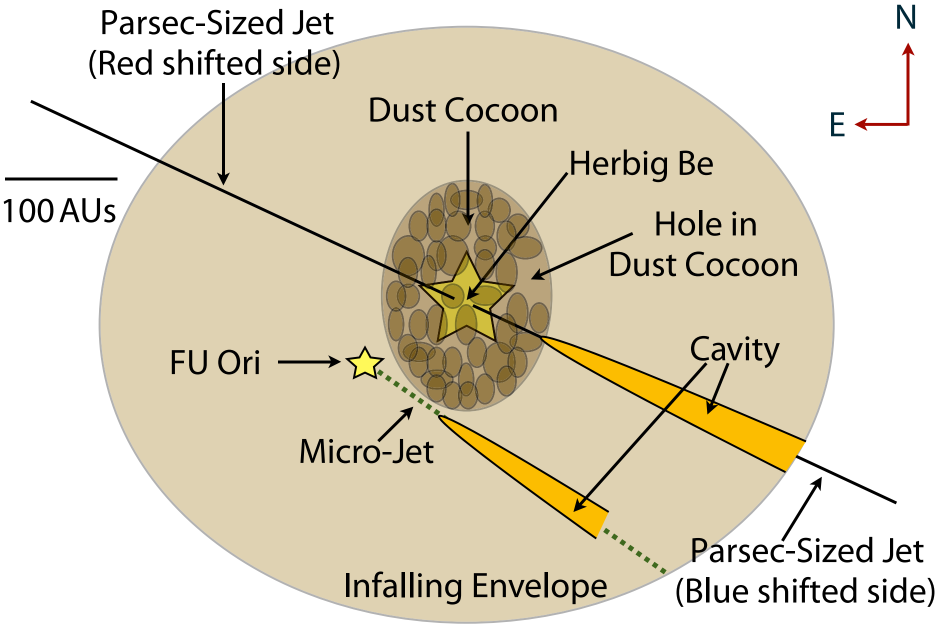

Figure 3.3: Schematic (non-scaled) picture of the Z CMa system, as seen from Earth. The two stars are separated by $\sim 0.1''$(100 AU assuming a distance to Z CMa of 1150 pc). The large jet associated to the primary, with an orientation of 245° is indicated by the black line, while the micro-jet, with an inclination of 235°, is indicated by the green dashed line. From Canovas et al. (2012).

use of theoretical models. In all the cases, I used AMES-COND models (Allard et al. 2003), that is consistent with a hot-start planetary formation due to disk instability, to compare predicted luminosity with the contrast limit and derive the mass limit. These models predict lower planet mass estimates than cold-start models (Marley et al. 2007) which, instead, should better reproduce the core accretion scenario, and affect considerably detection limits. However, these last imply that no planets (only brown dwarfs) will be seen around typical stars in the SPHERE sample, and cannot reproduce, for example, neither HR 8977bcde spectra (Currie et al. 2014a) nor β Pictoris b (Bonnefoy et al. 2014), because the implied large masses will be incompatible with dynamical constraints. Mordasini (2013) discuss this point more in depth.

3.1 Z CMa[1]

Z CMa is a young binary system. It is composed of a Herbig Be star embedded in a dust cocoon (Szeifert et al. 2010), the NW one, and a FU Orionis object (Hartmann et al. 1989; Hartmann & Kenyon 1996). FU Ori stars are believed to be T Tauri stars experiencing episodes of extremely rapid disk accretion (see e.g. Hartmann & Kenyon 1996). Both stars are driving an extended jet (Whelan et al. 2010) at slightly different position angles (P.A.): 245° (east of north) for the Herbig and 235° for the FU Ori (Fig. 3.3). The system is located

---

[1] Section mostly re-edited from Antoniucci et al. 2016. In this work I was in charge of ZIMPOL data reduction and differential imaging. In this section and in the following, I'll use the first persons singular when describing the activity I was directly involved.

Frame id	DIT	NDIT	mode	FW0	FW1	FW2
OBS090_0084.fits	30	5	I	OPEN	CntHa	B_Ha
OBS090_0085.fits	30	5	I	OPEN	CntHa	B_Ha
OBS090_0086.fits	30	5	I	OPEN	CntHa	B_Ha
OBS090_0087.fits	30	5	I	OPEN	B_Ha	CntHa
OBS090_0088.fits	30	5	I	OPEN	B_Ha	CntHa
OBS090_0089.fits	30	5	I	OPEN	B_Ha	CntHa
OBS090_0090.fits	30	5	I	OPEN	CntHa	B_Ha
OBS090_0091.fits	30	5	I	OPEN	CntHa	B_Ha
OBS090_0092.fits	30	5	I	OPEN	CntHa	B_Ha
OBS090_0093.fits	30	5	I	OPEN	B_Ha	CntHa
OBS090_0094.fits	30	5	I	OPEN	B_Ha	CntHa
OBS090_0095.fits	30	5	I	OPEN	B_Ha	CntHa
OBS090_0096.fits	30	10	I	OI_630	OPEN	OPEN
OBS090_0097.fits	30	10	I	OI_630	OPEN	OPEN
OBS090_0098.fits	30	10	I	OI_630	OPEN	OPEN
OBS090_0099.fits	30	10	I	OI_630	OPEN	OPEN
OBS090_0100.fits	30	10	I	OI_630	OPEN	OPEN
OBS090_0101.fits	30	10	I	OI_630	OPEN	OPEN

Table 3.1: Overview of the observations for Z CMa. DIT, in seconds, NDIT, observation mode and filters used are reported.

at a distance of 1150 pc, in the CMa OB 1 association (Herbst et al. 1978), and has an age of 0.3 Myr. The two sources are separated by $0.1''$ and only recently high angular resolution observations with adaptive optics systems and interferometers have allowed the separate determination of the properties of the two sources (Benisty et al. 2010; Hinkley et al. 2013; Canovas et al. 2015; Bonnefoy et al. 2017). The masses of the two stars are 12 $M_{\odot}$ and 3 $M_{\odot}$ respectively (Alonso-Albi et al. 2009), but more recent observations lead to a more massive HBe, in the range of 16-38$M_{\odot}$ (Bonnefoy et al. 2017).

I analysed the structure of the two jets of Z CMa exploiting ZIMPOL high angular resolution optical observations in the [OI] 6300Å and Hα lines. The extreme AO performance of SPHERE allowed me to have direct images of the Z CMa system at unprecedented high contrast and spatial resolution ($\sim$0.03$''$). Simultaneous images of Z CMa in H_{α} and in the adjacent continuum were acquired with the two ZIMPOL cameras using the B_Ha (λ_c=655.6 nm, $\Delta\lambda$=5.5 nm) and Cnt_Ha (λ_c=644.9 nm, $\Delta\lambda$=4.1 nm) filters. Exposures were taken in field-stabilized mode using two different field rotation angles and swapping the filters in front of each camera to optimize artefact removal during the reduction. This resulted in 60 frames per filter (15 for each set-up) for a total exposure time of 30 minutes. Images in the [O I] line with the OI_630 filter[2] (λ_c=629.5 nm, $\Delta\lambda$= 5.4 nm) were obtained in field-stabilized mode using two different field rotation angles for a total of 30 frames and an integration time of 30 minutes. Details are reported in Table 3.1. The atmospheric conditions remained stable during observations (seeing $\sim$ 0.8-1$''$, $\tau_0 \sim$ 2.5 ms).

---

[2] Simultaneous observations on the continuum are not possible with this filter, which is mounted on the common wheel of the two cameras.

The raw data were processed using the SPHERE-ZIMPOL IDL pipeline (version 1.1) developed at ETH Zürich, which performs bias, dark, flat-field correction, re-centering of the dithered frames, and allows for derotation, selection, subtraction, and average or median combination of the frames. The Cnt_Ha exposures were used to remove the continuum emission from the B_Ha and OI_630 filter images, so as to produce continuum-subtracted H_α and [O I] images in which the line-emitting structures around the components are evidenced. For the H_α observations, I performed a frame-by-frame subtraction of the B_Ha and Cnt_Ha images to remove the continuum emission and evidence the line-emitting structures around the components. Prior the subtraction, each Cnt_Ha frame must be normalized to the corresponding B_Ha frame to account for the different filter band-passes. The normalization factor was empirically computed from the ratio of the total counts measured in the same region of the two images. The comparison between the photon count ratios between the two Z CMa components in the continuum and in the H_α frames clearly reveals a strong H_α emission from the NW component, in agreement with previous observations of the separate spectra of the two stars (Hinkley et al. 2013). This makes it difficult to find a normalization that efficiently removes the intense continuum from both stars at the same time. Indeed, if I normalized to the signal of the SE component, the point-like H_α emission from the Herbig star creates a very strong residual PSF signal that hampers the detection of the structures around both objects. Conversely, by normalizing to the Herbig component, I oversubtracted the signal from the FU Ori and eventually create a deep residual negative region around the binary where no information can be retrieved. The best compromise is found with a normalization factor calculated over a region including both components. After de-rotating the observations taken at a different field position angles, I finally performed a median of all the subtracted frames.

For the [O I] data, I produced a median [O I] image from all the frames, after de-rotating those obtained at a different field position angle. I also created a median image of the Cnt_Ha frames, which I normalized to the signal of the Herbig star and then subtracted from the median [O I] image. The residuals from continuum subtraction are more compact for [O I], probably because the point-like [O I] emission from the NW source is much weaker than H_α.

The final continuum-subtracted [O I] and H_α images are shown in the Fig. 3.4. My images reveal extended emission from both sources: an extended collimated jet from the FU Ori component and a more compact and poorly collimated emission SW of the Herbig star. These structures are especially evident in the [O I] image, which is much less affected by subtraction residuals than the H_α image. In the [O I] continuum-subtracted image it is possible to trace the flows down to about ~ 90 mas from the sources (corresponding to ~ 105 AU). The collimated jet from the FU Ori object can be identified with the Jet B observed in [Fe II] by W10, which travels at radial velocities between -100 and -400 km/s. The morphology of the jet in our [O I] image is however much more structured than in the [Fe II] images.

In the paper Antoniucci et al. (2016), we describe in detail that this detailed data analysis and the comparison of SPHERE images with images in Whelan et al. (2010), allow retrieving several system properties:

- Our images reveal extended emissions from both sources: a fairly compact and poorly collimated emission SW of the Herbig component and an extended collimated and precessing jet from the FU Ori component.
- The compact emission from the Herbig star is compatible with a wide-angle wind and

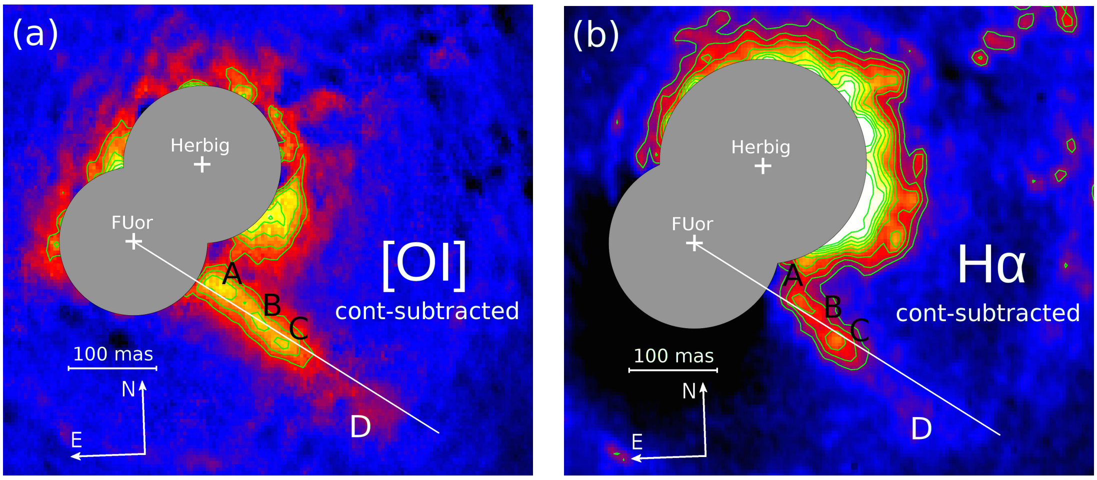

Figure 3.4: Continuum-subtracted [O I] and H_α images of the Z CMa system.The centroids of the two stars and the position of the main knots of the FU Ori jet are indicated. Areas heavily corrupted by artefacts around the star centroids have been masked.

is possibly connected to the recent outburst events shown by this component.

- The FU Ori jet is traced down to 70 mas (80 AU) from the source and is highly collimated with a width of 26-48 AU at distances 100-200 AU, which is similar to the width of jets from T Tauri stars. This strongly suggests that the same magneto-centrifugal jet-launching mechanism also operates in FU Oris.
- The observed jet wiggle can be modelled as originating from an orbital motion with a period of 4.2 yr around an unseen companion with mass between 0.48 and 1 $M_\odot$.
- The jet mass loss rate $\dot{M}$ was derived from the O [I] luminosity is between 1×10^{-8} and 1×10^{-6} $M_\odot$/yr. This is the first direct $\dot{M}$ measurement from a jet in a FU Or. If we assume previous mass accretion rate estimates obtained through modelling of the accretion disk, the derived range of $\dot{M}$ would imply a very low mass-ejection efficiency ($\dot{M}/M_{acc} \lesssim 0.02$), which is lower than that typical of T Tauri stars.

3.2 HD 100546: two candidate planets embedded in a transitional disk

HD100546 is a well studied Herbig Ae/Be star with spectral type B9Vne (Levenhagen & Leister 2006) which harbours a large disk. Several studies have been conducted in the past years on this disk, spanning from spectroscopic and photometric analysis to direct imaging. The first evidence of the presence of the disk was obtained spectroscopically by Hu et al. (1989). The disk was first imaged in scattered light by Pantin et al. (2000) and many successive works revealed the complexity of its geometry by means of both (sub-)millimeter images (e.g., Walsh et al. 2014; Pineda et al. 2014; Wright et al. 2015) and scattered light images (e.g., Augereau et al. 2001; Ardila et al. 2007; Quanz et al. 2011; Garufi et al. 2016). Today it is thought HD100456 may host at least two planets (Quanz et al. 2013, 2015; Currie et al. 2015) located at ∼ 55 AU (hereafter CCb) and ∼ 13 AU (hereafter CCc) from the central star. This makes the system a powerful laboratory to study planet formation and planet-disk interaction. Quanz et al. (2015) inferred the temperature and emitting radius of CCb in the L' and M bands and concluded that what they imaged could be a warm circumplanetary disk rather then the planet itself. An extended emission at near-IR wavelengths linked with this candidate planet was also detected by Currie et al. (2015) at $0.469 \pm 0.012''$, PA=7.04°±1.39°. Its spectrum is extremely red, indicating that it could still be embedded by accreting material. The existence of an additional embedded planet (CCc) was proposed by Brittain et al. (2013), who ascribed the variability of the CO roto-vibrational lines to a compact source of emission at ~15 AU from the central star. A claim of detection of this second planet was also advanced by Currie et al. (2015) but this last observation might also be interpreted as a bright region of the disk inner rim (see Rameau et al. 2017).

First observations of HD100546 with VLT/SPHERE were presented in Garufi et al. (2016), where it was found that the disk around HD 100546 is truncated at about 11 AU and the cavity is consistent with being intrinsically circular. In this section, I present the results of a 2 yr campaign of observations in direct imaging with VLT/SPHERE that includes both pupil tracking and polarimetric observations. I am the leader of the analysis of these data and I'll be the firt author of a paper in preparation that describe it. The observing strategy, sky conditions and the reduction of these dataset are described in Sect. 3.2.1. The results for the disk and planets are given in Sect. 3.2.2 and 3.2.3 respectively, and, lastly, a discussion on the possible relation between the HD100546 planets and the disk is given in Sect. 3.2.4. For the analysis, we consider a source distance of d=109 ± 4 pc (Gaia Collaboration et al. 2016), a stellar mass of M_*=2.4$M_\odot$ (Brittain et al. 2014), and apparent magnitudes of J=6.42, H=5.96, and K=5.42 (Cutri et al. 2003), as well as L'=4.52 and M'=4.13 as in Quanz et al. (2015). For the disk, we assume an inclination i=42° (Ardila et al. 2007; Pineda et al. 2014) and PA=146° (Pineda et al. 2014). We refer to the companion candidates HD100546b as CCb and HD100546c as CCc.

In the last months, two papers on the same target based on GPI data (Follette et al. 2017; Rameau et al. 2017) were published. Several results are common between our study and the GPI ones, but there are also a few differences. They will be highlighted in the text.

3.2.1 Observations and data reduction

Observations

HD100546 was observed with SPHERE at different epochs as part of the SHINE program using IRDIS and IFS simultaneously: the IRDIFS mode and the IRDIFS_EXT mode were used. These observations were all carried-out with the `N_ALC_YJH_S` apodized Lyot coronagraph (IWA ~ 0.1″) except for two sequences which were acquired without the coronagraph in order to study the central region (at less than 0.1″ from the star). In this case, to avoid heavy saturation of the star, a neutral density filter with average transmission ~ 1/100 was used. All data were taken in pupil stabilized mode.

HD100546 was also observed in PDI, as a part of the DISK GTO program, using IRDIS with the same coronagraphic mask as for the classical imaging. The source was observed for a total time of 21 minutes in the J band (1.26 μm) and 38 minutes in the K band (λ_0=2.181 μm) during the night of March 31st, 2016, and May 25th, 2016, respectively. We oriented the instrument position with respect to the sky in order to attenuate the low polarimetric efficiency suffered by IRDIS at certain derotator angles (de Boer & the SPHERE consortium in prep.).

Date	Obs. mode	t_{exp} [s]	Rot [°]	r_C [mas]	ND Filter	σ [″]	τ_0 [ms]	SR
Feb 6 2015	IRDIFS	1280	8.5	92.5	no	1.95		
May 3 2015	IRDIFS_EXT	3840	22.32	92.5	no	0.83	1.64	
May 29 2015	IRDIFS	6048	36.37	92.5	no	0.74	1.70	0.75
Jan 17 2016	IRDIFS_EXT	4096	22.23	92.5	no	1.95	2.20	0.83
Mar 26 2016	IRDIFS_EXT	4096	22.25	92.5	no	2.52	0.98	0.98
Mar 31 2016	IRDIS DPI J	1280	-	92.5	no	1.98	0.93	0.85
Apr 16 2016	IRDIFS_EXT	9024	29.42	no	2.0	1.24	4.20	0.77
May 25 2016	IRDIS DPI K	2304	-	92.5	no	0.75	5.10	
May 31 2016	IRDIFS_EXT	4400	28.95	92.5	no	0.87	3.71	0.45
Feb 7 2017	IRDIFS_EXT	nnnn	nnnnn	no	2.0	nnn	nnn	0.76

Table 3.2: Observations summary: Date, SPHERE observing mode, Total integration time (t_{exp}), Total field rotation (Rot), Coronagraph radius (r_C), Neutral Density Filter, average DIMM seeing FWHM on source (σ), the average coherence time τ_0 and average strehl ration (SR) coming from SPARTA data are presented.

Several of the observations were carried-out under moderate and good weather conditions (with an average coherence time, τ_0, longer than 2.0 milliseconds). Details on the full set of observations are in Table 3.2, τ_0 and Strehl ratio were measured by SPARTA, the ESO standard real-time computer platform that controls AO loop.

IRDIFS and IRDIFS_EXT data reduction

We performed the basic data reduction of IRDIS and IFS (bad pixel removal, flat fielding, image alignment) with version 0.15.0 of SPHERE Data Reduction and Handling (DRH) pipeline (Pavlov et al. 2008). Further elaboration of the images (deconvolution for lenslet-to-lenslet cross talk, refinement of the wavelength calibration, correction for distortion, fine centering of the images, frame selection) was performed at the SPHERE Data Center (DC) in Grenoble. I then applied various algorithms for differential imaging such as classical ADI (cADI, Marois et al. 2006), Locally Optimized Combination of Images (LOCI, Lafrenière et al. 2007), template-LOCI (TLOCI, Marois et al. 2014), and Principal Component Analysis (PCA, Soummer et al. 2012; Amara & Quanz 2012). These procedures are available at the SPHERE DC through the SpeCal software (R. Galicher, priv. comm.). All these procedures treat each individual spectral channel separately, or can perform a spectral differential imaging (SDI, Racine et al. 1999). I also performed Reference Star Differential Imaging (RDI), subtracting to each datacube frame a reference PSF obtained from the most similar (in terms of luminosity) star observed during the same or a close night, with the same set-up.

In addition, I used a set of customized data analysis procedures set up for the IFS data. They allow performing the PCA with 10, 25, 50, 100 and 150 principal components and then calculate the signal-to-noise map for each image. With respect to SpeCal, these custom PCA routines use simultaneously spectral and time information allowing us to perform ADI and SDI simultaneously, with a substantial gain in contrast. A detailed description of this procedure is found in Mesa et al. (2015).

I also produce coincidence maps: I multiply pixel-by-pixel differential images or signal-to-

noise maps coming from two or more different datasets. Such procedure gives as result a negative value in the coincidence image whenever at least one of the image has a negative value for a given pixel. This technique enhances stationary objects and in principle allows a statistical assessment of the probability that any (static) detected feature is real, under the assumption that noise at different epochs is uncorrelated.
The IRDIS data were also post-processed with the Karhunen–Loève Image Projection (KLIP) algorithm, using the pipeline presented in details in Zurlo et al. (2014) and Zurlo et al. (2016), and I refer the reader to these publications to have an exhaustive description of the method. In this case, I did not employ SDI between the IRDIS filter pairs.

I found that the highest quality coronagraphic observations are those from May 2015 and May 2016 while the observations obtained in February 2015, January and March 2016 are of poor quality due to poor atmospheric conditions or low system performances (set up of the Deformable Mirror was not optimal in January 2016). For the no-coronagraphic datasets, the lack of a coronagraph implies much stronger diffraction patterns and the need of using the neutral density filter, common to IFS and IRDIS, to avoid saturation close to the center. This strongly reduces the signal; for this reason the sensitivity of these images is far from optimal at separations larger than 0.1″ but they allow access to the closest separations with unprecedented spatial resolution.

IRDIS PDI data reduction

In IRDIS PDI observations, the stellar light is split into two beams with perpendicular polarization states. A half-wave plate allows to shift the orientation of the polarization four times by 22.5° in order to obtain a full set of polarimetric Stokes vectors. The data presented in this work are reduced following the double difference method (Kuhn et al. 2001) as described by Ginski et al. (2016). The resulting Q and U parameter are finally combined to obtain the polar Stokes vector Q_ϕ and U_ϕ as from:

$$Q_\phi = +Q\cos(2\phi) + U\sin(2\phi)U_\phi = -Q\sin(2\phi) + U\cos(2\phi), \tag{3.1}$$

where ϕ is the position angle of the location of interest (Schmid et al. 2006b). With these definitions, positive Q_ϕ values corresponds to azimuthally polarized light, while negative signal is radially polarized light. U_ϕ contains all signal with 45° offset from radial or azimuthal.

3.2.2 The Disk

Disk morphology

The central part of HD100546 disk resulting from RDI is shown in Figure 3.5 for both IFS and IRDIS. Here I show the result obtained for the May 3rd, 2015 observations with HD 95086 as reference star. The disk and the close companion to this last star are so faint that they do not alter the photometry of HD100546 (Chauvin & the SPHERE consortium in prep.). In both instruments, the light distribution appears elliptical, in agreement with PA=146° and the ratio between major and minor axis is consistent with an inclination of 42° (Ardila et al. 2007; Pineda et al. 2014). The SE part is brighter than the NW one. Both images show that on the near side (SW) of the minor axis there is a strong depletion in the light distribution at separation of about 0.2". The two wings detected in the H2H3 and K1K2 bands by Garufi

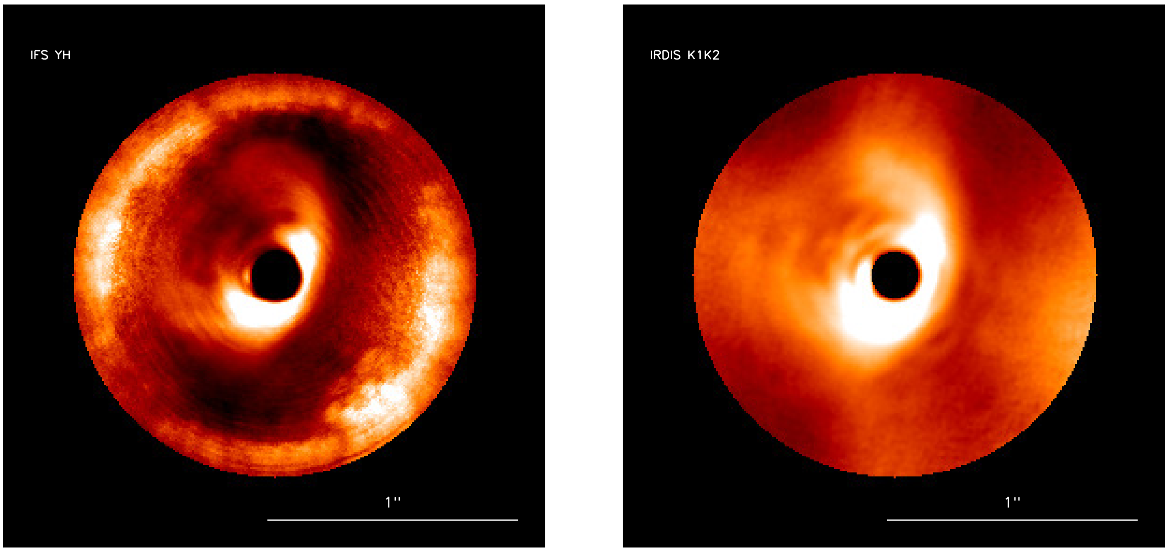

Figure 3.5: IFS collapsed YH (left) and IRDIS K1K2 (right) results for HD100546 using RDI. Both images are r^2-scaled to also enhance structures at larger radii.

et al. (2016) are distinguishable, especially the northern one. In the IRDIS data there is a thin spiral arm like structure, almost circular, at separation of $0.2''$, from PA$\sim 4°$ to PA$\sim 100°$ that is barely visible also in the IFS images. No relevant features are detected at separations greater then $\sim 0.65''$. The bright ring seen in IFS data at a separation of $0.65''$ corresponds to the SPHERE control radius [3]. The control radius at the wavelengths of IRDIS is outside the selected area. I also notice that the disk increases in luminosity going to longer wavelengths.

Fig. 3.6 shows the results of the cADI analysis of the SHINE observations of HD100546, where several disk structures are well visible. The IFS YJ collapsed image (Fig. 3.6a) shows the two wings described in Garufi et al. (2016) with a higher resolution, that allows to detect an additional curved structure in the NW side, between 284° and 350°, at separation of about $0.3''$ and a southern spot. IFS also recovered the SE fainter arm. The IFS YH collapsed image (see Fig. 3.6b) reveals a single wider northern wing. The prominent southern wing extends up to $0.7''$ and PA=90°. Two additional spiral arm-like features are also clearly present. The one that lies above the wing, and originates from it, seems to extend in the E direction up to $\sim 0.6''$ and PA=90°; the southern one has a pitch angle similar to that of the southern wing. No bright PSF-like knots are recovered along the arms at these wavelengths. I confirm the presence of a dark area just offset from the wings in the W direction, also detected in the RDI, where disk shape is less altered thanks to a negligible self subtraction. This area is consistent with that observed by Avenhaus et al. (2014) in NACO H and K_s PDI images. This dark area is also present in the IFS YJ images but it is less deep. In Fig. 3.6c a combination of the non-coronagraphic YH collapsed images clearly reveals the two bright wings and the SE arm but it appears clear that distribution of the light is uninterrupted between the wings with only a small light depletion along the minor axis that is likely an artefact of the ADI analysis: the two wings appear instead as a unique structure, symmetric to the minor axis,

---

[3] Within $r \approx 20 \times \lambda/D$ (with 20 being half the number of deformable mirror actuators along a side) the SPHERE AO system efficiently suppresses the PSF down to the level of a residual stellar halo. At this radius, the AO-corrected image may show a circular artefact which is highlighted by the spatial filtering.

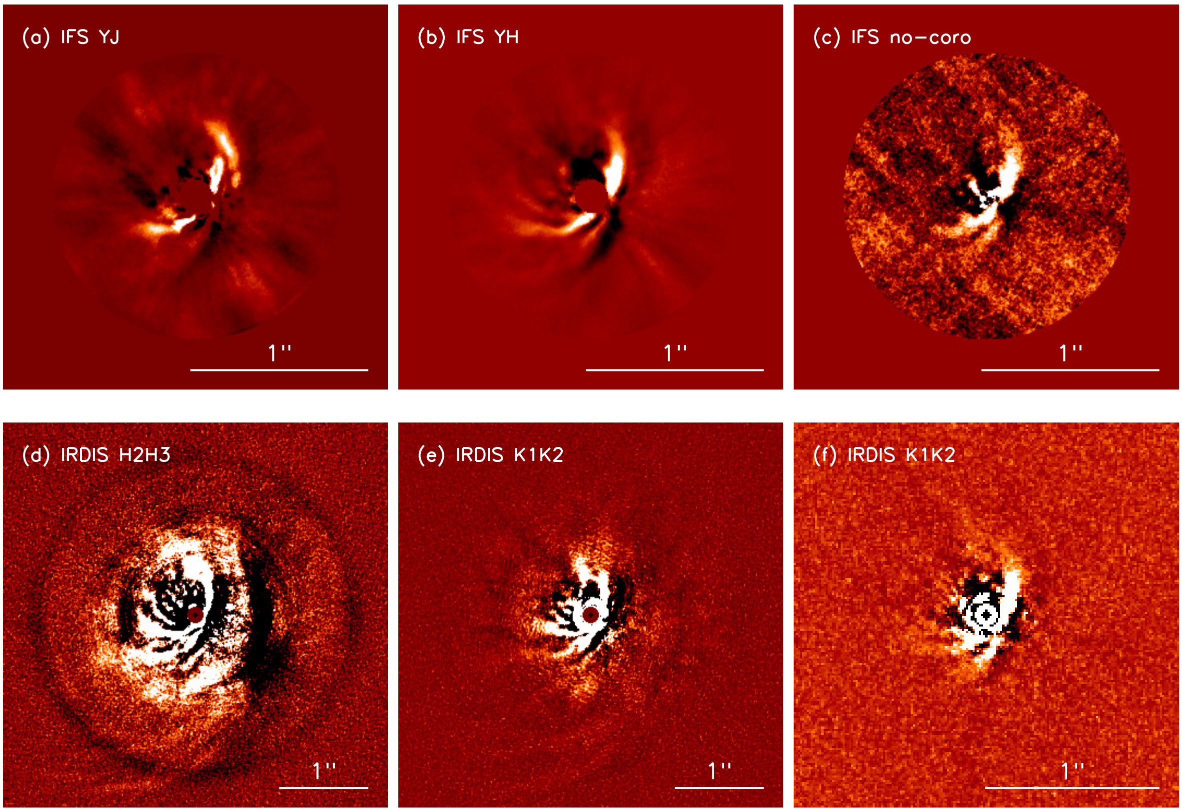

Figure 3.6: ADI images obtained for HD 100546. Top: IFS cADI images: (a) YJ from June 15; (b) YH from May15:, (c) JH no coronagraphic image from Apr 16; Bottom: IRDIS TLOCI images (d) H2H3 from June 2015; (e) K1K2 from May 2015, (f) K1K2 no coronographic image.

whose central part lies very close to the star. A bright structure slightly offsets from the minor axis is detected in the NE part up to $r \sim 0.12''$. This structure seems to lie in the position of the diffraction spikes and therefore it is likely non physical. The darker area in the West is still visible.

In the bottom row of Fig. 3.6 I present IRDIS TLOCI images. In Fig. 3.6d and 3.6e, I show the median H2H3 and K1K2 images, respectively. The two wings, the SE arm, the E arm and the dark area appear clearly in both the images, but show some differences with respect to shorter wavelengths. A diffuse signal is visible on the top of the northern wing in H2H3 and also in K1K2, but is less luminous. This is located close to expected position for CCb. The E arm extends till r=0.7$''$ and PA=64° in the H2H3 filter pair but only to r ∼0.4$''$ and PA∼ 90° in K1K2. Some small radial structures are present in the inner NE part of the disk with PA=50°, extending from the rim of the coronagraph up to ∼0.4$''$. Even though they appear at all epochs, it is difficult to infer their origin due to the vicinity with one of the instrument spikes. In the H2H3 image, a second dark area is visible into the west side starting at $\sim 0.6''$ till $\sim 0.9''$. At larger separations, at least two spirals are visible in the south, ranging from $\sim 1.1''$ to $\sim 2.3''$.

I could detect the same structures using only half of the time and at worse seeing conditions compared to the GPI observations presented by (Follette et al. 2017). The only notable difference in the disk morphology concerns their "S4" spiral, that in our data is less extended, and differences on the extended structure around the CCb that will be described in Sec. 3.2.3.

The polarimetric images resulting from the data reduction described in Sect. 3.2.1 are shown in Fig. 3.7. We found that the outer disk ($> 1''$) is well imaged in the short exposure in the J band, whereas an imperfectly corrected light leakage within the detector prevented us from obtaining similarly good results at large radii in the K band. Thus, we show the large-scale structures in the J band only but the small-scale structures in both the J and the K band.

The Q_ϕ image of the whole system is shown in Fig. 3.7a, whereas the respective U_ϕ is shown in Fig. 3.7b. Strong signal is detected from both images. In particular, the U_ϕ image shows positive values to North and South and negative values to East and West. Four prominent stellar spikes are left from the data reduction in both images. A possible explanation for these artifacts is that the bright (J=6.42 mag) central star is partly polarized and therefore its spikes are not perfectly cancelled throughout the process of subtraction of the beams with different polarizations states. This would be plausible since there is also a compact polarized inner ring (0.24-0.7 AU) that can contribute, even if the near-IR excess originating from that region is not particularly large for this source and this effect is not appreciable in other stars with similar sub-AU disk.

The circumstellar disk is clearly visible in Fig. 3.7a. We did not scale here the polarized flux by the squared distance from the star, as recurrently done in works with PDI, to avoid *a-priori* assumptions on the disk geometry. To image a larger flux range, the images are shown in logarithmic scale. In the image, a number of wrapped arms at radii 1.5$''$-3 $''$from the central star are visible at all azimuthal angles. In particular, we recover the arms to South imaged by Boccaletti et al. (2013) and Garufi et al. (2016) and those to North visible from the Hubble Space Telescope (HST) image by Ardila et al. (2007).

To highlight elusive disk features from Fig. 3.7a, we applied an unsharp masking to the image similarly to what is described by Garufi et al. (2016). This technique consists in subtracting a smoothed version of the original image to the image itself. The result of the unsharp masking, obtained by smoothing Fig. 3.7a by ∼ 10×FWHM of the observations, is

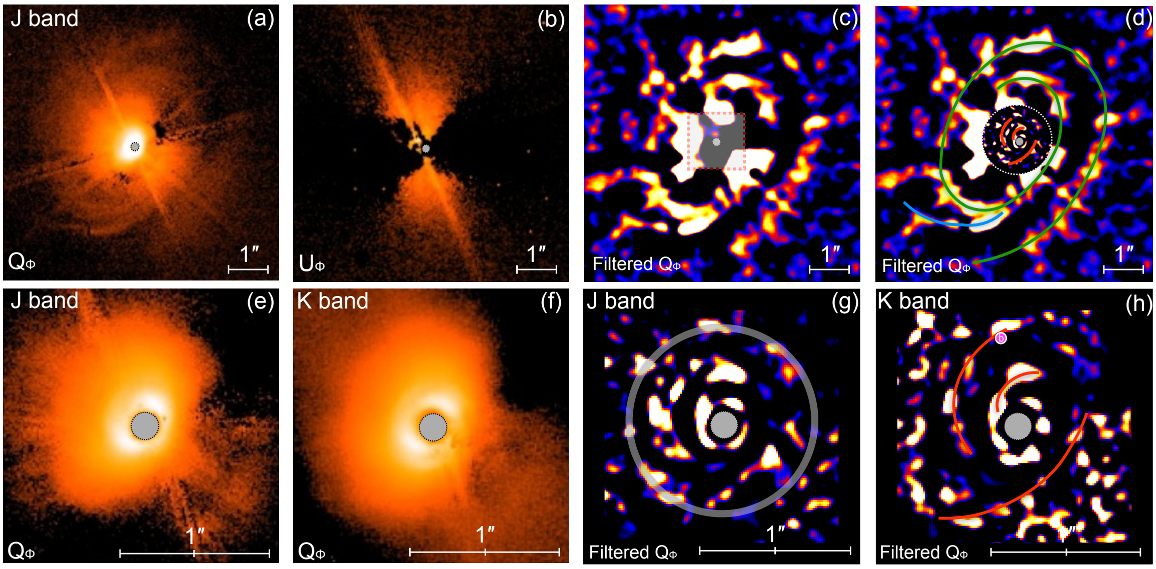

Figure 3.7: Polarized light imagery of HD100546 from SPHERE/IRDIS. **(a)**: The Q_ϕ image in the J band. **(b)**: The U_ϕ image in the J band. **(c)**: Unsharp masking of the Q_ϕ image in the J band (see text). The inner box defines the region displayed in the bottom row. **(d)**: Labeled version of (c). The inner inset circle is from (g). **(e)**: Inner detail of the Q_ϕ image in the J band. **(f)**: Inner detail of the Q_ϕ image in the K band. **(g)**: Unsharp masking (see text) of (e). The grey circle indicates the SPHERE control radius at $r \approx 20 \times \lambda/D$ (see text). **(h)**: Unsharp masking (see text) of (f). Features visible from both (g) and (h) are labeled. The purple dot indicates the location of CCb from Quanz et al. (2013). In all images, the central star is in the middle of the grey circle, symbolizing the instrument coronagraphic mask. The logarithmic color stretch is relatively arbitrary , except in (a) and (b) where it is the same. North is up, East is left.

shown in Fig. 3.7c. From this image, it is possible that the majority of the structures visible from Fig. 3.7a is part of a unique arm which is wrapping for at least 540°, as indicated by the green line in Fig. 3.7d. Another bright arm visible to South seems to have a similar origin but to extend Eastward with a larger aperture angle (see the cyan line of Fig. 3.7d).

In the inner zone of the disk, inside $\sim 1''$(Fig. 3.7a), the polarized flux is dramatically higher, even though two regions with reduced flux (appearing black in the image) are visible at P.A.$\sim 160°$ and P.A.$\sim 300°$, similarly to Quanz et al. (2011) and Avenhaus et al. (2014). This innermost disk region is also shown in the enlarged images of Fig. 3.7e (in the J band) and of Fig. 3.7f (in the K band). Two bright lobes are visible to the SE and to the NW, with the former being brighter than the latter. Inward of these lobes, the disk cavity is marginally visible just outside of the instrument coronagraphic mask.

Similarly to Fig. 3.7a, disk features are not easily recognizable. Therefore, we also apply an unsharp masking to these images, with smoothing by $\sim 6\times$FWHM, which results in Fig. 3.7g and Fig. 3.7h respectively. In both images, a number of possible features are visible. Among them, we only give credit to those that are persistent across unsharp masking procedures (i.e., by varying the smoothing factor) and, more importantly, across wavebands. Features that are radially distributed at $r \approx 20 \times \lambda/D$ (~ 60 au) are masked out in Fig. 3.7g, because this region corresponds to the SPHERE control radius. Features present in both the J and K band images are labeled in red in Fig. 3.7h. Further credence to these features is lent by their morphology, resembling the shape of the arms at larger radii and consistent with the known disk geometry. The innermost of these features was also detected by Avenhaus et al. (2014) and Garufi et al. (2016), whereas the others were not. Interestingly, CCb as from Quanz et al. (2013) lies in correspondence of one of these possible features. From this dataset, we cannot infer whether a spatial connection between the inner arms (in red) and the outer arm (in green) exists.

Disk spectrum

In general, disk flux in the NIR is dominated by scattered light, while the brightness of a young planet is dominated by thermal emission. Therefore, to distinguish between a self shining planet and the disk I studied the total spectrum of the HD100546 disk. In order to derive the disk spectrum, I estimated the ratio between the total disk flux and the stellar one. I used the RDI datacube obtained with IFS in May 2015, where self subtraction is less aggressive, and the flux at each wavelength was estimated as the integrated flux in a constant area, defined as the pixels of the wavelength-combined RDI image, with a value above a determined threshold. An adequately rescaled mask was also applied on the IRDIS frames. This method was tested on different HD100546 RDI datacubes obtained with different reference stars obtaining a very good agreement ($> 98\%$) that confirms that the specific reference star does not affect the final contrast spectrum. The relative flux spectrum is shown in Fig. 3.8. The uncertainties on each wavelength (blue bars) were estimated as the standard deviation of the pixels. Moreover I also show the intensity 1σ range (light blue area), taking into account the pixel-to-pixel cross-talk. The regions between 1.08-1.15 μm and 1.35-1.48μm are affected by strong water absorption due to the Earth atmosphere absorptions that cannot be perfectly recovered during the RDI process and were therefore removed.

Since the difference in magnitude is close to 0 between H and K bands (K-H ~ 0.03, in agreement with similar analysis presented by Avenhaus et al. (2014), exploiting NACO H, K_s and L' filters), and the spectrum appears featureless, I tried to represent this spectral

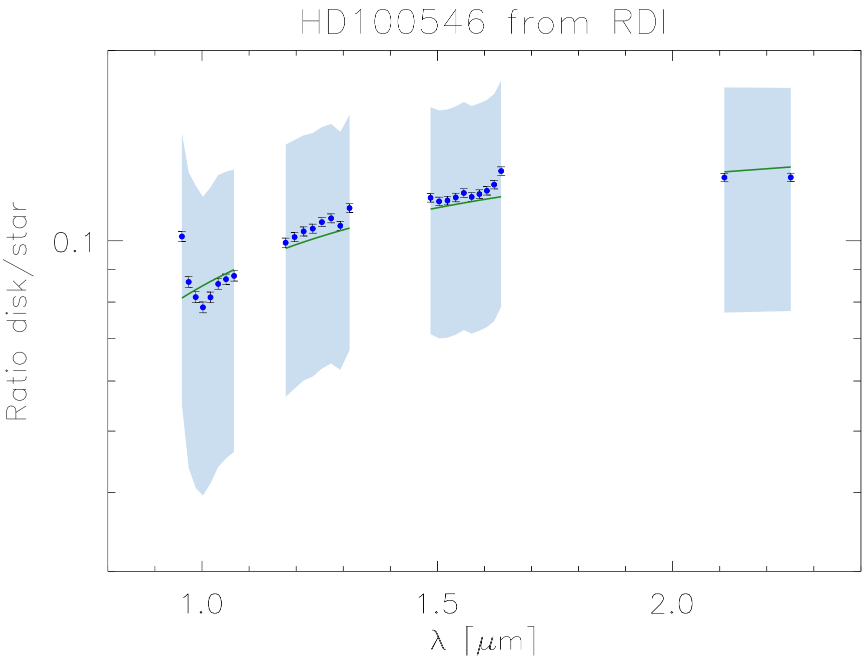

Figure 3.8: Disk mean spectrum of HD 100546 along the wings.

distribution assuming light reflected by dust with a chondritic mixture[4]. I took into account a possible reddening due to the presence of the inner disk (0.24-0.7 AU, Panić et al. 2014) that can absorb stellar light ; this was done following Cardelli et al. (1989). The reddening I see could also be explained as an effect of the coronograph that could better stop the shorter wavelengths very close to the star. The free parameters are then reddening and the (total) disk reflectivity. The first is related via A_V and R_V to the slope of the spectrum, the latter is the combination of the albedo and the disk emitting area. From disk model, I assume that the flaring is about 20°. The best solution gives A_V=0.8 and R_V=3.1. This model (green line in Fig. 3.8) is in agreement with the observations within 0.05 dex. The presence of H_2O and CO_2 ices is not clear from the spectrum, but it can be inferred throughout multi-wavelength imaging in NIR as described by e.g. Inoue et al. (2008); Honda et al. (2016), exploiting the K2-K1 color map[5]: when subtracting the RDI images obtained in these two bands, two brighter areas appear along the semi-minor axis at deprojected separations of 26 AU and 105 AU (Fig. 3.9). Since water ice molecules absorption is expected to be relevant at small angles in K2 band, I could derive that water ice is possibly present in HD100546 disk and its effect is dominant along the semi-minor axis, in the backward scattering dominated regions. This would confirm Honda et al. (2016) results, that used NICI near-infrared multicolour observations to derived the presence of water ice grains, that is most evident in their NE-SW extracted spectra (e.g. close to the minor axis) then in the SE-NW one (close to the major axis).

---

[4] For this purpose, I used a L6 ordinary chondrite, Paranaiba spectrum (from RELAB Public Spectroscopy Database).

[5] the K1 band at 2.09 μm is within a strong H_2O ice band, while the K2 band at 2.25 μm is out of it.

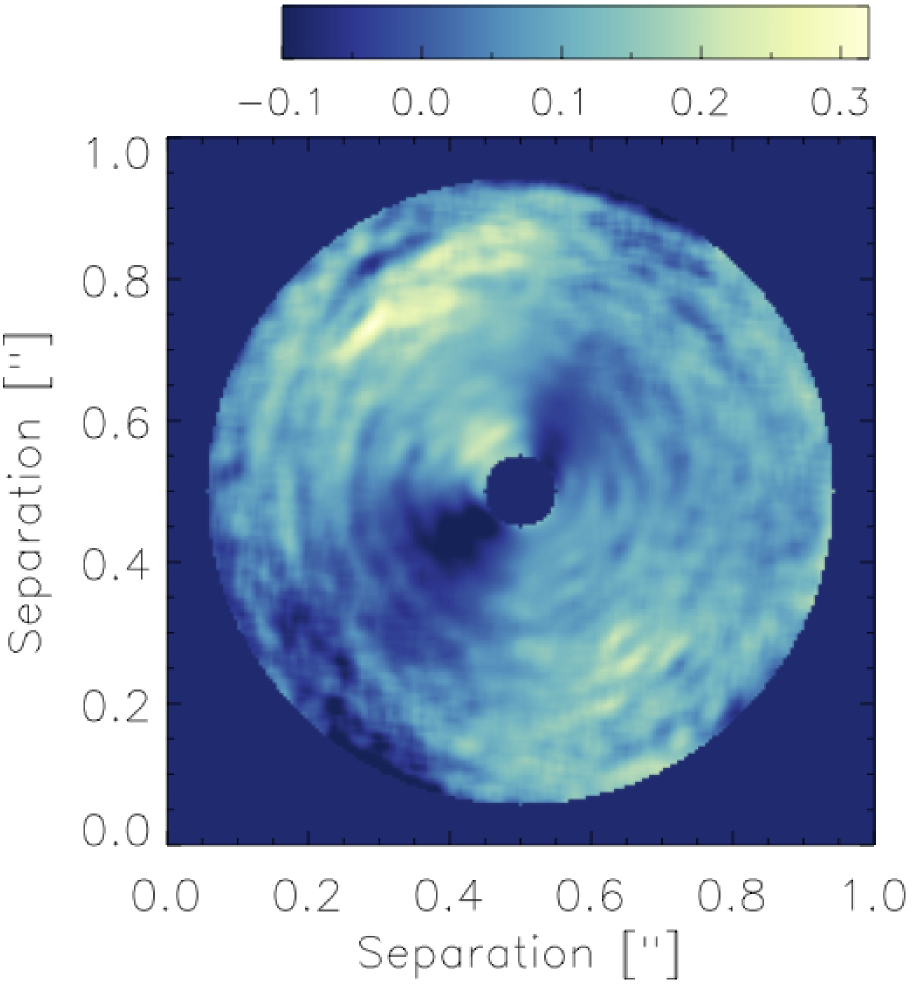

Figure 3.9: IRDIS K2-K1 colormap for HD 100546. Bright regions which could represent ices appear along the semi-minor axis.

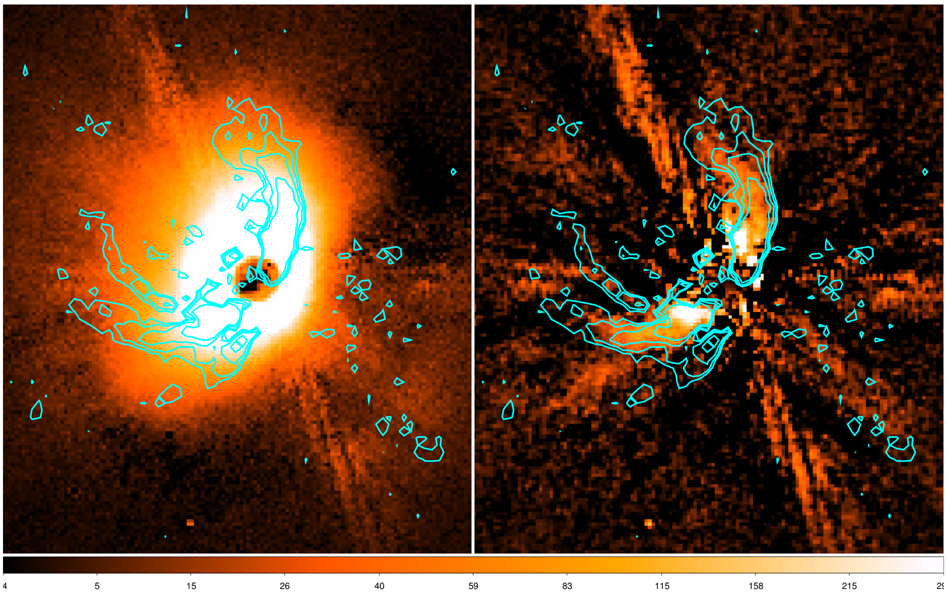

Figure 3.10: IRDIS PDI J band Q_ϕ image (left) and the results of a simulated cADI analysis on this image. Overplotted in cyan the isophotes of IRDIS cADI H2 observations.

Comparison between ADI and PDI

While the southern spiral arms of the outer disk ($> 1''$) in the IRDIS H and K images are well detected also in the IRDIS PDI J, the central part of the PDI data does not show any axis-symmetric structure. Comparing ADI results with the PDI ones is not straightforward. We have then performed pseudo-ADI on the IRDIS DPI J-band images as follows: we use the parallactic angle values of the tree different IRDIFS_EXT observations to simulate a simple cADI analysis based on the IRDIS DPI image. The results are given in Fig. 3.10: the simulation generates an image that is perfectly in agreement with the IRDIS cADI images. On the other hand, PDI images are directly comparable with RDI images. These two methods allow to better study the light distribution in the disk without self subtraction effects.

Radiative transfer model

The analysis of the SPHERE and previous data suggests that HD100546 disk hosts, in its central part (within ~ 10 and beyond ~ 60 au), two gaps that shape three dusty rings. Such a suggestion was also made by Panić et al. (2014) who modelled the disk emission obtained with interferometric data in the mid-infrared wavelength regime (hence tracing micron-sized dust) with an inner (between ∼0.3 and 0.7 AU) and an outer disk (between ∼9 and 25 AU). In addition, the presence of an outer disk is clearly indicated by scattered light, NIR and sub-millimeter imaging. Recent hydrodynamical simulations performed by Dong et al. (2016) coupled with simple radiative transfer models, demonstrate that a giant planet can open a gap in a disk creating a ring that when seeing at in intermediate viewing angle appears as two pseudo-arms placed symmetrically around the minor axis winding in opposite directions and they state that it can describe HD100546 as well. They also predicted the presence of a "dark lane" parallel to these disk pseudo-arms That is due to the self shadowing by the disk. A similar multi-rings configuration is also seen around other objects. I mention in

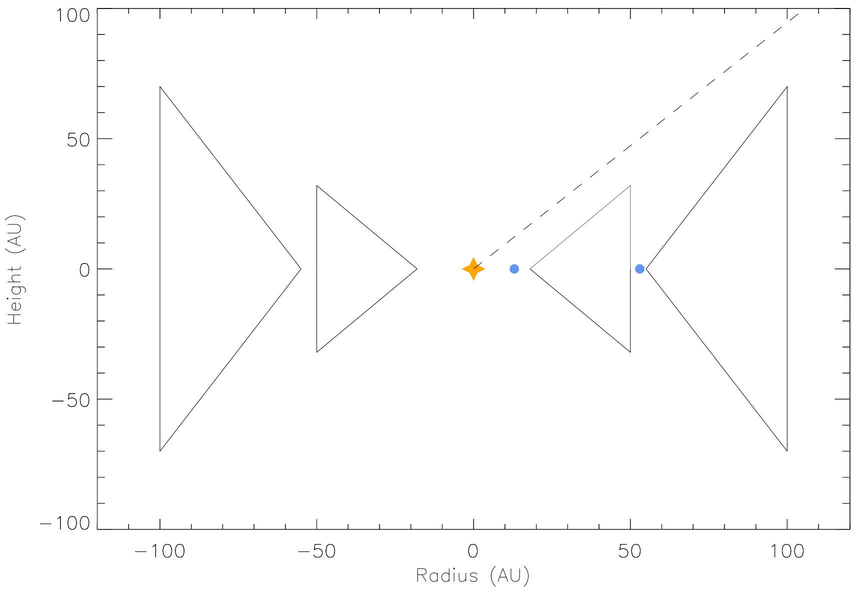

Figure 3.11: 2D sketch of the central part of the disk around HD 100546. The star is show as a yellow cross and the two putative planets (light blue dots) orbits near the edge of two thick rings (in this sketch I user triangles for simplicity). The innermost ring (0.24-0.7) au is not shown.

particular HD 141569A, where rings and outer spiral arms were observed with HST in the visible (Augereau et al. 1999; Mouillet et al. 2001; Clampin et al. 2003), and in the near-IR with NICI (Biller et al. 2015; Mazoyer et al. 2016) and SPHERE (Perrot et al. 2016). Moreover, in face-on disk of TW Hya (van Boekel et al. 2017), three rings and three gaps within ∼2″ from the central star were identified using optical and near-infrared scattered light surface brightness distribution, observed with SPHERE. Multiple rings were also observed in the inclined system RX J1615.3-3255 (de Boer et al. 2016) combining both visible polarimetric images from ZIMPOL with IRDIS and IFS in scattered light. However, planet sculpturing one single cavity is not a unique explanation to the gaps. Also some models with planets located outside of the gap can reproduce the gaps, or a single planet can open, under particular circumstances, multiple gaps (Dong et al. 2017).

A first schematic model of the rings around HD100546 is presented in Fig. 3.11, and an image obtained with a 3D RADMC radiative transfer model and based on a similar geometry is in Fig. 3.12. This last is in good agreement with the PDI results (Garufi et al. 2016) and can also explain the dark area seen in the SW region. I thought this to be the result of the 15AU ring shadowing the outer one, and not the front edge of the bottom side of the disk as inferred by Follette et al. (2017), for their ”A” structure. In the disk plane, indeed, the two wings and also the southern spiral arm become off-centred rings. This off-set is proportional to the height of the optical surface of the tori above the median plane as explained by de Boer et al. (2016) for RX J1615.3-3255 becaused the disk is flared. The off-centering of the ring gives then the angle ”top of the tori”-star-”median plane” that result to be of about 30°. The gap I see between the two brightest arms is an artefact of the coronagraph: the distribution

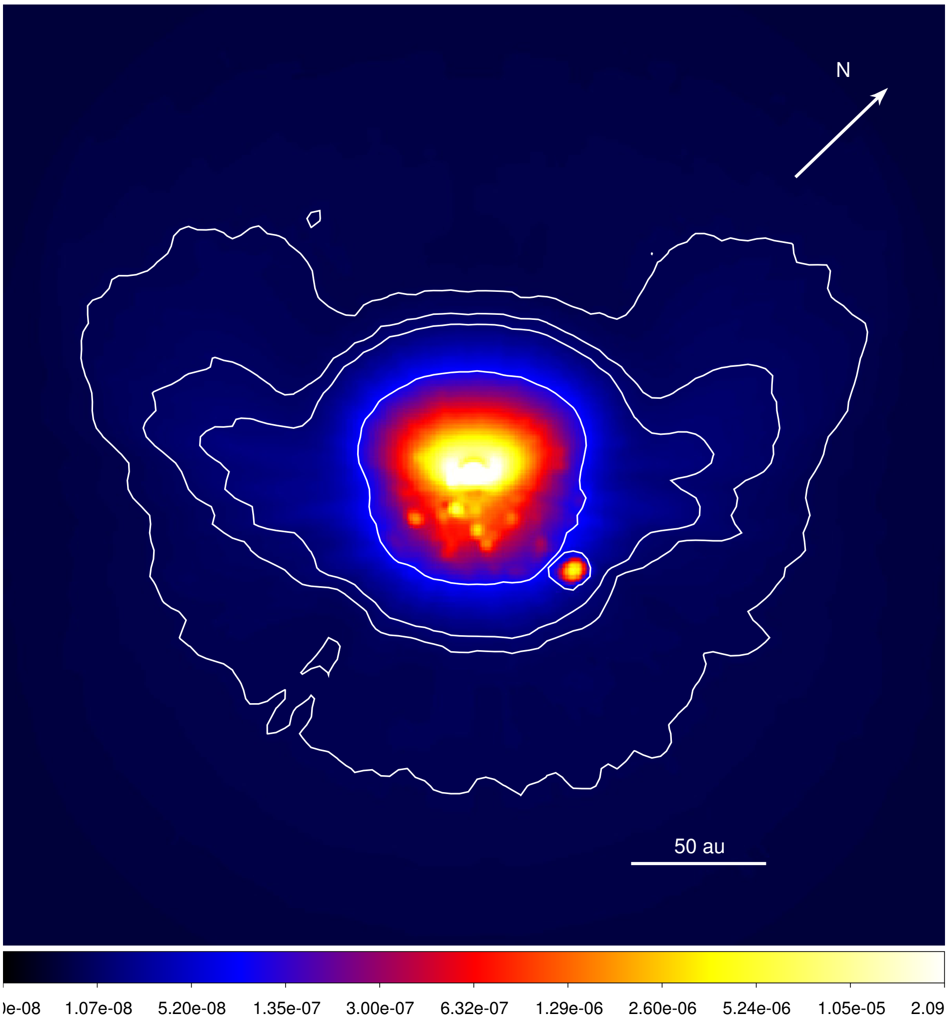

Figure 3.12: The disk model based on RADMC code, originated from the gaps described in Fig. 3.11. Contours were added to highlight the outer regions structure.

of the light in the April 2016 dataset taken without coronagraph is almost uninterrupted save for a small gap that can be attribute to the use of ADI in generating this image (see Fig. 3.6c): it is well known that ADI removes signal in tangential structures. In this scheme, it is possible that the two putative companions of HD 100546 were not visible at the epochs of our observations because hidden by one of these flared rings.

Several disk three-dimensional (3D) radiative transfer calculations using the Monte Carlo code RADMC-3D[6](Dullemond et al. 2012) were performed, mainly comparing their prediction with the IRDIS PDI images in J band, and with the IFS images obtained in J band after applying RDI. The comparison is based on the radial profile along the two system axis, taken into account the coronagraph transmission curve. The disk is described by:

$$\frac{H}{r} = h_0 \left(\frac{r}{r_0} \right)^{plh}, \tag{3.2}$$

with *phl* being related to the disk flaring; three gaps were injected: the first between 0 and 0.24 au, the second is between 0.7 and 10 au, the third between 36 and 150 au. These gaps are described by a Gaussian function in the first few models while from model 5, the gaps are described by the Moffat function:

$$f(r) = 1 - \Delta_{gap} \left(1 + \frac{(r - r_{gap})^2}{\sigma^2} \right)^{-\alpha} \tag{3.3}$$

where r_{gap} and Δ_{gap} are the position and depletion of the gap (with Δ_{gap}=1 being a gap with a total depletion of disk light) while α and σ describe the profile and the width of the gap.

The best fit is with model 19, that present with h_0=0.2, flaring of $phl = 0.35$ and gaps depth $\Delta_{1,2,3} = 0.9$ for all the gaps. The results are shown in Fig. 3.13: on the major axis, the light distribution between the coronograph and $\sim$ 65 au is well described, while there is a discrepancy at wider separation, that could be however due to the low signal coming from the source, that makes, we think, the observations not reliable (below a threshold of about 10^-8) On the other hand, the minor axis cannot be properly described since the spikes contribution to the signal is not negligible (see Fig. 3.10). The work is still ongoing. While the disk inclination assumed (42°) does not modify the results spanning in an interval of $\sim$ 20°, the grain sizes plays an important role, especially on the minor axis, where the light undergoes both backward- and forward-scattering, that fraction is strongly related to particles sizes.

3.2.3 The planets

Detection limits

The presence of the proposed planets of HD 100546, as well as of any additional candidate companions is not evident in any of IFS datasets I collected. In the IRDIS field of view I identified 7 objects that were soon recognized as background stars. Details are provided in Section3.2.4.

The IRDIS 5σ detection limits for point sources were obtained through the SpeCal software which applies anamorphism correction and flux normalization, followed by applying different angular and spectral differential imaging algorithms (Galicher et al., in prep): it estimates

---

[6] The RADMC-3D source code and more details are available online at http://www.ita.uni-heidelberg.de/~dullemond/software/radmc-3d/.

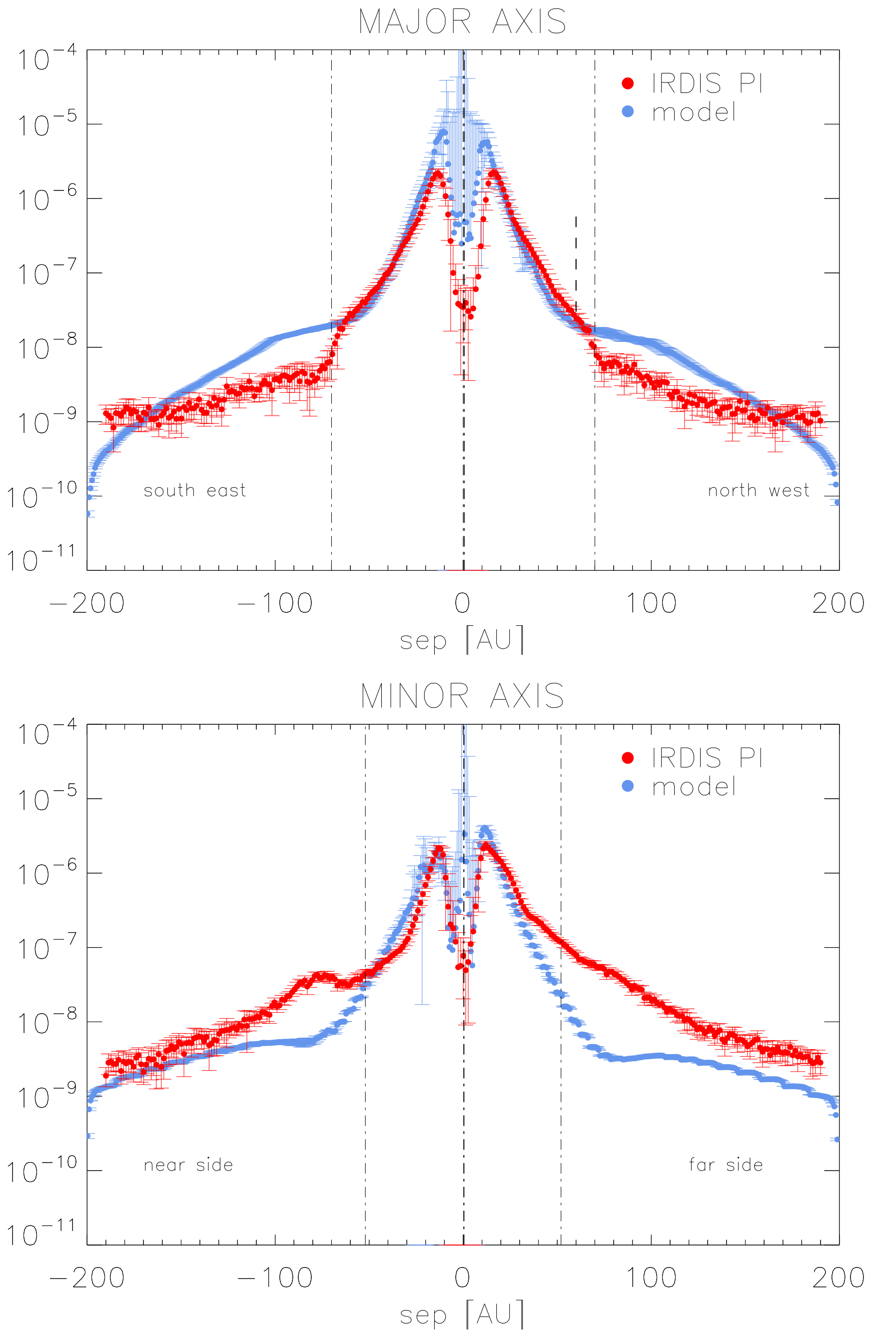

Figure 3.13: Comparison between the model 19 and the IRDIS PDI J radial profile of HD 100546 along the major (top) and the minor (bottom) axis.

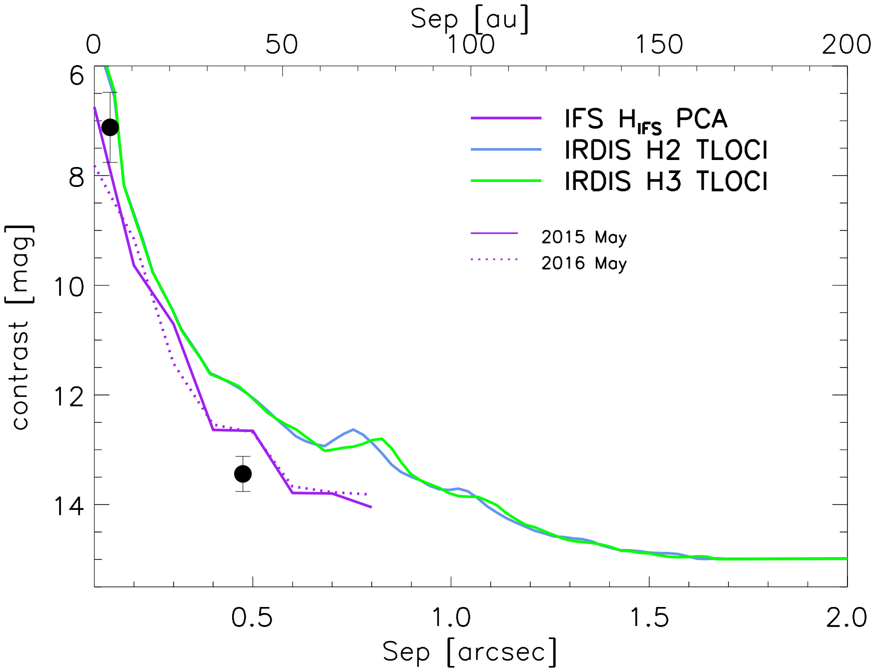

Figure 3.14: Contrast curves for HD 100546 obtained in the H_{IFS} band for the two best IFS dataset and for IRDIS H2H3. The planets contrast values measured in the H band obtained by Currie et al. 2015 with NACO are reported.

the noise level σ as the azimuthal standard deviation of the flux in the reduced image inside FWHM/2 wide annuli at increasing separations, and rescales it as function of the stellar flux derived from the off-axis PSF images, taking into acount the transmission of the neutral density filter used to avoid the star image saturation. I evaluated the IFS 5σ contrast limits in the PCA images following the method described in Mesa et al. (2015), which in summary determines for each pixel the standard deviation of the flux in a $1.5 \times 1.5\lambda/D$ box, centred on the pixel itself and divides it by the proper stellar flux (as described above). For a given separation, the 5σ is then computed as five times the median of the values obtained for all the pixels at that separation. Finally both IRDIS and IFS 5σ values are corrected for the algorithm throughput: some fake companions, 10 times more luminous than the noise residuals in the final reduced image, were injected in the pre-processed frames at separations from $0.1''$ to $0.8''$ from the star and the datacube is reduced as before. This is then repeated at several different position angles and the throughput final value is the average of fake planets flux depletion at the same distance. All these approaches, widely used for isolated point-like sources, likely underestimate the contrast limits in the presence of a disk, where the disk flux can enter both in the estimation of the background and in the attenuation effect. The TLOCI-based analysis shows that IRDIS could reach, in both H2 and H3 bands, a 5σ contrast of 12 magnitudes at separation $> 0.5''$ and even 15 magnitudes at separations of $1.5''$. In Figure 3.14 I show the deepest 5σ contrast curves obtained with this method for the H band. IFS detection limits for point sources in H band are overplotted. In this Figure, I also show the H magnitudes of the two candidate companions around HD100546 from Currie et al. (2015) using NACO. I note here that CCc with a contrast of 7.12 mag should be clearly visible in the IFS May 2015 and May 2016 datasets, where the contrast limits at the candidate separation

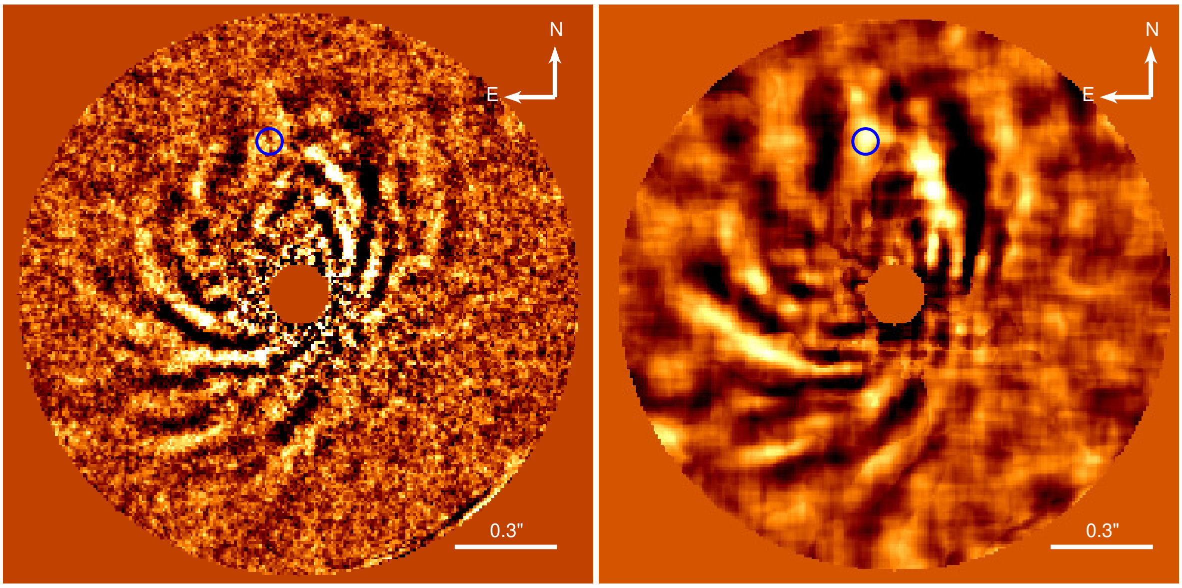

Figure 3.15: Left: Median H-band image of HD 100546 obtained using PCA 150 components. The red circle marks the position of planet b in 2013 according to Quanz et al. (2015); Right: the same, after smoothing by a median filter with width equal to 15 pixels.

are 7.7 mag and 8.4 mag, respectively. CCb ($\Delta H = 13.44$, $sep \sim 0.47''$), instead, is below the detection limit in the H band.

CCc

Since no obvious PSF-like structure appears at the expected position of CCc in each of our IFS and IRDIS datasets, I analysed the disk spectrum at its proposed location, but I did not found any significant variation respect to the disk. The blob seen by Currie et al. (2015) at similar wavelength than those used in our analysis seem to be a bright structure of the disk. In principle, since our observations were acquired a few months later, one could also think that I could not recover CCc because the orbital motion moved it behind the coronagraph or the circumstellar disk. during this interval of time. However, the reanalysis of the same GPI data used by Currie et al. (2015) by Rameau et al. (2017) also rehash the claimed detection of CCc. I conclude that CCc, if it really exists, has not yet been detected.

CCb

From what concerns CCb, recent results obtained from Rameau et al. (2017) with GPI imaging in H band found out a bright source on the top of the N wing, that they identify as a disk artefact instead of a planetary source, located at r=0.471 $\pm$ 0.009$''$ and PA=7.14°±1.7°. To see what can be obtained form our SPHERE images, I focused on the J and H part of the IFS images separately: I produced the median of all our PCA images coming from different epochs (5 in the J band and 4 in the H band). The HD 100546b signal is not evident in our images for both the J and the H band. But if I degrade the spatial resolution of these images, applying a Gaussian filter with σ=7 pixel, I found a clear local maximum close to the expected position, both in the J and in the H image, that coincides with the enhanced feature seen in the K band. This structure does not overlap the northern wing but is separated by more than one resolution element. The right panel of Fig. 3.15 shows the median H-band image of HD 100546 obtained using PCA 150 components, smoothed by a median filter with width equal to 15 pixels. The blue circle marks the position of CCb in 2013 according to Quanz et al. (2015). The fact that this signal is only present in the smoothed PCA images suggests that it is related to same extended structure.

The effects of ADI on extended structures were studied by several authors (see e.g. Milli et al. 2012) and they all demonstrate that the original light distribution is twisted. In Appendix B I present a number of numerical experiments on this effect of ADI, that confirms this fact. They also indicate that the maximum signal from a uniform, extended, structure in ADI is obtained after smoothing by a Gaussian filter whose σ is compatible to the actual size of the source. I then think that this peak can originate from an extended structure that is partially self subtracted by the ADI technique. The uncertainty on the position of this extended source is very large and can be inferred by the filter width that maximize the S/N of the source: from the median of all our images, I obtain that it is located at separation of 456 ± 105 mas and a position angle PA=$10.8 \pm 12.7°$. The brightness is even more uncertain; however, a source with a total contrast of 10 mag with respect to the star can match data.

Comparing our IFS results with GPI ones, I see they are compatible mostly due to the great uncertainty introduced by our method. However, since their source lies on the top of the disk wing, while in our images it appears as isolated, I did not try to remove the disk contribution to perform astrometric and photometric measurements. Additional informations on planet b cannot be retrieved by the polarimetric data: no emission is seen in the IRDIS Q_ϕ images as shown in Figure 3.7(h), while in the PDI+ADI image the residuals due of the telescope spider are not negligible and fall at the location of CCb, so it is impossible to tell whether or not a disk structure at that location could be interpreted as a point source after filtering by ADI.

Is the diffuse source detected physically connected to planet b?

The coincidence between the peak seen in the smoothed images and the position of CCb is striking. In order to estimate the probability that this alignment is random, I proceeded as follows. First, I rebinned the original H datacube to a 70x70 pixel image, in order not to oversample the smoothed images, and determined in which pixel of this rebinned image is planet b according to the 2013 position by Quanz et al. (2015). I then counted how many pixels in this image are more luminous than this pixel in the rebinned smoothed image and estimated the ratio of this number to the total number of useful pixels in that image. This ratio is 0.00157. This result implies that there is a 0.16% probability that the alignment between the peak found in the Quanz et al. (2015) is completely random. I conclude that the alignment has a very low probability of being a chance effect, and in the rest of this section I will assume that the feature observed in J- and H-band is physically associated to CCb whatever this object really is.

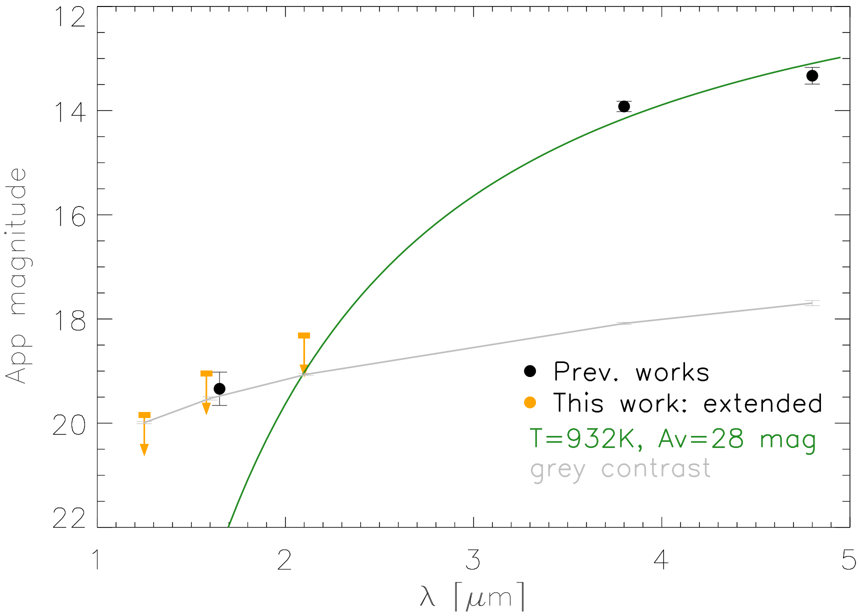

Figure 3.16: SED of HD 100546b planet and disk combining previous results (black) with our upper limits (orange). The green line represent a black body of 932 K with an absorption Av 28 mag (see text). The grey curve represent a grey contrast of 14 mag fitting the short wavelengths observations.

Photometry

Our datasets can put a 5σ limit to the magnitudes of a point source at the presumed location of CCb. With IFS I obtain that it is fainter than the apparent magnitude 19.84 in the J band ($1.20 - 1.30\mu$m), fainter than 19.80 in J broad band ($1.15 - 1.35\mu$m) and fainter than 19.05 in H.

Putting together all the results and the literature ones (see Tab. 3.3) I obtain the SED plotted in Fig. 3.16. Some important arguments that one should take into account interpreting this SED are: (a) we cannot see CCb in our IFS data, so we only estimated the contrast limits in the area where we suppose CCb to be located; (b) it is difficult to determine the motion of CCb: literature data suggest a clockwise motion whereas I expect a counter-clockwise motion from observations of the outer disk gas and dust at (sub)mm wavelengths (Walsh et al. 2014) and the orientation of the disk from the radiative transfer model; (c) what we see in the IRDIS data at positions corresponding to CCb could be simply bright structure of the disk; (d) we are not subtracting the disk contribution to the flux, if exists; The limits we put refer therefore to the observation itself and not to the real object, which we suppose to be heavily absorbed by the disk at least at short wavelengths.
Similar to what discussed above, the self subtraction on extended sources is not negligible and it is difficult to estimate because it depends on the specific distribution of light. This implies that the ADI technique alters the photometry of the extended object. What I can conclude is simply that the structure seen in our smoothed images (Fig. 3.15) is compatible with an extended object which apparent magnitude is brighter than what is expected for a

Table 3.3: Contrast or upper limits for the contrast of CCb at different wavelengths.

λ [μm]	m_*	*cont*	err_{cont}	Reference
4.8	4.13	9.2	0.16	Quanz et al. (2015)
3.8	4.52	9.4	0.1	Quanz et al. (2015)
3.8	4.52	8.54	0.51	Quanz et al. (2013)
3.8	4.52	9.38	0.1	Currie et al. (2014c)
2.2	5.83	> 9.09		Boccaletti et al. (2013)
2.1	5.83	> 9.60	0.06	Quanz et al. (2015)
2.1	5.83	> 12.49	0.8	this work
1.65	5.96	13.44	0.32	Currie et al. (2015)
1.58	5.96	> 13.09	0.49	this work
1.25	6.43	> 13.41	0.91	this work

point source at the same ocation and is compatible, within the uncertainties, with the flux observed at longer wavelengths.

Are we looking at some material orbiting a newly born planet?

Previous works suggested that HD 100546 b is surrounded by circumplanetary disk. In Quanz et al. (2015) the presence of a spatially unresolved circumplanetary disk ($r \sim 1.4$ au around a $2M_{Jup}$ object) is considered as an explanation of the discrepancy between the observed values of radius and effective temperature with those obtained by models for very young gas giant planets. Also the infrared colors of the object favours this idea (Currie et al. 2015) even if the circumplanetary disk was not resolved, given the GPI pixel scale of 14.17 mas/pixel. I can exclude that the diffuse source seen in the IFS J an H band as well in the IRDIS images is the circumplanetary disk hypothesized by Quanz et al. (2015) and Currie et al. (2015). In fact the size of this extended source is of the order of r=47 mas$\simeq$ 5 au; if this was a circumplanetary disk, the corresponding R_{Hill} of the planet wold be expected to be about 3 times larger, following models by (e.g. Shabram & Boley 2013; Ayliffe & Bate 2009; Quillen & Trilling 1998). Therefore, the observed structure at the location expected for CCb would imply an un-plausible mass of $\sim 200 M_J$: such a small mass star would have greatly modified the disk morphology and is not in agreement with hydrodynamical models such as those of Pinilla et al. (2015). On the other hand, a 1.4 au circumplanetary disk, as expected for a small mass companion of $< 10M_J$, would not be resolved by IFS or IRDIS and would appear as a point-like source. In Fig 3.16 I present the SED of this source. Given the loose difference of contrast between the J/H-band diffuse source and L/M-band possibly point-sources, I could represent this emission as the sum of two different sources. The grey line represent the diffuse source; it fits the short wavelength points but it largely fail to reproduce the L and M data., The orange line represents the SED of the point-source. It is clear that this is more redder than the star and cannot be explained as stellar scattered light alone. I could fit these values using a 1 Myr AMES-Dusty model (Allard et al. 2001). Combining this result with the L' and M' magnitude found by Quanz et al. (2015) I found a good fit with a very higly reddened substellar object, with T_{eff}=2630 K, M=25M_J, R=3.4 R$_J$. The required absorption by dust in the V band is A_V=32 mag that implies an absorption of $\sim$ 6 mag in the H band and $\sim$ 1 mag in the L and M bands. This result is quite insensitive to the adopted age, at least in the 1-5 Myr range, to the adopted reddening law (Rv=3.1) and to the adopted atmospheric model (Dust vs Cond vs black body). This result can also describe the observed magnitude in H band for our central source as well as Currie et al. (2015) finding.

To justify the extended emission, I further consider a spherical cloud around CCb, located at a separation of d=59 AU from the star, that reflects stellar light. I derive that this cloud could have a radius of r=5 AU. If its optical depth is $\tau >> 1$, then I expect that the total reflected light is c=$A\pi r^2/(4\pi d^2)$ where A is the Albedo. If A=0.1 then the expected contrast is c=1.8×10^{-4} , that is 9.5 mag that is compatible with our observations. This feature would be unresolved at L and M wavelength and therefore contribute to the flux of the compact source: its luminosity is compatible within the uncertainties with reflected stellar light from the J to the M band. However, in this scenario I am not considering the absorption due to the circumstellar disk material between the star and the circumplanetary disk. This also depends on the thickness of the circumstellar disk and on the height of the planet orbit on the circumstellar disk plane. This effect, and the presence of shadows due to the circumstellar disk, could be not negligible and cause an irregular illumination of the circumplanetary disk. Of course the truth can be a combination of these factors.

I conclude that the origin of this emitting area is still unclear. It could be a highly reddened substellar object surrounded by a dust cloud, but I cannot exclude other interpretations, such as the super imposition of two spiral arms, the northern wing and the small IRDIS N arm (see Fig. 3.6), or with disk material flowing to the planets due to its perturbation induced on the disk.

3.2.4 Relation between HD100546b and the circumstellar disk

In order to understand the dynamical relation between CCb (assuming it is a real object) and the circumstellar disk, it is useful to compare our observations with the relation between Jupiter and the asteroid belt in the Solar System. Of course, we should remind that HD 100546 is much younger than the Sun; I then expect that the cleaning of dynamical unstable regions is less complete than in the case of the Solar System. For the same reason, I might expect that the growth in size of asteroids is less advanced. On the other hand, it is still well possible that a non-negligible fraction of the dust I observe in the HD 100546 disk has a secondary origin, being produced by the destruction of larger bodies. The external edge of the asteroid belt in the Solar System is at 3.3 AU, that is, at the 1:2 resonance with Jupiter. External to this area, I only have the Trojans. I might then expect that the 1:2 resonance might represent the outer edge also for the (intermediate) disk of HD 100546. Fig. 3.17 shows the H-band image of the disk of HD 100546 obtained with RDI. The intensity scale in this image is according to asinh (that is, logarithmic) to show the faintest areas of the disk. I over-plotted (white curve) a circular orbit on the plane of the disk for planet b, as well as the 1:2 corresponding resonance (red curve). This figure shows that the brightest part of the innermost region of disk is within the distance of the 1:2 resonance to planet b, in analogy with the asteroid belt in the Solar System. On the other hand, there is one relatively bright region, N of the star, that is roughly at the PA of the planet. This relatively bright region is within the putative orbit of b. These facts suggest a dynamical relation with b. One possibility is that some material is extracted from the inner region of the disk due to instabilities that are expected in correspondence to the higher order resonances with the planet orbit. A comparison with ADI or high order PCA images of the disk is also useful. I

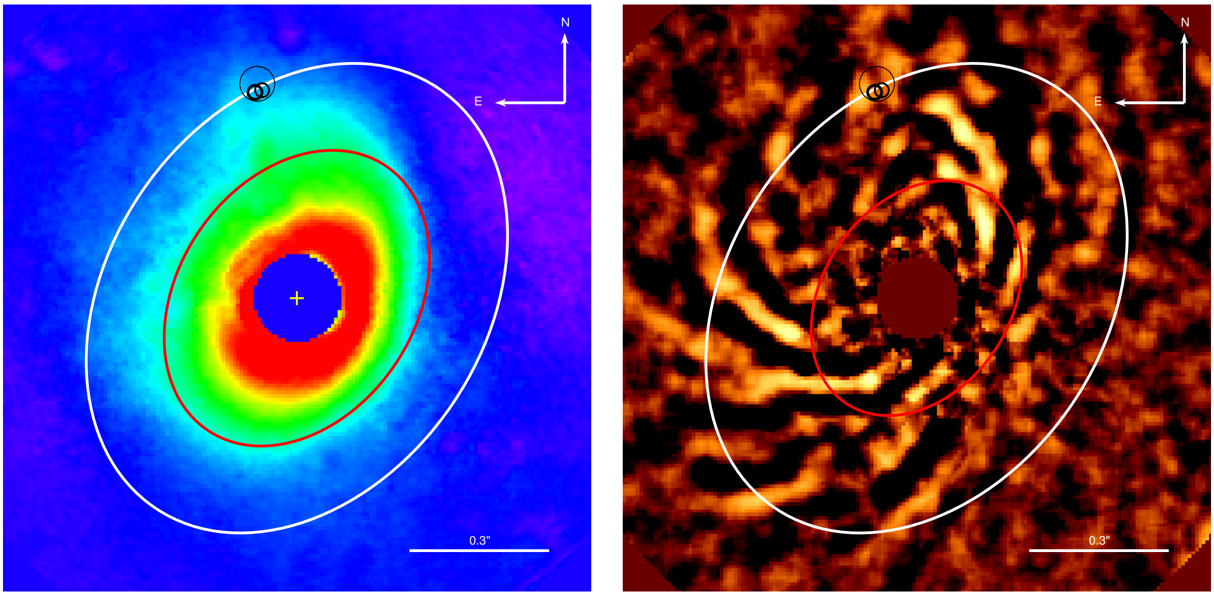

Figure 3.17: Left: Median RDI H-band image for HD 100546. An asinh intensity scale was adopted in this image to better show faint disk structures. The black circles mark the position of b as measured in this paper. The white ellipse represents a circular orbit on the plane of the disk fitting the observations. The red ellipse is the orbit corresponding to a 1:2 resonance on this same plane. Right: Median high order PCA (150 components) H-band image for HD 100546. An asinh intensity scale was adopted in this image to better show faint disk structures.

show such a comparison in Fig. 3.17. I remind that these images enhance tiny fluctuations around the mean values making visible very weak structures that are not obvious in the full intensity images. Even in this IFS image, there is no signal beyond the planet orbit; I think this is because this region is actually empty. There actually is an outer disk around HD 100546 at separation $\sim$ 200 AU, (see Walsh et al. 2014); this disk is seen in IRDIS and ZIMPOL PDI images at a separation about three times that of planet b, but this is beyond the edge of the field visualized in Fig. 3.17. At separations smaller than the orbit of b, a number of ellipse arcs appear, that can be interpreted as surfaces of rings at different separations from the star, visible in scattered light (mainly forward scattering). Since these ellipses look de-centered with respect to the star, these rings should have a considerable vertical height above the disk. In analogy with the Solar System asteroid belt, I may think that these rings may be related to resonances with b. In this scenario, the presence of dust at a substantial height over the plane is expected; in fact this is also observed for the asteroids of the main belt, whose orbit inclination may be as high as $\sim 20^\circ$. I should stress again that differential imaging strongly enhance fluctuations in the intensity of the scattered light, allowing to detect very faint structures. That is, the structure seen in these differential images may well reflect only a tiny fraction of the star light and then have a very small optical depth. The actual contrast of the observed features is of $\sim 10^{-7}$ per resolution element; since a resolution element intercepts $\sim 10^{-4}$ of the star light, only a fraction of $\sim 10^{-3}$ is scattered by these features. For any reasonable value of the albedo, most of the light crosses these features without being scattered, that is their optical depth is very low. I can then well see through these high altitude clouds down to much lower heights within the disk. This might explain why I can see the cloud around planet b in spite of the presence of these rings.

Background Objects in the IRDIS field of view

As described in Sect. 3.6, seven points sources are detected in the IRDIS FoV. Their astrometry and photometry are listed in Table 3.18 and Fig. 3.18 unambiguously shows that all of them are background objects.

3.2.5 Conclusions

We observed HD100546 with SPHERE using its subsystems IRDIS and IFS in direct imaging and in polarimetry. Our observations confirm the presence of a very structured disk and reveal additional features. I could not confirm the presence of the two claimed planets. I can summarize our results as follows:

- We propose that the intermediate disk is made of at least two rings. These structures are dominant in the IR at separations closer than 500 mas. The presence of the coronagraph and the use of the ADI technique contributed to cancel out the light in the rings region closest to the star. We do not exclude the presence of additional spiral arms.

- The positions of these rings and also their pitch angle seem to be wavelength-dependent, in agreement with the idea of different optical depth at different wavelengths. However, the spectrum of this disk does not show obvious evidence for segregation of dust different size and is well explained by micro size particles.

- The system shows evidence of the presence of ices.

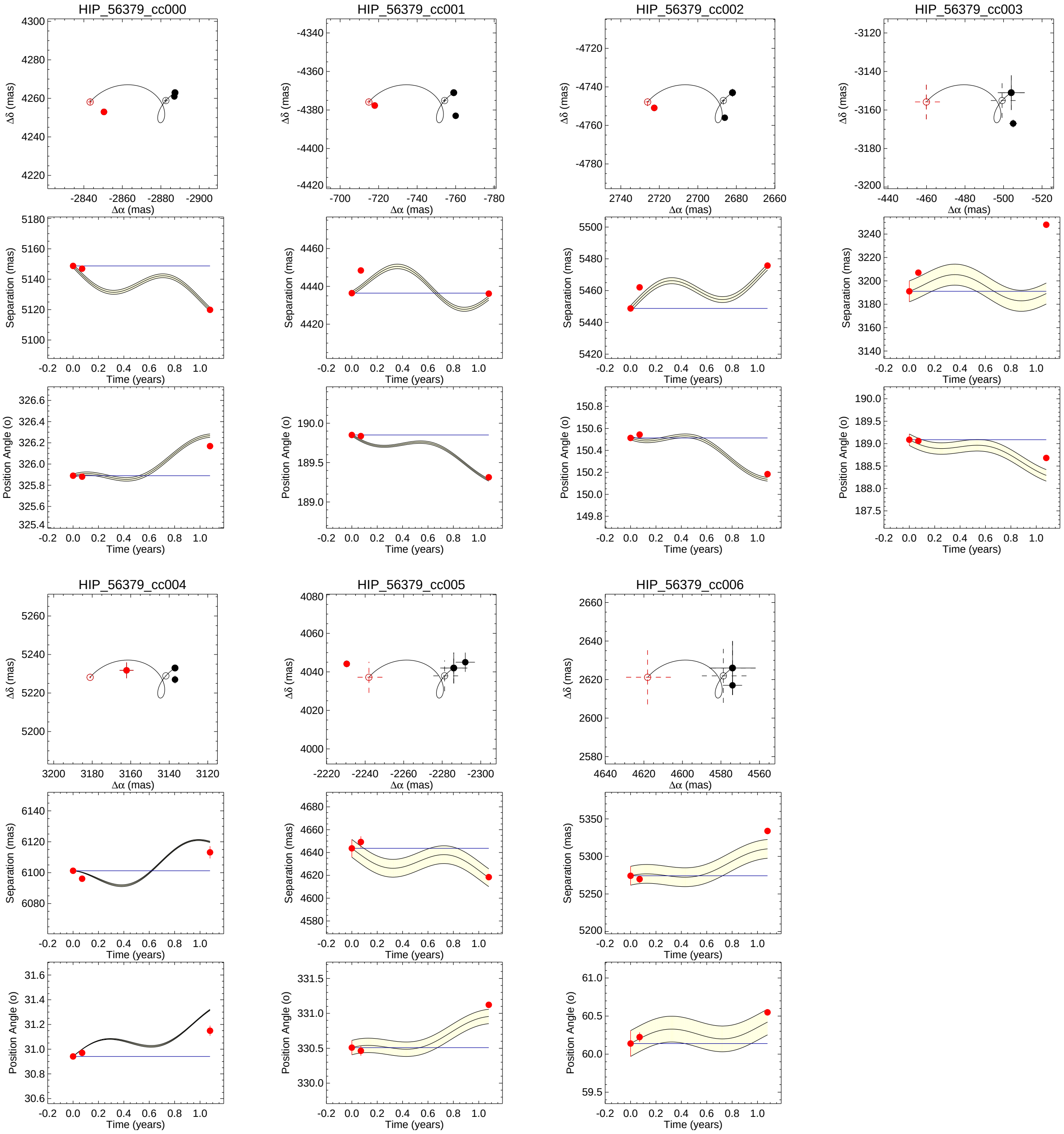

Figure 3.18: Top panel: proper motion in α and δ of the background objects in the IRDIS FoV of HD100546 considering data from 4 May 2015 (filled black), May 29th 2015 (open black), May 31st 2016 (filled red). Dotted points and errorbars represent the expected position for a background object. Middle panel: observed time variation of the separation compared with the expected one for a background object. Bottom panel: observed time variation of the position angle compared with the expected one for a background object.

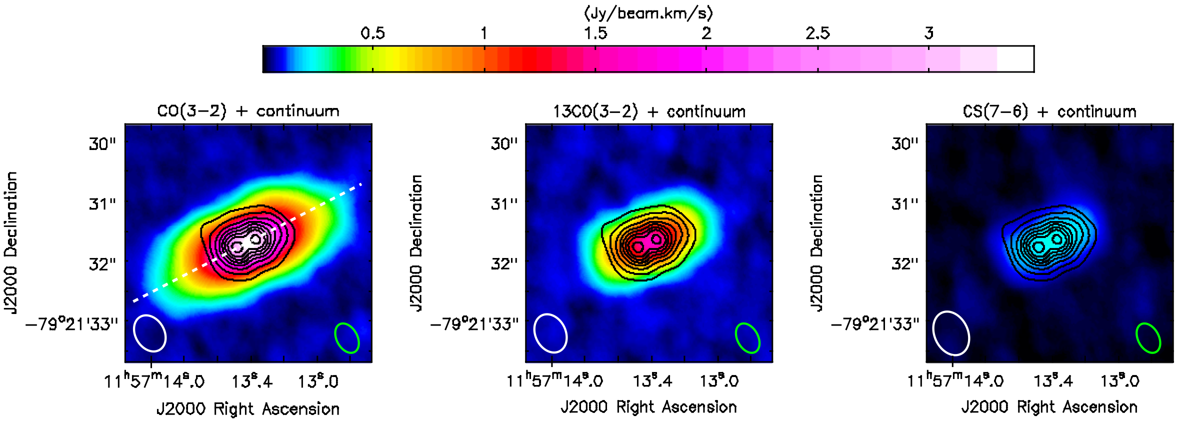

Figure 3.19: Integrated emission maps of the CO(3–2), 13CO(3–2), and the CS(7–6) transitions (from left to right) of T Cha. The black contours represent the continuum emission at 850 μm at 5, 15, 30, 45, 60, 75, 90, and 110σ where 1σ is 0.7 mJy beam-1. the authors detect two emission bumps separated by 40 au and an outer dust radius of 79 au. The white ellipses are the synthesized beams for the spectral emission lines and the green ellipse is the synthesized beam for the continuum map. From Huélamo et al. (2015).

- Comparison with preliminary radiative transfer model is in agreement with the idea of two rings.
- CCb is not detected in our data. The flared rings could likely have big impact on the visibility of CCb, if exists, possibly hiding it at short wavelengths. However, there is evidence for an extended source coincident with the position of CCb. The nature of this latter is not clear: it might be a highly reddened massive planet or brown dwarf surrounded by a dust cloud, in agreement with L and M observations. Other hypothesis are also possible, such as the overimposition of two spiral arms at the location of the L' and M' detections.
- CCc claimed by Currie et al. (2015) should be visible in our data according to our contrast limit but it is not. We suggest that is simply a bright spot of the disk, in agreement with Rameau et al. (2017).

3.3 T Cha[7]

T Chamaeleontis (T Cha) is a ~2–12 Myr old (Brown et al. 2007; Murphy et al. 2013) T Tauri star (spectral type G8, Alcala et al. 1993) at an estimated distance of 107 ± 3 pc (first GAIA data release, Gaia Collaboration et al. 2016) surrounded by a transition disk. Several recent studies covering a wide wavelength range constrained the disk geometry around T Cha. Brown et al. (2007) studied its spectral energy distribution (SED) which shows a significant deficit of mid-infrared (MIR) dust emission. With radiative transfer based SED fitting they modelled this deficit by defining a gap between 0.2 and 15 au, dividing the disk into two spatially separated parts. Hence, it became a prime candidate for investigating signatures of ongoing planet formation. Olofsson et al. (2011) presented spatially resolved, interferometric

---

[7] Section re-edited from Pohl et al. (2017).

observations at high angular resolution in the NIR from the VLTI/AMBER instrument to study the inner disk's structure. The inner disk is found to be extremely narrow and located close to the star with an extension from 0.13 to 0.17 au. Olofsson et al. (2013) presented a radiative transfer model accounting for several further interferometric and photometric observations, including VLTI/PIONIER, VLTI/MIDI and NaCo/Sparse Aperture Masking (SAM) data, which further constrains the inner disk to extend from 0.07 to 0.11 AU. Further SED modeling of T Cha by Cieza et al. (2011) suggests that there is a high degeneracy especially for the outer disk geometry, since a very compact outer disk provides an equally good fit to the Herschel data as a much larger disk with a very steep surface density profile. High-resolution ALMA observations of the 850 μm dust continuum as well as of several emission lines presented by Huélamo et al. (2015) spatially resolve the outer disk around T Cha. They report a compact dusty disk, where the continuum intensity profile displays two emission bumps separated by 40 au, indicating an inner gap size of 20 au and an outer disk radius of ~ 80 au. In contrast, the gaseous disk is larger by almost a factor of three, giving a radius of ~ 230 au based on the detection of CO(3–2) molecular emission. Huélamo et al. (2015) derive a disk inclination of $67^\circ \pm 5^\circ$ and a position angle of $113^\circ \pm 6^\circ$ by fitting a Gaussian to the CO(3–2) integrated emission map.

All previous observations clearly confirm that there must be a significant gap in the disk dust density distribution, while its origin is still debated. In general, radial gap structures can be created by a number of processes, including grain growth, effects of the magneto-rotational instability at the outer edge of a dead-zone, a close (sub-)stellar companion or the dynamical interaction of a planet formed within the disk. For the latter the disk density modification results from the torques exerted on the disk by the planet and by the disk itself. The planet pushes away the surrounding material, the outer part of the disk outward and the inner part inward, hence, it tends to open a gap (Lin & Papaloizou 1979; Crida et al. 2006). Using Sparse Aperture Masking (SAM), Huélamo et al. (2011) detected a companion candidate at a projected distance of 6.7 au from the primary, which is well within the previously described disk gap. However, an analysis of several L' and K_s data sets covering a period of three years ruled out this companion hypothesis (Olofsson et al. 2013; Cheetham et al. 2015). The absence of relative motion for the companion candidate favors a stationary structure consistent with scattered light from a highly inclined disk. Sallum et al. (2015a) checked if the closure phase signal from their VLT/NaCo and Magellan/MagAO/Clio2 data shows any variation in time, which is not expected for the disk scattering model. While NaCo L' data from 2011 and 2013 support the hypothesis of constant scattered light from the disk, the best fits for two other NaCo data sets are inconsistent, requiring temporal variability in the amount of scattered light.

3.3.1 IRDIS H2H3 and IFS YJ observations

In Pohl et al. (2017) we present new total intensity images obtained with the angular differential imaging (ADI) technique based on SPHERE GTO data. The observations provide the first spatially resolved high-contrast images of T Cha in the optical and NIR. The total intensity images are used for a detailed search of substellar companion candidates and, in case of non-detection, to place constraints on putative companions. Reduction and analysis of the NIR data was my main contribute to the paper.

Table 3.4: Overview of observational SPHERE data sets for T Cha used in this work. Observing mode and related filters, DIT, original NDIT, used NDIT, in parenthesis, total integration time t_exp in minutes, polarimetric cycles (PC), DIMM seeing FWHM on source during the exposures and H-band strehl ratio (SR) are presented.

Date	Ob. mode	Filter	DIT×NDIT [s]	PC	t_{exp} [min]	σ [$''$]	SR [%]
2015 May 30	IRDIFS	YJ H2H3	64 × 96	–	102	0.5–0.85	0.27±0.13
2016 Feb 19	IRDIS DPI	*H*	32 × 1	30	64	0.9–1.0	0.76±4

Observations of T Cha were performed during the nights of 30 May 2015, 19 February 2016 and 31 March 2016 with several sub-instruments of the high-contrast imager SPHERE. Data were taken simultaneously with IRDIS in dual-band imaging mode and the IFS. In this IRDIFS mode, IRDIS is operated in the filter pair *H2H3* and IFS in *YJ* ($0.95 - 1.35\,\mu$m) mode. Table 3.4 summarizes the observations and instrumental setup for each instrument. The Strehl ratio estimation (provided by SPARTA files) is based on an extrapolation of the phase variance deduced from the reconstruction of SAXO open-loop data using deformable mirror, tip-tilt voltages and wavefront sensor closed-loop data (Fusco et al. 2006).

T Cha IRDIFS observations were taken in pupil stabilized mode and lasted about 6100 seconds with a field rotation of $\sim 28°$. Unstable weather conditions (DIMM seeing varied from $0.5''$ to $0.85''$ and clouds passing by) caused flux variations of up to one order of magnitude during the sequence. After sorting the datacubes, the average Strehl became of $\sim 33\%$ in the H band. Because of the variable atmospheric conditions during the observations, a very strict frame selection was applied at the end of the basic reduction and eventually only 42 out of 96 frames were used.

The basic IRDIS data reduction consists of flat field and bad-pixel correction, cosmic ray detection and correction, and sky subtraction. A parallel analysis using the pipeline described in Vigan et al. (2016) was performed. I remind here briefly the different steps of the analysis. The calibrations were created using the latest release of the SPHERE DRH software (Pavlov et al. 2008). Each of the images in the coronagraphic observing sequences were background subtracted, divided by the flat field and corrected for bad pixels. Finally, all images were aligned to a common center using the star center data acquired at the beginning of the observing sequence. The full calibration process was applied independently to each of the two data sets in the *H2* and *H3* filters. The ADI data cubes were processed with the LAM-ADI pipeline (Vigan et al. 2012, 2015, 2016), using a PCA implementation following the KLIP approach (Soummer et al. 2012). In the PCA analysis the number of subtracted modes was varied between 5 and 20 (between 8 and 35% of the total number of modes).

Data reduction for the IFS data was performed using tools available at the SHINE Data Center at IPAG following the procedure described in Mesa et al. (2015) and in Zurlo et al. (2014). Using the SPHERE DRH software (Pavlov et al. 2008), I applied the appropriate calibrations (dark, flat, spectral positions, wavelength calibration and instrument flat) to create a calibrated datacube composed of 39 images of different wavelengths for each frame obtained during the observations. As done for IRDIS, to take into account the very variable weather conditions I applied a frame selection resulting in 76 frames out of the original 96.

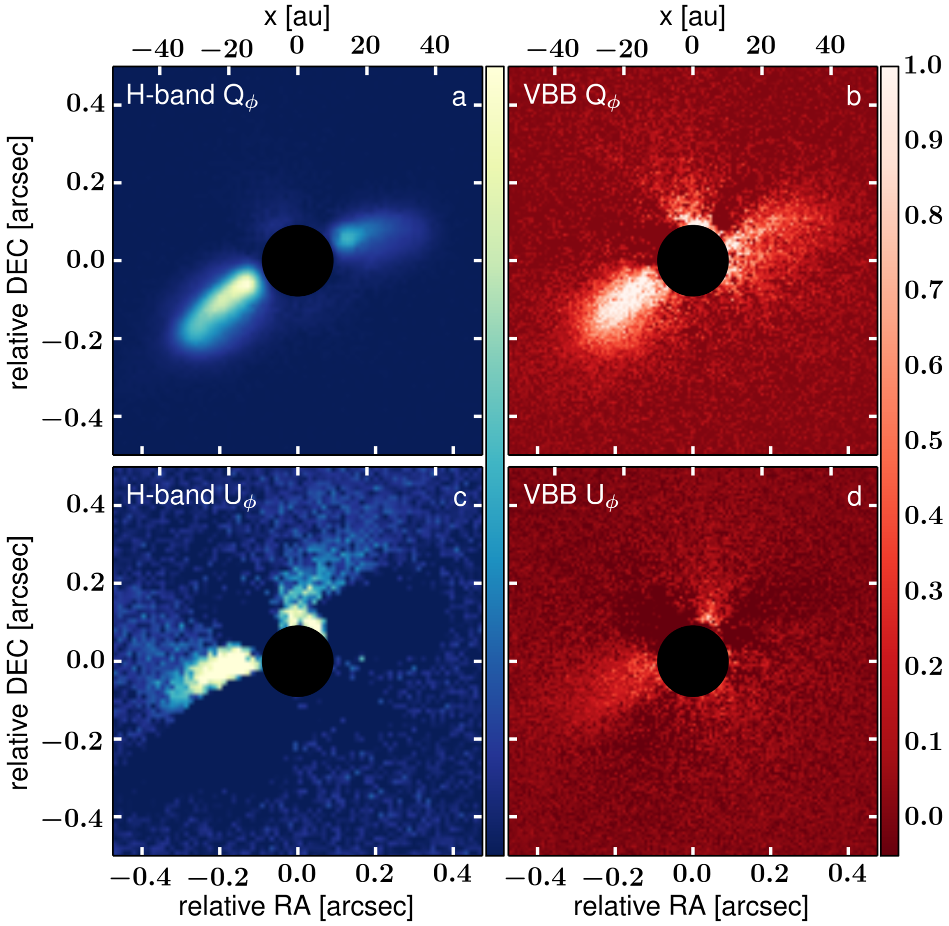

Figure 3.20: IRDIS-DPI *H*-band and ZIMPOL P2 *VBB*-filter Q_ϕ (top row) and U_ϕ (bottom row) images of T Cha. North is up, east is toward the left; all images are normalized to the highest disk brightness. The dynamical range for the color scaling is the same for the two images of the top and bottom row, respectively. An apodized Lyot coronagraph with a mask diameter of ∼185 mas was used. Negative values of U_ϕ are saturated at dark blue color.

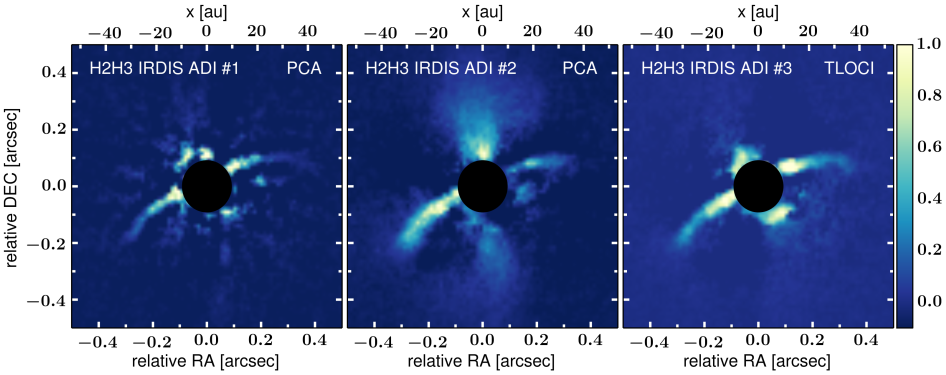

Figure 3.21: IRDIS-ADI *H2H3*-band images (mean across the wavelengths) of T Cha based on two different reduction pipelines (#1: MPIA-ADI, #2: LAM-ADI). North is up, east is toward the left; the images are normalized to the highest disk brightness and the color scales consider the same dynamical range.

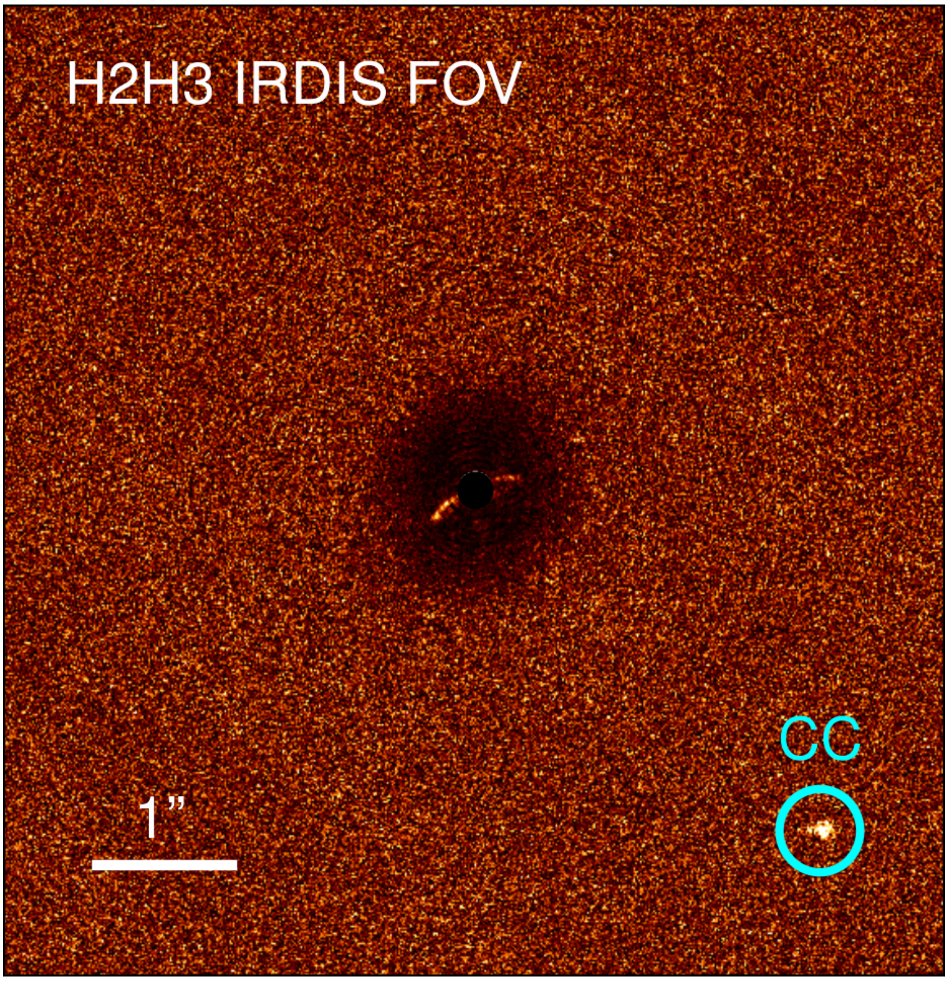

Figure 3.22: Signal-to-noise ratio map of the classical ADI reduction of the IRDIS *H2H3* data for T Cha. The point source considered as a companion candidate (CC1) is marked with a circle.

The position of the star behind the coronagraph is determined with special calibrations images that shows four satellite spots symmetric with respect to the central star, taken just before and after the standard coronagraphic observations. Exploiting the same images I then defined the rescaling factor for images at different wavelengths to have a speckle pattern as stable as possible and to be able to combine them using the principal components analysis algorithm (PCA; e.g. Soummer et al. 2012), to implement both ADI and spectral differential imaging (SDI, Racine et al. 1999) and to remove the speckle noise.

The disk of T Cha is detected in all datasets presented in this study, the ADI images are used to search for point-source signals with regard to companion candidates.

3.3.2 Point source analysis

One candidate companion (CC) is detected in the IRDIS field of view (Fig. 3.22), whereas no point-like sources are found in the IFS image. CC is located at a separation of $3.55''\pm0.01''$ with contrast $\Delta m_H = 11.63 \pm 0.04\,\mathrm{mag}$ (see Table 3.5). The same companion was already

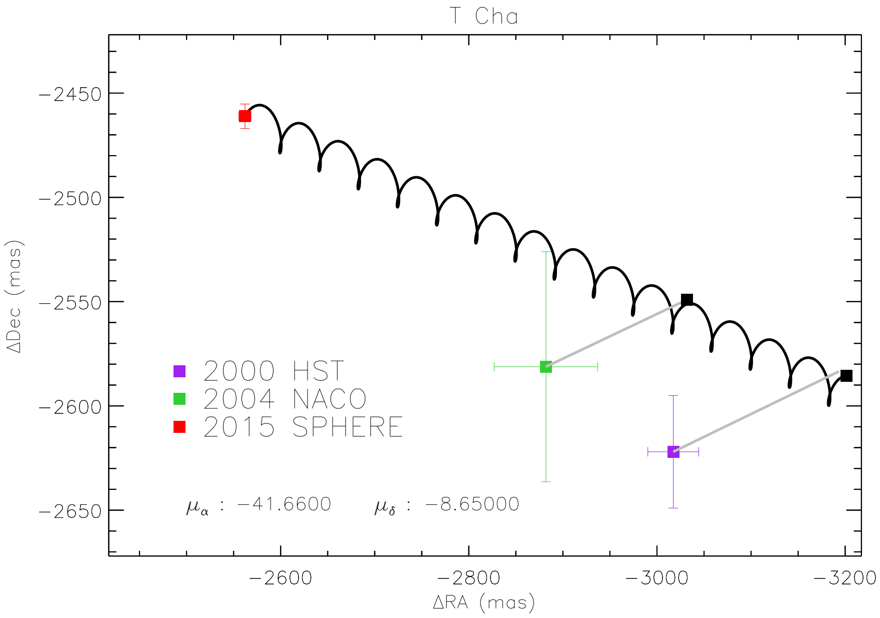

Figure 3.23: Relative astrometry of the companion candidate to T Cha labelled as 'CC' in Fig. 3.22 measured in SPHERE, NACO and HST data. Black squares are the positions expected at the time of HST and NACO observations

Table 3.5: Final astrometry and photometry for the companion candidate in the T Cha system from SPHERE data.

IRDIS companion candidate		
Filter	*H2*	*H3*
λ [μm]	1.593	1.667
Contrast [10^{-6}]	21.8 ± 0.7	22.9± 0.7
Contrast [mag]	11.65 ± 0.04	11.60 ± 0.04
SNR	31.1	31.4
Separation [mas]	3542.2 ± 6.7	3543.3 ± 7.0
PA [deg]	226.0 ± 0.1	226.0 ± 0.1

Table 3.6: Astrometry for the companion candidate to T Cha from different instrumental data.

	NACO	SPHERE
Date	5 March 2004	30 May 2015
JD	2453070	2457173
Separation [mas]	3868.9±55.0	3542.8±6.8
PA [deg]	228.2±0.8	226.0±0.1

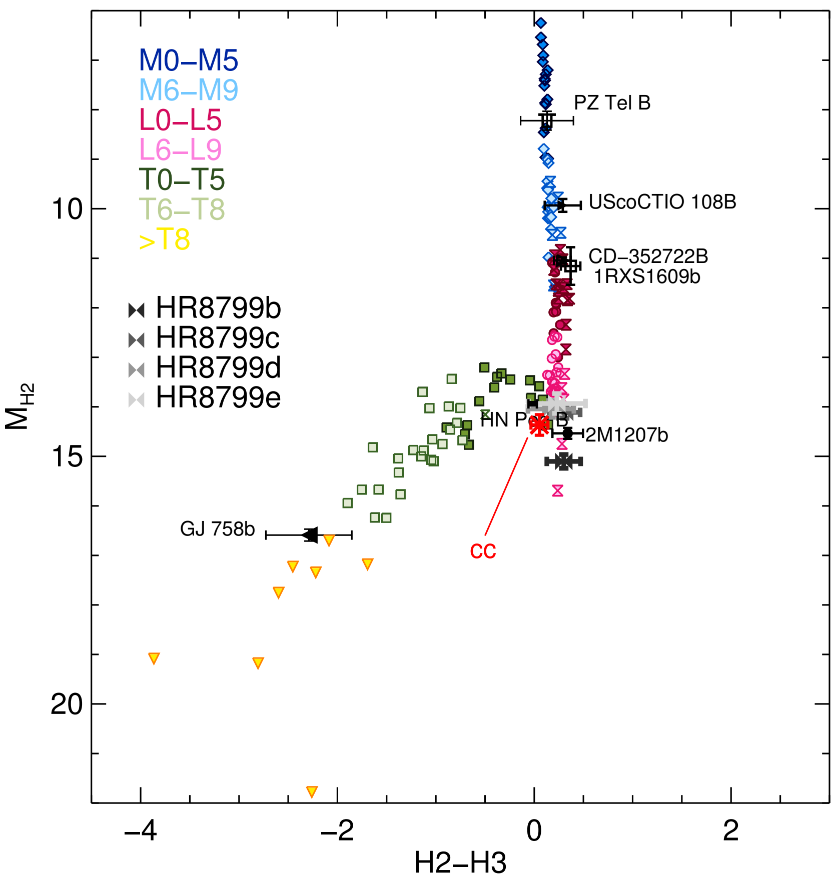

Figure 3.24: Color-magnitude diagram displaying our candidate companion, which is marked in red and labeled with CC, compared to known substellar field (colored symbols) and young objects. Note that this plot assumes that CC is at the same distance as the star. Since CC is eventually classified as a background object based on a common proper motion test (cf. Fig. 3.23), it is likely located much further.

detected by Chauvin et al. (2010) with $m_K = (11.4 \pm 0.1)$ mag and is also present in HST data taken in coronagraphic mode with STIS in March 2000. Combining the new SPHERE position with the old data (see Table 3.6) I exclude this object to be bound because the motion observed over these 15 yr is too large to be explained by a Keplerian orbit around this star. It is then a contaminant object; given that T Cha proper motion is $\mu_\alpha = (-41.66 \pm 0.2)$ mas/yr and $\mu_\delta = (-8.65 \pm 0.19)$ mas/yr (Gaia Collaboration et al. 2016), I also notice that CC has a moderately relative proper motion with respect to a very far quasi stationary object (Fig. 3.23). For completeness, I show the CMD in Fig. 3.24. I note that this plot assumes that CC is at the same distance as T Cha, since its actual distance is unknown. This is rather unlikely based on my previous conclusion that it is not physically associated with T Cha. CC is likely located much further, and thus, likely intrinsically much brighter than an object at the L-T transition. Given the H2-H3 color ~ 0 (see Fig. 3.24), I conclude that this object could be a floating BD or a very small mass ($M < 0.3 M_\odot$) star of the thick disk or the Halo. This can be confirmed with new HST images in the optical.

3.3.3 Detection limits on substellar companion candidates

The IRDIS detection limits for point sources are determined using the TLOCI data reduction. I estimate the 5σ noise level, where σ is the azimuthal robust deviation of the residual flux in annuli of λ/D width rejecting pixels with no flux. Finally, the 5σ noise levels are divided by the stellar flux estimated from the unsaturated off-axis PSF images. The maximum contrast reached with IFS is obtained by applying the PCA technique. The contrast limits are estimated by an azimuthal standard deviation, i.e. between pixels at the same separation from the star, for each angular separation. This is corrected by the star flux, obtained from the off-axis PSF images taken just before and just after the coronagraphic observations, and the algorithm throughput, using synthetic companions injected into the data. To properly take the effect of self-subtraction into account the algorithm throughput was estimated by injecting fake companions into the pre-processed data cubes, regularly spaced from $0.1''$ to $4.0''$. They were injected at a level ten times higher than the noise residuals in the final images in that position. This process was repeated ten times with different orientations of the pattern of fake companions to average out possible variations of the throughput as a function of the position in the field. The throughput at each separation was then calculated to be the mean throughput over the ten measurements.

In Fig. 3.25 the contrast curves obtained for the different data sets are shown. The IRDIS data gives a 5σ contrast for a separation larger than $1.0''$ of greater than 12.5 mag and 12.6 mag in the *H2* and *H3* bands, respectively. The maximum contrast reached with IFS is obtained applying the PCA technique: it is deeper in contrast for separations closer then $0.7''$, assuming a grey contrast between the two objects. Compared with NACO K_s band results (see e.g. Chauvin et al. 2010), these observations are deeper by more than three magnitudes at a separation of $0.7''$, e.g. at the outer rim of the NACO coronagraph, while the contrasts reached at larger separation are comparable.

Using the theoretical atmospheric models AMES-COND (Allard et al. 2003) I converted the contrast limits into upper limits on the mass of possible objects orbiting around T Cha. These models are valid for $T_{eff} < 1400K$ and consider that the dust immediately rains-out from the photosphere after its formation. I assumed a system age of 7.5 Myr (Torres et al.

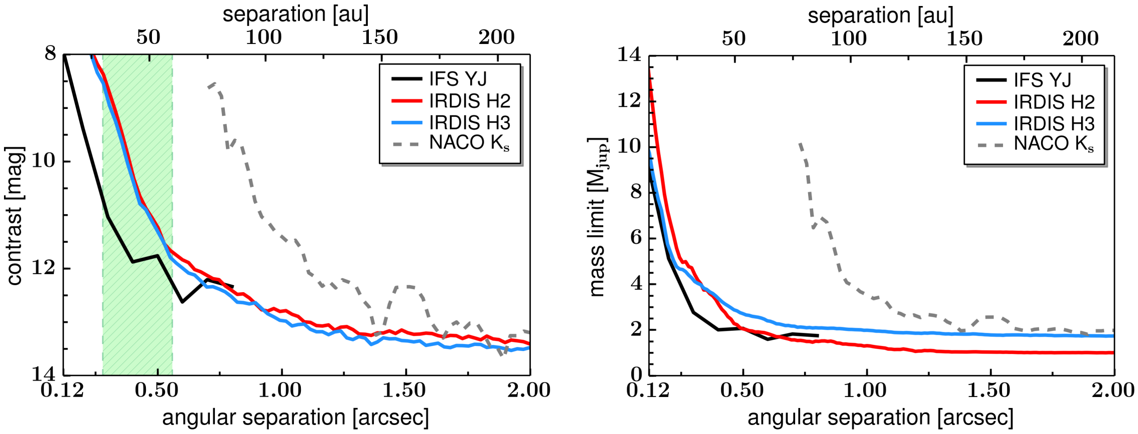

Figure 3.25: Contrast curves and companion mass limits for T Cha derived for IFS (black) after applying PCA, and for IRDIS *H2* and *H3* bands (red and blue, respectively) after applying the procedure from Vigan et al. (2016). Both curves have a lower cut at 0.12″. The detection limits from NACO K_s band data is given for comparison (grey dashed line, cut at 0.70″).

2008). This leads to a mass limit of $\sim 8.5\,M_{\rm jup}$ in the innermost regions ($\sim$0.1″-), decreasing to $\sim 2\,M_{\rm jup}$ for a separation between 0.4″ and 5.0″. Our new SPHERE observations, therefore, improve the NACO mass limits especially up to $\sim$ 1.5″. Both, the contrast and mass curve are cut at 0.12″. The whole coronagraph system (apodizer, mask, stop) produces a radial transmission profile, which has not been accounted for in the derivation of the detection limits. The effect of the coronagraphic mask is visible at the region near the edge of the mask plus λ/D; thus, I exclude the inner 0.12″. Furthermore, I note that the detection limits represent an average value around the star, which might be slightly affected by the disk signal at the location of the disk. However, I expect this effect affect only a small portion of the image given the compactness of the disk around T Cha, even if that region is the one in which we expect to found an object.

In Pohl et al. (2017), we studied this system and its disk in detail. We used also IRDIS-DPI images taken with the BB_H filter ($\lambda_c = 1.625\mu m$) and the SlowPolarimetry detector mode of ZIMPOL using the very broad band filter (VBB), that covers a wide wavelength range from R- to I- band (0.55–0.87μm). These observations were aquired using an apodized pupil Lyot coronagraph and a pupil Lyot coronagraph respectively, both with a mask diameter of ∼185 mas (Soummer 2005; Boccaletti et al. 2008). The conclusions of that paper are summarized below.

- Our RADMC-3D radiative transfer model with updated disk parameters accounts well for the main geometry of the disk, the cavity and the outer disk with its bright inner rim located at 0.28″ ($\sim$30 AU). This is significantly further out than previously estimated. A disk inclination of $i = 69°$ and a position angle of PA = 114° matches the SPHERE data set best.

- We confirmed that the dominant source of emission is indeed forward scattered light from the near edge of the disk, given the high disk inclination. While small grains in the

Rayleigh limit scatter photons rather isotropically and absorb very efficiently, large dust grains with sizes ($2\pi a > \lambda$) have strong forward scattering properties. This demands a certain range of grain sizes to be present in the disk. We found out that a power-law distribution with $a_{\min} = 0.01\,\mu$m and $a_{\max} = 1000\,\mu$m reproduces the total intensity observations well, but fails to be consistent with the polarimetric images. Thus, we propose a dominant grain size in the disk of $\sim$ 10 microns[8]. Such grains bring the desired amount of forward scattering and lead to a model which is in accordance with the complete SPHERE data set presented. We note that we restricted ourselves to the analysis of Mie theory and spherical compact grains. However, for aspherical aggregates with high porosity the phase function is supposed to differ, which might alter our grain picture for T Cha.

- Although our highly inclined disk model shows a significant U_ϕ signal at H-band, which is in accordance with theoretical studies on multiple scattering events, the geometrical U_ϕ pattern observed with IRDIS cannot be reproduced.

- The brightness asymmetry between east and west side can be reproduced with a slight offset of the star's position. A planetary companion on an eccentric orbit could force the outer disk to become eccentric, causing this offset. However, a locally different grain size distribution and therefore a change of the scattering properties, or illumination effects due to asymmetric structures in the inner disk could also contribute to the brightness contrast observed.

- A previously known close companion candidate is detected in the IRDIS field of view at a separation of $3.54'' \pm 0.01''$ with contrast $m_{\rm H} = (11.63 \pm 0.04)$ mag. We, however, exclude this object to be bound and, thus, conclude that it is not part of the T Cha system.

- Our analysis rules out the presence of companions with masses larger than $\sim 8.5\,M_{\rm jup}$ between $0.12''$ and $0.4''$ from the central star, and larger than $\sim 2\,M_{\rm jup}$ for wider separations. There could still be low-mass planets in the outer disk regions and/or planets in the very inner disk.

3.4 LkCa 15: a young proto-planet in a transitional disk

LkCa 15 is a young ($\sim$ 2Myr) K5-type star, located in the Taurus-Auriga star-forming region (Simon et al. 2000), at the distance of . It has an effective temperature T_{eff} = 4730K, a luminosity of $L_* = 1.22 L_\odot$, and mass $M_* = 1.01 M_\odot$ (from Thalmann et al. 2014). Resolved imaging ranging from the visible to millimeter wavelengths (e.g., Andrews et al. 2011; Thalmann et al. 2014; Isella et al. 2014) confirmed the morphological structure implied from spectral energy distribution (SED) fitting (Espaillat et al. 2007): LkCa 15 is surrounded by a disk truncated inward $\sim$50 AU. Recent scattered light imaging also revealed an additional inner disk component within the gap structure (Thalmann et al. 2015; Oh et al. 2016). Isella et al. (2014) used VLA images to study the distribution of the disk: the 7 mm continuum

---

[8] grains of such a size would produce a spectrum slightly raising toward the red over the IFS wavelength range. This agrees with the Y-J color of 0.315 I found for this disk in the Appendix C.

Table 3.7: ZIMPOL LkCa 15 Images used for the analysis.

Frame id	DIT	NDIT	mode	coronograph	FW1	FW2
OBS344_0004.fits	300.	3	I	CLEAR1	CntHa	N_Ha
OBS344_0005.fits	300.	3	I	CLEAR1	CntHa	N_Ha
OBS344_0006.fits	300.	3	I	CLEAR1	CntHa	N_Ha
OBS344_0007.fits	300.	3	I	CLEAR1	CntHa	N_Ha
OBS344_0008.fits	300.	3	I	CLEAR1	CntHa	N_Ha
OBS344_0009.fits	300.	3	I	CLEAR1	CntHa	N_Ha
OBS344_0010.fits	300.	3	I	CLEAR1	CntHa	N_Ha
OBS344_0011.fits	300.	3	I	CLEAR1	CntHa	N_Ha

emission traces a dusty annulus of 45 AU in radius that is consistent with the dust morphology observed at shorter wavelengths. No emission is observed between the star and the dusty ring.

A embedded candidate companion was detected for the first time by Kraus & Ireland (2012), using the aperture masking interferometry at three epochs between November 2009 and November 2010, located at the middle of the known gap in LkCa 15 disk (sep∼85 mas). This is a relatively blue point source, surrounded by co-orbital emission that is red and resolved into at least two sources (one of them appear relatively blue and two relatively red).

Subsequently two more candidates were proposed by Sallum et al. (2015b). These sources are located at separations of 71.9 mas, 100 mas and 88.2 mas respectively and have position angles between PA = 5° and PA = 304°. Hereafter, I follow the three-object nomenclature of Sallum et al. (2015b), in which 'b' refers to a candidate at ∼14.7 AU which displays Hα emission, with 'c' and 'd' following counterclockwise. The Hα emission of 'b' makes a particularly compelling case for a protoplanet, as it implies active gas accretion.
My work on this targets consisted in the H_α and IFS data reduction and analysis, focusing on the non detection of such candidate companions.

3.4.1 H_α observations with ZIMPOL

This target was observed with ZIMPOL in the SV program 60.A-9360(A) proposed by N. Huelamo. The observations include 8 pupil stabilized images of LkCa 15 for a total amount of 2 hours and 28 minutes during the night of the 9 December 2014. The total rotation angle is ∼ 26°. The selected filter were N_Hα and its adjacent continuum (Cnt_Hα). No coronagraph was used. Data are listed in Tab 3.7. The observations were done during a poor weather conditions night, `ESO UT3 Visitor Telescope Report 9 / 10-Dec-2014` reports that the Grade of this OB is `X` (Uncertain). During these observations, thin clouds, mainly cirrus, passing by are reported. At the end of this program, the wind speed was 12 m/s. The seeing corrected by airmass, as reported in the header of the images, span between 0.95″ and 1.12″. I estimated the SN of these images by a central aperture of 20 pixel radius with respect to a reference aperture located in the RoN dominated area of the image. I show the results in Fig. 3.26. The bad weather conditions implied strong changes in the quality of the data along the dataset.

The data analysis was carried out with the Consortium internal pipeline for ZIMPOL[9],

---

[9] Version 1.0 - Andreas Bazzon - 04.08.2015

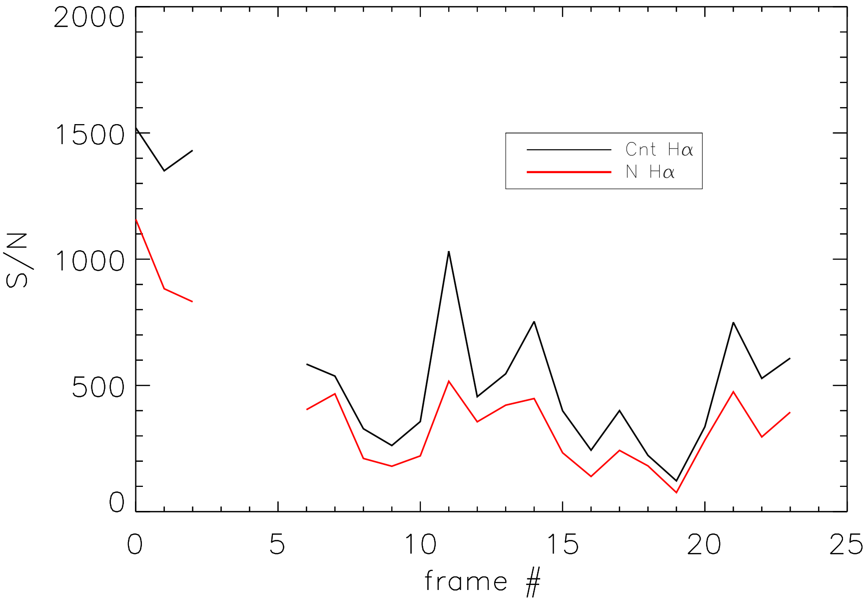

Figure 3.26: Signal to noise estimation for all the DITS of the iLkCa 15 mages.

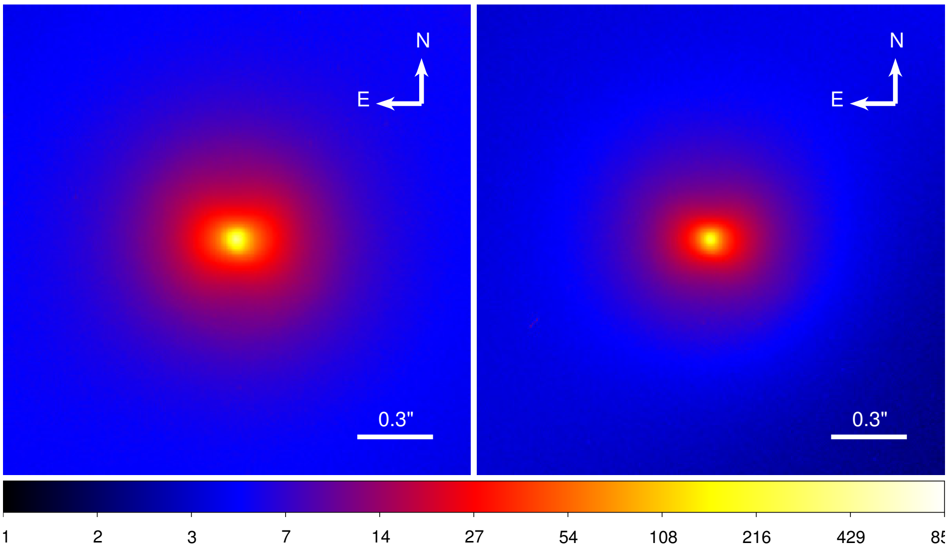

Figure 3.27: Reduction of LkCa 15 ZIMPOL data. The output images of the ZIMPOL pipeline for Cnt_Hα (left) and N_Hα (right).

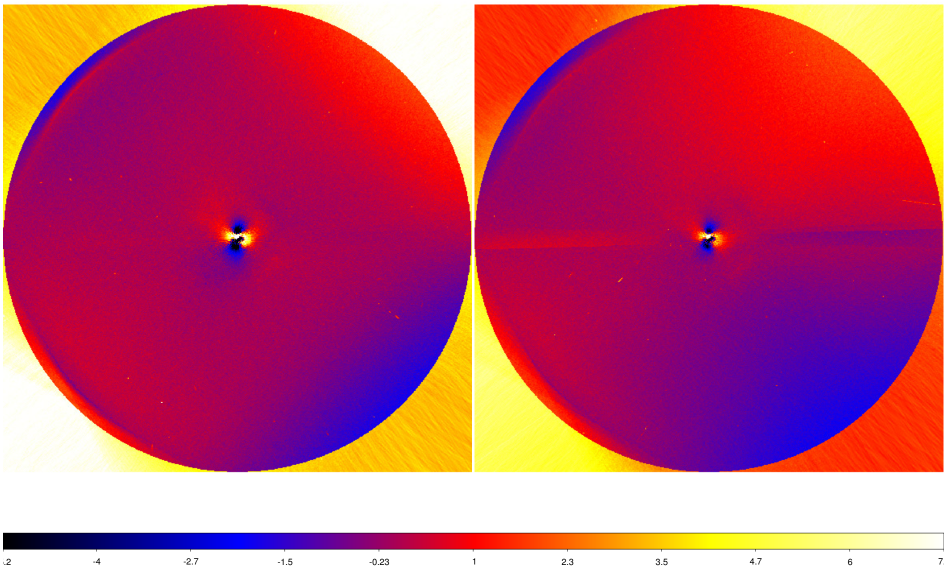

Figure 3.28: Reduction of LkCa 15 ZIMPOL data. The output images of the ZIMPOL pipeline for Cnt_Hα (left) and N_Hα (right) after removing the radial mean.

exploiting different tools. I first collapsed all the frames together using the sigma-clipping tool of the pipeline. In this case I had to enlarge the radius for centering up to 35 pix in order to align all the frames: due to the very poor weather conditions, the center of the PSF moves of about 28 pixels among the frames. The results are in Fig. 3.27. I then applied a spatial filter with a FWHM of $\sim$ 11 pix and subtracted a radial mean to the two images: results are in Fig. 3.28. In both images there are some point-like sources with FWHM comparable with the resolution, but none appears in both the images. Furthermore at this level of reduction, LkCa 15 b, if exists, is embedded in the butterfly-like structure in the center.

With the aim of enhance H_α emitting regions, I tried to align the two camera images using the pipeline option `/camalign` but the result was of very poor quality as shown in Fig. 3.29, on the left: the difference between cam1 N_Hα and cam2 Cnt_Hα images shows a clear offset of about 13 pixels between the two and some artefacts appear.Therefore I applied one of the alignment tools derived for RAqr (see Section A.1) and I obtained that the two images of the two cameras were already well aligned at the end of the ZIMPOL science imaging pipeline without the `/camalign` options as shown in the right panel of Fig. 3.29.

From these two last images, I then obtained the N_Hα-Cnt_Hα image (in Fig. 3.30): in the central part of the disk, at separations comparable with LkCa 15 inner disk, I observed at least 3 lobes, in three directions (NE, SE, SW). The first and the third seem to have a darker hole in the center and they also seem to be opposite with respect the star. Also the NW region of this structure seems to be relatively brighter in N_Hα. In the SW direction, at separations larger than $0.08''$, there is a brighter area. In this image I can also see some bright pixels that are cosmics.

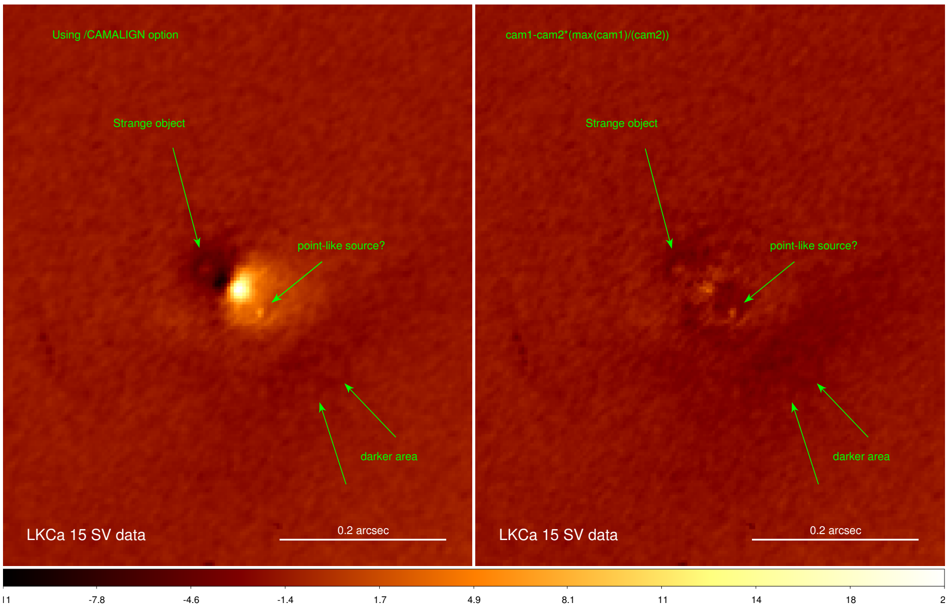

Figure 3.29: Reduction of LkCa 15 ZIMPOL data. Left: difference between cam1 and cam2 using the camalign option clearly shows that they are not aligned. Right: if the option is not used, the residuals are quite good.

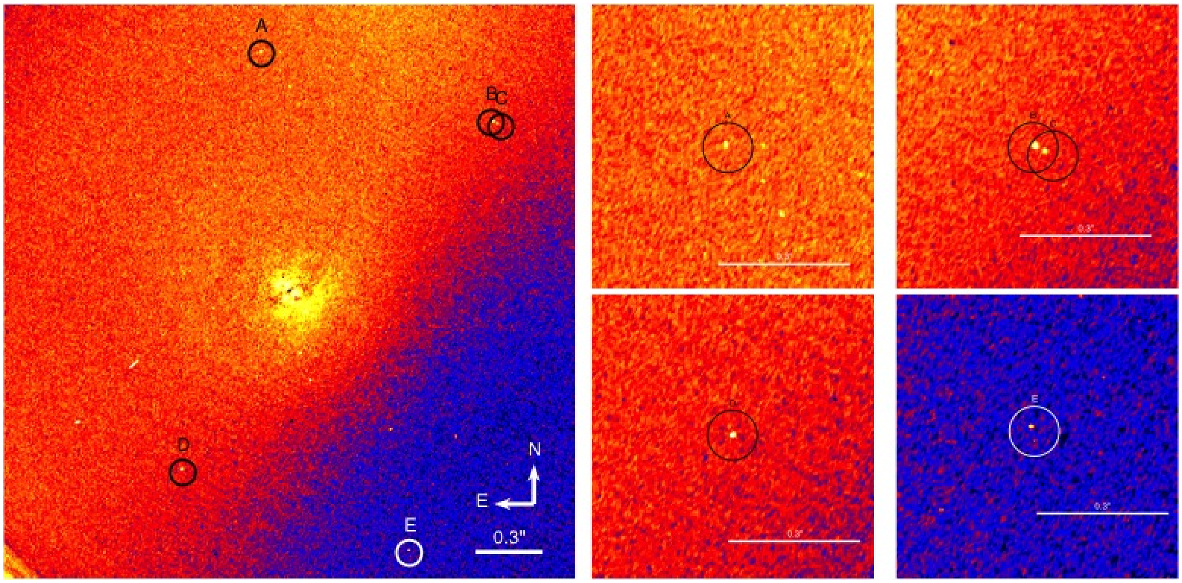

Figure 3.30: Reduction of LkCa 15 ZIMPOL data. N_Hα-Cnt_Hα image with ZIMPOL pipeline. Point like sources are zoomed on the right.

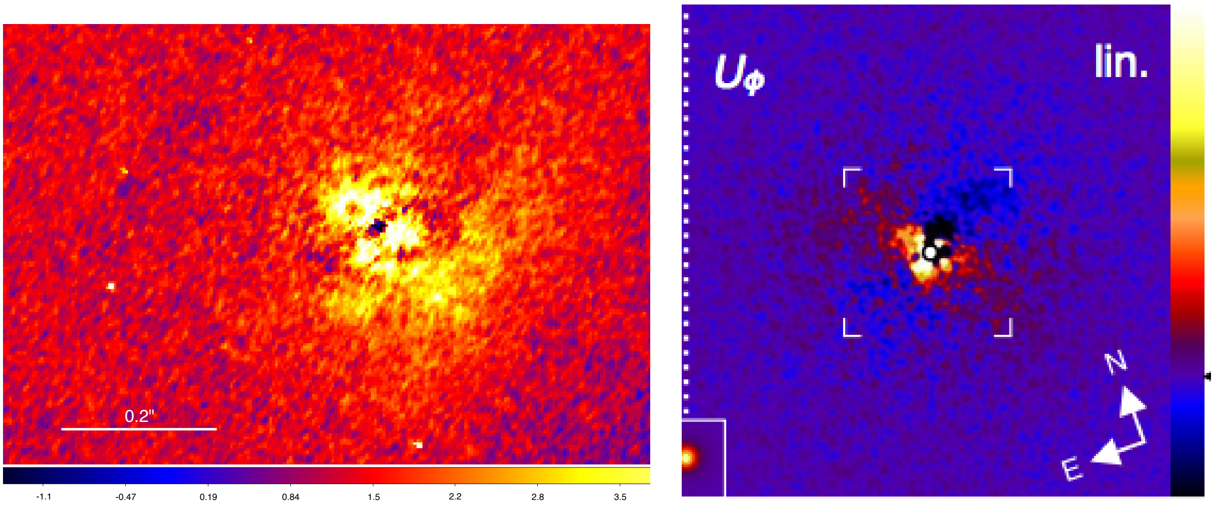

Figure 3.31: Reduction of LkCa 15 ZIMPOL data. Left: Residual image after subtracting Cnt_Hα from N_Hα weighed mean image. Right: Image 1.a U_Φ from Thalmann et al. (2015). The white square represent 0.2" area. All our images are oriented N up and E left.

Mean, median and weighed mean

Since these data have so variable S/N values, I proposed to implement in the pipeline an option that introduces the median of the frames instead of the mean. In addition to this, I created a procedure also for the weighted mean of the frames. All mean, median and weighted mean approaches on this dataset give positive and negative features, as in Fig.3.30.
In Fig. 3.31 I show the central part of the image obtained subtracting the two weighted mean images one to the other, that is quite similar to the previous result. The H_α emission is clear and I also have some hints on the structure. However, the three lobes are very similar to those found by Thalmann et al. (2015), in U_Φ image (their Fig. 1.a), and therefore I conclude they are related to the noise of the image.

Contrast estimate

I can have an estimate of the contrast limit: the first frame is the best one, due to the highest S/N. The star maximum value is 1123 ADU in Cnt_Hα and 639 in N_Hα. The gain is 10.5 e^-/ADU, therefore the two peaks are respectively $\sim 12000e^-$ and $\sim 7000e^-$. Since a better estimation of the RoN gives 16 e^-, I obtain that 1 over σ is equal to 440 counts and 5 over σ is 90 counts. This correspond to a contrast of 4.9 mag.

When I consider the whole data set (21 DITS), the quality of the output images gets worse, so that ... does not scale with the square root of the minutes of observations, and I can expect at best a contrast limit of $\sim$ 6.0 mag. This is exactly what we obtain for the contrast in the weighted mean images (see Fig. 3.32). The differential imaging improve the contrast in the central area of the image ($r \leq 0.1$"), but not at wider separations because the noise of the two original images is dominated by the RoN.

In this case the ADI is not a useful tool to improve the results: ADI might work well on this data set only for $r \geq 0.15$", but in this area the N_Hα-Cnt_Hα image is dominated by

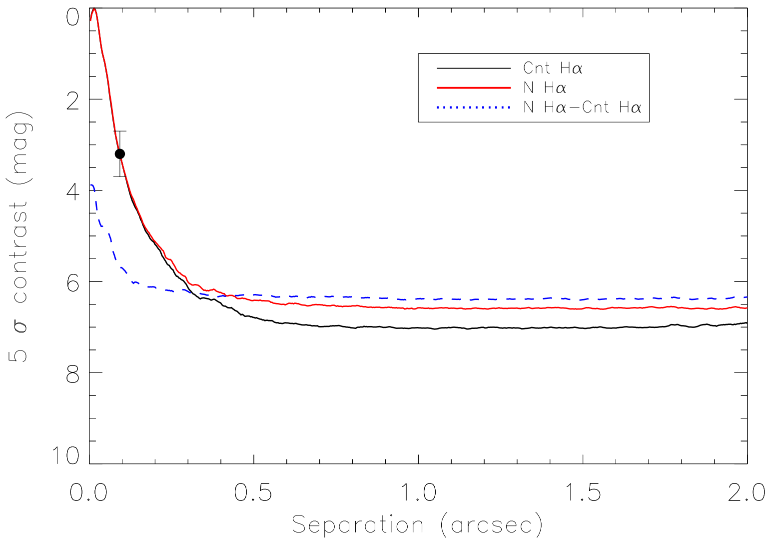

Figure 3.32: Contrast limit before and after the differential imaging at the H_α wavelengths, compared with the contrast obtained by (Sallum et al. 2015a) in rescaled to the ZIMPOL N_Hα filter.

RoN. On the other hand, in the central area the results will not be improved by performing a SDI (e.g. rescaling the images to take the wavelength dependence of speckles into account), because of the small shift we should apply to combine images whereas in the outer part the RoN is the predominant source of noise and SDI cannot remove it.

Comparing our result with those from Sallum et al. (2015a), they found a contrast for LkCa 15 b in H_α of 5.2 ± 0.3 mag. This result was obtained with MagAO H_α filter with $\lambda_0 = 6563$Å and FWHM= 60Å and would implies, assuming a flat spectrum of both LkCa 15 and its companion in this band, a contrast of 3.2 mag in the ZIMPOL N_Hα filter, so that the companion appear at the limit of the 5σ detection with ZIMPOL. However, both the line profile and the time variability of H_α emission from both the star and its companion vary the contrast at H_α wavelength between them, therefore a direct comparison that takes into account the different filters curves is not thorough.

False Alarms

This field is rich in point like sources. At least 5 bright spikes are visible in our images. Are they real? I performed a statistical analysis on LkCa 15 field. According to SIMBAD, LkCa 15 has magnitude R = 11.61. Given that the contrast limit is $\Delta R \sim 6.5$ mag, I looked for all the sources with R < 18 at separation smaller than 120″ in the PPMXL Catalog (Röser et al. 2008). I found only 4 stars. This implies that the chance to have a detectable field star in the ZIMPOL field of view (3.5″ of diameter) is ∼ 1/1000. If I study the signal to noise map of our results and then apply the `find.pro` DAOPHOT-like routine, we found 4 sources in Cnt_Hα and 9 sources in N_Hα, but each source appears only in one filter. This suggests that all the sources we see are cosmics.

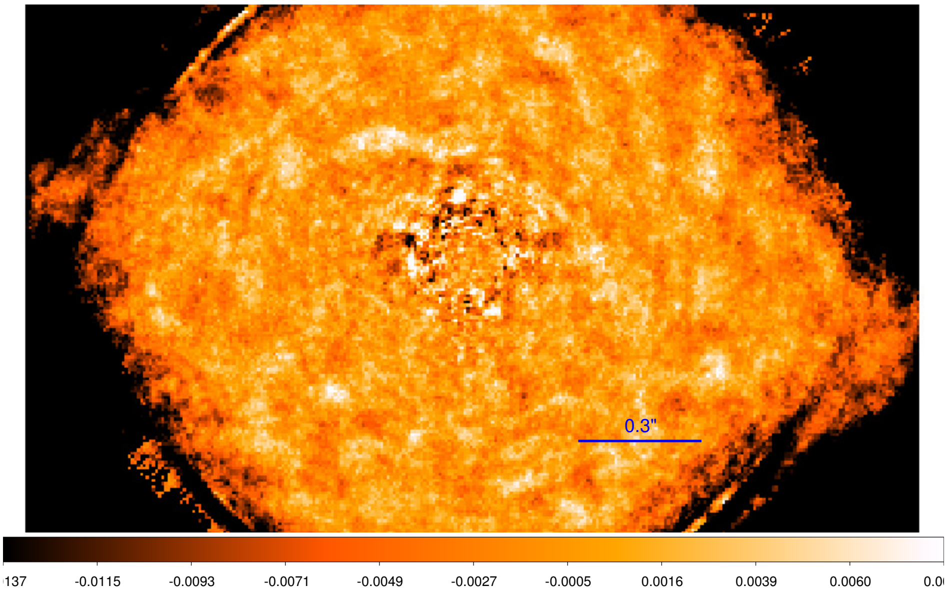

Figure 3.33: LKCa 15 system imaged by IFS in YH wavelength after applying 50 PC.

A lesson for the future ZIMPOL observation
From this analysis I understood that:

- quality of H_α observations are strongly weather dependent;
- observations are mostly RoN dominated;
- cosmic rays and other detector flaws are frequent.

3.4.2 Near-IR observations with IFS

This target was also imaged as a part of the SHINE GTO program, in the night of November, 28th 2015. The observations lasted 4480 s for a total FoV rotation of $\sim$ 24.5°. The observation mode used is IRDIFS_EXT. Pupil tracking was used to allow for angular differential imaging (ADI, Marois et al. 2006), using the `N_ALC_YJH_S` coronagraph (apodized Lyot, inner working angle 93 mas). Non-coronagraphic frames were obtained before and after the coronagraphic sequence for photometric calibration. The dataset was reduced through the SPHERE Data Center (sky subtraction, flatfielding, bad-pixel correction, and centering) and then post processed exploiting the SpeCal software (R. Galicher, priv. comm). As in the case of HD 100546, the IFS dataset was also post processed with the internal OAPD pipeline that performs ADI and SDI simultaneously. The results for the IFS with 50 modes of principal components are in Fig. 3.33: the northern part of the disk is fairly visible, while a bright spot arise at the rim of the coronagraph. This is not in agreement with any of the proposed candidates, as shown in Fig. 3.34. It was soon recognized as a bright speckle through its shift with wavelength as expected for a speckle.

For this target, RDI is not possible, due the lack of a comparable star without disk observed in IRDIFS_EXT mode and to the low intensity of the disk itself.

The contrast limit obtained from the PCA reduction method on LkCa 15 IFS images are reported in Fig.3.35 and gives 8 mag at 30 AU from the star and 11.5 at separation of $\sim$ 60

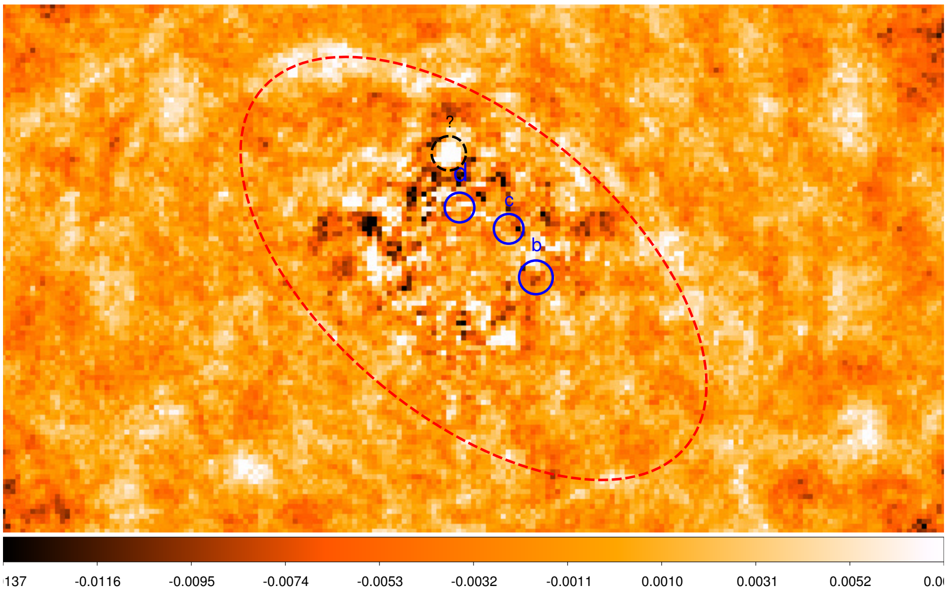

Figure 3.34: LKCa 15 system imaged by IFS in YH wavelength after applying 50 PC. Positions of the proposed b, c and d companions are indicated as solid circles whereas the dotted circle shows the bright speckle. The disk structure is also indicate with a dashed ellipse.

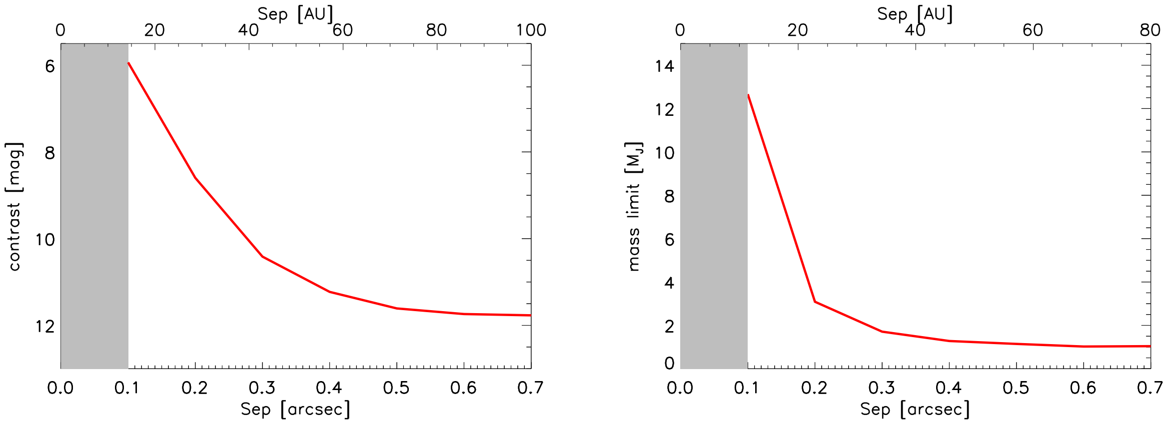

Figure 3.35: Contrast curves for LkCa 15 obtained with PCA in the YH band. For comparison, the contrast of LkCa 15 b in the K' band is $6.0^{+0.2}_{-0.5}$Sallum et al. (2015b).

AU. Using the theoretical atmospheric models from Allard et al. (2003) on detection limit in the J band, I can therefore rule out the presence of companions of $M_p > 13M_J$ in the innermost region and $M_p > 3M_J$ at separations of $0.25''$. No other candidate companions were found further out in the IFS FoV.

Chapter 4

Accreting planets after disk dispersal

Detection of planets during the accretion phase is of paramount importance because it may provide direct evidence of the crucial phase of planet formation. In this phase, close interaction between the planet and the disk is expected: on one side, the planet growth is due to the existence of the disk, on the other side the disk geometry is expected to be strongly altered by the formation of the planet (or more than one) that may ultimately contribute to dispersion of the disk. Evidence for accretion and quantification of the mass accretion rate may help to set the timescale for these complex phases. Systems observed in this phase may give direct information on the migration mechanisms by studying the planet-disk geometry, since the observed location of the planets is very likely close to the original one. And finally, systems with accreting planets may be so young that secular instabilities due to planet-planet interaction might have had not time enough to determine the final architecture of the system. While in the early phase of accretion the planet is expected to be embedded into the protoplanetary disk and then to be undetectable at short wavelengths, we might find evidence for later accretion (likely at a lower rate) once the protoplanetary disk is partially dispersed.

Planet accretion might be in principle detected by emission lines (mainly H) that form in the hot shock interface between the accreting material and the planet itself. Models of the accretion may be used to translate observational parameters, such as the equivalent width of the H lines, into the accretion rate. On the other hand, the presence of strong emission lines might be utilized to reduce the monochromatic star-planet contrast, favoring detections. This has been actually exploited in a few cases to detect faint accreting companions, such as in the case of HD142527 (see Fig. 4.1, Close et al. 2014), GQ Lup and GSC6214-210 (Zhou et al. 2014), that have ages of $\sim$ 5 Myr, $\sim$ 2 Myr and $\sim$ 2 Myr respectively. The strongest emission line in the accessible wavelength range is expected to be H_α (at 656 nm). The equivalent width of this line may be as wide as 20 nm corresponding to accretion rates of several $10^{-10} M_\odot$/yr (Close et al. 2014). While weaker, Paschen β (at 1282 nm) lies at a longer wavelength where the expected achievable contrast is better: it might then represent a competitive alternative to H_α. In addition, observations at different wavelength may be used to better characterize the local environment, in particular the absorption by local dust. Determination of the spectral energy distribution of the faint companion may provide the surface temperature and possibly the radius of the very young planet (see e.g. Quanz et al. 2013). Finally, emission lines are expected to be variable both on short timescales (mainly

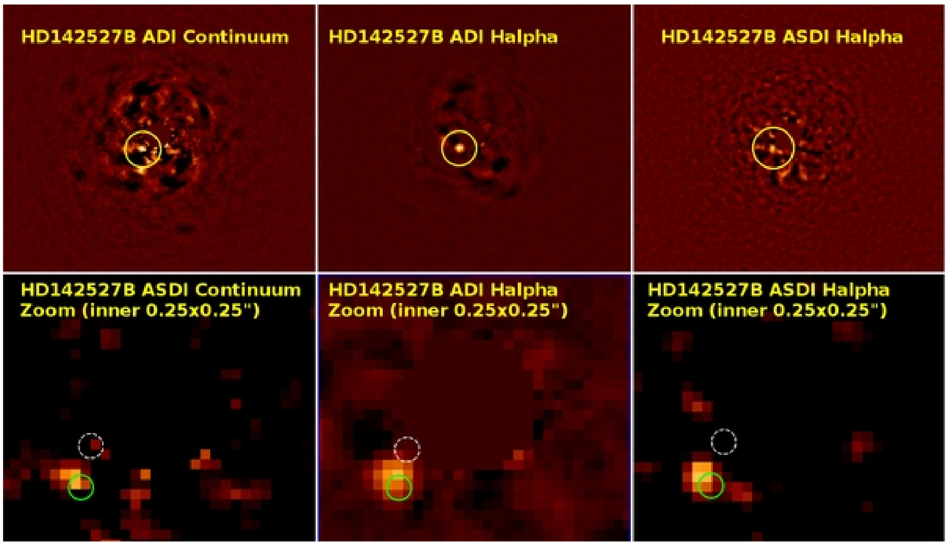

Figure 4.1: Evidence for accretion from the small mass companion of HD 142527 (From Close et al. 2014). Left: Continuum (643 nm) ADI reduced image. (Bottom zooms): Note the weak ($\sim 3\sigma$) detection near the location of the candidate of Biller et al. (2012) (green circle). The source is inconsistent with the background star position (white circle). Middle: H_α ADI images. Note the unambiguous 10.5σ H_α point source at sep = 86.3 mas, PA = 126°, hereafter HD 142527B. Right: ASDI data reduction, here NCP narrow-band filter ghosts are not as well removed as with ADI.

due to variation in the visibility of the emitting region related to planet rotation) and on longer timescales (due to variations in the accretion rate). On even longer timescale orbital movement of the accreting planet might be detected. This indicates that multiple observations may be very useful for a better characterization of such systems.
Many more accreting objects are thought to be detectable with much more sensitive instruments such as SPHERE, using both its visual channel (ZIMPOL) to be used for H_α, and possibly the near infrared Integral Field Spectrograph, to be used for Paschen β. Within this program in the SHINE survey, we planned to observe a number of very promising targets – very young stars with circumstellar disks whose shape is strongly suggestive of the presence of planets. I was responsible for this project.
A few promising targets to show accretion signatures were selected among the SPHERE GTO program.They are all very young (age < 10 Myr) and host substellar companions or candidates down to planetary masses within ZIMPOL field of view. In two cases (GQ Lup and GSC 6214-610) there are indication of H_α emission from HST photometric data (Zhou et al. 2014). Considering the significant improvement in detection limits of faint companions close to the parent star with respect to previously available instruments, we expect several new detections that we will consider for ZIMPOL H_α follow-up depending on the stellar and planetary properties.
The H_α observations of stars with potential substellar companions with H_α emission features will combine two differential analysis techniques; angular differential imaging and simultaneous spectral differential imaging. The short wavelength observation with ZIMPOL will be complemented by those at longer wavelength with simultaneous observations with IFS and

IRDIS. These observations aim to detect the accreting object in Paschen β and to determine its spectral energy distribution. The IRDIS observation, extending over a wide area, can be also used to study the disk geometry.

4.1 Preparing the observations

4.1.1 Paschen β observations with IFS

Standard IRDIFS and IRDIFS_EXT observations, with spectral resolution of 50 and 30 respectively, can be used to estimate the Pa_β emission. All images are taken in pupil stabilized mode and then processed with Angular Differential Imaging techniques and Spectral Differential Imaging simultaneously. `More details can be found in Maire et al. (2016a) .`

4.1.2 Paschen β observations with IRDIS in LSS mode and IFS

IRDIS LSS includes a low-resolution mode (LRS), which covers the Y JHKs bands at resolutions of ∼50 in one shot, and a medium-resolution mode (MRS), which covers the Y JH bands at a resolution of ∼350, two different slits and two dispersive elements (prism and grism) (Vigan et al. 2012). Moreover, IRDIS offers the unique combination of a classical Lyot coronagraph with LSS. The LSS observations are always performed in field-stabilized mode to keep the object within the slit during the whole integration. A sequence consists of images with the star behind the coronagraph, an off-axis reference PSF, in which the star is shifted out of the coronagraph within the slit, and finally a series of sky backgrounds. We acquired also a telluric standard to remove the telluric absorptions. The sky backgrounds are particularly important for the LRS mode, since the thermal background of the instrument and sky are much higher in the Ks band. The sequences do not differ between the LRS and MRS modes except for the change of the dispersive element. An example of raw and processed spectra of IRDIS LSS mode is given in Fig. 4.2, where the spectral dimension of our spectra is along the horizontal axis, and the spatial dimension along the vertical axis. The companion spectrum appears as a horizontal line, while the speckles produce oblique path, since their separation from the star and size have a linear dependence with wavelength. This property is used to separate the light coming from the planet from the light coming from the star scattered into the speckles, as described in Vigan et al. (2008).

4.1.3 H_α observations with ZIMPOL

In order to observe these objects with ZIMPOL, the following initial configuration was devised:

- use ADI for stars up to about 8 mag;
- for fainter stars the integrations become so long (100s) that there could be rotational smearing. In this case, field stabilized mode is suggested. In addition, the scheduling is much easer.
- no use of coronagraph: PSF are unsaturated with DIT of 3 sec for a 5 magnitude star, with DIT of 30 s for a 7.5 magnitude star.

This provides:

- good sensitivity for H_α point source detection;

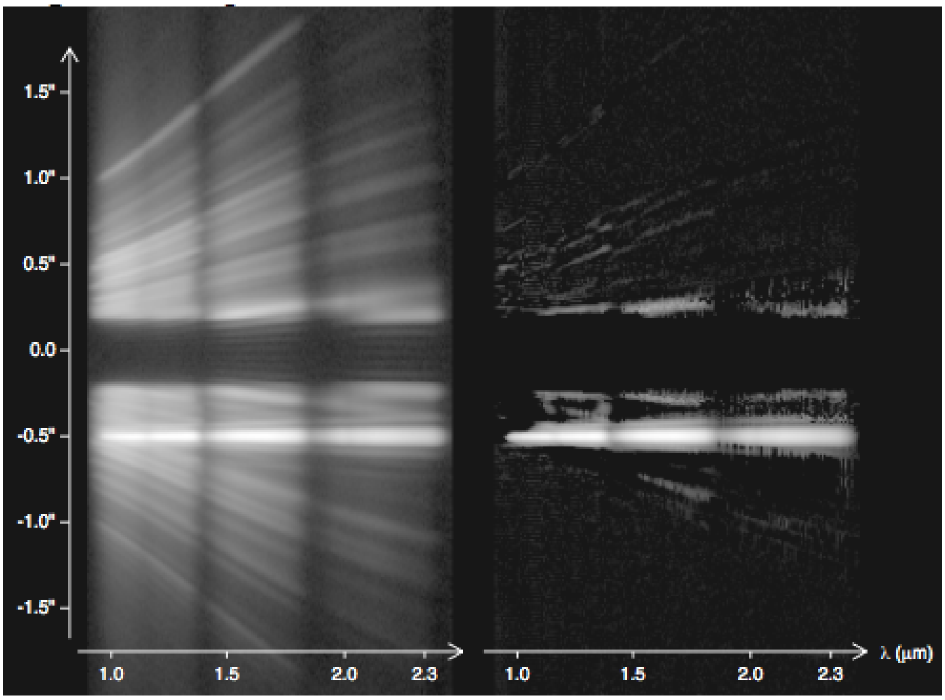

Figure 4.2: IRDIS LRS data obtained on PZ Tel (H=6.5). The left image is the spectrum after preprocessing and cleaning using the data reduction and handling pipeline (DRH). It corresponds to a 20 minutes exposure (DITxNDITxNEXP=20x10x6) in good conditions (seeing of 0.5″-0.6″). The spectrum of the companion PZ Tel B is visible as a straight line amidst the speckles at an angular separation of $sim0.5''$. The obscured part between ±0.2″ corresponds to the position of the opaque coronagraphic mask. The contrast of the companion is $\sim$ 5.4 mag in H-band (Biller et al. 2010). The right image is the data after stellar halo and speckles subtraction using the spectral difference approach described in (Vigan et al. 2008). The spectra are displayed with the same logarithmic color scale.

Table 4.1: Estimation of contrasts and magnitude limits for H_α observations of star hosting accreting companions.

Star	V	R	Type	contrast at 534 mas (ETC)	(linear)	mag H_α lim
HD 100546	6.30	6.30	B9	10.75	11.3	17.6
HD 169142	8.16	8.20	A5	10.74	10.6	18.8
ROXs 42B	11.00	10.00	K7	10.69	9.5	19.5
GQ Lup	11.40	10.58	K7	10.63	9.4	20.0
T Cha	11.86	11.00	K0	8.72	9.2	20.2
GSC 6214-210	12.60	12.11	M1	8.65	8.9	21.0
CT Cha	13.00	11.60	K7	8.09	8.8	20.4
DH Tau	13.10	13.01	M1	8.25	8.7	21.7

- easy type of observations.

The standard instrument setup could be, therefore:

- use of the dichroic beamsplitter between ZIMPOL and the WFS;
- use of the H_α continuum filter Cnt_Hα in one arm and B_Hα filter in the other;
- For the flux calibration, swap the filters in the two arms in the middle of the observations. The beam splitter of ZIMPOL is indeed sensitive to the polarization, dependent throughput of the inclined mirror of the telescope and derotator. Swapping between the two channels can also be performed to suppress instrumental effects in one individual detector channel, after an analysis of the differential effects.

A standard observation sequence includes:

1. Reference flux exposure, using N_R filter in both arms;
2. Reference center exposures with H_α filters (only for off-axis observations);
3. Several science exposures (for a total of about 1 hr) with filter swapping, dithering and/or field rotation;
4. Reference center exposures with H_α filters (only for off-axis observations);
5. Reference flux exposure, using N_R filter in both arms.

4.2 Interesting Objects

About 10 objects of the SPHERE GTO program are thought to host companions in the late accretion phase. I first study the feasibility of the observations in ZIMPOL H_α for a few of them as indicated in Table 4.1. Among these, an embedded accreting companion was claimed in the disks of HD 100546 and HD 169142 as described in Chapter 3, while the case of T Cha b inside the disk gap is controversial (Sec. 3.3). The other stars host a companion that is thought to be in the last stage of accretion phase, when the protoplanetry disk is mainly already dispersed, but some material is still accreting on the planet and on the central star, as shown in Table 4.2. I planned to observe six of them:

Table 4.2: for known companions, mass and their mass ratio with respect to the stellar mass, the age and the separation are listed. In column 6 I indicate if the companion lies inside or outside the primary debris disk and if a circumplanetary disk (CPD) was detected.

STAR	M_c $[M_J]$	M_*/M_c	Age_c [Myr]	Sep_c [AU]	I/O	CPD	Ref.
T Cha	?	?	7	6.7	In	?	1
CT Cha	17 ± 6	23	~ 2	430	Out	?	$2, 3, 4, 5$
GQ Lup	10-30	28-85	2 ± 1	~ 100	Out	?	$6, 7$
GSC 6214-210	15 ± 2	~ 43	2	320	Out	Yes	$8, 9$
DH Tau	30-50	7-33	3-10	330	Out	Yes	$10, 11$
ROXs 42B	6-15	16-40	1-3	150	No	?	12

1 Huélamo et al. (2011); 2 Natta et al. (2000); 3 Zhou et al. (2014); 4 Wu et al. (2015); 5 Pascucci et al. (2016); 6 Neuhäuser et al. (2005); 7 Wu et al. (2017); 8 Bowler et al. (2011); 9 Lachapelle et al. (2015); 10 Gräfe et al. (2011); 11 Furlan et al. (2011); 12 Currie et al. (2014b).

T Cha: for this star there is a claim of a very close candidate at about $0.1''$(Huélamo et al. 2011), albeit recent works seems to reject it (Olofsson et al. 2013; Cheetham et al. 2015), as described in Sec. 3.3. So very challenging case, and in any case we should aim for the closest possible separation. Howerer, ADI is really challenging due to target faintness and very souther declination (slow rotation even at meridian). It will be fine to observe in field stabilized mode.

CT Cha: the substellar companion of CT Cha, which is likely accreting (it has an emission seen in Pa_β and an excess in r' broad band) and then good target for H_α imaging, lies a bit outside of the ZIMPOL field of view (projected separation about $2.7''$, PA 298°) and the off-axis mode should be used. Field stabilized mode and perhaps dithering could be useful. From the results by Wu et al. (2015), the BD companion is too faint in R continuum (out of H_α) to be detected (r' = 21.9 mag, expected r'=24.9 mag without H_α). We plan to use two different filters setup: N_R + N_R and then B_Ha + B_Ha.

GQ Lup: its companion is located at about $0.72''$ (Neuhäuser et al. 2005). No angular differential imaging is needed for this separation.

GSC_6214-210: in this system the companion lies at $2.2''$(Ireland et al. 2011). This implies the use of field stabilized observations and to define suitable rotation in order to include the known companion in the field of view.

DH Tau: the companion of DH Tau was observed at 330 AU from its star, that is $2.3''$ of separation. This implies to use the off-axis mode of ZIMPOL. The accretion of this object was detected by Zhou et al. (2014) and appears brighter than GQ Lup b.

ROXs 42B: the 9 M_J companion of this star lies $1.16''$ away and therefore the pupil stabilized mode can be used. Accreting signature are not confirmed for this star.

Up to now, observations were executed for GQ Lup and partially executed for CT Cha. I'll describe the main results in the following Sections.

Table 4.3: Summary of the planned ZIMPOL targets, their position, R magnitude and proper motions. The last column present the observing mode planned and the presence of a companion (C) or candidate companion (CC); for TCha the off-axis observation is needed.

Object	RA	dec	R	μ_α	μ_δ	Remarks
CT Cha	11:04:09.09	-76:27:19.38	11.98	-15.00	5.00	FS, C, off-axis
GQ Lup	15:49:12.10	-35:39:05.12	10.38	-15.10	-23.40	FS, C

4.3 GQ Lupi

GQ Lup is a young T Tauri star with K7eV spectral type (Herbig 1977). It is located in the Lupus I group at about $\sim$ 150 pc (Tachihara et al. 1996). The magnitude in R band is $R = 11.0$ (Cutri et al. 2003) and shows strong emission lines with variability in flux as, for example, in the Balmer continuum (Batalha et al. 2001) and of about 0.5 mag in K_s (Broeg et al. 2007; Neuhäuser et al. 2008). It hosts a circumstellar disk that is well detected with ALMA (MacGregor et al. 2017; Wu et al. 2017).

A brown dwarf companion was discovered by Neuhäuser et al. (2005) comparing existing HST/WFPC2 and Subaru/CIAO observations with direct K-band imaging with NACO. GQLup b is located at a separation of $0.713''{\pm}0.006$ and $PA = -83.6°{\pm}0.7°$ according to Zhou et al. (2014) with a orbital motion of $\Delta\rho \sim -1.4\,\mathrm{mas/yr}$ and $\Delta PA \sim 0.16°/\mathrm{yr}$ (Ginski et al. 2014). In GQ Lup b, Seifahrt et al. (2007) found a prominent Pa$_\beta$ emission line at 1.282 μm, with an equivalent width of $EW(Pa\beta) = -3.83 \pm 0.15$ Å, in a SINFONI spectrum. Using the near infrared IFS unit of the Gemini North Telescope, Lavigne et al. (2009) found out that the Pa$_\beta$ emission was much weaker ($EW(Pa\beta) = -0.46 \pm 0.08$Å) and that the spectrum appeared redder then that observed by Seifahrt et al. (2007) two years earlier. Spectrum contamination in the oldest data cannot explain this discrepancy. Moreover, the spectral slope by Lavigne et al. (2009) is consistent with KeckII/OSIRIS observations by McElwain et al. (2007). This discrepancy can be due to a real variability of the source, that would be of paramount importance in planet formation theories, or an effect of different instruments data reduction.

The source was revealed also at H$_\alpha$ in direct imaging by Zhou et al. (2014), using the HST F656N filter ($\lambda_{eff} = 6561.24, FWHM = 17.89$ Å, data from SVO2) with a flux of 5.92×10^{-16} erg cm^{-2} s^{-1}Å^{-1} which corresponds to a magnitude of 15.9 in this filter. In the two adjacent filters F625W ($\lambda_{eff} = 6155.90, FWHM = 1572.62$ Å) and F673N ($\lambda_{eff} = 6765.50, FWHM = 120.20$ Å), the mean flux is 4.94×10^{-17} erg cm^{-2} s^{-1}Å^{-1}, therefore GQLup b in F656N band is 15 times brighter ($\sim$ 3 magnitudes), whereas the H$_\alpha$ contrast with respect to the star is $\sim$7.1 mag (Wu et al. 2017). As a consequence, they found $\log L_{H\alpha}/\log L_\odot = -4.69$. MagAO observations by Wu et al. (2017) with an H$_\alpha$ filter ($\lambda_{eff} = 656nm, \Delta\lambda = 6.3nm$) revealed the source with a S/N $\sim$ 3.6 but no signal can be found at the GQ Lup b position in the reference continuum ($\lambda_{eff} = 643nm, \Delta\lambda = 6.1nm$) filter. H$_\alpha$ observations give a contrast of $\Delta H_\alpha \sim 8.60 \pm 0.16$ mag, that gives $\log L_{H\alpha}/\log L_\odot = [-5.9, -5.4]$, and a 3σ upper limit to the contrast of 8.81 mag in the adjacent continuum filter. For what concerns Pa$_\beta$, intrinsic variability or wrong data reduction can be the origin of the discrepancy, but in any case it is clear that GQ Lup b is an object still accreting at moderately low level, even if it does not show a prominent disk, as shown in Fig. 4.3 (Wu et al. 2017).

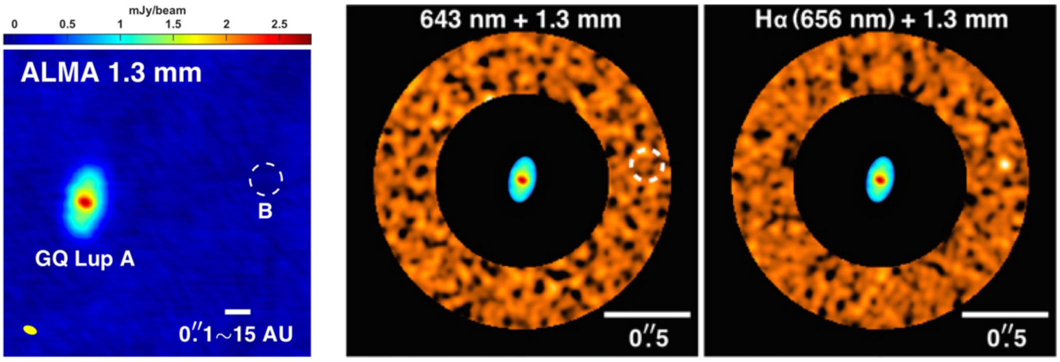

Figure 4.3: From Wu et al. (2017). Left: ALMA 1.3 mm continuum map showing GQ Lup A's accretion disk. They did not detect B's disk (dashed circle). The 0.054″× 0.031″beam (8.1 au × 4.7 au at a distance of 150 pc) is shown as a yellow oval. North is up and east is left. Right: GQ Lup B in MagAO continumm and H_α filters. We mask out the central 0.5″ and overlay the ALMA 1.3 mm disk image. GQ Lup B is glowing at H_α but not the 643 nm continuum, indicating active accretion. North is up and east is left.

4.3.1 IFS observations

GQ Lup was observed with SPHERE in the nights of May 4th, 2015 and June 27th, 2016, in the standard IRDIFS mode (IFS in the YJ mode, IRDIS in the H band) in pupil stabilized mode in order to exploit the ADI technique. The total FOV rotations were 24.88° and 101.09° respectively, and the median DIMM seeing on the source was of 1.06″ and 0.62″. As for other stars with previously known substellar companions, the main scientific goals were (i) astrometric and photometric/spectroscopic characterization of the known substellar companion; (ii) search for additional substellar companions in the system. As GQ Lup b lies within the IFS FoV, we expect the IFS low resolution spectrum to constrain the Pa_β emission.

The companion is clearly detected in our IFS data: the SNR is of ~ 39.5 in a simple PSF subtraction reduction and > 500 if classical ADI is applied. No other candidate companion was found with contrast lower than 12 magnitudes at separations greater then 0.3″ (see Fig. 4.4). This implies, using AMES-Cond models, a mass limit of 3.6 M_J for objects with projected separations >40 au and 25 M_J at 0.15″. The disk that is well detected in the ALMA data is not visible in the SPHERE scattered light images. GQ Lup b has a contrast $\Delta J = 5.88$ mag with respect to the star and its spectrum is shown in Fig. 4.5.

I estimated the EW of the Pa_β line by considering the contrast flux, corrected for the GQ Lup A spectrum, in two continuum windows ($F_{c1} = sp[29:31]$ and $F_{c2} = sp[35:37]$) and the Pa_β interval ($F_{P\beta} = sp[32:34]$) in the ADI-derived spectra. The EW is then defined as:

$$EW = 1 - \frac{mean(F_{P\beta})}{mean(F_{c1}, F_{c2})} \tag{4.1}$$

and gives $EW_{P\beta} = -6.8 \pm 0.5$ Å for the first observation and $EW_{P\beta} = -2.0 \pm 0.3$ Å for the second. The errors are evaluated according to the detection signal to noise ratio (~ 0.3 Å), the photon noise (~ 0.2 Å) and the uncertainty of attenuation effect introduced by the ADI technique (~ 0.15 Å). Since the EWs are derived from the contrast spectrum, in principle these values should be corrected for the stellar contribution: GQ Lup A is indeed emitting in Pa_β with EW of the order of 2Å, as obtained from the quasi simultaneous long slit spectrum

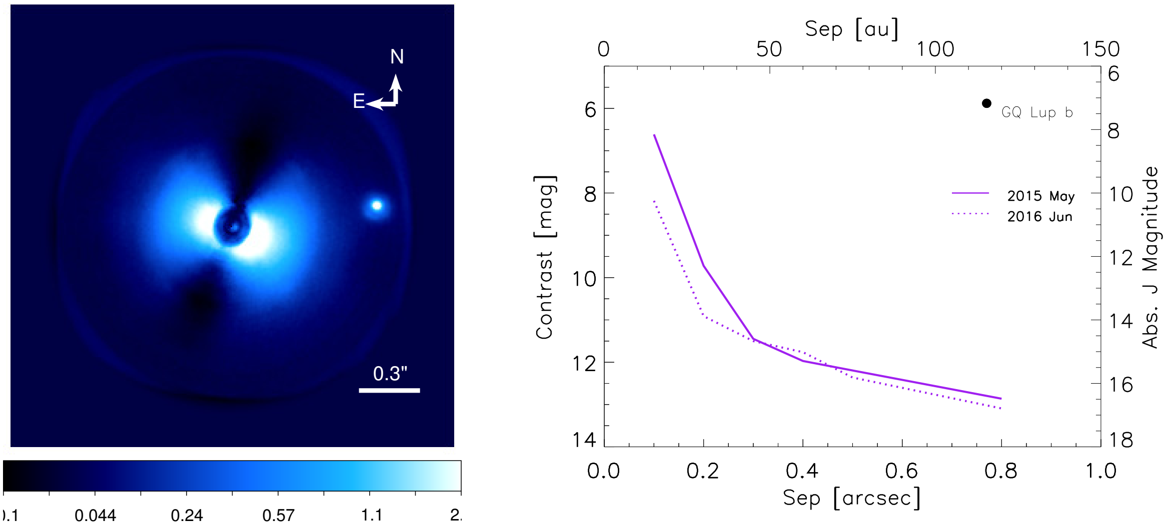

Figure 4.4: GQ Lup b with IFS after a simple psf subtraction (left) and the respective contrast curves for the two epochs in J band (right).

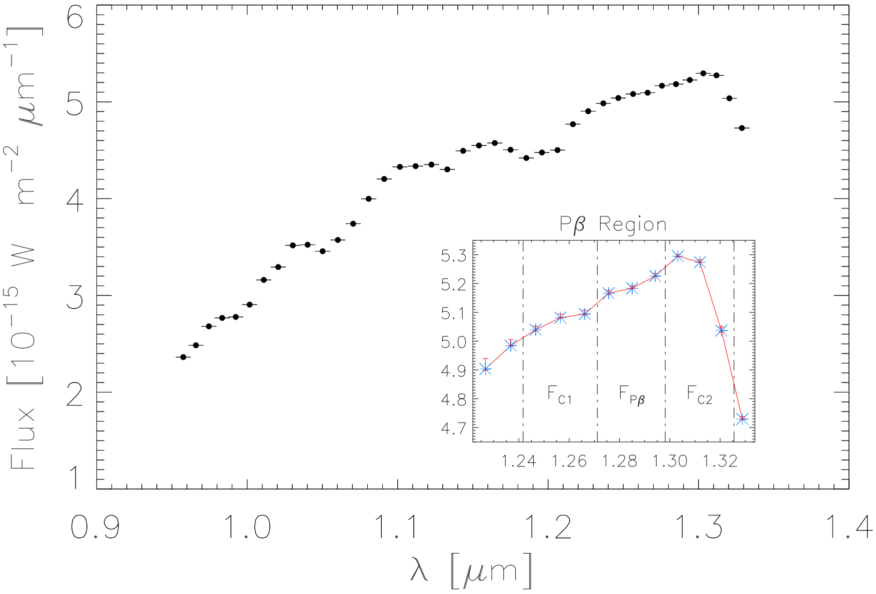

Figure 4.5: GQ Lup b IFS spectrum obtained with ADI technique.

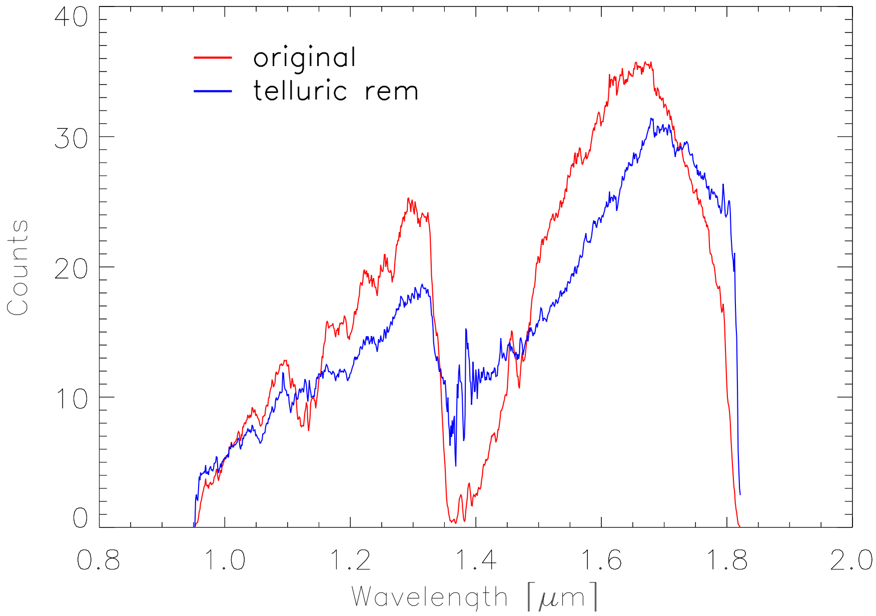

Figure 4.6: IRDIS LSS spectrum of GQ Lup b. The original spectrum (in red) and the corrected one for the telluric spectrum (blue) are shown.

(see below). In the future, GQ Lup observations with the aim of measuring the accretion need to be well calibrated in flux, that is, a priori evaluation of the stellar accreting phase is needed.

4.3.2 LSS observations

GQ Lup b was also observed with IRDIS in LSS in the night of March 31st, 2016 in MRS mode (R∼400) and a follow up is planned in P99 (June 2017), with the aim of better characterize Pa_β emission.

I first remove from the BD spectrum the telluric contribution: to do so, I use the `telluric` task within IRAF that allows to take into account for shifts in wavelength between the standard and the GQ Lup spectrum, as well as for tiny differences in the line strengths of atmospheric features due to very small differences in the air masses (see Fig. 4.6). I did not perform a new wavelength calibration actually because for my purpose I did not need the contrast spectrum.

4.3.3 H_α observations with ZIMPOL

Images of GQ Lup with ZIMPOL were acquired during the night July, 3^{rd} 2015 (see Table 4.4). GQ Lup was observed in field stabilized mode in both the continuum close to H_α (Cnt_Ha) and the broad band H_α filter (B_Ha) with swapping of filter position and two different derotator zero point angles (0° and 60°)[1].

---

[1] see Appendix A for more ZIMPOL technical details

Table 4.4: Images used for the GQ Lup analysis.

Frame id	DIT	NDIT	mode	coronograph	FW0	FW1	FW 2	posang
OBS185_0002.fits	300.	3	I	CLEAR1	OPEN	B_Ha	CntHa	0.
OBS185_0003.fits	300.	3	I	CLEAR1	OPEN	CntHa	B_Ha	0.
OBS185_0004.fits	300.	3	I	CLEAR1	OPEN	B_Ha	CntHa	60.
OBS185_0005.fits	300.	3	I	CLEAR1	OPEN	CntHa	B_Ha	60.

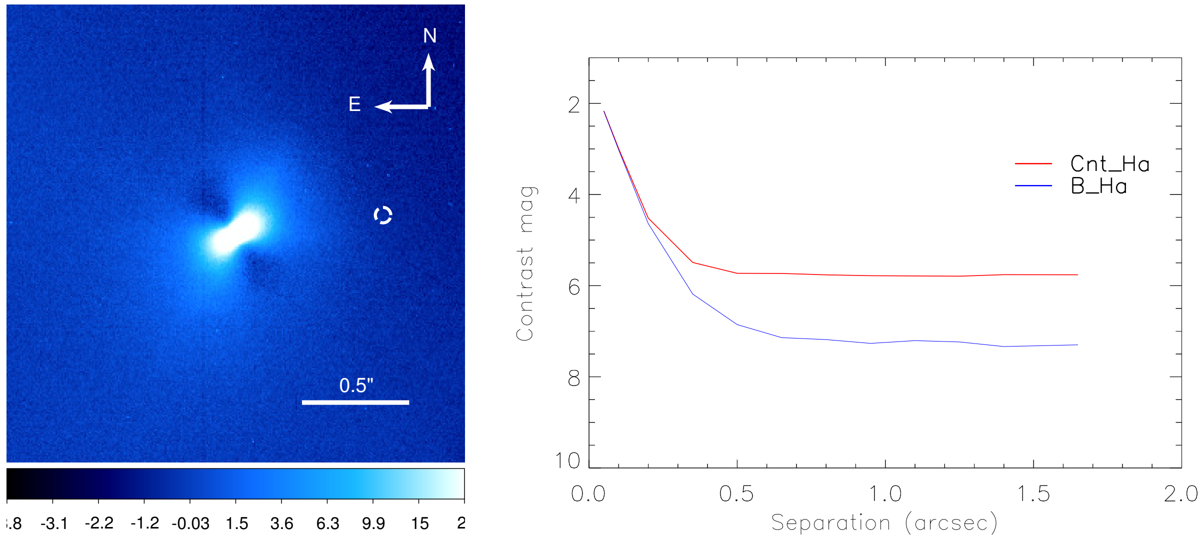

Figure 4.7: Image of GQ Lup with ZIMPOL in B_Ha after a simple psf subtraction (left) and the respective contrast curve (right) compared to the contrast limit in the Cnt_Ha band. GQ Lup b is not detected on this image.

Table 4.5: PSF parameters for idividual DITS of GQ Lup.

File	Filter	S_0	$\mathrm{ct}(r)/\mathrm{ct}_{3\mathrm{dia}}$ [%]				
		[%]	0	5	10	30	100
OBS185_0002	B_Ha	0.360	0.013	0.919	2.849	11.776	38.967
OBS185_0002	B_Ha	0.324	0.012	0.836	2.672	11.842	40.397
OBS185_0002	B_Ha	0.207	0.008	0.558	1.861	9.372	37.114
OBS185_0003	CntHa	0.049	0.002	0.143	0.520	3.328	18.311
OBS185_0003	CntHa	0.061	0.002	0.173	0.623	3.883	20.777
OBS185_0003	CntHa	0.072	0.003	0.202	0.701	3.870	18.899
OBS185_0004	B_Ha	0.597	0.022	1.436	4.132	14.300	40.672
OBS185_0004	B_Ha	0.554	0.020	1.358	3.965	13.928	40.467
OBS185_0004	B_Ha	0.383	0.014	0.986	3.015	11.920	38.056
OBS185_0005	CntHa	0.122	0.004	0.324	1.043	4.693	18.511
OBS185_0005	CntHa	0.052	0.002	0.151	0.533	3.096	15.275
OBS185_0005	CntHa	0.042	0.002	0.118	0.422	2.661	14.603

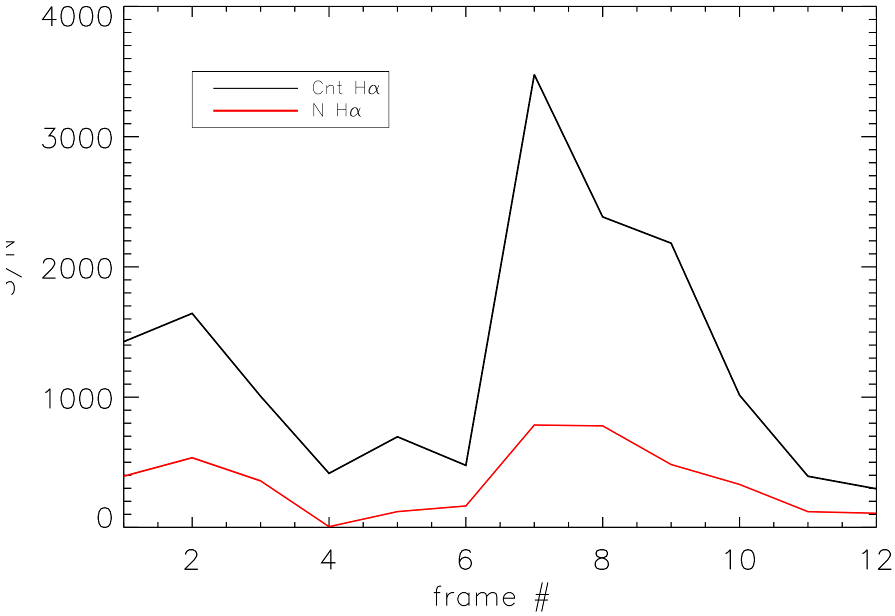

Figure 4.8: Time variation of GQ Lup flux in the center for both cameras.

Table 4.5 reports on the values for the Approximate Strehl value S_0 and the radial counts distribution, as described in Schmid et al. (2017). Encircled counts Ct(r) are given for round synthetic apertures with radius r and total number of pixels npix and expressed as ratio ct(r)/ct$_{3dia}$ relative to the counts ct$_{\rm 3dia}$ in an aperture with a diameter of $3''$ or $r = 416$ pix (npix = 543657).

Even if the sequence was bad with highly variable conditions (the corresponding S/N is shown in Fig. 4.8), our B_Hα observations can reach a contrast limit of 7.1 mag, but GQ Lup b is not visible in the ZIMPOL H$_\alpha$ channel (see Fig. 4.7). The limits are obtained as follows: I stacked all the reduced frames (both cam 1 and cam2) with the same filter; I then calculated the median radial profile and subtracted it from each frame and stacked them again. The 5σ detection limit is then the median standard deviation of the flux at different separations in this last image.

The final SNR ratio is consistent with expectations given the low SR of most of the observations. Noise is dominated by the detector read out[2].

Zhou et al. (2014) gives an EW for GQ Lup in F656N filter equal to 180Å. The observed magnitude in the F656N HST filter is 15.9 mag (Zhou et al. 2014). We correct this value for the filter FWHM for both HST (17.89 Å) and ZIMPOL (55.00 Å) obtaining a difference

---

[2] I am focusing on the B_Hα filter. The first two exposures of OBS_0004 seem to be the best of the sequence, in terms of signal to noise, and they are also better than the final processed image. I then selected the best frame (dc004 0). The peak in the center is equal to $t = 1839.62$ counts. The standard deviation in an area of 21×21 pixels at separation of GQ Lup b, RoN dominated, is $\sigma = 0.690$. We assume that the detection limit is $5 * noise * \sqrt{2}$, we obtain 4.87, which corresponds to 0.0026 in flux contrast and 6.473 in magnitude contrast (Table 4.6). Our non detection in ZIMPOL is therefore compatible with the previous detection. If we select the three best frames we obtain that the final S/N is 695.6 with a contrast limit of 7.11 (Table 4.7), again too weak to allow GQ Lup b detection.

t	peak in the best frame	1893.62
σ	stddev in the best frame	0.689858
detection limit	$5\sigma * \sqrt{2}$	4.87803
flux contrast limit	$5\sigma * \sqrt{2}/t$	: 0.00257603
mag contrast limit	$-2.5 * \log 5\sigma * \sqrt{2}/t$	6.47262

Table 4.6: Results for the best ZIMPOL frame for GQ Lup.

t	peak in the best frame	1842.21
σ	stddev in the best frame	0.374536
detection limit	$5\sigma * \sqrt{2}$	2.64837
flux contrast limit	$5\sigma * \sqrt{2}/t$	: 0.00143761
mag contrast limit	$-2.5 * \log 5\sigma * \sqrt{2}/t$	7.10590

Table 4.7: Result combining the three best ZIMPOL frames of GQ Lup.

in magnitude of -1.22 mag that implies that the GQ Lup expected contrast in the ZIMPOL B_Ha filter is of 8.32 mag, if the line strength has not changed since the HST observations. This is about 3 times fainter than the detection limit of the ZIMPOL H_α observations. So the non detection in ZIMPOL is not surprising.

Starting from our best contrast limit ($5\sigma = 7.11 mag$) I estimated an upper limit to EW. Since the position of GQ Lup b is well known due to the quasi simultaneous IFS/IRDIS data, we can use the 2σ contrast of ZIMPOL to infer an upper limit to H_α emission: in this case, ZIMPOL will have a limit in contrast magnitude of 8.10 at GQ Lup b location. ZIMPOL and HST filter have a difference in magnitude due to the filters band width of -1.22, that would imply a contrast of 6.88 mag in the HST filter for an object at the ZIMPOL 2σ contrast limit. This implies an upper limit to the H_α EW of 220 Å.

4.3.4 Accretion Rate

I built up a catalogue for the Pa_β and H_α observations in order to infer the variability of GQ Lup b. I considered the synthetic spectra for GQ Lup b given in Zhou et al. (2014) that consists of the photosphere (from the BTSettl grid with CIFIST opacities by Allard et al. (2012)) plus a flat accretion spectrum (Herczeg & Hillenbrand 2014), corrected for interstellar absorption of $A_V = 1.5$. I then applied to this spectrum the EW given in the literature both for Pa_β and H_α and SPHERE values, as shown in Table 4.8. These values were then converted into accretion rates using Alcalá et al. (2017) relations for H_α and Pa_β. These relations are based on the complete sample of class II YSOs belonging to Lupus I, II, III and IV and gives:

$$\log L_{acc}/L_\odot = 1.74 \pm 0.19 + (1.13 \pm 0.05) \log L_{H\alpha}/L_\odot \quad \text{for } H_\alpha \tag{4.2}$$

$$\log L_{acc}/L_\odot = 2.76 \pm 0.34 + (1.06 \pm 0.07) \log L_{P\beta}/L_\odot \quad \text{for } P_\beta \tag{4.3}$$

The results are in Fig. 4.9: except for the first two detections, all other observations clustered around $\log L_{acc} = -3.55 L_\odot$. The first IFS detection lies at $\log L_{acc}/L_\odot = -3.0$ but the original spectra is of worse quality with respect to the other. Nevertheless we cannot exclude a real bump of the accretion at that epoch. A higher accretion rate, followed by a drop is possibly also seen between the SINFONI and the OSIRIS observations. It should be noticed that

Table 4.8: Summary of all GQ Lup b observations in both H_α and Pa_β. Epochs are in JD-2450000, EW are in units of Å, fluxes are expressed in units of $[ergs^{-1}cm^{-2}\AA^{-1}]$, masses in $M_\odot$.

line	Epoch	EW	F_{cont} $[10^{-16}]$	F_{line} $[10^{-15}]$	$\log \frac{L_{line}}{L_\odot}$	$\log L_{acc}$	$M_{*,acc}$ $[10^{-10}]$
IFS1*	7147	6.80	7.50	5.10	-5.39	-2.95	7.09
IFS2	7566	2.00	7.50	1.50	-5.92	-3.52	1.94
SINFONI	3997	3.83	7.50	2.87	-5.64	-3.22	3.86
OSIRIS	4251	0.46	7.50	0.35	-6.56	-4.19	0.41
IRDIS LSS	7479	1.50	7.50	1.13	-6.05	-3.65	1.43
HST	5983	180.00	1.32	23.8	-4.72	-3.59	1.62
MagAO	6753	160.00	1.32	21.1	-4.77	-3.65	1.41
ZIMPOL	<7207	<220.00	1.32	<29.0	<-4.63	<-3.50	<2.03

* uncertain values for this epoch.

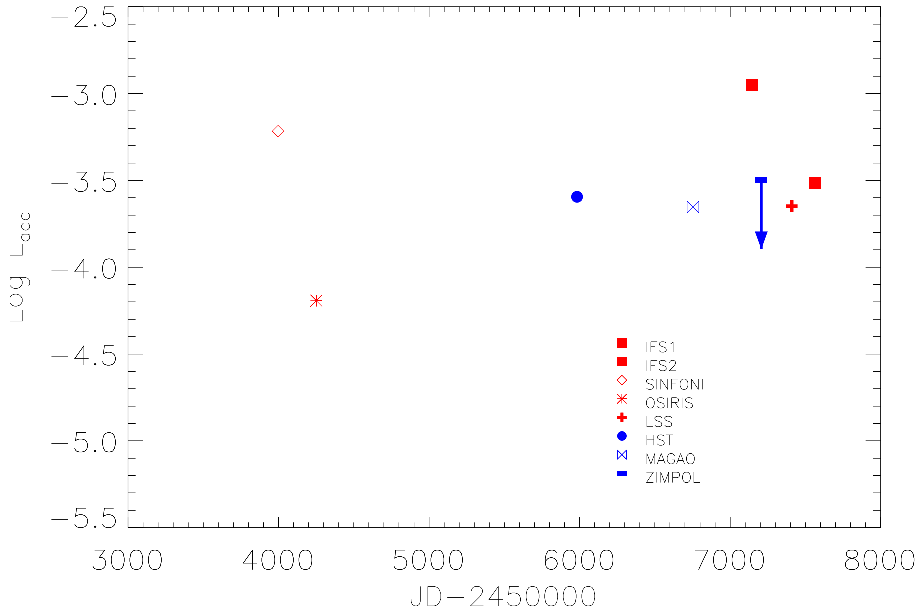

Figure 4.9: Accretion rate estimation for GQ Lup b

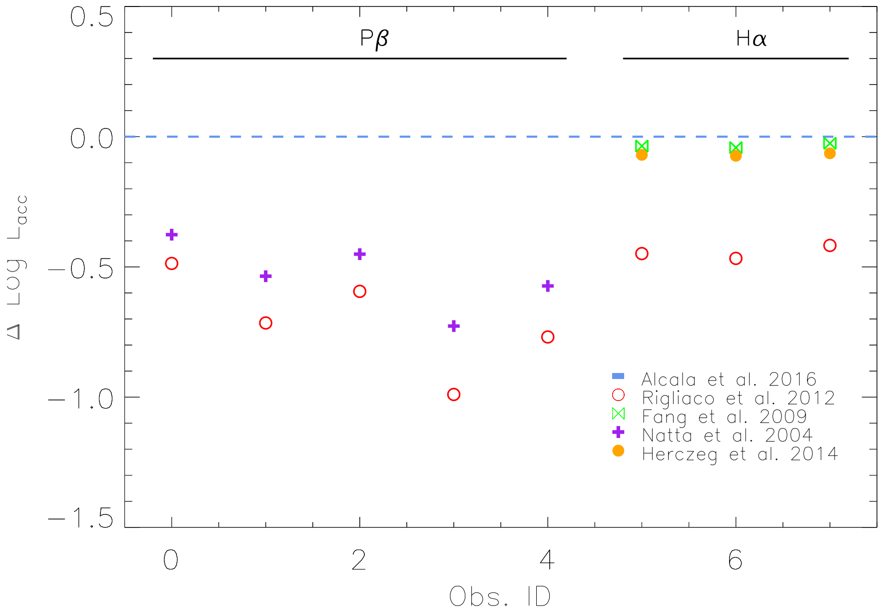

Figure 4.10: Accretion rate estimation for GQ Lup b obtained with different relations. Valuer are rescaled to the result with Alcalá et al. (2017) law.

accretion rates estimated from EWs of H lines have large uncertainties. In fact, the accretion luminosity can vary up to an order of magnitude if I applied a different $L_{line} - L_{acc}$ relation. To show this, I used relations from Rigliaco et al. (2012); Fang et al. (2009); Natta et al. (2004); Herczeg & Hillenbrand (2014) for H_α and Pa_β lines, when applicable, and I obtained that Alcalá et al. (2017) shows the highest accretion rate, as shown in Fig. 4.10. This is in particular true for the case of $L_{P\beta}$, if using the relation found by Natta et al. (2004), that are based on a sample of 19 brown dwarfs (instead of those by Alcalá et al. (2017)). On the other hand, the difference between different relations is negligible for H_α-based relations. The last column of Table 4.8 gives the mass accretion rate $\dot{M}$ on GQ Lup b, inferred from the accretion luminosities L_{acc} using the formula by Gullbring et al. (1998):

$$\dot{M} \approx \frac{1.25 R_* L_{acc}}{G M_*}. \tag{4.4}$$

Typical values for L_{acc} are of the order of a few $10^{-9} M_\odot/yr$, that is a few of $10^{-6} M_J/yr$. Given that the mass of GQ Lup b is estimated to be in the range $10 - 36 M_J$ (MacGregor et al. 2017) and its age is $2 \pm 1 Myr$ (MacGregor et al. 2017),these accretion rates agree well with expectations for a late accretion phase. On the other hand, the accreting material should come from the disk region. On this aspect, I notice that an optically thin disk as described in MacGregor et al. (2017), with a dust mass $< 0.04 M_\oplus$ and a gas to dust mass ration of 100, implies a disk life time of the order of $\sim 7 \cdot 10^4$ yr with the observed accretion rate. Given the stellar age, I expect, instead, the disk lifetime to be an order of magnitude longer. This suggests that the optically thin approximation underestimates the disk mass. The optically thick dust emission for the circumplanetary disk assumptions, give instead a disk radius upper limit, $R_{dust} < 1.1 AU$. Independently from the system geometry definitions, if the disk fills the 1/3 of the R_{Hill} as expected from hydrodinamical models (see e.g. Shabram & Boley 2013; Ayliffe & Bate 2009), the disk should extend more than this upper limit. This suggests that the disk may be truncated and more massive than in the optically thin case. Possible explanations of a such small disk radius (few tenths of the Hill radius) are the influence of the central star gravity (e.g. Ayliffe & Bate 2009; Martin & Lubow 2011) (Szulágyi et al. 2016), photoionization of the disk material due to the UV flux of the star and the presence of a satellite with a mass of the order of $1 M_{\oplus}$ able to clean out the outer orbits. In this last scenario, the signal on GQ Lup b radial velocities will be however too low to be detected with currently available instruments.

4.3.5 Best technique to detect accretion signatures with VLTs

GQLup b is not detected with ZIMPOL, that can reach a contrast of 7.1 mag in B_Ha filter. At the separation of GQ Lup B, our images are readout noise dominated, and the contrast limit is not enough to detect (even at 2σ level) the brown dwarf, if we assume that its luminosity did not change between HST and our ZIMPOL observations. Of course, these ones give indication of a strong variability and more systematic follow up observations are needed to confirm the variability of this source and/or to disentangle it from the uncertainty given by the inhomogeneous observations we collected. However, as described in Sec. A, ZIMPOL was designed to perform high quality polarimetry and imaging mode is an additional opportunity offered. Among the three SPHERE observing mode used, LSS seems to be the most sensitive, while the ZIMPOL H_{α} observations required better performances[3].
Moreover, an additional advantage of LSS observations is that this do not have a strong constrain on the meridian passage of the target during the observations, which is instead a strong constraint for the IFS-ADI observations. However, speckle subtraction is needed also for this observing mode in order to reach contrast of the order of 10^{-5} 10^{-6} at $0.5 - 0.6''$. Moreover, LSS allow to resolve a few molecular bands (FeH, VO, H_2O) that can be used for the spectral characterization of substellar objects and also atomic lines, such as Na and K, from which we could derive the gravity of the body. This gravity estimation lead to an age-estimation. The advantage of the use of IRDIFS images, instead, is that we do not need to know the object position *a priori*, even if this is not the case of our target, and could allow the detection of additional companion candidates or the study of the morphology of the circumstellar disk, if any. SINFONI spectra, instead, have higher spectral resolution (2000-4000 between 1.1μm and 2.5μm), and could reach a spatial resolution of $0.025''$with a $0.8''$x $0.8''$FoV, but it hasn't the coronagraphic units and therefore, depending on the Strehl ratios, GQ Lup B spectrum can be contaminated from the GQ Lup A halo. A further issue is that the star is also emitting in $Pa_{\beta}$and therefore the derived accretion ust be corrected for this. Further observations are already planned both with IRDIS LSS (in GTO) and SINFONI (099.C-0760).
In the coming years, two new instruments will be available at LBT: SHARK-NIR and SHARK-VIS. This two imagers could provide simultaneous imaging from the Y to the visible. In particular, SHARK VIS is designed to optimize narrow band imaging, and will provide higher quality results. These instruments will have the capability to reach the contrasts needed for GQ Lup b in both channels, but its observations will not be of high quality due to GQ Lup b declination. However these instruments have to be taken into account for the observation

---

[3] See Appendix A for more details.

of other accreting objects.

Chapter 5

Self luminous planets in mature systems

In the previous Chapters I studied systems with (claimed) planets or brown dwarfs that are still embedded (Chapter 3) or in a late accretion phase (Chapter 4). However, most of the objects observed in the SHINE survey are young stars that have already dispersed the protoplanetary disk gas and for which there are no previous claims of companions. These systems are still young enough for the planets to emit due their own thermal emission in the near-IR wavelengths. In these objects, the molecular absorption bands represent a unique opportunity to characterize physical properties of planets (e.g. temperature), exploiting the detection by differential imaging. At low temperatures (T types), the spectra are nearly invariant with temperature, and are dominated by the strong methane bands. The warmest planets ($T_{\mathrm{eff}} > 900$ K) should show very strong features also in the visible (such as alkali lines). In the range 1.0 to 1.7 μm, the strongest spectral bands are those of CH_4, NH_3 and H_2O.

These stars are observed with IRDIS and IFS simultaneously in the IRDIFS standard mode, looking for previously unseen companions. IFS and IRDIS H2H3 filters were, indeed, designed to allow a first characterization of the objects with only one epoch exploiting SDI (see Sec. 1.2.3): a (H2-H3) color lower then -0.5 can be considered as a good indication that the object presents CH_4 absorption and can be considered as good planetary-mass candidate and therefore distinguish T dwarfs from background objects, but it cannot disentangle L dwarfs from background objects. On the other hand, IFS spectra can be compared to template ones and given the J-H2 color it is possible to discriminate L dwarfs from background contaminants, as shown in Fig. 5.1. However, these two diagnostics cannot be considered conclusive (see e.g. Nielsen et al. (2017)) so that a second epoch of follow-up observation is needed to confirm physical association by measures of the common proper motion. This can be retrieved from archival data or new SPHERE observations are needed. This is performed using the same instrument and within the same project as the first epoch observations, but in several cases available datasets taken with other instruments (such as NACO, NICI, NICMOS, NIRC2 ...) or with SPHERE for other projects) can be exploited reducing the need for second-epoch observing time. When additional observations are performed with different set-up, the magnitudes in different bands (e.g. K band and L band) can be used for additional diagnostic to the candidate characteristics.

Detection of unbound candidates is frequent, since the highest contrast in SPHERE is reached

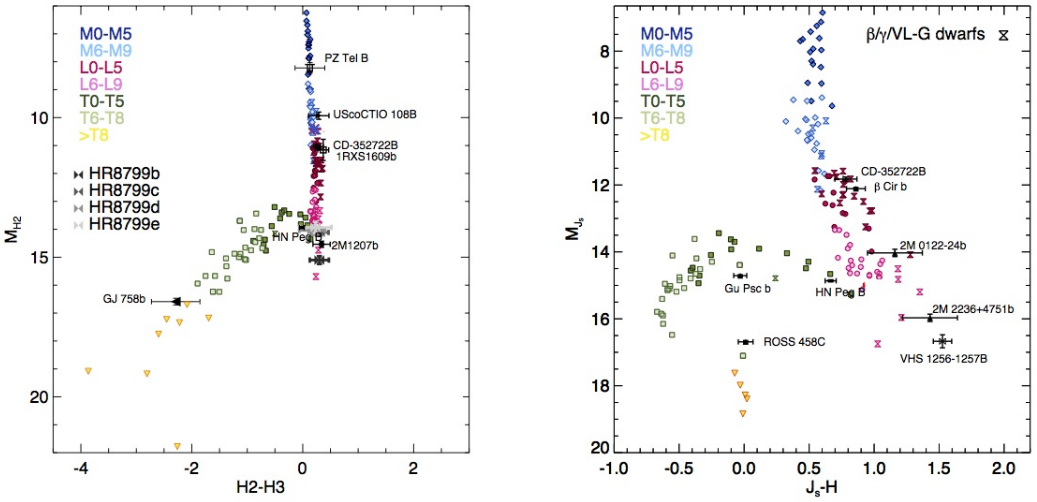

Figure 5.1: Color magnitude diagrams for different class of objects from M0 to T spectral types. In H2-H3 color, planets differs from the L and M sequence that lies vertically at H2-H3 ∼ 0, like the reddening vector, while in J-H the sequence is more spread ad allows a better characterization of objects at the L/T boundary. From Bonavita et al. submit., Mesa et al. in prep.

at typical separations larger than 50-100 AU from the star and several SPHERE targets are observed at low galactic latitude where field contamination is large.

In this Chapter I'll show a few examples of objects in which at least one candidate companion was identified. In the case of HIP 80591, the proper motion analysis allows me to recognize that the two objects in the field are background stars, while HIP 65426 revealed the first SPHERE planet. On this last target, I was involved especially in the early phase of the study: comparing the first two observations taken close in time in 2016, I found out three good indications that one of the CC visible in the IRDIS FoV, the closest to the star, was bound to the star. This first analysis allowed to push up the priority of the target among the SHINE survey, and follow-up observations confirmed the first findings. In the dedicated section I'll describe in detailed my contribution together with the spectroscopic and physical properties analysis presented in Chauvin et al. (2017).

5.1 HIP 80591

HIP 80591 (HD 148055) is an A5V star located in the Lower Centaurux Crux Association, at 140.8 ± 8.0 pc from the Sun (Gaia Collaboration et al. 2016). This star belongs to the SHINE statistical sample. The star has a mass of $1.6 \pm 0.1 M_{\odot}$ and its age is 16 ± 4Myr (Tetzlaff et al. 2011), with a temperature of ~ 8200 K (Wright et al. 2003).

Table 5.1: Overview of observational data sets of HIP 80591. Date, Instrument, filters, total exposure time and the average DIMM seeing on source are reported.

Date	Mode	Filter	DIT [s] × NDIT	t_{tot} [min]	Seeing [″]
2016 Mar 28	IRDIS	*DB_H23*	64 × 64	54.55	1.45
2016 Mar 28	IFS	*YJ*	64 × 64	54.55	1.45

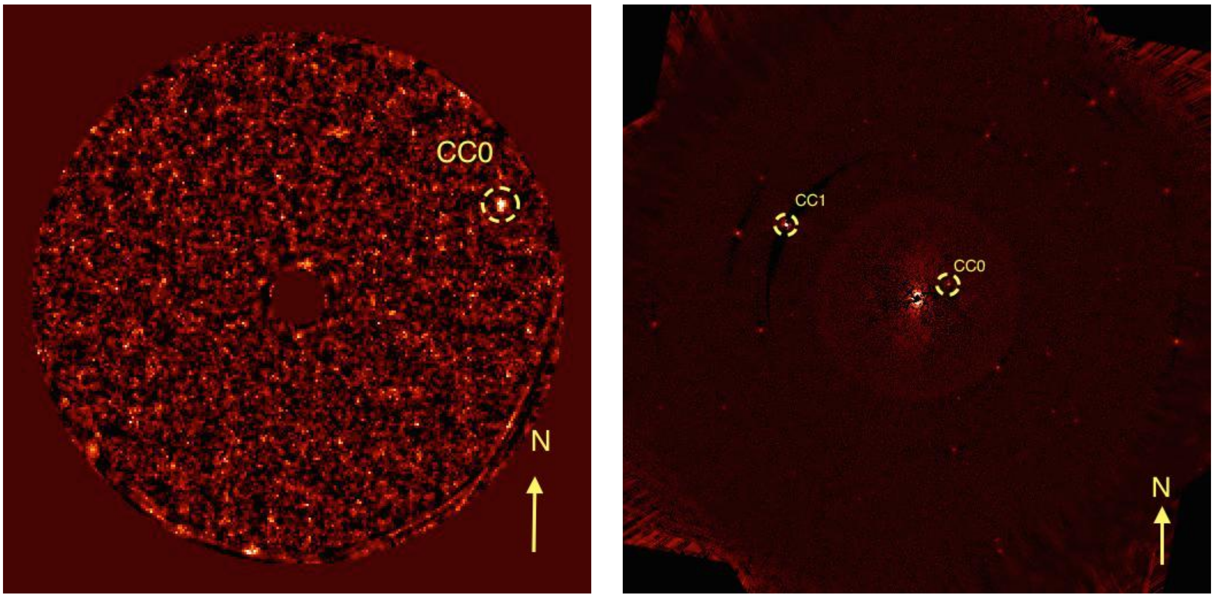

Figure 5.2: IFS 50 PC modes image (left) and IRDIS TLOCI image (rigth). Two relevant candidate companions are indicated.

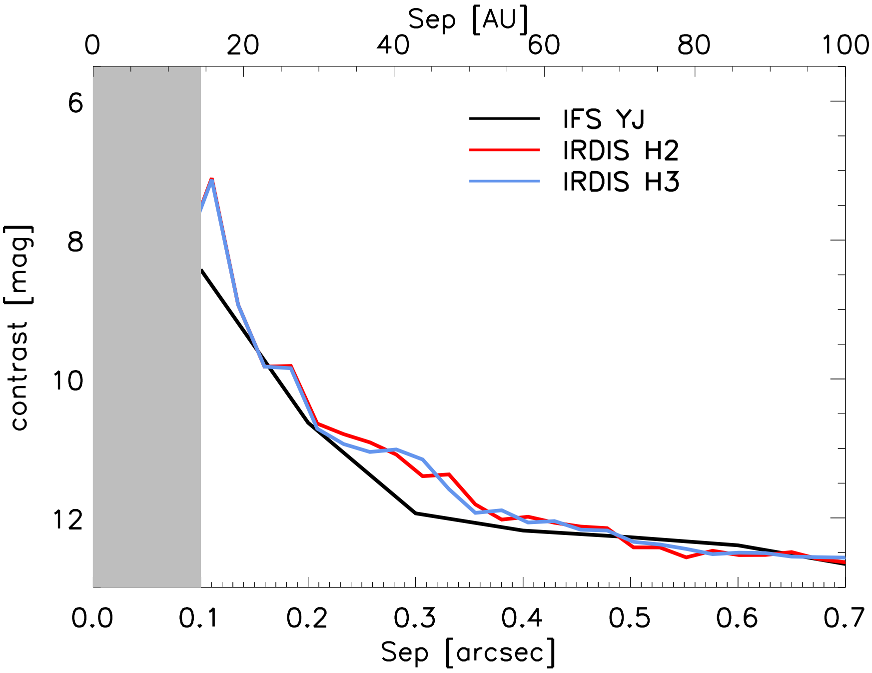

Figure 5.3: IFS YJ and IRDIS H2H3 contrast curves for HIP 80591.

5.1.1 Near-IR observations

SPHERE observed this star in the night of March, 28th 2016 as part of the GTO in the SHINE standard mode, IRDIFS. The exposure time was 3072 s, allowing a rotation of the FoV of 54.55°. Sky conditions were fair, with an average DIMM seeing on source of 1.45″(see Table 5.1). The images were first processed using SPHERE DRH pipeline (Pavlov et al. 2008) hosted at SPHERE DC in Grenoble. I then applied high contrast imaging tools on the reduced data using both the SpeCal software and the internal OAPD IFS pipeline, as described in Sec. 3.2. In Fig. 5.2 I show the results obtained by applying the PCA analysis on the IFS in the J band, using 50 principal components modes, and IRDIS H band using TLOCI. IFS data shows the presence of one candidate companion (CC0), while about 37 candidate companions are visible in the IRDIS FoV. Two candidates were ranked as promising for being bound on the basis of their photometric properties while the other ones are most likely background objects. I'll focused on these two candidates in this section.

Moreover, for HIP 80591 I obtained the 5σ limiting contrast curves shown in Fig.5.3:

5.1.2 Candidate companions characterization

As mentioned above, a candidate companion (CC0) was identified around the star HIP 80591 at a separation of $\sim$ 732 mas. It is visible in both IFS YJ and IRDIS H2H3 datasets.

Photometry of this object is obtained taking into account the interstellar reddening in the direction of HIP 80591 that is likely not negligible. As upper limits, I may use the values from the interstellar reddening maps used in extragalactic astronomy, based on the distribution of dust in the Milky Way as derived from far infrared maps[1], that gives Av

---

[1] I used data from the following URL: `http://irsa.ipac.caltech.edu/applications/DUST/`

Table 5.2: Photometry of CC0 around HIP80591: contrast limit at 0.5″, apparent magnitude and absolute magnitude of the CC0 in the IFS and IRDIS bands are reported.

	Y	J	H2	H3
Contrast	12.60	12.02	11.14	11.11
App.magnitude	20.61	19.95	18.99	18.95
Abs.magnitude	14.86	14.21	13.25	13.21

Table 5.3: Astrometric data of CC0 in the IFS images of HIP 80591.

Date	ΔRA [mas]	$\Delta\delta$ [mas]	Sep [mas]	PA [°]
4/5/15	-681.5	277	735.67	292.12
3/28/16	-663.2	309.8	731.97	295.04

= 3.71 mag (Schlafly & Finkbeiner 2011) and Av = 4.32 mag (Schlegel et al. 1998), from which I obtained E(J-H)< 0.48 mag. Using the reddening law by Cardelli et al. (1989), the photometry of this object is then given in Table 5.2 assuming that the object was bound, and combining IFS and IRDIS data I obtained J-H=1.63 and H2-H3=0.04. These values suggest a very red companion, compatible with a very cool L6-L9 object. In this case, the informations retrieved by the spectra are not enough to rule out that this object could be of planetary mass.

Given the quite large apparent separation of CC0 from the star, the real physical separation should exceed 100 AU from the star. The orbital period should then be larger then several hundreds years; we then expect that the orbital motion cannot be larger that about 10 mas over a year. Hence, we expect that if CC0 is indeed gravitationally bound to the star, the relative proper motion should be very small. On the other hand, if CC0 is a background object much further than the star, the relative proper motion should be similar to the reflex motion of this star, that is about 30 mas/yr. The relative proper motion give then a stringent test on the link between the star and the cc0, if we observe in two epochs that differ by at least one year. For this reason I used images of the same target coming from the SPHERE program 095.C-0389(A) (P.I. Daniel Apai) taken on April 5th, 2015. The two epochs available for HIP 80591 are separated by slighty more than one year. This is enough for the test being applicable. The astrometric data are described in Table 5.3, I was able to perform the proper motion test based only on the two IFS images. Assuming a proper motion of -13.09 ± 0.05 mas/year in RA and -28.91 ± 0.04 mas/year in δ (Gaia Collaboration et al. 2016), the result is shown in Fig. 5.5, where the green square represents the position of April 2015, the orange square is the position at the SPHERE GTO observation epoch and the black square is the position that the companion should have if it is a background object with negligible proper motion. Given that the position of the black and the orange squares are almost coincident, I can conclude that the detected candidate companion is very likely a background object.

Table 5.4: Astrometric data of CC1 in the IRDIS images.

Date	ΔRA [mas]	$\Delta\delta$ [mas]	Separation [mas]	PA [°]
5 Apr 2015	2782.8	1566.96	3193.61	60.6
28 Mar 2016	2794.8	1567.60	3204.42	60.7

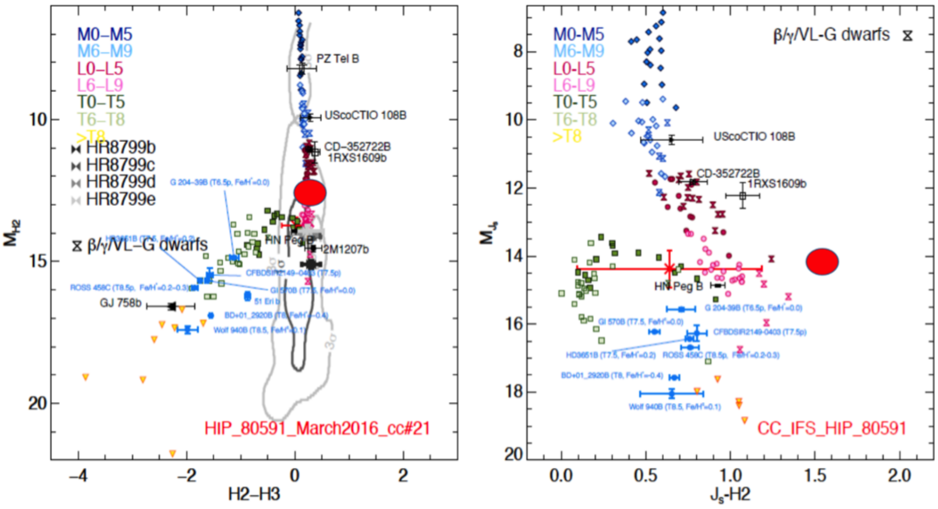

Figure 5.4: Color magnitude diagrams for CC0 (red dot) around HIP 80591, compared to that of the field brown dwarfs.

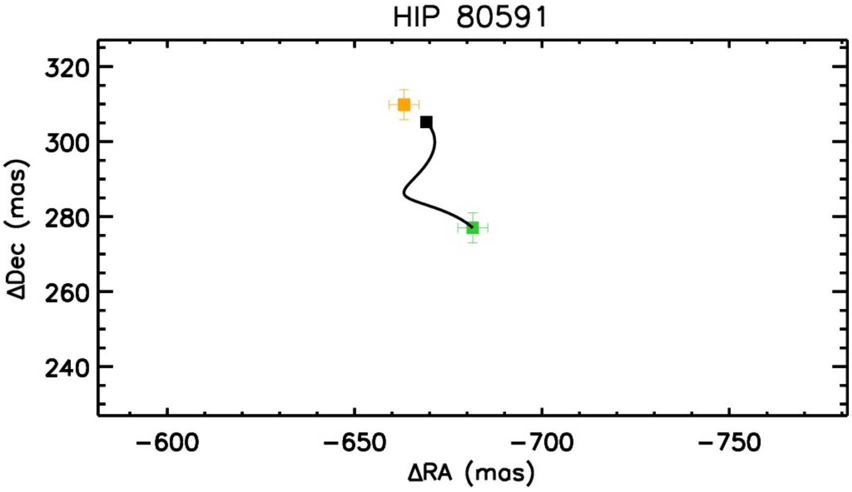

Figure 5.5: Proper motion diagram for the HIP 80591 candidate companion based on two IFS observations. The black square is the expected position at the epoch of the 2016 observation. If the object were a very far background star. The black line is the combination of parallactic and proper motion between the two observations. All the coordinates are centred on the star.

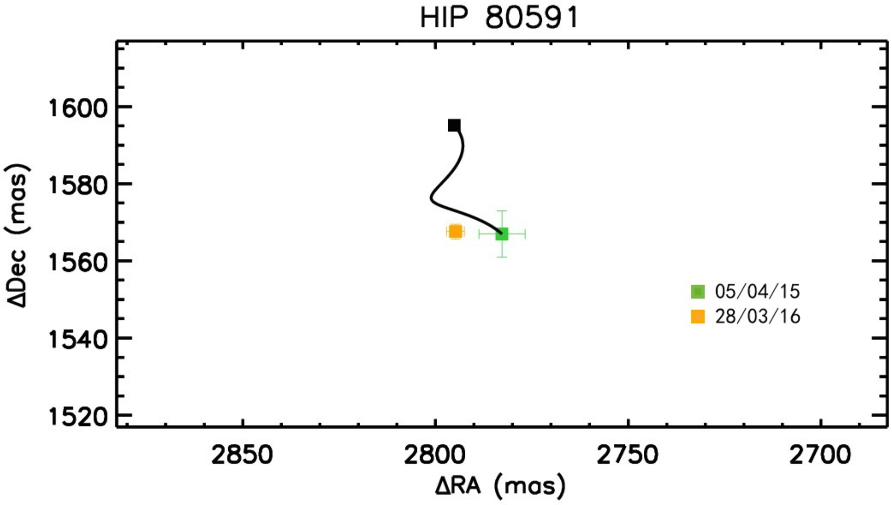

Figure 5.6: Proper motion diagram for the HIP 80591 CC1 based on two IRDIS observations.

Table 5.5: Astrometric data of CC1 as obtained from HST calibrated images.

Date	ΔRA [mas]	$\Delta\delta$ [mas]	Separation [mas]	PA [°]
07 Sep 2003	2595	1240	2876	64.5

Beside the candidate in the IFS field of view, 37 additional candidates were identified in the IRDIS field of view. One of these candidates (CC1 in Fig. 5.2), the brightest one, was flagged as promising by WP3 ranking criteria while the other ones have low probability to be bound objects. The ranking tools, in the case of only IRDIS data are available, is based on the derived (H2-H3) color and the first estimation of the absolute magnitude. CC1 shows (H2-H3)=0.06 and an absolute magnitude, if located at 140 pc from the Sun, of $M_{H2}=10.86$. Therefore, I focused my attention on this candidate, that lies at separation of $\sim 3.2''$ from HIP 80591. This object was visible during the April 2015 observation of Apai, as well. The astrometric values obtained for this object are listed in Table 5.4.

From these values I obtained the proper motion diagram in Fig. 5.6, where the green square is the companion position at the May 2015 observation while the orange square is the companion position at the Mar 2016 observation. This result seems to be compatible with a bound object.

However, I found in the archives an HST observation of this target acquired on Sep 07th 2003 (PEP 9834, P.I. Debes J. H.), taken with NICMOS NIC2 in three different Near-IR filters: F100W, F160W and F205W covering the spectral range between 0.8 and 2.4 μm. The candidate companion was fairly visible on these data (see Fig. 5.7) and it was then possible to obtain an estimate of astrometric values, exploiting HST calibrated data, that are listed in Table 5.5. I used these data to obtain a proper motion diagram with a much larger temporal coverage than possible using only SPHERE data; this diagram is shown in Figure 5.8. Colors are the same as in Fig. 5.6, where I added the blue square to represent the HST data. In this case the results indicate that the candidate is actually a background object.

There is therefore an inconsistency (that remains to be investigated) between the results

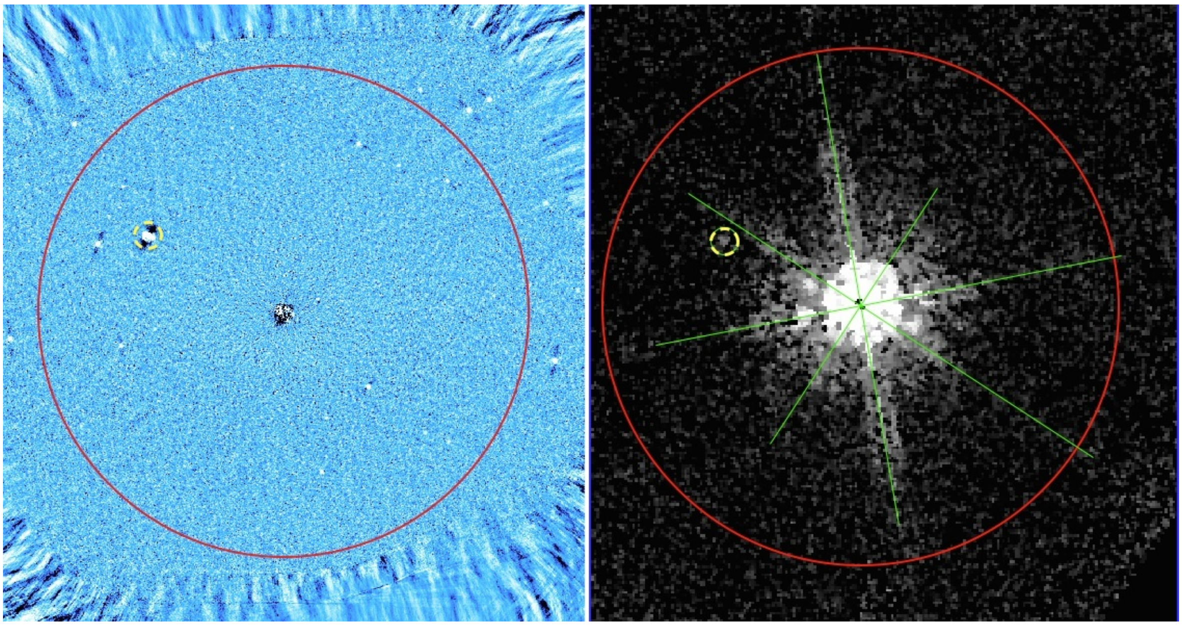

Figure 5.7: Comparison between IRDIS (left) and HST (right) observations. Green lines indicate the direction of HST spiders, whereas CC1 is circled in yellow.

from SPHERE data and the results including HST data. The most likely explanation is linked to the speckle issues of the astrometric calibration of SHINE datasets (Maire et al. 2016b). Effects such as field distortion, image timing and True North are self-consistently take into account in the reduction performed at SPHERE DC but they are not for independent reduction. Therefore, it is plausible that many/some reduction of the open time datasets suffer for systematics, which are more relevant at wide separation (and then not affecting our results for the close candidate CC0). For this reason, if true, this inconsistency could create some problem when evaluating the companionship of any candidate through the proper motion test. Some possible explanations could be found in the lack of inclusion of all the corrections needed for the best IRDIS astrometric calibration of the Apai data. For this reason I think it could be useful to treat the open time images with the SPHERE Data Center software, in order to have two homogeneous reductions and indeed this activity is currently in progress. Based on these results I recommended that the star was not re-observed during following GTO observing runs.

5.1.3 Conclusion

Two close companions candidates with interesting photometric properties were found close to HIP 80591, an A type star of the Sco-Cen association. One of them is within the IFS FoV. Few such candidates were found in the SHINE survey. Unluckily, both these candidates turned out to be background stars by analysis of their proper motion. This is an example of the procedures needed to verify that candidates found in the SHINE survey are indeed close companions bound to their star or rather background stars.

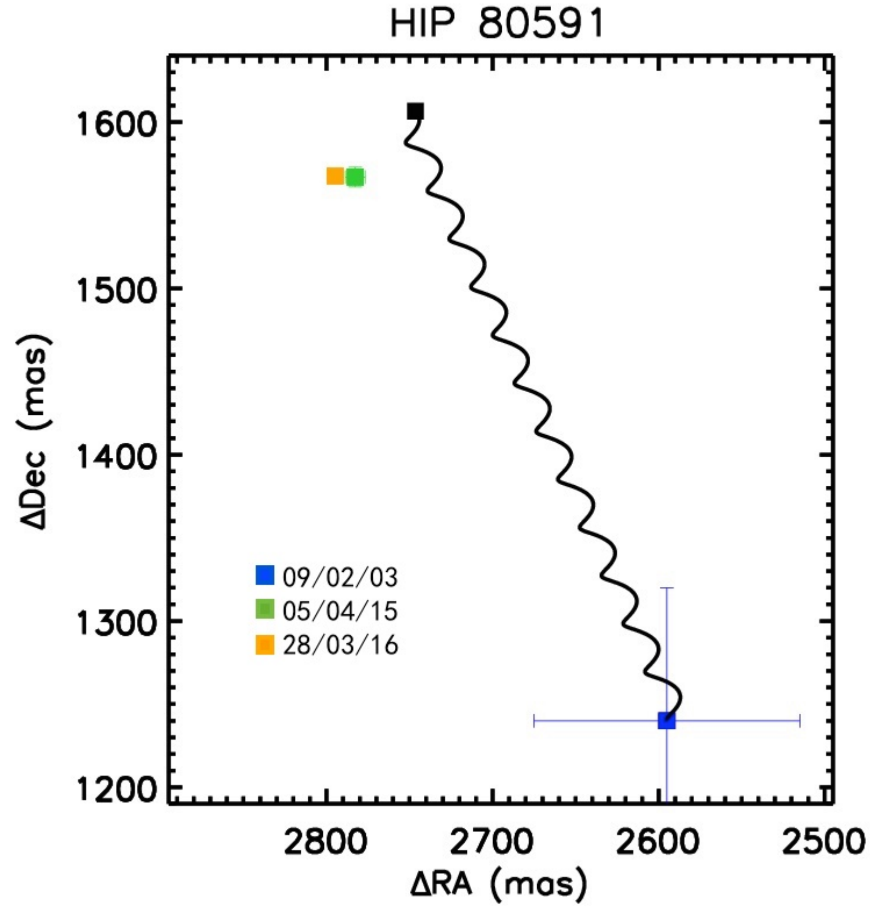

Figure 5.8: Proper motion diagram for the HIP 80591 CC1 based on two IRDIS observations and HST one (blue). Symbols and colors are the same as in Fig. 5.6.

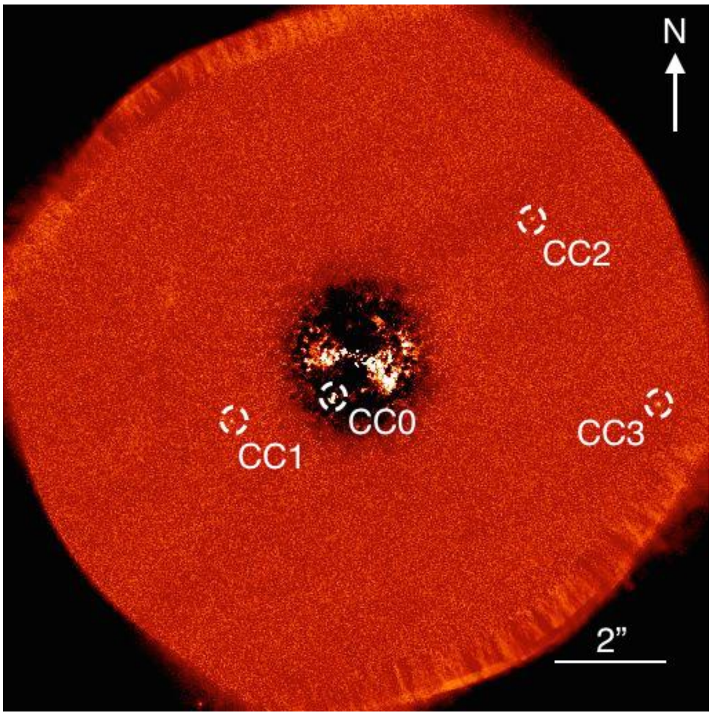

Figure 5.9: IRDIS field of view of HIP 65426. The candidates companions are also highlighted.

5.2 HIP 65426[2]

Like HIP 80591, HIP 65426 belongs to the Lower Centaurux Crux Association (Age 16 ± 4 Myr) and is part of the SHINE statistical sample. It is a A2-type star, with a mass of $M_{star} = 1.96 \pm 0.04$ (Chauvin et al. 2017), located at 111.4 ± 3.8 pc (Gaia Collaboration et al. 2016). Its proper motion is $\mu_\alpha = -33.923 \pm 0.030$, $\mu_\delta = -18.955 \pm 0.031$ (Gaia Collaboration et al. 2016).

5.2.1 Near-IR observations

HIP 65426 was observed on May 30th, 2016 under unstable conditions (strong wind) with SPHERE, and therefore the observations were then repeated on June 26th, 2016, in good conditions. The data were acquired in the standard SHINE mode, IRDIFS. The calibration observations for the star position behind the coronagraph and the PSF were taken at the beginning and the end of the sequence.

In the deep coronagraphic images, four faint candidates were detected in the close vicinity of HIP 65426 as shown in Fig. 5.9. The companion candidate located at about 830 mas and position angle of 150° (hereafter CC0) is also seen in the IFS FoV, at the rim of the images: it revealed promising photometric properties and had a peculiar position in the color-magnitude diagrams used to rank the SHINE candidates. So that, the source was then re-observed on February 7th, 2017 with the same IRDIFS mode to test that this close candidate is comoving with HIP 65426. On February 9th 2017, the IRDIFS-EXT mode was used to further constrain

---

[2] Section partially re-edited from Chauvin et al. (2017).

Table 5.6: Overview of observational datasets for HIP 65426. Date, instrumentation, filters, total exposure time and the average sky conditions (seeing and Strehl in the H band) are reported.

Date	Instr.	Filter	DIT^a (s)	N^a_{exp}	$\Delta\pi^a$ (°)	ω^a (")	Strehl^a
2016 May 30	IRDIFS	YJ + H2H3	64	60	34.2	0.62	0.60
2016 Jun 26	IRDIFS	YJ + H2H3	64	75	42.2	0.53	0.66
2017 Feb 02	IRDIFS	YJ + H2H3	64	80	44.2	0.38	0.84
2017 Feb 09	IRDIFS_EXT	YH + K1K2	64	80	49.1	0.45	0.76

Epoch	Sep [mas]	PA [°]	$\Delta\alpha$[mas]	$\Delta\delta$ [mas]
57539.0859669	829.6±2.0	150.45±0.15	409.1±3.0	-721.7±3.0
57566.0260975	828.4±2.0	150.33±0.25	410.1±2.0	-719.8±2.0

Table 5.7: Preliminary astrometry for CC0 close to HIP 65426 from IFS PCA images.

the planet physical and spectral properties. The details of the observing settings and sky conditions at all epochs are described in Table 5.6.

All IRDIS and IFS datasets were reduced at the SPHERE DC[3] using the SPHERE Data Reduction and Handling (DRH) automated pipeline (Pavlov et al. 2008). Basic corrections for bad pixels, dark current, flat field were applied. For IFS, the SPHERE-DC complemented the DRH pipeline with additional steps that improve the wavelength calibration and the cross-talk and bad pixel correction (Mesa et al. 2015). The products were then used as input of the SHINE Specal pipeline. For the February 7th 2017 and February 9th 2017 datasets, the waffle-spot registration was included in the observations, to apply a frame-to-frame recentering and reach an higher astrometric precision. The TLOCI (Marois et al. 2014) and PCA (Soummer et al. 2012; Amara & Quanz 2012) algorithms were specifically used on angular differential imaging data (i.e without applying any combined spectral differential processing) given the relatively good SNR ($10-30$ in the individual IFS channels, ≥ 50 with IRDIS) detection of CC0. Its position and spectra were extracted using injected fake planets and planetary signature templates to take into account any biases related to the data processing. Both algorithms gave consistent results. The resulting extracted TLOCI images from IFS and IRDIS for the February 7th, 2017 epoch are shown in Figure 5.10. A full analysis of all SPHERE data for HIP 65426 is published in Chauvin et al. (2017). In the following, I report also the preliminary analysis based only on the 2016 datasets that allowed to define it as a very promising candidate. I greatly contributed to this preliminary analysis.

5.2.2 Preliminary analysis of the candidate companions

While CC1 and CC2 were quickly recognized (already for the 2016 observations) to be background objects form the comparison of their positions in the IRDIS field of view, I focused on the CC0 that is visible, as a very bright object, at the rim of a few DITS of IFS. As shown in Fig. 5.11, the positions of the companion at the two 2016 epochs did not rule out that this

---

[3] http://sphere.osug.fr

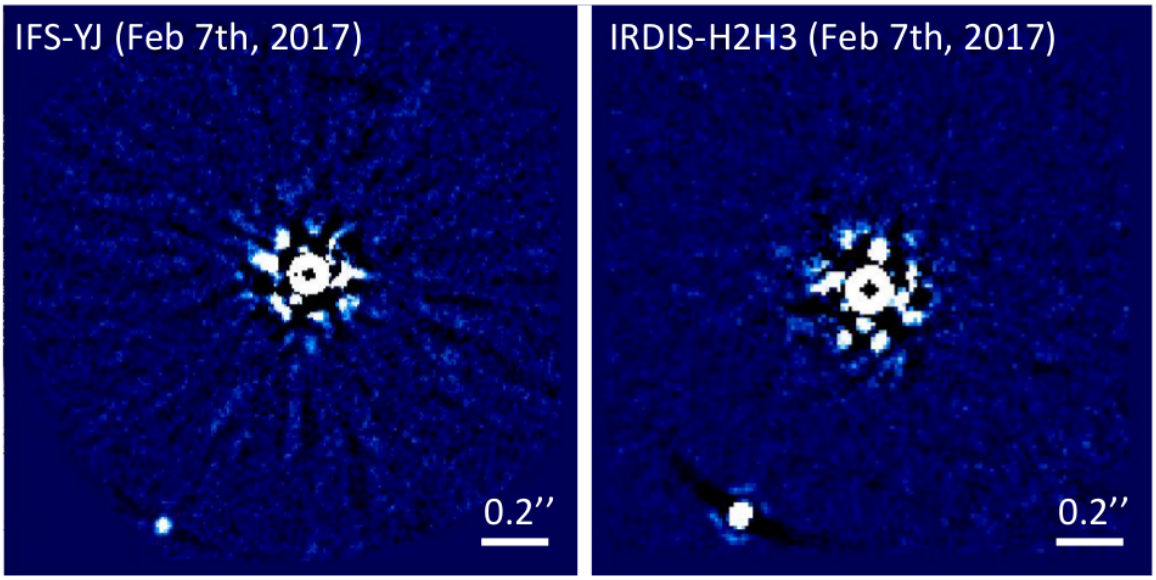

Figure 5.10: Left: IFS YJ-band TLOCI image of HIP 65426 A and b from February 7th 2017. The planet is well detected at a separation of 830 ± 3 mas and position angle of 150.0 ± 0.3° from HIP 65426. Right: IRDIS H2H3 combined TLOCI image of HIP 65426 A and CC0 for the same night. In both images, North is up and East is left. From Chauvin et al. (2017).

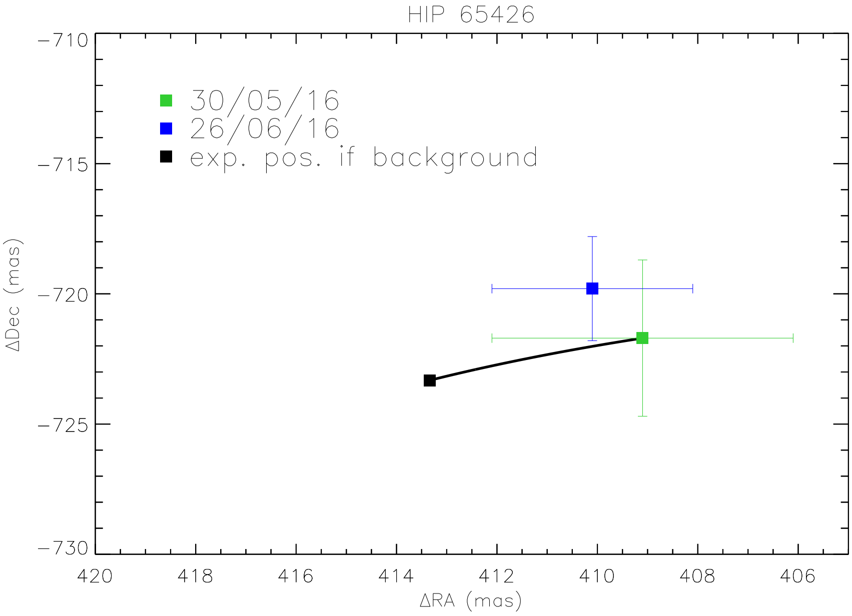

Figure 5.11: Motion of cc0 with respect to the star between the two observations (green and blue respectively). The black square shows where cc0 is expected to be if it moves like a background objects.

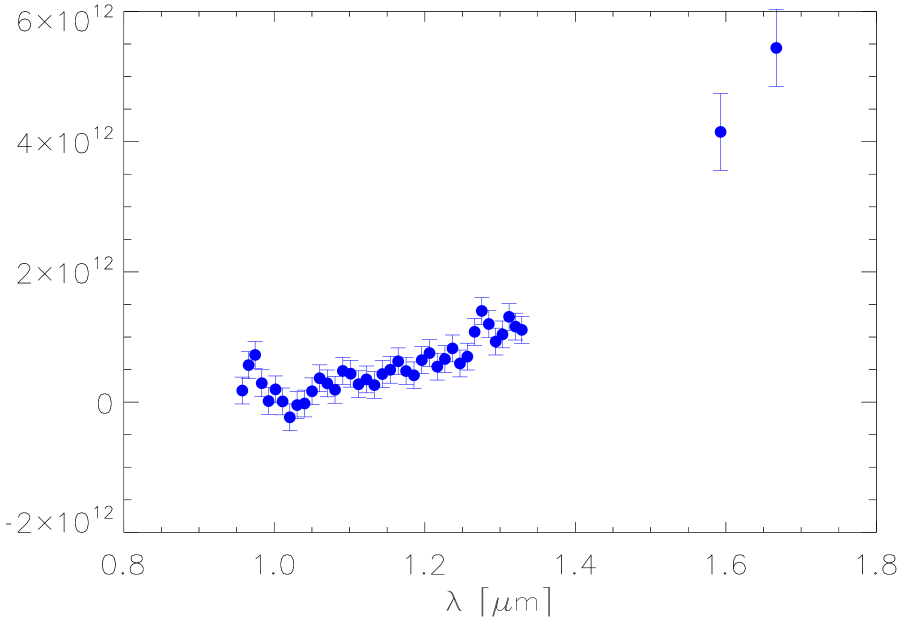

Figure 5.12: Preliminary spectra of CC0 close to HIP 65426 obtained from the June observation.

can be an object bound to its star: its motion with respect to the star is of 1.0 ± 3.0 mas in RA and 1.9 ± 3.0 in declination and is compatible with a negligible motion and about 1.5σ out with respect to the value expected for a field star (Table 5.7).

More interestingly, CC0 spectrum appears to be very red, as shown in Fig. 5.12, where also IRDIS H2 and H3 data were added. the red slope is the expected one for a L type object $(\mathrm{J}-\mathrm{H}>0.8)$, and is not compatible with a background stellar object unless it is significantly reddened. The interstellar reddening in the direction of HIP 65426 was checked through the NASA/IPAC Infrared Science Archive[4] and I found out that $\mathrm{A_V} = 0.7011$ mag according to Schlafly & Finkbeiner (2011) and $\mathrm{A_V} = 0.8152$ mag according to Schlegel et al. (1998) that imply $\mathrm{E(J-H)} < 0.09$ mag. This values refers to the total absorption within the Milky Way, then represent upper limits for any galactic background objects in the direction of the target. The derived photometry from this first reduction lead to J=14.19 and H=12.91, J-H2= 0.156 and H2-H3=0.32. Since E(J-H)=0.07, $(\mathrm{J}-\mathrm{H})_0 = 1.56$, this very red spectrum is only compatible with a very cool object; this makes very likely that the object is a real companion of HIP 65426.

I also explored the possibility to find contaminant objects in the IFS field of view around HIP 65426 exploiting the Field Contaminant Tools developed by G. Chauvin available for the SPHERE consortium. The result gives a probability of having at least one background contaminant of similar brightness or brigther at the same separation than CC0 and with proper motion less than $5\,\sigma$ deviant from the HIP 65426 proper motion. This probality is 0.53% given

---

[4] `http://irsa.ipac.caltech.edu/applications/DUST/`

UT Date	Filter	Separation [mas]	P.A. [°]
30/05/2016	H_2	830.4 ± 4.9	150.28 ± 0.22
26/06/2016	H_2	830.1 ± 3.2	150.14 ± 0.17
07/02/2017	H_2	827.6 ± 1.5	150.11 ± 0.15
09/02/2017	K_1	828.8 ± 1.5	150.05 ± 0.16
		Δ [mag]	M_{abs} [mag]
07/02/2017	J_{2MASS}	12.67 ± 0.40	14.26 ± 0.42
	J_{IFS}	12.18 ± 0.08	13.78 ± 0.11
07/02/2017	H_2	11.14 ± 0.05	12.76 ± 0.11
07/02/2017	H_3	10.78 ± 0.06	12.39 ± 0.12
09/02/2017	K_1	10.01 ± 0.31	11.55 ± 0.33
09/02/2017	K_2	9.69 ± 0.31	11.22 ± 0.33

Table 5.8: IRDIS relative astrometric measurements of HIP 65426 b to HIP 65426 and IRDIS and IFS relative photometric contrast and absolute magnitudes for HIP 65426 b. The composite J_{IFS}-band is estimated between 1.20 and 1.32 μm.

the galactitic coordinates of HIP 65426 and the predicted space and velocity distribution of field stars from the *Galaxia* galactic population model of Sharma et al. (2011).

While not conclusive, from the first two epochs images I obtained several hints that CC0 is a real companion of HIP65426:

- The probability to find a background object as bright and close as cc1 around HIP 65426 is 0.53% according to the contaminant estimation tool developed by WP3;
- Positions at different epochs are compatible with a negligible motion relative to the star and about 1.5-sigma out with respect to the value expected for a field star;
- The object is very red (J-H∼ 1.63) and unlikely to be reddened since ($E(J - H) < 0.10$ in the HIP 65426 direction.

This analysis allowed me to classify CC0 around HIP 65426 as a very promising planet candidate. Indeed, it was the highest rank among the candidates in the SHINE survey. Despite the strong evidence that we were facing a planetary companion, the SHINE team decided to wait for the astrometric confirmation of physical association. This was obtained on the first chance in the 2017 observing season. The confirmation of the physical association of the candidate also represented a relevant confirmation od the adopted criteria for candidate classification.

5.2.3 Final results on HIP 65426 b

Astrometry

To test the physical association of CC0, multi-epoch measurements showing a shared motion (if non-negligible) with the stellar host is a first robust diagnostic before resolving orbital motion. Therefore follow-up observations were executed in February 7th and 9th, 2017 and

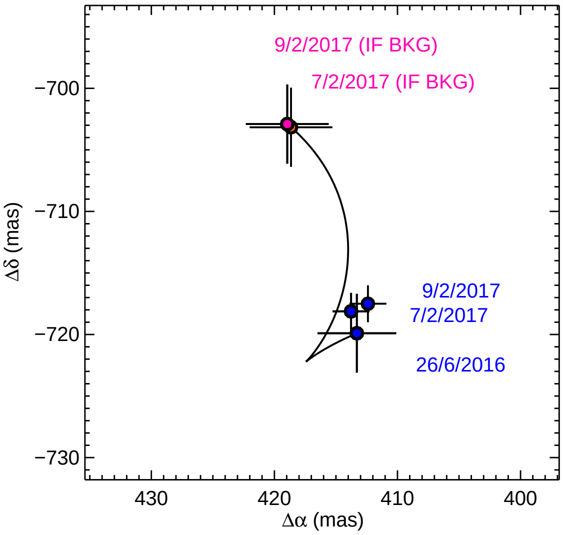

Figure 5.13: IRDIS multi-epoch measurements of the position of HIP 65426 b relative to HIP 65426 in blue from June 26th 2016 and February 7th 2017 in H2 and February 9th 2017 in K1. Predictions of the relative position of a stationary background contaminant for the same observing epochs are shown in *pink* and in *black* for the continuous evolutive predictions in time. From Chauvin et al. (2017).

a deeper analysis was carried out by a little group of people inside the SHINE team. We decide to not consider the first observation of May, 30th 2016 which was acquired under unstable conditions. The astrometric uncertainties are derived at each epoch by quadratically summing errors from the stellar position calibrated with the waffle-spots, the candidate extracted position with Specal and the uncertainties related to the initial pupil-offset rotation, the platescale and True North, the anamorphism and the IRDIS dithering. The astrometric results obtained with IRDIS are reported in Table 5.8 and in Figure 5.13. Consistent astrometric results were found with IFS. They both unambiguously confirm that CC0 is not a stationary background contaminant but is comoving with HIP 65426 and therefore likely a planet (hereafter HIP 65426 b). The new, more accurate, photometric results obtained with both IRDIS and IFS are given in Table 5.8 considering the SPHERE filter transmissions[5]: as shown in Fig. 5.14, this object lies within the L-type locuss, close to L/T transition.

Spectral typing analysis

The TLOCI extracted spectro-photometric measurements of HIP 65426 b between 0.95 to 2.26 μm (converted to physical fluxes using the VOSA[6] tool) are reported in Figure 5.15. We compared them to a large variety of reference low-resolution spectra of late-M and L dwarfs compiled from the literature (Burgasser 2014; Best et al. 2015; Mace et al. 2013; Allers & Liu 2013) as well as spectra of young imaged exoplanets and brown dwarfs close to the L/T transition (Patience et al. 2010; Zurlo et al. 2016; De Rosa et al. 2014; Artigau et al. 2015; Gauza et al. 2015). We considered the *G* goodness-of-fit indicator defined in

---

[5] https://www.eso.org/sci/facilities/paranal/instruments/sphere/inst/filters.html

[6] http://svo2.cab.inta-csic.es/theory/vosa/

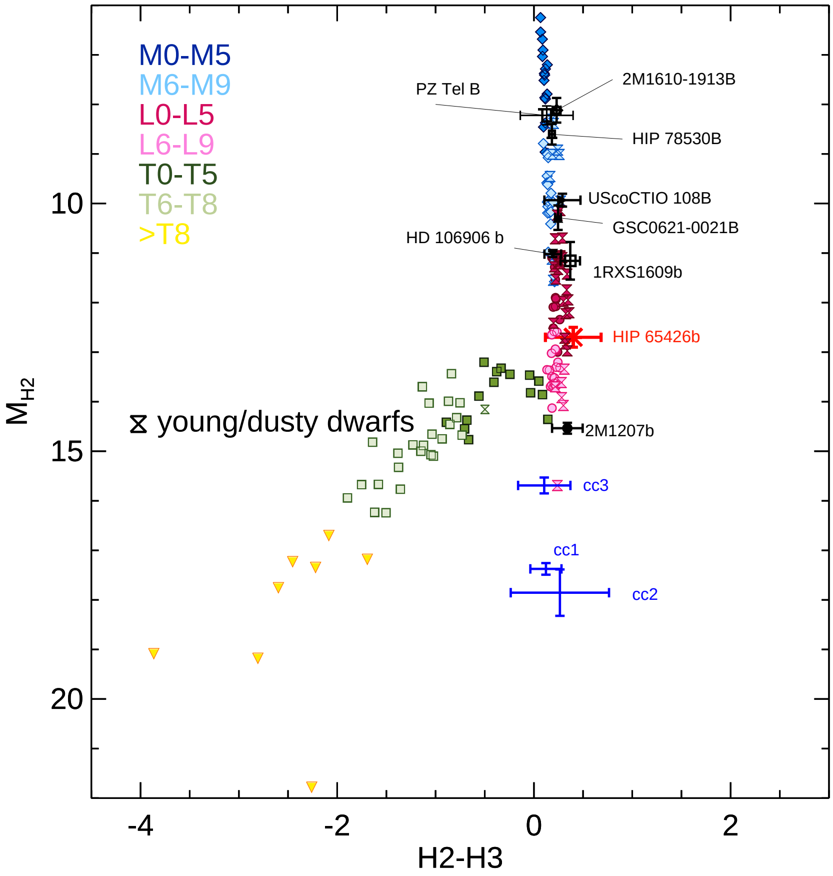

Figure 5.14: Color-magnitude diagram considering the SPHERE/IRDIS H_2 and H_3 photometry. HIP 65426 is indicated with error bars in *red* and the other companion candidates are shown in *blue*.

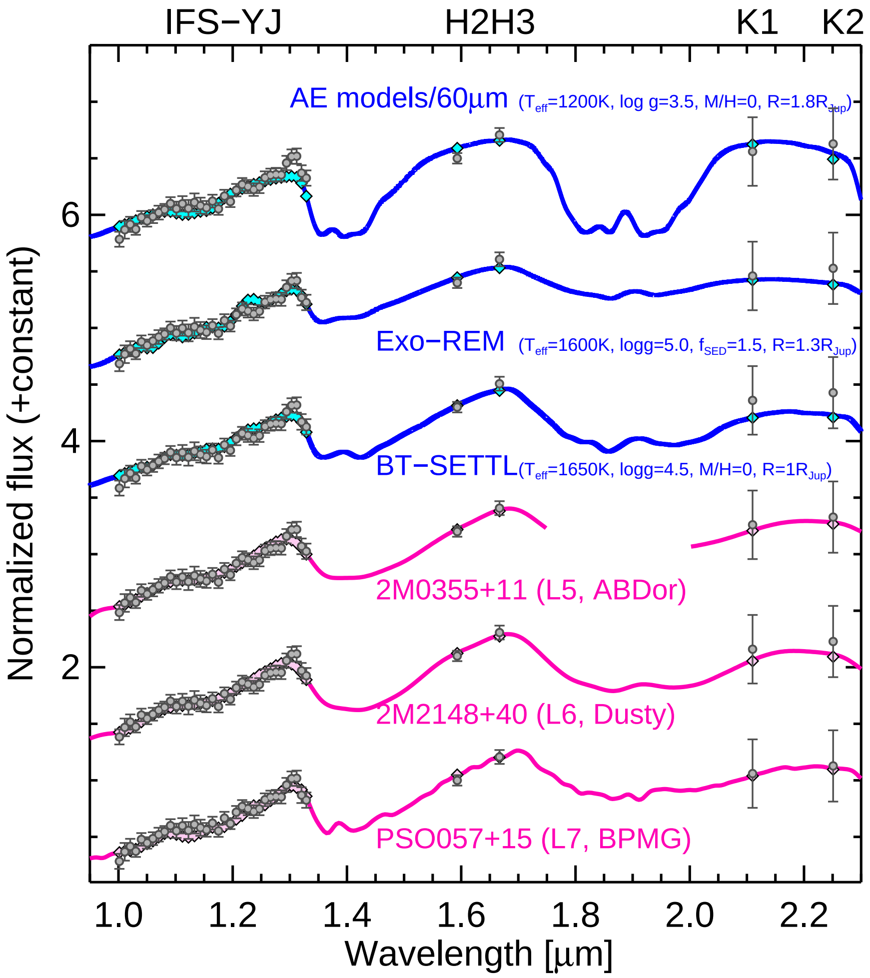

Figure 5.15: Near-infrared spectrum of HIP 65426 b extracted with TLOCI compared with (i) the best-fit empirical spectra in *pink*, and (ii) the best-fit model atmosphere from the Exo-REM, PHOENIX BT-Settl-2014 and thick AE cloud atmospheric models in *blue*. From Chauvin et al. (2017).

Cushing et al. (2008) which accounts for the filter and spectral channel widths to compare each of the template spectra to the spectrophotometric datapoints of HIP 65426 b. The best empirical fits are obtained for the young L5 and L7 dwarfs 2MASS J035523.37+113343.7 and PSO J057.2893+15.2433 recently identified as candidate members of the young, moving groups AB Doradus ($50 - 150$ Myr) and β Pictoris ($20 - 30$ Myr), respectively, (Faherty et al. 2013; Liu et al. 2013; Best et al. 2015) and the dusty L6 dwarf 2MASS J21481628+4003593 (Looper et al. 2008). Figure 5.15 shows how well they reproduce the near-infrared slope of the spectrum of HIP 65426 b between 0.95 to 2.26 μm as well as the water absorption at 1.33 μm. This comparison confirms a low surface-gravity atmosphere of spectral type L6 ± 1 for HIP 65426 b consistent with a young massive planet at the age of the LCC association.

Physical properties

Using a bolometric correction derived from the ones found by Filippazzo et al. (2015) for the dusty L5 to L7.5 dwarfs 2MASS J21481628+4003593, 2MASS J035523.37+113343.7, PSO J318.5338–22.8603, and WISEP J004701.06+680352.1, we derive a bolometric luminosity of -4.06 ± 0.10 dex for HIP 65426 b. Considering an age of 14 ± 4 Myr and a distance of 111.4 ± 3.8 pc, it converts into the following predicted masses, effective temperatures and radii by the Lyon's group hot-start models: $M = 7^{+2}_{-1}\,M_{\rm Jup}$, $T_{\rm eff} = 1500^{+100}_{-200}$ K and $R = 1.5 \pm 0.1\,R_{\rm Jup}$ for the COND03 models (Baraffe et al. 2003) and $M = 10 \pm 2\,M_{\rm Jup}$, $T_{\rm eff} = 1500^{+100}_{-200}$ K and $R = 1.5 \pm 0.1\,R_{\rm Jup}$ for the DUSTY models (Chabrier et al. 2000). Consistent results are found with the models of Mordasini (2013) for the hot-start solutions and higher masses for the warm-start solutions ($M = 12\,M_{\rm Jup}$, $T_{\rm eff} = 1260$ K and $R = 1.3\,R_{\rm Jup}$). To further explore the physical properties of HIP 65426 b, we compared our data to the synthetic grids of three atmospheric models previously used in the characterization of the planets around HR 8799 (Bonnefoy et al. 2016). They are the Exo-REM models (Baudino et al. 2015), the 2014 version of the PHOENIX BT-Settl atmospheric models described in Allard (2014) and Baraffe et al. (2015) and the thick AE cloud parametric models of Madhusudhan et al. (2011). The best fits for each grid are reported in Figure 5.15. The Exo-REM and PHOENIX BT-Settl models favor an effective temperature of $T_{\rm eff} = 1600^{+100}_{-200}$ K, slightly higher than the one derived by the semi-empirical scale of (Filippazzo et al. 2015) for young L6 ± 1 ($T_{\rm eff} = 1200 - 1400$ K), but consistent with the evolutionary model predictions. They however favor high surface gravity solutions of $log(g) = 4.0 - 5.0$ with smaller radii ($1.0 - 1.3\,R_{\rm Jup}$). On the contrary, the thick AE cloud parametric models that predict solutions with $T_{\rm eff} = 1200 \pm 100$ K and $log(g) = 3.5$ reproduce the spectral morphology but predict luminosities which are too low, thus leading to radii above the evolutionary model predictions ($\sim 1.8\,R_{\rm Jup}$).

The inferred chemical and physical properties of HIP 65426 b place this new planet in a very interesting sequence of young brown dwarfs and exoplanets discovered in the $5 - 20$ Myr-old Scorpius-Centaurus association (hereafter Sco-Cen). It is lighter and cooler than the late-M brown dwarf companions discovered by Aller et al. (2013); Hinkley et al. (2015) and the massive planetary mass companions GSC 06214-00210 b ($14 - 17\,M_{\rm Jup}$ at 320 au; M9 at 5 Myr; Lachapelle et al. 2015; Ireland et al. 2011), UScoCTIO 108 b ($6 - 16\ M_{\rm Jup}$ at 670 au; M9.5 at 5 Myr; Bonnefoy et al. 2014; Béjar et al. 2008), HD 106906 b (11 $M_{\rm Jup}$ at 650 au; L2.5 at 13 Myr; Bailey et al. 2014) and 1RXS J160929.1-210524 b ($7 - 12\ M_{\rm Jup}$ at 330 au; L2 – 4 at 5 Myr; Lachapelle et al. 2015; Manjavacas et al. 2014; Lafrenière et al. 2008). On the other hand, HIP 65426 b is probably more massive and hotter than the planet HD 95086 b ($4 - 5\ M_{\rm Jup}$ at 56 au, L8-type, 17 Myr; Rameau et al. 2013). This spectral and physical sequence is particularly interesting to study the main phase of transitions occurring in the atmosphere of brown dwarfs and exoplanets and influencing their spectra and luminosity, such as the formation of clouds and their properties as a function of particle size, composition, and location in the atmosphere or the role of non-equilibrium chemistry processes. Further characterization in the thermal-infrared domain with *JWST* or ground-based instrument like NaCo will allow us to explore in more detail the young planetary atmosphere of HIP 65426 b. Dedicated photometric variability monitoring would be also opportune as HIP 65426 b shares a similar spectral type and young age as the two highest-amplitude (7-10%) variable L-type dwarfs known (PSO J318.5-22, L7 member of β Pic, Biller et al. 2015; Liu et al. 2013) and WISE 0047, L6.5 member of AB Dor, Lew et al. 2016; Gizis et al. 2012) and as radial velocity measurements suggest that we may be observing the system close to edge-on.

5.3 Discussion

HIP 65426 b is today the first planet discovered with SPHERE. The planet is orbiting at a relatively large projected physical distance of about 92 au from the intermediate-mass primary HIP 65426. Contrary to most of the young, intermediate-mass stars hosting an imaged planet, no evidence of a debris disk, tracing the reprocessed dust of the primordial protoplanetary disk, has been found for HIP 65426. The analysis of the optical to mid-infrared photometry shows that, if the star is still hosting a debris disk, it would be located at distances larger than 100 au (i.e. farther out than the planet location) and with an upper limit to the dust mass of $3.2 \times 10^{-4}\, M_{\oplus}$. No signs of multiplicity have been observed so far for HIP 65426, which could have explained a rapid dispersal of the primordial protoplanetary disk, but this should still be investigated. Another intriguing aspect of the system is that HIP 65426 is an extremely fast-rotator as evidenced by our HARPS observations. No similar cases are known among the Sco-Cen and young, nearby intermediate-mass association members, neither among the intermediate-mass primaries hosting young imaged giant planets. Although fast stellar rotation is consistent with the picture of a rapid disk dispersal disabling disk-braking, planetary formation must have time to occur to explain the formation of HIP 65426 b. The planet location and the very low planet-to-star mass ratio ($q \sim 0.004$) would not favor a formation by core accretion unless HIP 65426 b formed significantly closer to the star followed by a planet-planet scattering event. An increases of angular momentum by engulfing the inner massive scatterer could explain the fast rotation of HIP 65426, but this remains to be tested by dedicated simulations. From our observations, we cannot exclude the presence of unseen inner massive planets in that system that could have scattered out HIP 65426 b. However, our current detection limits set relatively good constraints on their possible masses ($\leq 5\, M_{\rm Jup}$ beyond 20 au), as shown in Figure 5.16. As a consequence of a scattering event, the orbit of HIP 65426 b would be also rather eccentric which could be probed with further astrometric monitoring. If formed in-situ at its current location, formation by disk instability would be a better alternative, which would be consistent with the metallicity of the host star not enhanced with respect to the solar value. Finally, the formation of an extreme mass-ratio binary by gravo-turbulent fragmentation (Hennebelle & Chabrier 2011) cannot be totally excluded.

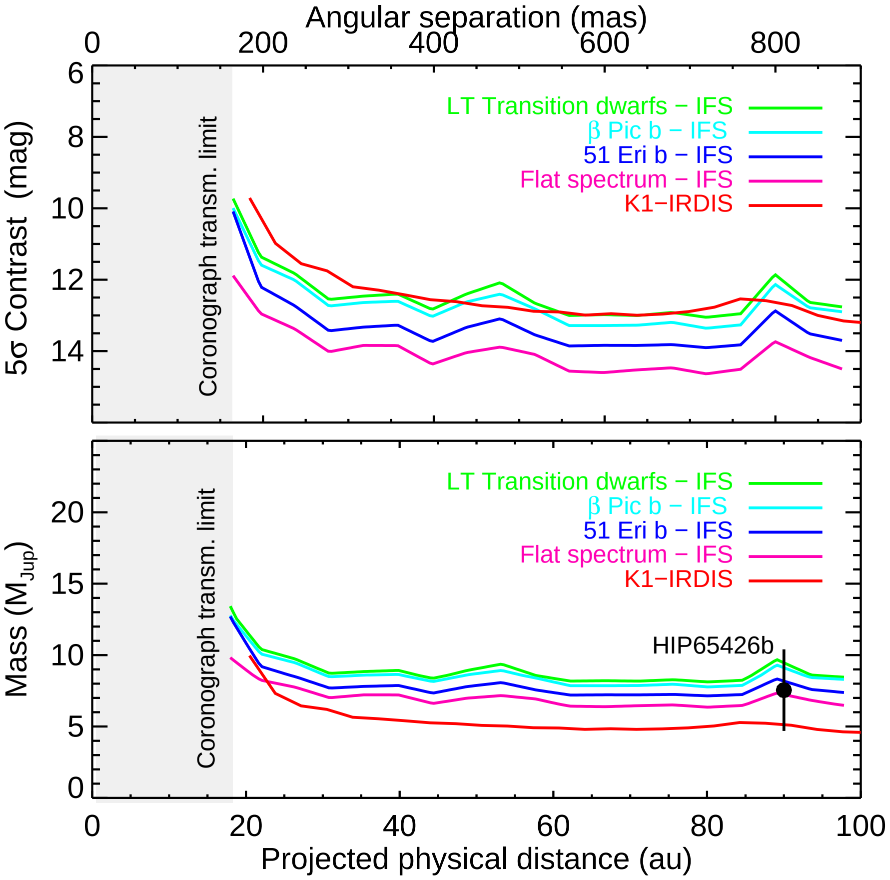

Figure 5.16: *Top*: SPHERE IFS and IRDIS 5σ detection limits for HIP 65426 as a function of the angular separation taken from February 7th and 9th, 2017. *Bottom*: SPHERE IFS and IRDIS 5σ detection limits converted in terms of masses using DUSTY model predictions as a function of the projected physical separation. For IFS, different spectral energy distributions were considered for the injected planets to explore the impact of the flux loss cancellation and different planet properties in the final detection limits. Contrast curves were cut at 0.15″ because of the low transmission of the coronagraph. The location and the predicted mass by the DUSTY models of HIP 65426 b are reported.

Chapter 6

H_α-activity and ages for stars in the SARG sample [1]

Studying the variation in the radial velocity (RV) induced by the chromospheric activity is important to distinguish it from the Keplerian motion of the star that may be caused by a planet (see e.g. Queloz et al. 2001; Desort et al. 2007; Dumusque et al. 2011; Robertson et al. 2014). On long timescales the active regions can modify measured RVs by introducing a signal related to the stellar activity cycle, while on short timescales the rotational period can become evident.

The most widely used activity indicators are based on the Ca II H&K lines (Isaacson & Fischer 2010; Lovis et al. 2011; Gomes da Silva et al. 2011), which have been shown to correlate with the radial velocity jitter. Other lines were investigated and it was found that the H_α line can be a good alternative (Robinson et al. 1990; Strassmeier et al. 1990; Santos et al. 2010; Gomes da Silva et al. 2011). However the correlation of H_α with Ca II H&K indices is high for the most active stars but decreases at a lower activity level, and sometimes becomes an anti-correlation (Gomes da Silva et al. 2011). Similar results were also found by Cincunegui et al. (2007), who added, using simultaneous observations of stars with spectral type later than F, that the correlation is lost when studying individual spectra of single stars and there is no dependence on activity. The correlation between the averaged fluxes for the Ca II and H_α lines can be clarified by considering the dependence of the two indexes on the stellar colour or the spectral type, while the absence of a general relation between the simultaneous Ca II and H_α index can be due to difference in the formation region of the two lines (Cincunegui et al. 2007; Gomes da Silva et al. 2014). Studying the solar spectrum as a prototype and extrapolating the results to other stars, Meunier & Delfosse (2009) discovered that plages and filaments in the chromosphere contribute differently to Ca II and H_α lines: while plages contribute to the emission of all these lines, the absorption due to filaments is remarkable only for H_α. Therefore the saturation of the plage filling factor seems to enhance the correlation between the two indexes in case of high stellar activity and low filament contribution. On the other hand, the anti-correlation between the emission in Ca II and H_α for low active stars seems to depend only on a strong filament contrast if the filaments are well correlated with plages (see also Gomes da Silva et al. 2014).

A search for planets around the components of wide binaries was performed using SARG (Spettrografo Alta Risoluzione Galileo) at the Telescopio Nazionale Galileo (TNG) in the

---

[1] Chapter re-edited from Sissa et al. (2016).

past years. Two planetary companions were detected around HD 132563B and HD 106515A (Desidera et al. 2011, 2012). Carolo et al. (2014) found strong variations in the RVs of HD 200466A that could not be explained by a stable planetary system, but which were well correlated to a H_α based activity indicator, showing that they are due to an ~1100-day activity cycle. Stimulated by this finding, we started a systematic analysis of H_α in the binaries of the SARG sample to identify activity-induced RV variations and distinguish them from planetary signatures. We report here on the main results of the activity study made within this survey. We also include the measurements for additional stars observed by our group for other programs carried out with SARG.

6.1 Observation and data reduction

SARG is the High Resolution Spectrograph at TNG, now decommissioned, which worked for about 12 years beginning in 2000 (Gratton et al. 2001). The SARG survey was the first planet research program entirely dedicated to binary systems and aimed to determine the frequency of giant planets up to a few AU separation from their star in nearly equal-mass visual binaries using high-precision radial velocities. The sample of the survey included 47 pairs of stars from the Hipparcos Multiple Star Catalog (Perryman et al. 1997), considering binaries in the magnitude range $7.0 < V < 10.0$, with magnitude differences between the components $\Delta V < 1.0$, projected separations larger than 2” (to avoid strong contamination of the spectra), parallaxes larger than 10 mas, and errors smaller than 5 mas, with $B - V > 0.45$ mag and spectral types later than F7. For more details on the sample see Desidera et al. (2007). The stars are typically at distance < 50 pc from the Sun.

Between September 2000 and April 2012 we collected up to 81 spectra per star with a typical exposure time of 900 s for a total amount of more than 6000 science images.

In this work we also include six bright stars that were observed with SARG looking to search for hot-Neptunes orbiting planets (Gratton et al. 2009). For these stars the integration time was set at 600 s except for 61Cyg B and 40 Eri, for which it was shorter to avoid saturation of the images because of their higher luminosity. τ Cet, 51 Peg and ρ CrB were used as RVs reference stars during the survey, and their signal-to-noise ratio (S/N) is typically greater then 270. In addition, HD 166435 was observed as benchmark active star (Martínez Fiorenzano et al. 2005). We decided to include this star in our sample as well.

Our data set therefore consists made of two sub samples: the binary sample and the bright stars sample. The first is unbiased with respect to activity (except for HD 114723, which was excluded because of its high rotation), while the latter has a bias toward low-activity stars except for HD 166435. For all the observations we used the SARG Yellow Grism (spectral range 4600-7900 Å) and the 0.27 arcsec slit to obtain a resolution $R = 144000$ with a 2×1 pixel binning. The observed spectral range was covered by two chips. The blue chip included the spectral range used for the RV determination: the accuracy was given by a iodine cell superimposing a forest of absorption lines used as reference for the AUSTRAL code (Endl et al. 2000), as shown in Desidera et al. (2011). The red chip data are affected by fringing effects at wavelengths longer than ~ 7000 Å; these were not used in our analysis. The depth of the iodine lines decreases toward longer wavelengths, and the lines are negligible at the wavelength of H_α.

Data reduction was performed with standard IRAF[2] procedures.

6.2 Stellar parameters

Table 6.1: **Stellar Parameters:** for each star we indicate the apparent V magnitude, the B-V color index, the method used to calculate $\log R'_{HK}$ and its value, the projected velocity $v \sin i$ and temperature. $\log R'_{HK}$ values were derived from direct measurement (D) of other authors, from the X-ray luminosity (X), or can be only an upper limits (U), still from X-ray luminosity data.

Star	V	B-V	$\log R'_{HK}$	method	$v \sin i$ [km/s]	T_{eff} [K]
BD+18 2366A	9.370	0.83	-4.56	U	2.0	5308
BD+18 2366B	9.427	0.93	-4.57	U	2.4	5290
BD+22 2706A	9.594	0.62	-4.97	D	2.3	5943
BD+22 2706B	9.828	0.69	-4.51	U	2.3	5674
BD+23 1978A	9.395	0.83	-4.46	D	3.5	4886
BD+23 1978B	9.530	0.75	-4.44	U	3.2	4911
HD 105421A	7.827	0.51	-4.70	U	4.6	6324
HD 105421B	8.358	0.57	-4.65	U	0.9	6102
HD 106515A	7.960	0.79	-5.04	D	1.7	5314
HD 106515B	8.234	0.83	-5.07	D	1.8	5157
HD 108421A	8.870	0.90	-4.57	X	2.6	4700
HD 108421B	9.274	0.88	-4.53	X	3.2	4779
HD 108574	7.418	0.56	-4.49	D	4.9	6205
HD 108575	7.972	0.67	-4.43	X	5.1	5895
HD 109628A	9.073	0.57	-4.51	U	3.0	6109
HD 109628B	9.087	0.55	-4.50	U	3.2	6127
HD 117963A	8.639	0.55	-4.65	U	6.2	6180
HD 117963B	8.924	0.49	-4.61	U	3.3	6097
HD 118328A	9.147	0.62	-4.61	U	0.7	5943
HD 118328B	9.426	0.69	-4.59	U	0.7	5887
HD 121298A	8.604	0.50	-4.91	D	1.9	6353
HD 121298B	8.937	0.52	-4.87	D	1.3	6266
HD 123963A	8.758	0.62	-4.63	U	1.6	5873
HD 123963B	9.511	0.60	-4.55	U	1.4	5438
HD 124054A	8.399	0.58	-4.97	D	2.7	6081
HD 124054B	8.785	0.64	-5.02	D	2.5	5896
HD 126246A	7.466	0.54	-4.40	D	7.9	6223
HD 126246B	7.697	0.60	-4.51	D	3.9	6074
HD 128041A	8.059	0.71	-4.53	U	3.4	5663
HD 128041B	8.827	0.78	-4.51	U	3.2	5192
HD 132563A	8.948	0.54	-4.62	U	3.9	6168
HD 132563B	9.402	0.57	-4.62	U	3.4	5985

---

[2] Tody (1993)

Table 6.1: Continued.

Star	V	B-V	$\log RHK$	method	$v \sin i$ [km/s]	$T_{\rm eff}$ [K]
HD 132844A	9.022	0.55	-4.66	U	3.4	5878
HD 132844B	9.114	0.63	-4.61	U	2.4	5809
HD 13357A	8.180	0.67	-4.70	D	1.7	5615
HD 13357B	8.647	0.73	-4.61	D	1.8	5341
HD 135101A	6.656	0.69	-4.99	D	2.3	5631
HD 135101B	7.500	0.75	-5.07	D	1.1	5491
HD 139569A	8.482	0.54	-4.55	U	8.5	6223
HD 139569B	8.783	0.57	-4.52	U	5.6	5922
HD 143144A	8.856	0.62	-4.61	U	1.9	5943
HD 143144B	9.025	0.61	-4.59	U	1.2	5894
HD 146413A	9.260	0.88	-4.68	D	2.1	4779
HD 146413B	9.492	0.87	-4.60	X	2.0	4818
HD 17159A	8.775	0.54	-4.64	U	3.4	6155
HD 17159B	8.923	0.53	-4.62	U	2.9	6051
HD 186858A	8.368	0.96	-4.73	D	3.6	4910
HD 186858B	8.578	0.93	-4.62	X	3.0	4885
HD 190042A	8.755	0.73	-4.71	U	3.5	5474
HD 190042B	8.778	0.80	-4.72	U	3.8	5406
HD 19440A	7.874	0.47	-4.73	U	4.5	6308
HD 19440B	8.574	0.53	-4.66	U	2.9	6108
HD 200466A	8.399	0.74	-4.77	D	2.0	5633
HD 200466B	8.528	0.76	-4.69	D	2.1	5583
HD 201936A	8.648	0.48	-4.55	X	8.8	6441
HD 201936B	8.851	0.50	-4.53	X	15.5	6452
HD 209965A	7.980	0.55	-4.96	D	4.2	6180
HD 209965B	8.414	0.57	-4.59	U	2.1	6115
HD 213013A	8.982	0.81	-4.59	U	1.7	5402
HD 213013B	9.612	0.93	-4.53	U	2.3	4990
HD 215812A	7.275	0.64	-4.66	U	1.3	5688
HD 215812B	7.576	0.71	-4.64	U	1.5	5586
HD 216122A	8.062	0.58	-4.73	U	6.5	6067
HD 216122B	8.186	0.58	-4.71	U	4.6	6066
HD 219542A	8.174	0.64	-5.07	D	2.1	5849
HD 219542B	8.547	0.72	-4.81	D	1.9	5691
HD 2770A	9.566	0.61	-4.39	X	2.8	5970
HD 2770B	9.660	0.73	-4.39	X	3.9	5844
HD 30101A	8.782	0.82	-4.72	D	1.9	5143
HD 30101B	8.848	0.91	-4.79	D	2.2	5061
HD 33334A	8.023	0.70	-4.99	D	1.9	5650
HD 33334B	8.857	0.80	-4.63	U	1.7	5201
HD 66491A	9.253	0.75	-4.65	D	2.5	5497
HD 66491B	9.312	0.67	-4.58	D	2.4	5492
HD 76037A	7.688	0.50	-5.14	D	7.9	6353

Table 6.1: Continued.

Star	V	B-V	$\log RHK$	method	$v \sin i$ [km/s]	T_{eff} [K]
HD 76037B	8.269	0.50	-5.03	D	9.5	6442
HD 8009A	8.819	0.64	-4.96	D	0.2	5688
HD 8009B	9.724	0.82	-4.95	D	0.0	5291
HD 8071A	7.312	0.57	-4.74	U	5.5	6218
HD 8071B	7.573	0.60	-4.71	U	6.0	6142
HD 85441A	8.907	0.70	-4.60	X	1.3	5701
HD 85441B	9.284	0.71	-4.56	X	1.6	5537
HD 86057A	8.839	0.60	-4.49	X	6.0	6012
HD 86057B	9.676	0.73	-4.40	X	4.6	5629
HD 87743A	8.734	0.62	-4.71	D	2.5	5943
HD 87743B	8.890	0.60	-4.59	D	3.0	5905
HD 94399A	9.407	0.61	-4.54	X	3.2	5970
HD 94399B	9.306	0.71	-4.56	X	3.6	6017
HD 9911A	9.428	0.90	-4.60	U	1.3	5000
HD 9911B	9.448	0.89	-4.60	U	1.3	4968
HD 99121A	8.162	0.46	-4.67	U	6.7	6501
HD 99121B	9.018	0.47	-4.57	U	5.0	6374
HIP 104687A	8.144	0.64	-4.41	D	3.0	5870
HIP 104687B	8.189	0.71	-4.48	D	3.4	5801
14 Her	6.610	0.88	-5.06	D	1.6	5388
40 Eri	4.430	0.65	-4.90	D	0.5	5151
51 Peg	5.450	0.67	-5.08	D	2.0	5787
61 Cyg B	6.030	1.31	-4.95	D	1.7	4077
83 LeoA	6.490	1.00	-4.84	D	1.4	5502
GJ 380	6.610	1.33	-4.72	D	1.9	3876
GJ 580A	6.580	0.78	-5.11	D	2.1	5174
HD 166435	6.840	0.58	-4.27	D	7.6	5964
ρ CrB	5.390	0.61	-5.08	D	1.0	5823
τ Cet	3.490	0.73	-4.98	D	1.0	5283

Table 6.2: **SARG data:** for each star we indicate the the number of observations acquired during the SARG survey, the data (JD-2450000) of the first and the last point, the average value of H_α, the value of $\Delta H\alpha$ and of the standard deviation of the points. In the last two columns we indicate the mean value of the RVs and its standard deviation, corrected for the known Keplerian motion, if applicable.

Star	n. obs	JD_0	JD_F	$\langle H\alpha \rangle$	$\Delta H\alpha$	$\sigma_{H\alpha}$	⟨RV⟩ [km/s]	RMS(RV) [m/s]
BD+182366A	20	1985.4166	4251.3874	0.255	0.039	0.025	11.00	12.67
BD+182366B	18	1985.4317	4251.3989	0.246	0.029	0.021	11.40	11.48
BD+222706A	18	2011.6073	4309.4345	0.225	0.008	0.019	-4.10	25.41
BD+222706B	18	2011.6264	4962.4638	0.258	0.045	0.012	2.41	21.55
BD+231978A	14	1825.7278	4398.6806	0.371	0.135	0.027	20.50	28.41
BD+231978B	13	1825.7152	4398.6929	0.383	0.149	0.025	23.50	35.19
HD 105421A	21	2011.4704	4902.4194	0.237	0.010	0.017	7.40	16.87
HD 105421B	19	2011.4840	4902.4333	0.290	0.069	0.014	0.44	12.76
HD 106515A	31	1986.5327	6026.5634	0.214	-0.002	0.006	0.43	6.00
HD 106515B	30	1986.5442	6026.5757	0.218	-0.003	0.007	18.80	8.69
HD 108421A	17	1986.5975	4250.4681	0.296	0.044	0.007	2.00	21.82
HD 108421B	13	2012.4862	4250.4796	0.360	0.116	0.018	2.00	38.30
HD 108574	22	1913.7615	4251.4385	0.287	0.064	0.008	-2.10	18.09
HD 108575	22	1913.7846	4251.4499	0.307	0.091	0.010	-1.50	33.09
HD 109628A	14	1986.5683	4961.3994	0.214	-0.007	0.012	0.00	10.18
HD 109628B	13	1986.5799	4961.4117	0.215	-0.007	0.010	0.00	16.16
HD 117963A	15	2012.5413	5968.6519	0.226	0.003	0.012	-5.80	33.22
HD 117963B	13	2012.5543	5968.6641	0.233	0.012	0.010	4.18	66.04
HD 118328A	15	2013.6231	4252.5454	0.212	-0.006	0.013	19.20	14.38
HD 118328B	14	2013.6353	4250.5043	0.217	0.001	0.013	18.40	15.93
HD 121298A	14	1912.7867	4161.5587	0.229	0.001	0.009	0.00	8.28
HD 121298B	12	1912.7733	4161.5702	0.231	0.006	0.018	0.00	12.58
HD 123963A	15	2011.5410	4309.4080	0.222	0.006	0.011	-24.40	12.23
HD 123963B	13	2011.5537	4309.4202	0.238	0.024	0.014	-24.40	17.28
HD 124054A	13	2011.5702	4251.4849	0.222	0.002	0.004	-14.60	8.25
HD 124054B	14	2011.5833	4251.4964	0.218	0.002	0.021	-13.40	10.99
HD 126246A	18	2012.5729	4488.7666	0.343	0.119	0.008	0.80	28.88
HD 126246B	16	2012.5846	4311.3850	0.312	0.092	0.012	1.70	14.71
HD 128041A	23	2013.4984	4276.4738	0.210	-0.003	0.020	-74.70	7.45
HD 128041B	21	2013.5115	4276.4852	0.230	0.010	0.034	-73.60	16.31
HD 132563A	63	2013.6508	5968.6857	0.227	0.005	0.021	1.80	16.47
HD 132563B	56	2013.6645	5968.7008	0.221	0.003	0.025	1.65	13.39
HD 132844A	27	2012.6152	4311.4244	0.259	0.044	0.016	-3.20	11.87
HD 132844B	26	2012.6027	4311.4359	0.318	0.103	0.012	-2.00	18.84
HD 13357A	29	1801.6950	4849.4490	0.235	0.021	0.013	26.20	10.55
HD 13357B	25	1801.7086	4849.4612	0.262	0.046	0.018	25.40	13.83
HD 135101A	14	1982.7540	4488.7807	0.202	-0.011	0.007	0.00	4.84
HD 135101B	12	1982.7697	4311.4614	0.212	-0.002	0.011	0.00	5.80

Table 6.2: Continued.

Star	n. obs	JD_0	JD_F	$< H\alpha >$	$\Delta H\alpha$	$\sigma_{H\alpha}$	< RV > [km/s]	RMS(RV) [m/s]
HD 139569A	18	2012.6615	4339.4064	0.281	0.057	0.013	-29.40	24.53
HD 139569B	20	2012.6733	4339.4179	0.279	0.062	0.015	-29.80	29.57
HD 143144A	19	1798.3625	4339.3805	0.223	0.006	0.015	-78.50	9.39
HD 143144B	18	1798.3768	4339.3923	0.221	0.004	0.017	-78.80	15.29
HD 146413A	20	2012.6910	4962.5618	0.350	0.105	0.013	4.20	8.61
HD 146413B	19	2012.7035	4962.5734	0.350	0.108	0.020	5.30	15.32
HD 17159A	28	1797.6565	4819.3558	0.219	-0.003	0.011	11.40	21.43
HD 17159B	28	1797.6727	4819.3679	0.219	-0.000	0.016	10.20	15.88
HD 186858A	44	1798.4744	4962.5879	0.310	0.076	0.010	-0.63	8.90
HD 186858B	41	1798.4601	4962.6015	0.297	0.061	0.013	1.54	7.64
HD 190042A	23	1825.4814	4783.3459	0.210	-0.004	0.010	-4.60	5.77
HD 190042B	22	1825.4615	4783.3593	0.212	-0.002	0.012	-3.50	7.74
HD 19440A	19	1828.6588	4339.6564	0.231	0.005	0.008	-15.40	12.31
HD 19440B	19	1828.6716	4339.6679	0.219	-0.002	0.019	-15.90	9.70
HD 200466A	79	1801.5721	5807.6025	0.251	0.038	0.019	-8.00	15.89
HD 200466B	71	1801.5850	5807.6137	0.247	0.034	0.014	-0.22	8.37
HD 201936A	15	2042.6381	4398.3978	0.289	0.058	0.015	3.70	32.87
HD 201936B	15	2042.6554	4398.4092	0.317	0.086	0.023	2.50	47.51
HD 209965A	26	2145.5472	4783.3759	0.223	0.001	0.008	-19.40	20.60
HD 209965B	22	2145.5634	4783.3878	0.218	-0.003	0.011	0.11	24.31
HD 213013A	34	1827.4669	4369.5700	0.245	0.031	0.016	-24.70	10.98
HD 213013B	32	1827.4540	4369.5824	0.264	0.035	0.024	-24.70	14.68
HD 215812A	29	1798.4923	4398.4798	0.210	-0.004	0.005	8.43	32.68
HD 215812B	18	1798.5063	4398.4912	0.212	-0.001	0.007	0.95	20.25
HD 216122A	24	1801.6229	4962.6771	0.220	0.000	0.007	-13.30	18.74
HD 216122B	27	1801.6366	4962.6895	0.225	0.006	0.012	-1.04	13.92
HD 219542A	43	1825.5176	4664.6807	0.216	0.001	0.007	-12.50	7.43
HD 219542B	48	1825.5048	4664.6931	0.230	0.016	0.011	-11.50	7.54
HD 2770A	21	1856.5704	4338.6438	0.301	0.084	0.017	-5.00	21.13
HD 2770B	21	1856.5841	4338.6587	0.313	0.098	0.023	-6.40	32.54
HD 30101A	33	1825.6514	5952.4781	0.252	0.030	0.021	-18.20	25.26
HD 30101B	33	1825.6652	5952.4943	0.252	0.027	0.023	-18.00	13.62
HD 33334A	57	1801.7517	5952.5179	0.207	-0.007	0.013	83.20	22.28
HD 33334B	51	1801.7439	5952.5299	0.216	-0.003	0.015	83.70	23.26
HD 66491A	24	1853.7409	4398.7585	0.264	0.051	0.023	48.40	18.04
HD 66491B	21	1853.7557	4161.4142	0.271	0.058	0.030	49.10	23.30
HD 76037A	35	1828.7406	5952.6152	0.228	-0.000	0.012	22.02	114.52
HD 76037B	34	1853.7833	5952.6280	0.240	0.009	0.014	-0.05	38.46
HD 8009A	33	2116.6201	4819.3811	0.217	0.004	0.022	-42.10	12.05
HD 8009B	26	2116.6334	4819.3929	0.223	0.006	0.020	-41.80	17.66
HD 8071A	12	1797.6224	4339.6225	0.217	-0.007	0.005	5.67	18.94
HD 8071B	9	1797.6397	3246.6791	0.210	-0.012	0.005	9.00	64.80
HD 85441A	15	1826.7408	4754.7425	0.246	0.032	0.022	-19.80	12.32

Table 6.2: Continued.

Star	n. obs	JD_0	JD_F	$< H\alpha >$	$\Delta H\alpha$	$\sigma_{H\alpha}$	< RV > [km/s]	RMS(RV) [m/s]
HD 85441B	15	1826.7535	4754.7538	0.264	0.051	0.016	-19.80	13.42
HD 86057A	18	1985.5083	4251.3612	0.324	0.105	0.018	11.80	24.94
HD 86057B	18	1985.5216	4251.3726	0.360	0.147	0.025	11.20	36.64
HD 87743A	23	2012.3936	4849.6255	0.249	0.032	0.023	0.00	19.33
HD 87743B	25	2012.3801	4849.6371	0.282	0.065	0.031	3.00	19.35
HD 94399A	19	1986.4614	4962.3837	0.346	0.128	0.026	-6.20	20.16
HD 94399B	17	1986.4731	4962.3953	0.338	0.119	0.014	-3.80	57.20
HD 9911A	22	1801.6656	4339.6330	0.236	0.007	0.030	-56.60	11.53
HD 9911B	20	1801.6528	4339.6445	0.223	-0.008	0.021	-56.30	11.36
HD 99121A	24	1986.5086	4250.4427	0.223	-0.010	0.015	-4.40	23.66
HD 99121B	20	1986.5205	4250.4552	0.217	-0.012	0.017	-3.10	30.57
HIP 104687A	30	2070.6622	4309.6015	0.300	0.084	0.015	-20.60	23.82
HIP 104687B	29	2070.6751	4309.6148	0.294	0.079	0.013	-21.20	14.20
14 Her	144	4515.7409	4902.6461	0.223	0.009	0.003	-2.97	4.06
40 Eri	42	4515.3574	4819.4971	0.232	0.011	0.002	-42.20	7.19
51 Peg	44	1774.6139	4783.4387	0.206	-0.009	0.003	0.57	6.00
61 Cyg B	127	2570.3207	4693.6690	0.343	-0.001	0.008	-0.29	2.92
83 Leo A	121	4512.5548	4819.6320	0.223	0.009	0.003	-2.90	6.54
GJ 380	145	4512.4711	4819.5728	0.403	0.013	0.012	-26.10	5.39
GJ 580 A	158	4512.6957	4694.3972	0.213	-0.008	0.004	-67.90	7.34
HD 166435	18	2775.6448	3872.7162	0.411	0.193	0.010	-13.70	95.27
ρ CrB	46	2011.7355	4663.5609	0.210	-0.006	0.004	-1.32	6.09
τ Cet	225	1773.7347	4819.3086	0.211	-0.006	0.003	-16.40	4.86

For a proper interpretation of the H_α measurements that we derived in Sect. 6.3, some stellar parameters were considered. We describe here the adopted sources or procedures to measure them.

Differential radial velocities were derived in Carolo (2012) and have a typical uncertainty of about 4 m/s for stars in the binary survey and less then 2 m/s for the bright stars.

We considered measurements of $\log R'_{HK}$ from the literature, with preference for studies including multi-epoch measurements to take temporal variations of activity into account. Overall, we retrieved $\log R'_{HK}$ for 36 stars from Wright et al. (2004), Isaacson & Fischer (2010), Desidera et al. (2006b), Strassmeier et al. (2000) and Gray et al. (2003). Finally, for the components of HD 8009, HD 30101, HD 121298, and HD 128041, the value of $\log R'_{HK}$ was derived from HIRES spectra available in the Keck[3] archive following the procedure described in Carolo et al. (2014).

For stars without $\log R'_{HK}$ values in the literature we estimated the value from the ratio of X-ray to bolometric luminosity, using the calibration by Mamajek & Hillenbrand (2008). This latter quantity was derived following the procedure described in Carolo et al. (2014) and Carolo (2012) for the sources identified in the ROSAT All Sky Survey (Voges et al. 1999, 2000) within 30" from our target stars. For the binaries composing most of our sample, the

---

[3] https://koa.ipac.caltech.edu/cgi-bin/KOA/nph-KOAlogin

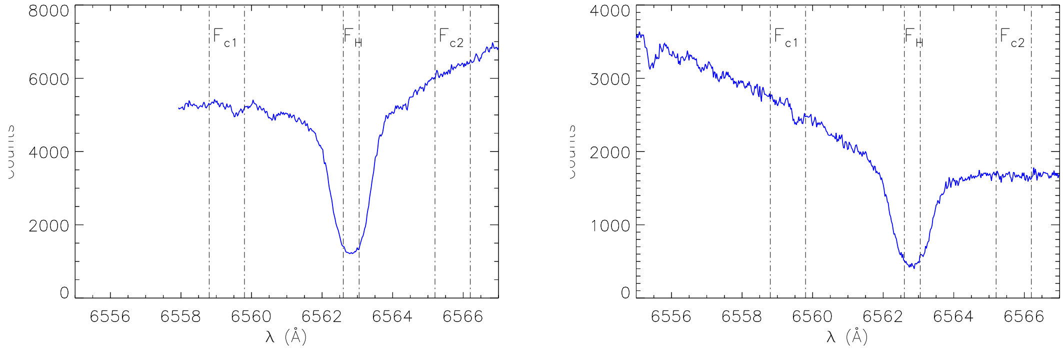

Figure 6.1: H_α profile in one of our stellar echelle spectra. The wavelength intervals used are delimited by the vertical lines. *Left:* order 93. *Right:* order 94.

components are not spatially resolved by ROSAT. We then assumed equal X-ray luminosity for the components. For stars that are not detected in the ROSAT All Sky Survey, this procedure yields an upper limit on $\log R'_{HK}$. The values of $\log R'_{HK}$ or the upper limits, as other additional parameters we used, are listed in Table 6.1.

The projected rotational velocity, $v \sin i$, was obtained from a calibration of the full with at half maximum (FWHM) of the cross-correlation function of SARG spectra. Details will be presented elsewhere. For the single stars we adopted the $v \sin i$ from literature sources such as Valenti & Fischer (2005).

The effective temperature $T_{\rm eff}$ of the primaries was derived from the B-V colour using the calibration by Alonso et al. (1996) and assuming no reddening, while for the secondaries we relied on the high-precision temperature difference measured as part of the differential abundance analysis of 23 binary systems in Desidera et al. (2004, 2006a) and preliminary results by Vassallo (2014) for the others. For the single stars (standard stars and targets of the hot-Neptune program) we adopted the effective temperature from high-quality spectroscopic studies (e.g. Valenti & Fischer 2005).

6.3 H_α index

Since the Ca II H&K lines wavelengths are not included in the SARG yellow grism spectral range, we defined a new activity index based on the H_α line to study the activity of the stars in this sample. We built an IDL procedure optimized for the SARG spectra format: we measured the instrumental flux (not corrected for the blaze function) in a wavelength interval centred on the line core, F_H, and in two additional intervals symmetrically located with respect to the centre, F_{c1} and F_{c2}. H_α is defined as

$$H_\alpha = 2\frac{F_H}{F_{c1} + F_{c2}}, \tag{6.1}$$

where $F_{c1} = flux$[6558.80Å- 6559.80Å], $F_H = flux$[6562.60Å- 6563.05Å], and $F_{c2} = flux$[6565.20Å-6566.20Å]. Typical spectra of the $H_\alpha$region in the SARG observations are in Fig. 6.1: since the SARG spectrograph was not built to study in the H_α spectral range, this line appears twice but close to the edges of two orders (close to the blue edge of the order 93 and to the red edge of the order 94), according to the RV of the star. When we choose a wider window for F_{c1} and F_{c2} or increase the distance from F_H, the number of spectra in which the selected wavelength exits the detector therefore increases. Our choice is the best compromise.

For the same reason we were unable to use the H_α index that was used by other authors (e.g. Kürster et al. 2003; Boisse et al. 2009; Santos et al. 2010; Gomes da Silva et al. 2014): for each order one of the two continuum reference windows used by these authors is outside of the region covered by the detector. Furthermore, we were unable to use a reference continuum to estimate the continuum flux because it is difficult to define the proper blaze function given the presence of the extended wings of the photospheric H_α absorption. To make our measurement more reliable, we used the weighted mean of two H_α values when fluxes for all these spectral bands could be measured in both orders.

6.3.1 Error estimation

We then analysed the possible sources of errors.

- Internal noise

We estimated the errors on the fluxes assuming photon noise.

The error on H_α index was then derived by error propagation:

$$err_{H\alpha} = H_\alpha \sqrt{\left(\frac{1}{SN_H}\right)^2 + \frac{1/c_{1err}^2 + 1/c_{2err}^2}{(F_{c1} + F_{c2})^2}} \tag{6.2}$$

where $SN_i = \sqrt{gain \cdot F_i}$, $c_{1err} = SN_{c1}/F_{c1}$, $c_{2err} = SN_{c2}/F_{c2}$. We note that because of the lower value of the blaze echelle function, the H_α indexes coming from the order 94 have a lower weight on average. HD 128041, HD 143144, HD 9911, 61 CygB and GJ 580A have high absolute radial velocities (RV < -50 km/s) so that their spectra are remarkably blueshifted. Their H_α indexes have a higher uncertainty because the H_α line is shifted out from the order 93 spectra, therefore we were only able to use the SARG order 94, which yields poorer results.

- Systematic error

We also considered that several other sources of noise can introduce errors on the H_α index: flat fielding, background subtraction, bad pixels, instrumental instability, fringing, etc. All these contributions, added to the possible intrinsic variations of activity, increase the standard deviation of the H_α values ($\sigma_{H\alpha}$). τ Cet was used as a test target for this purpose. It is very bright and its $\Delta H\alpha$ variation is lower than 0.005 dex (peak to valley) with low levels of variability in $\log R'_{HK}$ from the literature. We studied the variation of τ Cet night by night. We note that the standard deviation of H_α is about 10 times the intrinsic photonic error, therefore we decided to add a jitter to our measurement. Errors significantly larger than the photon noise error have been reported in other cases of 1 Å wide activity indices from echelle spectra, see for instance Wright et al. (2004). We found that this increase does not depend on the activity level of the star. It is instead described by a relation with the stellar magnitude as shown in Fig. 6.2: $\sigma_{jitter} = \sqrt{(0.0028)^2 + (5.27 \cdot 10^{0.4V-6})^2}$. Our adopted jitter is compatible with the single night variations of τ Ceti and we rescaled it for other stars according to their magnitude. The dependence on magnitude is that expected for error sources as background subtraction.

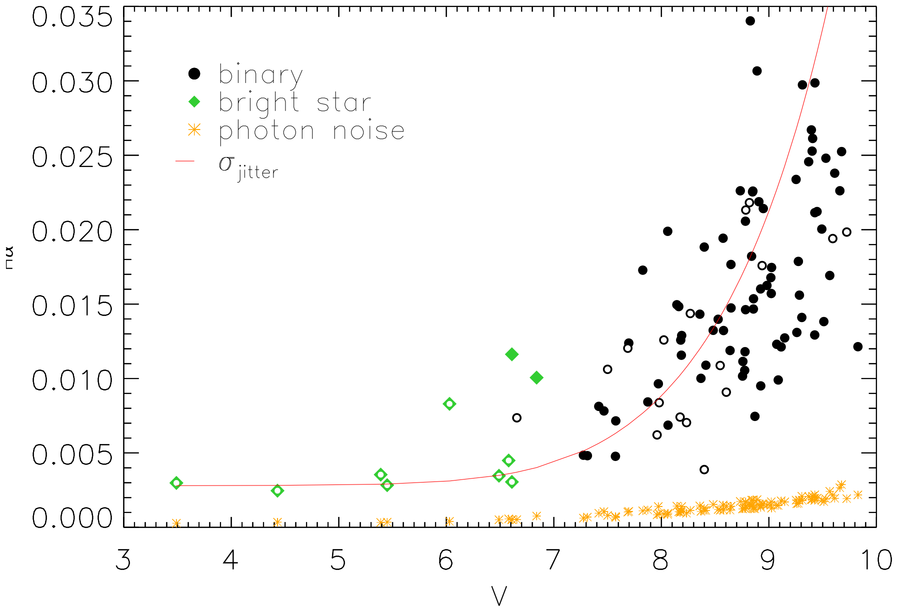

Figure 6.2: Relation between V magnitude of the stars and the standard deviation $\sigma_{H\alpha}$ of the H_α index. Open symbols indicate quiet stars (see Sect. 6.3.3 for details), green diamonds are the bright stars sample. The continuous line represents the σ_{jitter} we adopted, while the orange asterisks indicate the mean photon noise value for each star.

Finally the error applied to each measurement of H_α is the sum of the photonic error and the instrumental jitter as derived above. As the jitter is significantly larger then the photon noise, individual errors on H_α index of a given star are very similar. Therefore the estimate of the jitter term has a very limited effect on the periodogram analysis presented in Sec. 6.5.

- Contamination by telluric lines

In the spectral range of H_α we considered, there are several telluric lines mainly due to the water vapour. These lines can enter in our F_{c1}, F_{c2} and F_H intervals and influence the H_α index value. The strongest line is H_2O at 6564.206 Å. If this telluric line enters F_H, the H_α index will decrease of about 1.5%, giving an error by about 0.005 on a quiet star. This can occur when the geocentric velocity of the star is between 52 and 75 km/s. Therefore only a few of our spectra are involved, but none of those discussed below. The effect we have if this line enters F_{c2} is about 0.001 dex which is negligible. The H_2O line at 6560.555 Å can also enter the F_H interval with a comparable contribution if the geocentric radial velocities between -90 and -123 km/s are involved. These few spectra were rejected.

- Contamination estimation

Even though during the observations of the binaries the slit was oriented perpendicularly to the separation of the components, some spectra are strongly contaminated by the companion star and were rejected. Furthermore we modelled the contamination for each consecutive observation of the companions assuming a Moffat-like shape for the point spread function

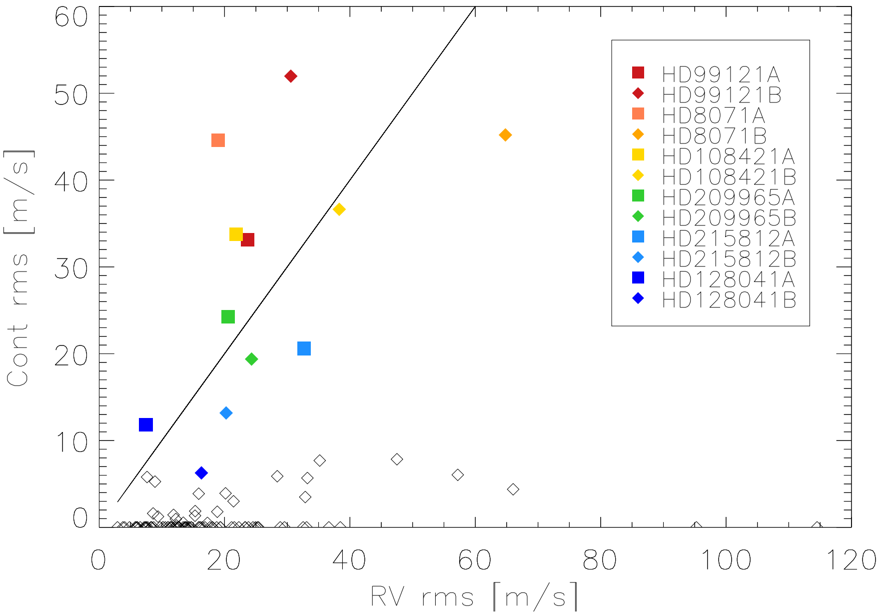

Figure 6.3: Relation between the standard deviations of the RVs (after the correction for known Keplerian motions) and that induced by the contamination. Systems with a non-negligible contamination are highlighted.

(PSF) and taking into account the separation, the magnitude and the seeing. We obtain that the contribution of the contamination to the H_α is lower than 1% in the majority of the case and therefore is negligible. We found instead that for six systems the variation induced by the contamination is greater than the intrinsic variation (Fig. 6.3).

For example, HD 8071 is a close binary system ($\rho = 2.183$" according to Hipparcos) and the primary star is a spectroscopic binary with an amplitude of a few km/s. The effect of contamination on the RV is further modulated by the velocity of the primary at the observing epoch. This causes the RV to vary around the true value by up to a few hundreds m/s in a quite unpredictable way. For more details see Martínez Fiorenzano et al. (2005).

6.3.2 Flux stability of the instrument

The stability in flux of the instrument over the time was tested using survey data: for stars in the binary sample, we normalised the H_α value for each spectrum to the median value of its star. We then binned these values into the synodic monthly mean over different stars and compared them to the same results for the τ Cet data series (see Fig. 6.4). For τ Cet data we found that points are located around zero with $\sigma_{H\alpha} = 0.003$. For the stars in the binary sample, the last two years of the campaign were devoted to observing mainly a few stars with candidate companions and/or RV trends, therefore the H_α monthly means depend on the variability of the individual targets, as in the case of HD 200466 (Carolo et al. 2014). We also verified the presence of periodicity by applying the generalize Lomb-Scargle periodogram

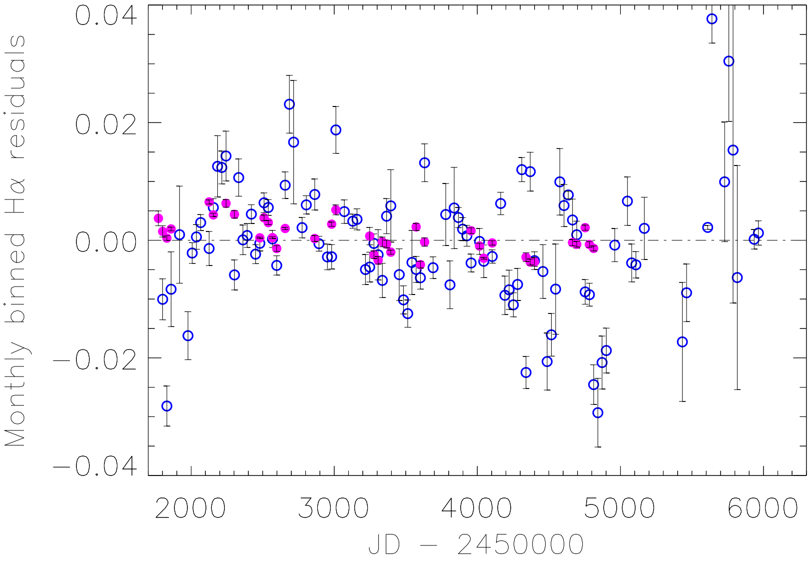

Figure 6.4: Time evolution of the H_α values of all the spectra normalised to the median value for each star, monthly bins (blue circles). The magenta points correspond to the τ Cet data series.

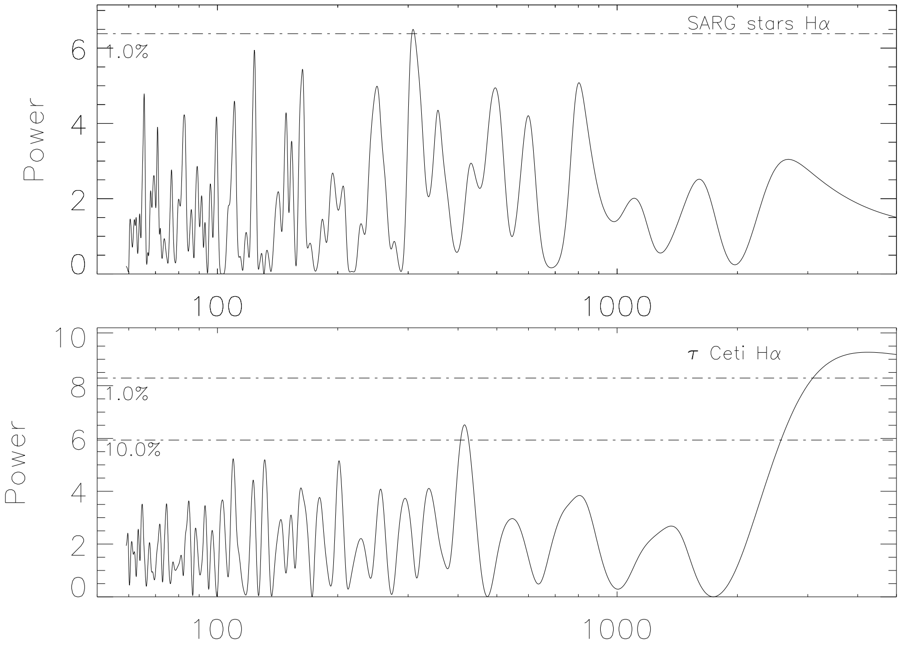

Figure 6.5: GLSP of the synodic monthly binned H_α values of the SARG sample (top) compared to τ Cet (bottom).

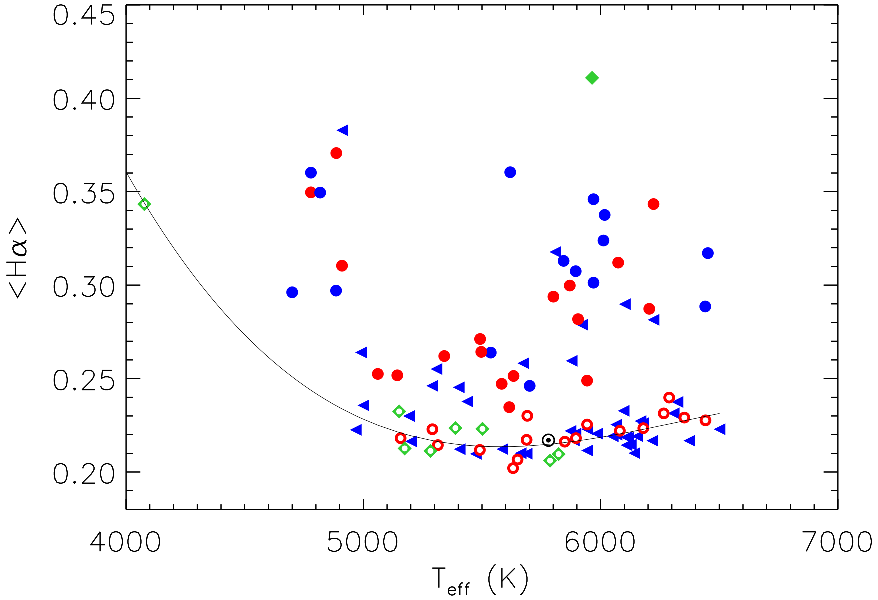

Figure 6.6: Relation between the temperature and the median value of H_α for each star. Colours are given according to $\log R_{HK}$ value sources: values from the literature are plotted in red, while for the blue dots the values are derived from X-ray luminosity. The blue triangles indicate that the $\log R'_{HK}$ value for a star is only an upper limit. Green diamonds indicate the bright stars sample. Open symbols correspond to quiet stars. The line only shows the fit of the binaries to have a sample unbiased by activity. The line shows the best fit for the quiet stars. The position of the Sun is also shown with $\odot$.

(GLSP) Zechmeister & Kürster (2009) [4] to the two sequences of the binned values: the whole sample sequence shows no significant peak and differs from the τ Ceti sequence, which shows a long-term trend (see Fig.6.5).
The radial velocity stability is discussed in Desidera et al. (2007) and our measurements are corrected accordingly.

6.3.3 Dependence on T_{eff} and $\Delta H\alpha$ definition

We divided our sample into two subgroups: as active stars we indicate stars with $\log R'_{HK}$ greater than -4.80, the others are called quiet stars.

Since our H_α index is defined as the ratio between the flux in the line centre and the flux in the wings, we expect that different stars with the same activity level can have different $\langle H_\alpha \rangle$ values because of the different photospheric spectrum. Therefore we compared effective temperature and $\langle H_\alpha \rangle$ to determine the appropriate relation for quiet stars (Fig. 6.6).

Most of the quiet stars lie at $\langle H_\alpha \rangle \sim 0.22$ for $T_{eff} > 5000$ K. At lower temperature, the $\langle H_\alpha \rangle$ index for quiet stars seems to increase. Active stars scatter mostly at higher $\langle H_\alpha \rangle$. We also made a comparison with the Sun: it has an effective temperature of 5780 K and its

---

[4] `https://github.com/callumenator/idl/blob/master/Routines/Periodogram/generalised_lomb_scargle.pro`

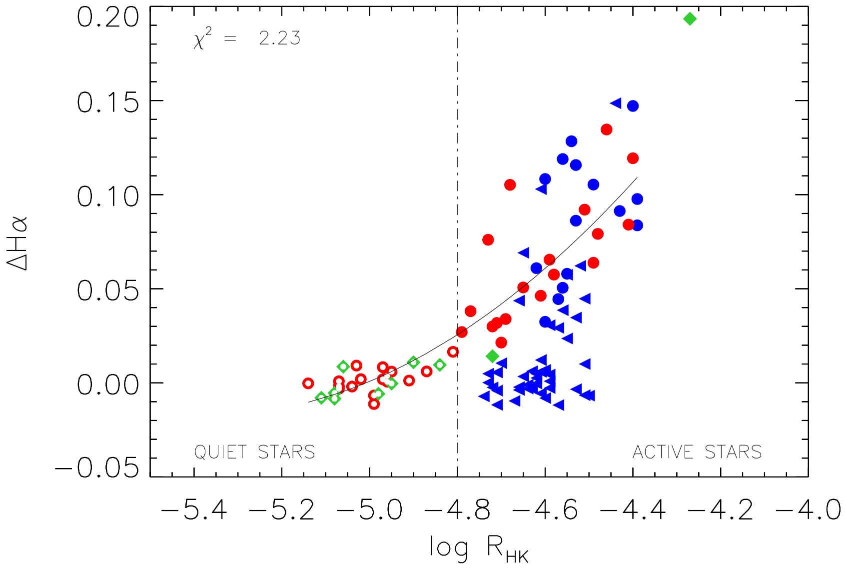

Figure 6.7: Relation between the $\log R'_{HK}$ and $\Delta H\alpha$. Colours are the same as Fig. 6.6. Bright stars and stars with upper limits for $\log R'_{HK}$were not considered to have a sample unbiased by activity.

$\langle H_\alpha \rangle$ is 0.217, as measured in the solar flux atlas (Kurucz et al. 1984), in agreement with the lower envelope for quiet stars. We describe the distribution of the quiet stars in this lower envelope with a three-degree function and define as H_α-excess ($\Delta H\alpha$) the point distance from this curve: $\Delta H\alpha$ is the difference in H_α index of a star with respect to a quiet star that has the same effective temperature. Therefore we decided to use $\Delta H\alpha$ as the activity index; it is more robust than H_α because it allows us to compare the activity of stars with different temperatures.

6.4 Sample analysis

6.4.1 Correlation with $\log R'_{HK}$ and rotation

$\Delta H\alpha$ correlates quite well with $\log R'_{HK}$ (reduced $\chi^2 = 2.26$, Fig. 6.7). Active stars are more scattered but typically show excess in the H_α index ($\Delta H\alpha > 0$). All the stars for which $\log R'_{HK}$ has been derived from the X-ray luminosity are in the active portion of the diagram. This is due to the flux limit of the ROSAT All Sky Survey, which is only sensitive to the active stars at the typical distance of our program stars. The stars for which only upper limits are derived populate the lower envelope of the distribution in most cases: this is consistent with a low activity level.

This new index appears to show that stars are distributed in two groups, which suggests the presence of the Vaughan-Preston gap at $\Delta H\alpha = 0.02$ (Vaughan & Preston 1980).

The results of Pace et al. (2009) also show the presence of a gap between $\log R_{HK} = -4.7$ and -5.0. This corresponds to the interval $\Delta H_\alpha \sim [0.01, 0.04]$.

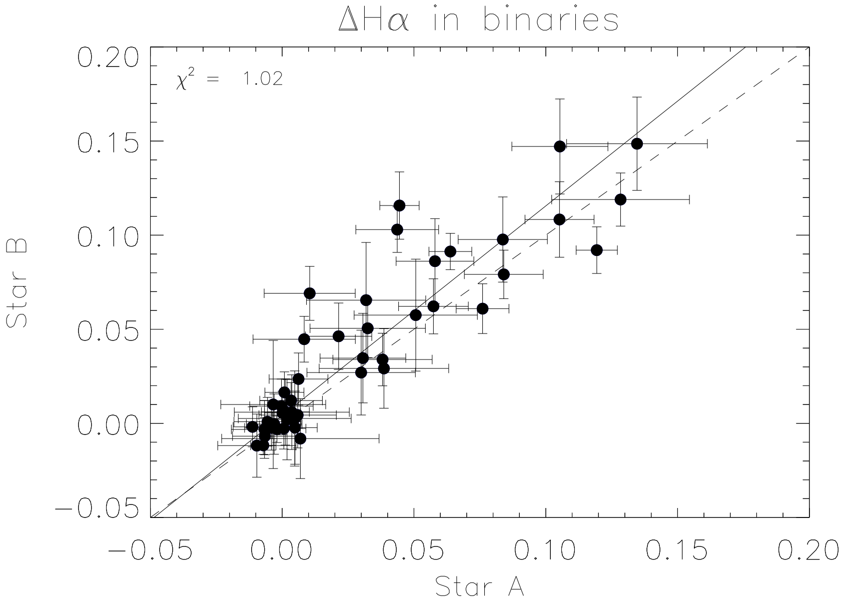

Figure 6.8: Relation between the $\Delta H\alpha$ of the two companion stars. The solid line corresponds to the best fit, the dashed line corresponds to the equivalence.

We also found a weak relation between $\Delta H\alpha$ and its standard deviation:

the intrinsic variation of the H_α index and internal errors contribute to the increase in scatter in the H_α index measurement for each star, but since the scatter is dominated by intrinsic errors for fainter stars, only the deviation seen in brighter stars is dominated by the intrinsic variability.

We also checked the well-known relation between rotation and activity (e.g. Noyes et al. 1984; Baliunas & Vaughan 1985; Santos et al. 2000)

We found, as expected, that a moderate rotation is enough to cause a high activity for cold stars and in this case the $v \sin i$ value increases with activity, while the hottest stars only have high activity values if $v \sin i$ is high: this behaviour can be related to the decrease in thickness of the convective envelope as the stars become hotter (Charbonneau & Steiner 2012).

6.4.2 Binary components

We can compare the $\Delta H\alpha$ index for the two components in each binary system: we find a very good relation between the two stars indexes, that is $\Delta H\alpha_B = (1.11 \pm 0.08)\Delta H\alpha_A + 0.004 \pm 0.004$, as shown in Fig. 6.8. The value of the reduced χ^2 suggests that the scatter is dominated by the measurement error. We tested that the long-scale activity cycles (like the solar cycle) induce a variation in H_α that is weaker than our adopted measurement error. HD 108421, HD 132844 and HD 105421 lie above the relation, but we did not note any evidence of errors in our analysis for these stars, so that the discrepancy seems to be real and the two stars of these systems could be in different activity phases. For HD 126246, which lies below the relation, the difference in the H_α activity level between the two components qualitatively agrees with the $\log R'_{HK}$ and $v\sin i$ difference found by Desidera et al. (2006a), supporting an intrinsic rotation and activity difference between the two components.

6.4.3 Age-activity relation

Prompted by this result, we tested whether our H_α could be an age indicator for these stars (e.g. Skumanich 1972; Baliunas & Vaughan 1985; Soderblom et al. 1993; Mamajek & Hillenbrand 2008; Pace 2013; Zhao et al. 2011). We computed the ages of the binary systems with the isochrone fitting algorithm developed by Bonfanti et al. (2015). The implementations details can be found in Bonfanti et al. (2015, 2016). Here we recall that it enables recovering the isochronal age of a field star when at least its [Fe/H], T_{eff} and $\log g$ are available. In our case we also considered $\log R'_{HK}$as input parameter, which allowed us to disregard unlikely very young isochrones, so that we could better constrain the stellar age. Since the evolution of low-mass stars is extremely slow, this method works well for stars with $T_{\mathrm{eff}} > 5500$ K; for cooler (less massive) stars, uncertainties in the exact location of a star on the Hertzspurng-Russel (HR) diagram leads to an error so large that practically all ages from 0 up to the age of the Universe are possible. We therefore did not consider such stars in our test.

From the differential abundance analysis, T_{eff} and $\log g$ have typical uncertainties of ~ 50 K and ~ 0.15 dex, respectively, while the differences $\Delta T_{eff} = T_{effA} - T_{effB}$ and $\Delta \log g = \log g_A - \log g_B$ are more reliable and their reference uncertainties have been estimated in ~ 20 K and ~ 0.06 dex, respectively. We therefore constructed a grid in T_{eff} and $\log g$ for each binary component, with step sizes of 25 K and 0.05 dex, respectively. We discarded all the points in the grid where the relations $\Delta T_{eff} - \delta T_{effB} < |T_{effA} - T_{effB}| < \Delta T_{eff} + \delta T_{eff}$ and $\Delta \log g - \delta \log g < |\log g_A - \log g_B| < \Delta \log g + \delta \log g$ were not satisfied. We computed the ages of each component for each remaining point in the grid and retained only those for which the stars could be considered coeval ($|\log t_A - \log t_B| < 0.05$; 0.05 is the resolution of the isochrone grids). For each analysed star, we built a catalogue reporting the plausible input parameters and the resulting age that was coeval to that of its companion. For each binary system, we synthesised these data providing the youngest and oldest feasible age of the system and the median age.

In Fig. 6.9 we plot for each star hotter than $T_{eff} = 5500$ K its $\Delta H\alpha$ as a function of the age of the system. We divided the systems into two subsamples according to the reliability of the input parameters, and in particular the T_{eff}: blue dots represent the systems analysed in Desidera et al. (2004), which are more accurate, while orange crosses correspond to preliminary results for systems analysed in Vassallo (2014). The result shows that the majority of the active star are younger than 1.5 Gyr, while for older stars the distribution is flattened around zero, that is, they are inactive.

We found that the activity for young stars is anti-correlated with the age, confirming that the relation between the $\Delta H\alpha$ in the components of the systems younger than 1.5 Gyr is mainly due to age. The position of the pairs HD132844A and B and HD13357A and B in the diagram of Fig. 6.9 does not follow the general trend: the position on colour-diagram of HD132844 below the main sequence (see Desidera et al. 2004) is indicative of substantial error in the trigonometric parallax. The two Hipparcos solutions for the parallax of HD13357 are inconsistent with each other. In both cases we can conclude that there is an underestimated error in the parallax. Indeed, the adopted parameters (especially the gravity) depend on the adopted trigonometric parallax: in the abundance analysis the effective temperatures were derived from ionization equilibrium and stellar gravities from luminosities, masses and

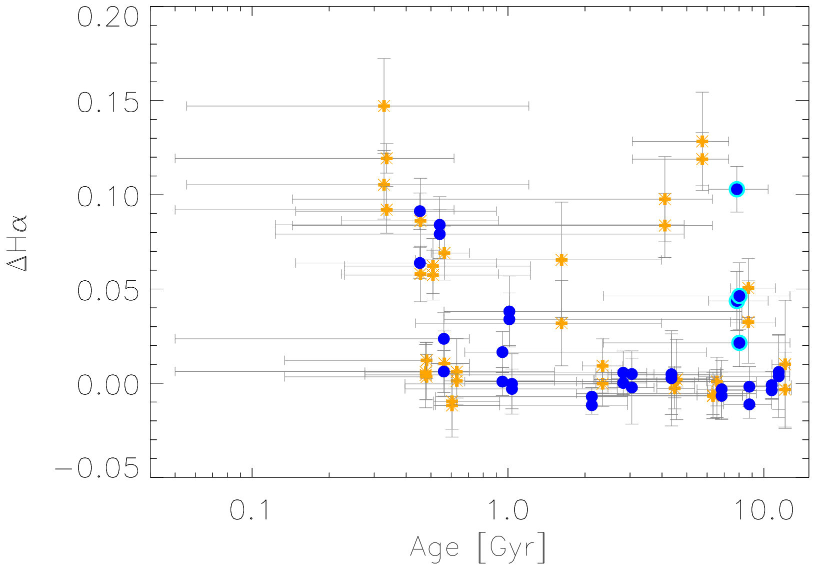

Figure 6.9: Activity as a function of the age. Blue circles represent the star in Desidera et al. (2004) for which we have solid constraints on the temperature; orange crosses show the other stars. The two systems with an uncertain parallax are highlighted in cyan.

temperatures, using iterative procedures. It seems therefore that a well-defined activity-age relation persists only for objects younger than ~ 1.5 Gyr, and that after this age H_α seems to be less efficient as an age indicator. Our data did not show significant correlation between these quantities: due to the lack of data with such an age, we cannot conclude whether if there is a discontinuity or if the activity of the star decreases with time. The activity-age anti-correlation for younger stars confirms results from Barry (1988), for example, and the apparent flatness of the plot for older stars seems to agree with Pace (2013);but owing to the uncertainty on our ages, we cannot confirm or reject the idea that the activity decreases with age also for older stars, with a different slope as found by Mamajek & Hillenbrand (2008), for instance. Finally, we found that a large portion (15 over 35) of the stars in our sample with age estimates from the isochrone method are younger than 1.5 Gyr: this could be due to the recent bump in the star formation rate in the solar neighbourhood as claimed by Barry (1988) or to a bias in the age distribution of the stars in the Hipparcos Multiple Stellar Catalog. Future observations of results from the GAIA satellite may clarify this question.

6.4.4 Activity vs RV scatter

We finally found the well-known relation between the activity of a star and the standard deviation of its radial velocities (Saar & Donahue 1997; Saar et al. 1998; Santos et al. 2000; Boisse et al. 2009, 2011). In addition, when considering the contamination of the spectra, we found that it is not negligible especially for the systems HD 8071, HD 99121, HD 108421 and HD 209965, which were omitted in this discussion and are detailed below. There are also a

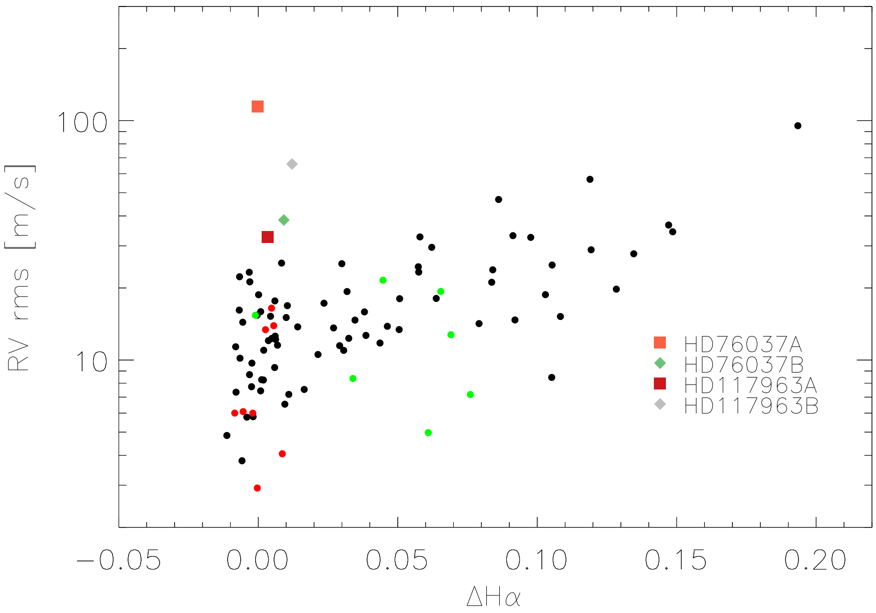

Figure 6.10: Relation between the $\Delta H\alpha$ and the RV standard deviation in the survey. The green dots indicate the RV standard deviation of the stars with a known Keplerian trend that is due to a companion, in red we plot the RV standard deviation of stars with a known companion. In both cases we correct the data for their known RV variation.

number of cases for which the spread in RV during the survey is high ($> 80m/s$) and which have a relatively low activity level.

Most of these objects have known RV trend of Keplerian origin and after the RV variation induced by the companion was removed, they became part of the main trend (Fig. 6.10). In addition there are at least four stars left outside the general trend. Since these are potentially very interesting objects, we examine them more in detail.

HD 76037A and B: this is a wide binary composed of two F-type stars. The SARG spectra show that the primary star is a long-period partially blended SB2 star, therefore we conclude that the excess scatter in RVs is due to the blending of the spectra of the two components. For the secondary, the excess of the RV scatter is fairly large even after resuming the long-term trend with time that indicates the presence of a low-mass companion; in addition, the $H_\alpha$index also has a trend with time - more likely related to a cycle.

The Hipparcos Multiple Stellar Catalog indicates that the HD 117963A system has a separation wide enough to rule out contamination effects ($\rho = 3.493$”). HD 117963B is a spectroscopic binary and some of the spectra were taken with low S/N (Desidera et al. in prep.).

We cannot exclude Keplerian motion as the origin of the scatter for both stars, therefore a deeper analysis with acquisition of additional data would be required.

6.5 Hα index time-series analysis

By analogy with the Sun, emission in the core of H_α is expected to show time variability mainly modulated by stellar rotation over a period of the order of days, and by the activity cycle over periods of hundreds or thousands of days. In addition, secular variations in the activity levels similar to the Maunder minimum can be present. Therefore the different properties of the time series of our objects should be taken into account. Stars in the Hot-Neptunes program were observed for a single season with a moderately dense sampling. In this case rotation periods could be found, but periodicities due to the activity cycle cannot be reliably identified. On the other hand, for the SARG survey objects, the observational campaign was longer and less dense. For only a few targets do we have a larger number of spectra because during the survey they were suspected to host a planet. This was the case of HD 106515A (Desidera et al. 2012) and HD 132563B (Desidera et al. 2011), for example. In addition we already know that for HD 200466A, the RV variations seen are mainly due to an activity cycle (Carolo et al. 2014).

It is known that more active stars have irregular periods that are not easy to determine with the analysis of periodograms. In spite of this, we computed the GLSPs for the H_α index that was obtained using the Zechmeister & Kürster (2009) procedure. To evaluate the significance of these periodicities, the false alarm probability (FAP) of the highest peak of the periodogram was estimated through a bootstrap method, with 1000 permutations. We used the spectral window function to rule out that our periodicity is due to the sampling. The results for the most interesting objects are listed in Table 6.3.

We found a signature of periodic variations (rotational periods or activity cycles) in 19 stars, whereas 10 stars show a clear overall trend in H_α with time. On the other hand the stars for which we were able to find evidence of activity cycles are all with moderate activity excess and temperatures of between 4800 and 6000 K. The stars showing a long-term trend are hotter than average.

It is noteworthy that of the binary stars that show promising cycles, only HD 76037A&B are quiet and show a long-term trend.

Of the bright stars, 51 Peg was used as a RV standard to monitor instrument performances during the binary program. The quite good temporal coverage of the data allowed us to detect a significant long-term period of about seven years with FAP of 0.6%. Added to this signal, we also found a periodicity of 86.49 d, which corresponds to an alias of the 21.9 ± 0.4 d period found by Simpson et al. (2010) with one sinodic month. This shortest period seems then to be the rotational signal. We obtained a similar result also for 61 Cyg b: the GLSP peaks at 16.44 d, which is an alias of the $\sim$ 37 d period (Böhm-Vitense 2007; Oláh et al. 2009). 14 Her shows a periodicity of 22.38 d. In this case the spectral window is complex and we cannot rule out that this period is fake. Wright et al. (2004) estimated a rotational period of 48 days from the $\log R'_{HK}$ mean value, but this was not detected by Simpson et al. (2010).

All the H_α time series are presented in Table 5, only available in electronic form at the CDS.

Star		$\Delta H\alpha$	Rotation [d]	Cycle [d]	Amplitude	FAP [%]
HD 186858	A	0.077	7.68	–	0.010	1.0
	B	0.062	–	2030	0.014	0.3
HD 200466	A	0.038	–	1500	0.024	< 0.1
	B	0.034	–	trend	> 0.015	< 0.1
BD+182366	A	0.039	–	1432	0.037	0.1
	B	0.029	–	–	–	
HD 139569	A	0.057	–	trend	¿ 0.21	2.2
	B	0.062	–	trend	> 0.30	0.6
HD 76037	A	-0.002	–	trend	> 0.014	1.0
	B	0.014	–	trend	> 0.022	1.3
HD 201936	A	0.059	13.70	–	0.020	0.7
	B	0.087	–	–		
HD 213013	A	0.031	–	–	–	
	B	0.035	3.59	–	0.019	2.1
14 Her		0.009	22.38	–	0.002	< 0.1
51 Peg		0.003	86.49	2069	0.001, 0.003	0.8, 0.6
61 Cyg B		-0.001	16.44	–	0.011	< 0.1
GJ 380		0.013	–	trend	> 0.017	< 0.1
τ Ceti		-0.006	–	trend	> 0.003	< 0.1

Table 6.3: Stars with cycles. In the second column we indicate the component, Col. 3 reports the $\Delta H\alpha$ for the stars, Col. 4 is the short period, compatible with the rotation in our analysis (where available), Col. 5 reports the period or long-term activity cycle. Column 6 shows the amplitude of the H_α variation. The last column indicates the false-alarm probability related to the identified periods.

Star	ρ_s	σ	n_σ
HD 200466A	0.556	0.000	-4.817
HD 76037A	-0.665	0.000	3.702
HD 99121A	0.6511	0.002	-2.84
HD 213013A	0.478	0.008	-2.576
GJ 380	0.535	0.018	-2.270

Table 6.4: Rank of the Spearman correlation coefficient ρ_s and its significance between H_α and RV for the stars of the sample. Column 3 reports its false-alarm probability and the last column reports the n_σ value. Only stars with significance < 0.02 are indicated.

6.6 Correlation between RV and H_α

The high uncertainty on the single measurements of H_α prevent us from properly studying the correlation with the RVs. However this was possible in some particular cases, such as spectra with high S/N or stars with a relevant trend in H_α. We used the Spearman correlation coefficient ρ_S and its significance σ to quantify the correlation between RV and H_α index (Table 6.4): we obtained an extremely high significance for HD 200466A (Carolo et al. 2014, see). For four other objects, the probability that the correlation is the result of a random effect is lower than 0.0075. HD 201936A and HD 213013A are active stars with a signature of an activity cycle, GJ 380 spectra have a high S/N and show a probable long-term cycle. Plots are presented in the Appendix. In HD 76037A the anti-correlation simply shows that both RV and activity are time-dependent on long scales. We can therefore rule out a strong physical connection between these two quantities for this star.

6.7 Conclusions

The activity of 104 stars observed with the SARG spectrograph was studied using an index based on the H_α line. We found that this index, $\Delta H\alpha$, correlates well with the index based on Ca II lines, $\log R'_{HK}$, and therefore it can be used to estimate the average activity level, confirming previous results. It also correlates with the rotation of the star: low activity corresponds to slow rotation, especially for cool stars. After removing a few targets for which contamination of the spectra by their companion is the dominant source of RV scatter, we found that $\Delta H\alpha$ also correlates with the scatter in RV. We obtain that a low-mass companion might be the source of a high residual RV scatter at least for HD 76073B. We also found a strong correlation between the average activity level $\langle H_\alpha \rangle$ of the two components in each binary system and that roughly a half of our systems are active. Finally, we showed that activity as measured by $\Delta H\alpha$ is correlated with the age derived from isochrone fitting. Although these have large error bars due to uncertainties in temperature and parallaxes, we found that active stars are typically younger than 1.5 Gyr, while older stars are typically inactive.

We then analysed the time series of the stars: 11 stars ($\sim$ 8.5 %) of the SARG sample show a periodicity in $H_\alpha$with false-alarm probability $< 0.5\%$. All these stars have a moderate activity level ($0.029 < \Delta H\alpha < 0.077$) except for the pair HD 76037A and B, but in these cases we only have a hint of a long-term period or magnetic cycle. When we focused on the long-term cycle, we obtained that the temperature interval of these stars is also limited to late-G and early-K stars. Other stars show variabilities on temporal scales certainly different from the rotational periods. In the bright stars sample, we found five stars out of ten with significant periodic variations in H_α. In some cases the physical origin of this type of signal is unclear.

Only five stars show a significant correlation between H_α and RVs timeseries.

We conclude that if care is exerted, H_α is a useful indicator for activity and can be a good alternative to Ca II $\log R'_{HK}$ for studies based on radial velocity techniques, especially for solar-type stars.

Stars with RV-H_α correlation

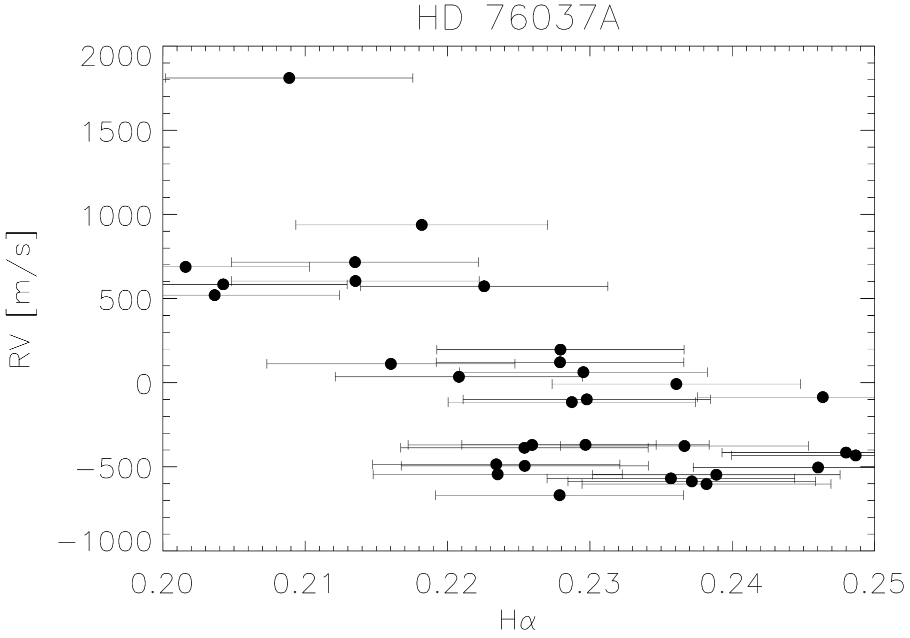

Figure 6.11: RV as a function of the H_α index for HD 76037A.

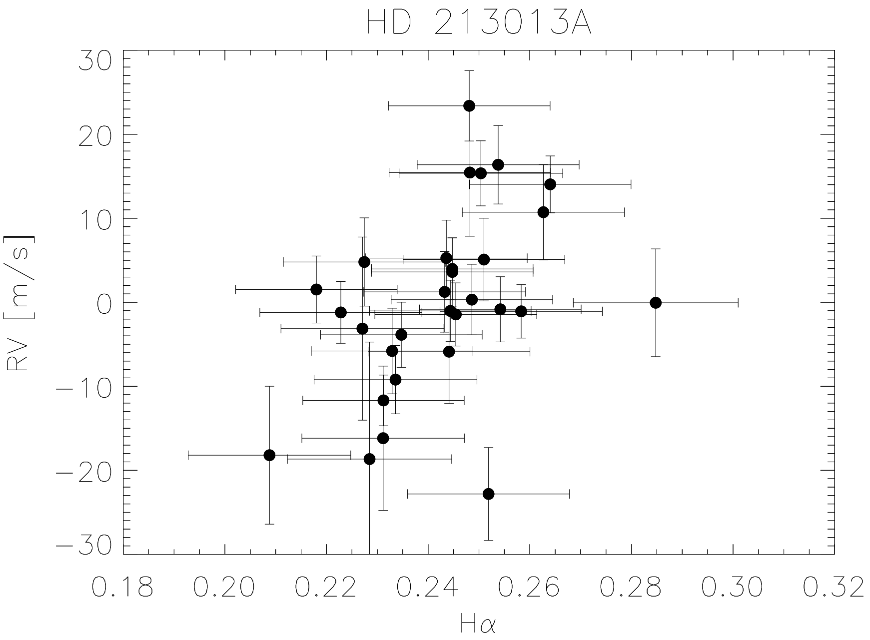

Figure 6.12: RV as a function of the H_α index for HD 213013A.

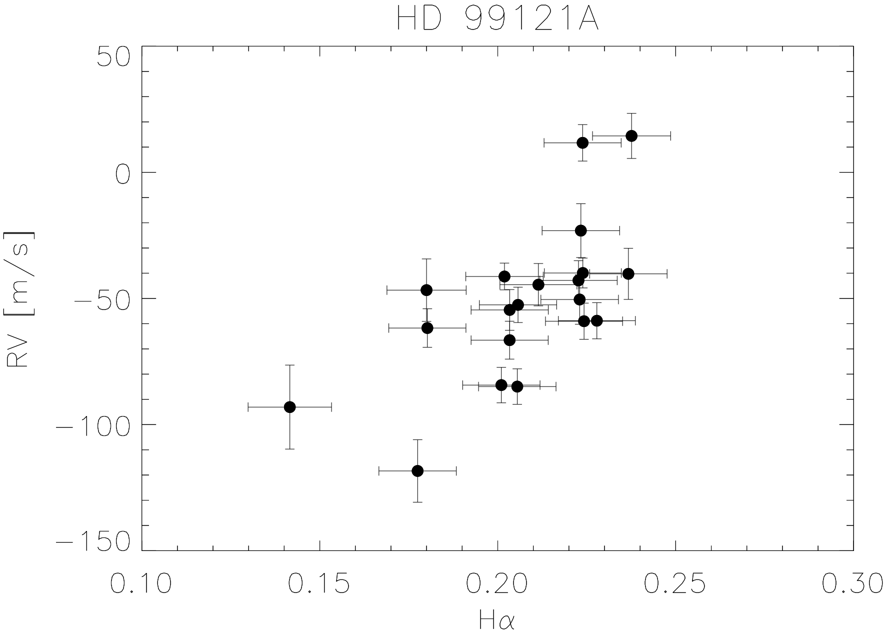

Figure 6.13: Decontaminated RV as a function of the H_α index for HD 99121A.

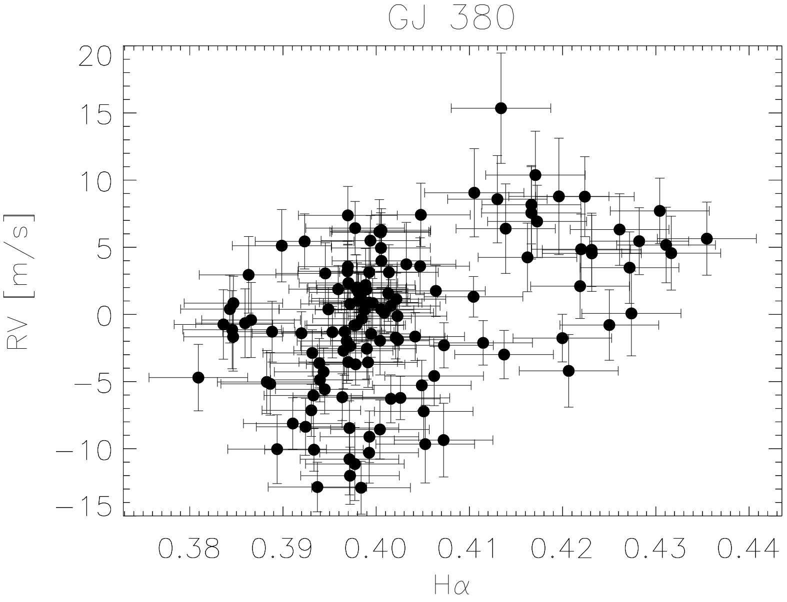

Figure 6.14: RV as a function of the H_α index for GJ 380.

Chapter 7

Conclusions

In the last decades the research of extrasolar planets underwent a steep increase of interest and different methods of detection were developed. Each of them has its own merit and lack in studying the extrasolar system architecture and the characteristics of extrasolar planets. Stars and their planetary entourage form and grow together, at least in most cases, tied by the circumstellar disk. A unique theory that can describe all the processes that happen between the protostellar cloud collapse and the final system stabilization is not available at the moment. Indirect methods are very useful to study more evolved systems, where the protoplanetary disk contribution is negligible, in their innermost regions. On the other hand, direct imaging with high-contrast instruments offers the possibility to study the early phases of the planet formation, that are not accessible to other indirect methods of planets detection, and plays a key role in current planet formation theories. In this thesis I show the capabilities of direct imaging with SPHERE, the new high-contrast imager of VLT, in detecting planets at different stages of their evolution, coupled with radial velocities observations of old systems obtained from SARG, the old TNG echelle spectrograph.

In Chapter 3 I present the case of four young objects. I exploit the ZIMPOL imaging capabilities to study Z CMa, a binary system composed of a Herbig Be and a FU Ori star, both showing two jets that extend for hundreds of AU. In particular, the H_α and O[I] narrow band filters allow to detect the wiggle of the FU Ori jet that can be induced by an unseen stellar companion with mass between 0.48 and 1 $M_\odot$, orbiting in ~ 4.2 yr. HD 100546 and T Cha are, instead, stars that host a transitional disk. I observed these two systems with IRDIS and IFS, looking for the presence of planets, and I can exclude that all the object detected in their surroundings are bound. At the same time, I was able to study the circumplanetary disk in a quite wide spectral range. The disk of the Herbig Be HD 100546 shows a complexity of structures that cannot be represented by simple, symmetric, models. In Section 3.2 I show that the system brightest structures suggest the presence of at least three gaps in the inner (< 100 AU) regions of the disk, coupled with other structures, such as spiral arms. The study of the disk spectrum and the detection of a diffuse source at the location of the claimed planet HD 100546 b (Quanz et al. 2015; Currie et al. 2015), allow me to put more stringent upper limits to the near-IR magnitude of the planet. Even if the probability that this cloud is connected to the presence of the planet, that is not visible in SPHERE images but is visible at longer wavelength (such as L and M), is very high, the nature of this diffuse emission is, however, still unknown. The T Cha disk (see Section 3.3) is simpler, but SPHERE images does not show any photometric evidence of embedded companions. Moreover, I couldn't contribute to the discussion on the close companion observed with sparse aperture masking (because it should lie behind SPHERE conoragraph), but I improved the detection limit of other possible planets. Finally, LkCa 15 was studied both in the visible and in the near-IR. The claimed companions (Sallum et al. 2015a) were not detected, but I improved the mass limit for additional companions to $2M_J$ at separation larger than $0.2''$.

In Chapter 4 I describe the study of the accretion signature in a few objects. Unfortunately only two of them could be observed in the SHINE GTO till now, but with not good conditions, so that I'll focused on GQ Lup b. The accretion was studied with a variety of instruments over more then 10 yr, that lead to detection of a high variability on the accretion rate. I observed this system both in H_α and in Pa_β, exploiting all three SPHERE subsystems. I conclude that to study the variability of this object, an homogeneous monitoring is needed and that IRDIS long slit spectroscopy observing Pa_β is the best set-up offered by SPHERE for this study.

Two systems that have already cleaned out their surroundings from gas and dust are presented in Chapter 5: HIP 80591 and HD 65426. I apply the typical SHINE analysis devoted to the identification and characterization of candidate companions around them: a total of 38 candidate companions are identified around the two stars, all of them are found out to be background objects. In the case of one candidate companion of HIP 80591 for which the SPHERE photometric informations are not conclusive, I use the HST data to test the proper motion and confirm the object is not bound. HD 65426 shows four candidate companions: three of them are found out to be background star, while for the closest I first found out that this object has high probability to be bound to the star due to its position and it spectral features, and these findings were later confirmed by a deeper analysis and follow up observations that demonstrate HD 65426 b is a warm Jupiter-like planet with mass between 6 and 12 M_J.

Finally, in Chapter 6, I study the chromospheric activity in a sample of older binary stars in order to detect a radial velocity signal hidden by the Doppler shift induced by the activity. I found out that $\Delta H\alpha$, an index based on the H_α line, is a good indicator of the star activity when the $\log R'_{HK}$ index is not available and can be used also to infer stellar ages in case of stars younger then 1.5 Gyr. This index also correlated with the scatter in radial velocities: HD 76073 B shows a high radial velocities scatter that can be explained by a low-mass companion (Sissa et al. 2016).

SPHERE scientific goal is to study the outer part of planetary system in reflected and scattered light. The instrument had the first light in Spring 2014 and therefore part of my work was devoted to study technical details of this new instrument, to improve instrument capabilities and data reduction, and to better defining the instrument set-ups needed to achieve different scientific aims. Part of these activities are presented in the Appendixes.

In Appendix A I describe different methods that I investigate to proper align the two ZIMPOL cameras when observing in classical imaging and I show that this step is very crucial in performing spectral differential imaging, especially when observing in narrow band filters. I also show that the DRH pipeline v 0.15.0, cannot properly reduce data because introduces a flux magnification. A few of my findings are now implemented in the ZIMPOL internal pipeline (A. Bazzon priv. comm.), together with some recipes useful for the planet analysis such as the contrast curves estimation and fake planets injection. I also contribute to the characterization of the ZIMPOL off-axis field observation mode, that is not yet offered by ESO, studying how the image is distorted in one of them.

The effects of angular differential imaging on extended sourced are described in Appendix B.

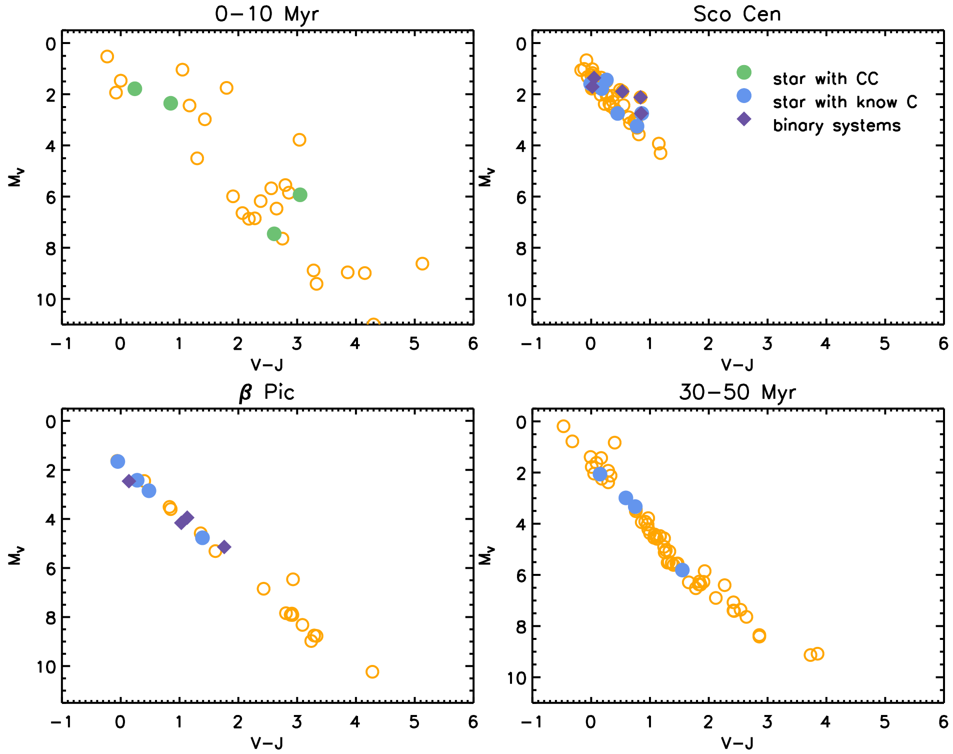

Figure 7.1: SHINE observed targets color magnitude diagram in four age bins. Stars with candidate companions are in green, blue dots represent stars with detected companions while purple diamonds identify the binary systems.

This work was needed in the study of the HD100546 disk and shows how the PCA algorithm used does not create new features but enhances the contrast between different areas and tends to cancel out homogeneous structures, especially in the azimuthal direction. In the case of a spatially resolved circumplanetary disk, I show that ADI can destroy its signal that can be, however, retrieved by applying a spatial filter, like the smoothing. Finally I show that classical imaging and polarimetric observations can be directly compared if a simulated angular differential imaging is applied to the polarimetric data.

Missing detection of the planets orbiting HD 100546

As described in Section 3.2, the confirmation of the presence of the planet HD 100546b, observed with NACO inside the circumplanetary disk, was not possible with SPHERE (Sissa & the SPHERE consortium in prep.) or GPI (Rameau et al. 2017); the same is for the claimed HD 100546c. This is a very intriguing results because the shape of the disk can be well described by the gravitational perturbation induced by one (or more) planet (see e.g. Dong et al. 2016). However, this is not the unique example in which planets detected in L or M band embedded in the circumstellar material are not visible with SPHERE (see e.g. Ligi et al. submitted). Motivated by this finding, I tried to infer the general planet distribution among the SHINE targets. In Fig. 7.1 I show the color magnitude diagrams for four different subsamples: stars younger than 10 Myr, the Sco Cen group ($\sim$ 15 Myr), the members of β Pictoris moving group ($20-26$ Myr Mamajek & Bell 2014) and the targets with ages between 30 and 50 Myr. β Pic is the system with the age-distance combination that maximize the possibility to detect planetary companion, or, in other words, that permits the smallest upper limits to the companions mass. Therefore, among these four subsamples, it is the less biased against44 planets research via direct imaging. At this time, 21 objects of this association have been observed with SPHERE, and 4 sub-stellar companions were clearly re-identified: PZ Tel b (Maire et al. 2016a), β Pic b (Lagrange et. al in prep, Cudel et al in prep.), and 51 Eri b (Samland et al. 2017), ηTel b (Ginski & the SPHERE consortium in prep.). All these companions orbit relatively massive stars ($1.1 M_{\odot}$), while no companions were found around smaller mass stars. This is not in agreement with the general exoplanets distribution that shows that only $\sim$ 22% of the detected exoplanets are found around stars more massive than $1.1 M_{\odot}$ (`exoplanet.eu` encyclopaedia). A more quantitative dissertation on the planet statistics is beyond the scope of my Ph.D. work, but this first result suggests that the presence of sub-stellar companion orbiting high mass star at large separation is quite high ($\sim$ 20%), while few if any detectable companions are expected around sub solar mass stars.

Among the Sco Cen association, only 100 objects are included in the SHINE survey. After observing 50 targets, SHINE observations found 6 companions: HD 95086 b (Chauvin & the SPHERE consortium in prep.), HD 106906 b (Lagrange et al. 2016), HIP 64892 b (Cheetham et al. in prep), HIP 74865, HIP 78530 and the new discovered HIP 65426 b (Chauvin et al. 2017). These leads to a companion frequency of 12%, lower than the one observed in β Pictoris group for a comparable mass range. However, since Sco Cen is almost four times more distant than β Pic ($100-150$ pc for Sco Cen versus 35 pc for β Pic), in Sco Cen SPHERE can only detect companions more luminous and/or at larger separation than those observed in the β Pic moving group: neither β Pic b nor 51 Eri b would be detectable if located at the Sco Cen distance. On the whole, the results of Sco Cen seems to be in agreement with what we found in βPic: massive stars have a higher probability to host planets, and are therefore the best targets for planets search.

Even in older systems, such as those with age between 30 and 50 Myr, the detected companions orbit massive stars: HD 1160 b (Maire et al. 2016a), HD 30447 b (Boccaletti & the SPHERE consortium in prep.), AB Pic b, HIP 114189 b.

We would therefore expect that also in the subsample of young stars a considerable number of sub-stellar companions will orbit massive stars. Moreover, due their young age, these objects are expected to be more luminous than those in β Pic, and therefore they will be more easily detected. Instead, we found no companions around the observed massive stars, and only dubious detections.

HD 100546 system belongs to the Sco Cen association and shows Y-J color of 0.26 with $M_V = 1.50$, that located the star in the region of Fig 7.1 where the frequency of planets is higher. This is another point in favour of the presence of unseen companion around the star, and appears as an instructive example of the difficulty in the detection of planets in transitional or gas-rich disks. It is clear that, the presence of these kinds of disks influences the possibility of detection, because they can absorb the planet light, but it is reasonable that this effect depends on the inclination and on the flaring of the disk, so that it is not valid for face-on disks. In these latter, the companions should be visible in the disk gap, and their light will be distinguishable from the circumstellar material. However, it was not the case for the systems observed with SPHERE and GPI till now.

I can conclude that the planets are likely in the disk but our capabilities are far from observing them directly in the near infrared wavelength if the circumstellar disk is not already dissipated enough. It is possible, instead, to observe the deformations induced on circumstellar disks by the presence of planets, even if those structures can also have a different origin. The transitional disk phase appear to be once again the most interesting phase for detecting planet and test the formation theories.

Future perspective

Since the evolution of planets and planetary systems mainly occur during their infancy, the most crucial observations concern transitional disks that can harbour still forming planets, very young planets and brown dwarfs. Fruitful future studies can be oriented to these very young objects through two different approaches: a deeper research for detection of accreting signatures and a wider multi-wavelength analysis.

The study of very young substellar companions still embedded within the disk may widely profit from a comparison of observation obtained over a wide wavelength range. Combining near infrared observations with those at longer (e.g. ALMA, NACO) and shorter (ZIMPOL) wavelengths we can study the disks from their deepest (dusty) region to their surface. The higher spatial resolution of the IR could resolve point sources from their accreting disk, possibly leading to the estimation of the mass of the sub stellar object if the dust cloud that surround it fills its Roche lobe. An additional powerful capability of IFS is to characterize disk spectra: applying this technique to different objects in the SHINE survey, it reveals a different spectral shape between different objects but also in different structures of the same object and could be used to constraint the disk properties. This approach can also help to disentangle disk-like feature from forming/embedded objects. For older system, where the objects have already cleared out from dust their surroundings, it is expected that the material still accreting might be detectable through H emission lines. At the corresponding wavelength (in particular, at that of Hα, at 656 nm), the contrast between the star and the planet may be substantially reduced, possibly leading to planet detection in spite of the strong background due to the halo of the stellar image. Confirming this expectation, Hα emission has been actually observed in a few cases, such as that of the companion of GQ Lup, GSC 6214-210 and DH Tau (Zhou et al. 2014). A few promising targets to show accretion signatures (Brown dwarfs and planets) were selected among the SPHERE GTO program, that could be studied both with ZIMPOL to be used for Hα, and with the infrared channel to be used for Paschen β (at 1282 nm) exploiting IFS or IRDIS in the Long Slit Spectroscopy mode.

These approaches can bring to the detection of a few (new) accreting small mass companions (down to planetary mass) in Hα and possibly Paschen β and nearby continuum bands. Their spectral energy distribution will be studied, with the ultimate goal of determining surface temperature, radius and (through use of evolutionary models) mass, to have a first quantification of the accretion rates, to study the accreting objects with respect to the geometry of the disk, and outline most relevant aspects of disk-planet interaction. A dedicated long term study can provide early informations on the photometric variability of the objects in order to design a more extensive follow-up campaign.

A useful instrument to this purpose is also SHARK-NIR, a system for coronagraphic imaging in the infra-red that was approved for construction (June 2017) and it is planned to be on sky in fall 2018. LBT will be the only one telescope that will allow simultaneous observation from R through H band ($\sim$ 0.5-1.7 μm) to L band (3.4μm), exploiting the parallel use of SHARK-VIS, SHARK-NIR and LMIRCam. This facility could be extremely powerful for characterization of young objects and their environment, covering the accretion signal (Hα and Paschen β), the dust scattering (H band) and the thermal emission of these sources (L band).

Appendix A

ZIMPOL H_α data reduction and early science

ZIMPOL has two camera arms, hereafter cam1 and cam2, and data are always taken simultaneously in both arms, each equipped with an own filter wheel (FW1 and FW2). This allows to take data in two different filters simultaneously for SDI. One can also use two equal filters in the two arms or use for both detectors the same filter located in wheel FW0 in the preceding common path. Available filters are listed in Table A.1 The pixel scale of ZIMPOL is 3.601 ± 0.005 mas/pix according to a preliminary astrometric calibration (Ginski & the SPHERE consortium in prep.), and the position angle of the vertical frame axis is rotated by $-2.0 \pm 0.5°$ with respect to North for both cameras. Finally, the field of view of the 1kx1k detectors is $3.6'' \times 3.6''$. Offset observations mode is implemented, but observations are only possible within $4''$ from a bright star ($m_R \lesssim 10$ mag), which is used as source for the visible (500-900 nm) AO wave front sensor. However, during the commissioning phase when the following analysis was performed, the preliminary values available at that time were slightly different: the pixel scale used was 3.63 ± 0.04 mas/pixel for both the camera. The SPHERE anamorphism, which is at the level of 1%, was not considered, while the position angle was properly estimated. This has only a small impact on the scientific data discussed in this thesis and then the original analysis is presented here.
ZIMPOL can also image an off-axis field, therefore is a good instrument for fain objects located at separations of a few arcseconds from the central star. The dithering, that moves the image by several pixels on the detector so that effects of individual pixels can be averaged-out or corrected, and off-axis fields mode permit to reach a field of view of 8” in diameter. We can therefore image a field without the central source: it allows deep observations of faint sources avoiding the saturation effects introduced by the bright central star.

My work focused on matching the two cameras images, trying to quantify the quality and the differences between the cameras, and finding how to combine images taken with different filters. The procedures I developed were later partially implemented in the ZIMPOL DRH.
In this Chapter I start with the deep analysis made on the R Aqr dataset that was aimed to align the two ZIMPOL cameras images, combine images taken with different filters and compare them. Moreover I tested the astrometry of one of the ZIMPOL off-axis fields. Images of GQ Lup were used to improve PSF subtraction techniques and develop ADI routines. Due to the quasi-simultaneous observations of GQ Lup with the SPHERE near-IR channel, it

FW0	FW1	FW2
OPEN	OPEN	OPEN
P_VIS	VBB	VBB
PQ_VIS	I_PRIM	I_PRIM
Q_VIS	R_PRIM	R_PRIM
ND_1.0	N_I	N_I
ND_2.0	N_R	N_R
ND_4.0	B_Ha	B_Ha
Ha_NB	CntHa	CntHa
OI_630	V	V
HeI	Cnt820	Cnt820
V_S	TiO_717	N_Ha
V_L	CH4_727	Cnt748
730_NB	KI	PUPIM
I_L		

Table A.1: Filter disposition in the common filter wheel(FW0) and in the two ZIMPOL arms filter wheels (FW1 and FW2).

was also used to test ZIMPOL photometry. A further development of both astrometric and photometric capabilities of ZIMPOL came with the analysis of data for CT Cha: another off-axis field was used to test the astrometry, the fake planets injections and the contrast limit estimation.

In the case of R Aqr I could study the southern part of the jet: the S/N values in the brightest structure of the off-axis image is ~ 4.0, twice the value obtained for the on axis field.

A.1 Cameras alignment

A.1.1 R Aqr: a ZIMPOL test target

During the Commissioning phase of SPHERE, the symbiotic binary R Aqr was observed as demonstration target for the ZIMPOL visual subsystem, as an on-sky test of line filter observations and imaging polarimetry. The data were mainly taken to test and evaluate the different observing modes of ZIMPOL which include:

- Demonstration and tests of the polarimetry using the scattered light from the circumstellar dust;
- Demonstration and test of the imaging mode, in particular the H_α imaging using the HI emission from the jet;
- Demonstration of the spatial resolution by resolving the binary and perhaps even the atmosphere of the red giant;
- Demonstration of the faint and bright flux capabilities by observing in the visual, where the system is relatively faint ($\sim$8 mag) and IN the I-band where it is very bright (2 mag) or so;

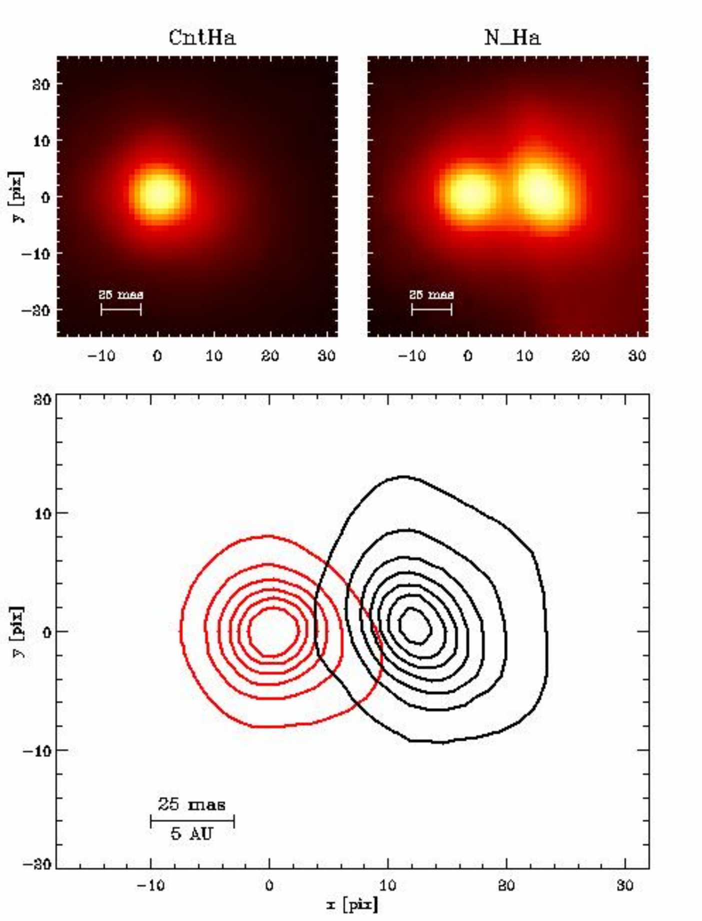

Figure A.1: R Aqr central binary as seen in the CntHa (top left) and N_Ha (top right) filters on Oct. 11, 2014. The contour plot shows the red giant for the CntHa filter(red) and the 'pure' H_α emission in the N_Ha image after subtraction of the scaled and aligned CntHa frame (black). Contour levels are given for 1000, 2000, .., 7000 ct/pix.

- Demonstrate the use of different broad band (150nm) and narrow band filters (1nm), coronagraphs, and detector modes.

This source is a symbiotic binary composed by a Mira and an accreting hot companion. This last has a jet ionizing an extended hourglass nebula. The distance of 220 pc makes R Aqr one of the nearest and most extensively studied systems since the first reports about the appearance of a “brilliant emission jet or spike” in 1980 (Wallerstein & Greenstein 1980; Herbig 1980). The structure and motion of he jet outflow features was studied with long slit spectroscopy (Solf & Ulrich 1985), radio interferometry (e.g. Hollis et al. 1985; Kafatos et al. 1989; Dougherty et al. 1995), HST imaging (Paresce & Hack 1994; Hollis et al. 1997), and Chandra X-ray observations (Kellogg et al. 2001), while the photosphere of the Mira variable and its immediate surroundings were investigated with maser line radio interferometry (e.g Hollis et al. 2001; Cotton et al. 2004; Ragland et al. 2008; Kamohara et al. 2010) and IR interferometry (Ragland et al. 2008; Zhao-Geisler et al. 2012).

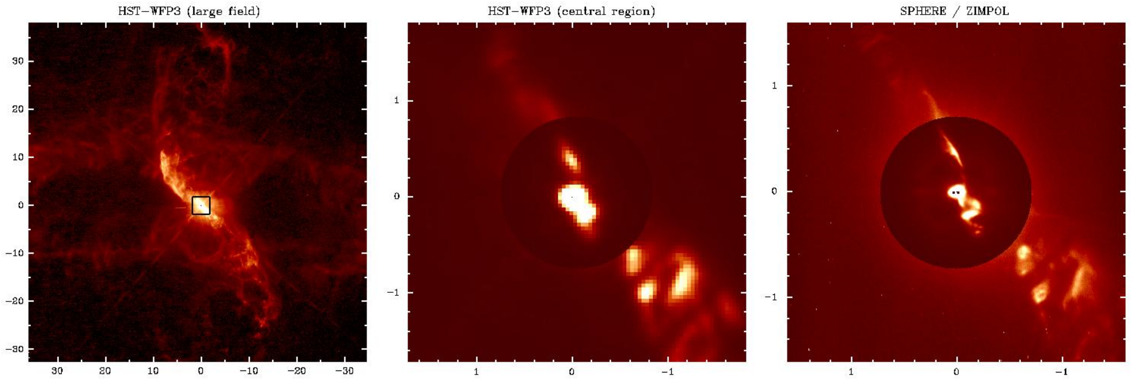

Figure A.2: $H_\alpha$images of R Aqr from HST-WFC3 and VLT-SPHERE-ZIMPOL taken quasi-simultanously in October 2014. Left: a 70″ ×70″ cutout of the WFC3 image of the strongly structured extended nebula. Middle: 3.5″ ×3.5″ region of the WFC3 image of the central star indicated with the square in the left. Right: central 3.2″ ×3.2″ area imaged with higher spatial resolution using SPHERE-ZIMPOL where also the two stars are marked with black dots.

For the first time, SPHERE-ZIMPOL images taken in the H_α filters resolve unambiguously the jet source and the Mira variable in the R Aqr binary (Fig. A.1) and with high astrometric precision (Schmid et al. 2017). They also allow a quantitative analysis of the H_α emission line clouds, and new insights on the structure and the physics of the jet outflow. The unique coincidence of quasi-simultaneous HST data provides an ideal opportunity for assessing and checking the quality of the Consortium measuring procedure and instrument calibrations (Fig. A.2). A very important aspect of the R Aqr jet is the proximity of this system allowing us to resolve jet cloud structures on scales of ∼5 AU and measure positions with a relative precision of ∼1 AU. I detected a large diversity of cloud structures, like pointlike unresolved clouds, elliptical and bubble-like features, short straight (transverse) and long waving (radial) filaments. In addition the jet clouds are very bright in H_α and it was possible to see a large range of bright and faint clouds in the outflow. All these features are expected to move, and evolve in brightness and shape within a few years.

Since R Aqr was used as on-sky test, the observations were made with several different setups during three different nights, in June (Comm2), August (Comm3) and October (Comm4) 2014.

The first two datasets, taken in Comm2, are H_α pupil stabilized standard imaging, with coronagraph and fast polarimetry in R and I bands. These suffer of many problems mainly due to the presence of the coronagraph, that hides the most important part of this source, and the short exposure time that was adopted in order to test this imaging mode. It was found that it is better to avoid low illumination of a large region and risk saturation of a small region: it is easy to get an additional short illumination for the small bright region, if needed. During Comm3, a different combination of filter, including H_α, Oxygen and Helium filters, were used to observe the source in direct imaging followed by an attempt of get Slow polarimetry in H_α filters (see Table A.2). It was found that the star position changes by several pixels if filters are exchanged in the filter wheels FW1 and FW2 in the individual arms whereas the star position seem to change by less than 1 pixel within two observations

Frame id	DIT	NDIT	mode	coronograph	FW0	FW1	FW2
OBS224_0092	100.	3	I	CLEAR1	OPEN	CntHa	B_Ha
OBS224_0093	100.	3	I	CLEAR1	OPEN	B_Ha	CntHa
OBS224_0094	100.	3	I	CLEAR1	OPEN	CntHa	N_Ha
OBS224_0095			IM		V_S	OPEN	OPEN
OBS224_0096			IM		OI_630	OPEN	OPEN
OBS224_0097			IM		HeI	OPEN	OPEN
OBS224_0098			SP		P2	Cnt_Ha	B_Ha

Table A.2: Comm3 R Aqr observations. DIT,in seconds, NDIT, observation mode, coronagraph and filter used are reported.

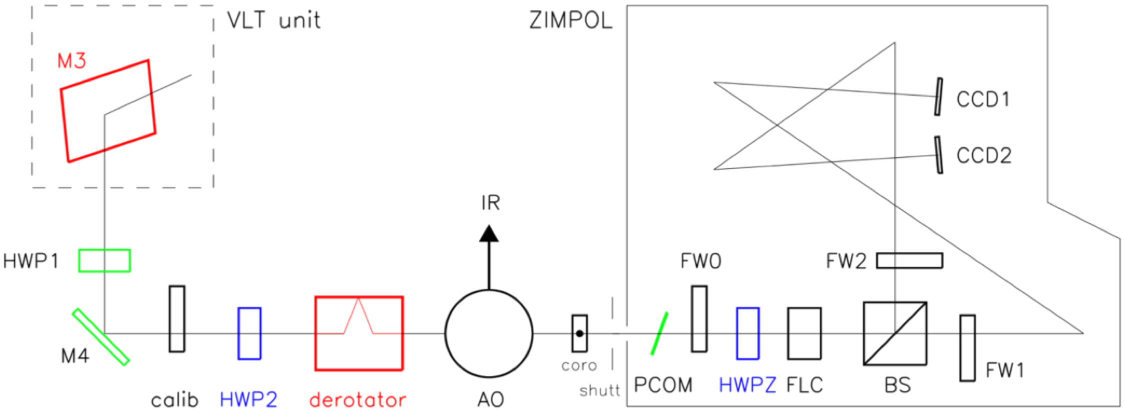

Figure A.3: ZIMPOL optical path

with the same filter combination. Moreover, the relative positions between Cam1 and Cam2 are very stable, and differ less by 1 pixel. The last and longest R Aqr dataset includes pupil stabilized narrow band H_α imaging, off-axis field observations, fast polarimetry imaging in V, I band and in narrow band, and slow polarimetry (see Table A.3). My work here concerns mainly the alignment of the images obtained with the two cameras, and their combination.

A.1.2 Align cam1 and cam2

ZIMPOL images OBS284_0030-34.fits were taken with the common narrow band H_α filter (Table A.3). In this case, after the beam splitter, both the two optical path pass through the empty position of the filter wheel and bounce twice on a folding mirror (Fig. A.3). This entails a different orientation of the images on the two cameras: in order to obtain images oriented with (approximately) North up and East left, the image in cam1 is flipped up-down, whereas the image of cam2 needs to be rotated of 180°. In order to increase the accuracy of the flat field correction, a dithering was introduced exploiting the folder mirrors, as described in Table A.4. I used this dataset to explore different methods to align the two cameras.
The images used for this star were reduced with SPHERE DRH version 13.6. Since only half of the rows (only even) are read out, the image must be modified to make its scale symmetric in both field directions. One ZIMPOL CCD has 2k×4k pixels (hardware pixels of 15×15 μm

Frame id	DIT	NDIT	mode	coronograph	FW0	FW1	FW2
OBS284_0030	40.	1	I	CLEAR1	Ha_NB	OPEN	OPEN
OBS284_0031	40.	1	I	CLEAR1	Ha_NB	OPEN	OPEN
OBS284_0032	40.	1	I	CLEAR1	Ha_NB	OPEN	OPEN
OBS284_0033	40.	1	I	CLEAR1	Ha_NB	OPEN	OPEN
OBS284_0034	40.	1	I	CLEAR1	Ha_NB	OPEN	OPEN
OBS284_0035	200.	1	I	CLEAR1	Ha_NB	OPEN	OPEN
OBS284_0036	200.	1	I	CLEAR1	Ha_NB	OPEN	OPEN
OBS284_0037	200.	1	I	CLEAR1	Ha_NB	OPEN	OPEN
OBS284_0038	200.	1	I	CLEAR1	Ha_NB	OPEN	OPEN
OBS284_0039	1.2	10	P2	CLEAR1	OPEN	V	V
OBS284_0040	1.2	10	P2	CLEAR1	OPEN	V	V
OBS284_0041	1.2	10	P2	CLEAR1	OPEN	V	V
OBS284_0042	1.2	10	P2	CLEAR1	OPEN	V	V
OBS284_0043	1.2	10	P2	CLEAR1	OPEN	TiO_717	Cnt748
OBS284_0044	1.2	10	P2	CLEAR1	OPEN	TiO_717	Cnt748
OBS284_0045	1.2	10	P2	CLEAR1	OPEN	TiO_717	Cnt748
OBS284_0046	1.2	10	P2	CLEAR1	OPEN	TiO_717	Cnt748
OBS284_0047	1.2	10	P2	CLEAR1	OPEN	Cnt820	Cnt820
OBS284_0048	1.2	10	P2	CLEAR1	OPEN	Cnt820	Cnt820
OBS284_0049	1.2	10	P2	CLEAR1	OPEN	Cnt820	Cnt820
OBS284_0050	1.2	10	P2	CLEAR1	OPEN	Cnt820	Cnt820
OBS284_0051	50.	2	P2	CLEAR1	OPEN	CntHa	N_Ha
OBS284_0052	50.	2	P2	CLEAR1	OPEN	CntHa	N_Ha
OBS284_0053	50.	2	P2	CLEAR1	OPEN	CntHa	N_Ha
OBS284_0054	50.	2	P2	CLEAR1	OPEN	CntHa	N_Ha
OBS284_0055	10.	4	P2	CLEAR1	OPEN	V	V
OBS284_0056	10.	4	P2	CLEAR1	OPEN	V	V
OBS284_0057	10.	4	P2	CLEAR1	OPEN	V	V
OBS284_0058	10.	4	P2	CLEAR1	OPEN	V	V
OBS284_0059	1.2	10	P2	CLEAR1	OPEN	I_PRIM	I_PRIM
OBS284_0060	1.2	10	P2	CLEAR1	OPEN	I_PRIM	I_PRIM
OBS284_0061	1.2	10	P2	CLEAR1	OPEN	I_PRIM	I_PRIM
OBS284_0062	1.2	10	P2	CLEAR1	OPEN	I_PRIM	I_PRIM
OBS284_0063	5.	6	P2	CLC3	OPEN	I_PRIM	I_PRIM
OBS284_0064	5.	6	P2	CLC3	OPEN	I_PRIM	I_PRIM
OBS284_0065	5.	6	P2	CLC3	OPEN	I_PRIM	I_PRIM
OBS284_0066	5.	6	P2	CLC3	OPEN	I_PRIM	I_PRIM
OBS284_0067	5.	6	P2	CLC3	OPEN	I_PRIM	I_PRIM
OBS284_0068	5.	6	P2	CLC3	OPEN	I_PRIM	I_PRIM
OBS284_0069	5.	6	P2	CLC3	OPEN	I_PRIM	I_PRIM
OBS284_0070	5.	6	P2	CLC3	OPEN	I_PRIM	I_PRIM
OBS284_0071	10.	20	P2	CLC3	OPEN	I_PRIM	I_PRIM
OBS284_0072	10.	20	P2	CLC3	OPEN	I_PRIM	I_PRIM
OBS284_0073	10.	20	P2	CLC3	OPEN	I_PRIM	I_PRIM
OBS284_0074	10.	20	P2	CLC3	OPEN	I_PRIM	I_PRIM

Table A.3: Comm4 R Aqr observations. DIT,in seconds, NDIT, observation mode, coronagraph and filter used are reported.

Image	Δx	Δy
OBS284_0030	0	0
OBS284_0031	+14	+14
OBS284_0032	+14	-14
OBS284_0033	-14	+14
OBS284_0034	-14	-14

Table A.4: Dithering shift in pixels used for the R Aqr considered dataset.

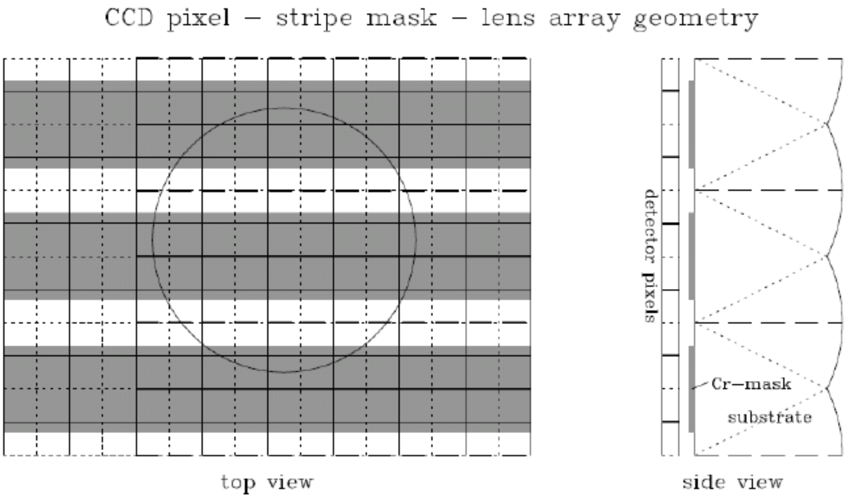

Figure A.4: Schematic illustration of the CCD pixel geometry with respect to the stripe mask / micro-lens assembly seen from the top (left) and as a side cut along a pixel column perpendicular to the cylindrical lens array (right). The physical 15 × 15 μm pixels are given with dotted lines and the 2 × 2 binned pixels by full lines on the very left. Also shown are the location of the focus line (thick dashed line) and the aperture of the cylindrical micro-lenses (full lines). The shaded areas illustrate the stripe mask. The round circle represents the PSF diameter $\lambda/D = 15$ mas (or about 120 μm on the detector) at $\lambda = 600$ nm. The substrate of the micro-lens has a thickness of 500 μm and is not drawn to scale.

ID	Output name of DRH v.13.6
P1	SPHERE_ZIMPOL_OBS♯♯♯_preproc_cam1.fits.fits
P2	SPHERE_ZIMPOL_OBS♯♯♯_preproc_cam2.fits.fits
OS1	SPHERE_ZIMPOL_OBS♯♯♯_preproc_cam1.fits_overscan_subtracted.fits
OS2	SPHERE_ZIMPOL_OBS♯♯♯_preproc_cam2.fits_overscan_subtracted.fits
FS1	zpl_science_imaging_cam1.fits_SPHERE_ZIMPOL_OBS♯♯♯_preproc_cam1.fits.fits
FS2	zpl_science_imaging_cam2.fits_SPHERE_ZIMPOL_OBS♯♯♯_preproc_cam2.fits.fits
FA1	zpl_science_imaging_cam1.fits
FA2	zpl_science_imaging_cam2.fits

Table A.5: DRH output images acronyms.

size) and two read-out registers which work in parallel, each reading out half line. The CCDs are equipped with a opaque mask that consists of 512 stripes aligned parallel to the pixel rows, which alternately covers two rows of the CCD and leaves the next two rows open. This opaque mask is mounted on the bottom of a micro-lens array composed by 512 cylindrical micro-lenses that send the light in the open rows pixels A.4. A 2 × 2 binning is therefore performed allowing faster read-out and providing an effective pixel size of 30×30 μm. This results in a rectangular (1kx1k pixels) image whose odd rows have no scientific signal. The DRH first split these raw data into ndit and even/odd frames for each camera for both science (P1 and P2) and calibration frames and then they are corrected for bias, dark and flat-field (OS1 and OS2). A new image of 1kx1k pixels is then recreated copying each even OS1 and OS2 row in the following (cover) row. Images are then de-dithered and centred (FS1 and FS2): dithering is foreseen for all ZIMPOL observations. It is implemented by keeping the telescope pointed at a fixed position on the sky and producing a series of movements of the tilt- and tip/tilt mirrors in front of the ZIMPOL cameras providing a series of x, y-shifts of the field of view by a certain number of pixels. Finally all the images are derotated (if in pupil stabilized mode) and collapsed together to produce FA1 and FA2. In Table A.5 I reported the DRH output images names related to the acronyms used in the text.
The method I exploited are the followings.

Method 1: combine dithering-combined images with a solid shift

Routine: `ditering_comb.pro`
Inputs: ZIMPOL DRH output images FA1 and FA2
Steps:

1. flip cam1 image up-down and rotate cam2 image of 180°;
2. find the maximum coordinates of both the images $(x_1; y_1), (x_2; y_2)$;
3. shift cam2 image in order to match the two peaks and calculate the standard deviation of the difference image obtained. The shift is $\Delta x = x_1 - x_2, \Delta y = y_1 - y_2$;
4. explore a 5 × 5 pixels square with subpixel steps ($\delta x = 0.1$) around $(\Delta x; \Delta y)$ in order to obtain the coordinates which give the lower standar deviation of the difference image.
5. Apply to cam2 the best shift that correspond to $X = \Delta x + \delta x$ and the same for the y-axis.

Cons: It is very time consuming. The maximum value pixel of both the images must be in the central source and not a hot pixel.

Method 2: combine prepocessed individual images with a solid shift

Routine: `preproc_comb.pro`
Inputs: ZIMPOL DRH output images FS1 and FS2
Steps:

1. flip cam1 image up-down and rotate cam2 image of 180°;
2. find the maximum coordinates of both the images $(x_1; y_1), (x_2; y_2)$;
3. shift cam2 image in order to match the two peaks and calculate the standard deviation of the difference image obtained. The shift is $\Delta x = x_1 - x_2, \Delta y = y_1 - y_2$;
4. explore a 5×5 pixels square with subpixel steps ($\delta x = 0.1$) around $\Delta x; \Delta y$) in order to obtain the coordinate which give the lower standar deviation of the difference image.
5. Apply to cam2 the best shift that correspond to $X = \Delta x + \delta x$ and the same for the y-axis.

Prons: It search for the best fit matching the whole image.
Cons: It is very time consuming. The maximum value pixel of both the images must be in the central source and not a hot pixel.

Method 3: combine dithering-combined images using gaussian fit

Routine: `ditering_combv1.pro`
Inputs: ZIMPOL DRH output images FA1 and FA2, positions of the reference star in both the images.
Steps:

1. flip cam1 image up-down and rotate cam2 image of 180°;
2. read the maximum coordinates of the reference star of both the images $(x_1; y_1), (x_2; y_2)$;
3. trim the image of cam1 in a 13x13 pixel image centered on the reference star. In the case of RAqr, if we take a bigger area, the trim image will include some light from the other source. Furthermore we selected the left source because the right one is elongated;
4. find the center of the star by fitting the light distribution with a 2D-gaussian profile;
5. rotate the trim image around this center, subtract it to the previous one and evaluate the standard deviation of the difference.
6. repeat step 5. moving the center of the rotation in a 5×5 pixels square using `mpfit` library in order to find the best star position.
7. repeat steps from 3. to 6. for cam2;
8. Estimate difference between the two stars position and shift the whole cam2 accordingly.

Prons: it is very fast.

Cons: we have to know a priori the approximate position of the reference stars in both the cameras images. It also does not care about other sources (the companion and jets).

Method 4: combine overscan-subtracted images with a solid shift

Routine: `squared.pro` (that includes the method of rows interpolation) and `preproc_comb.pro`

Inputs: ZIMPOL DRH output images OS1 and OS2

Steps:

1. select only every second row of cam1 image and do an interpolation between them;
2. repeat step 1 and 2 for cam2;
3. apply method 2 to these new images;

Prons: better row interpolation then that in the DRH.

Cons: It is very time consuming.

Method 5: combine images exploiting amoeba technique

This routine returns the shift to be applied to img2 in order to match img1. As the beam splitter between the two arms produces two light beam which are not exactly the same, I tried to match the images with the luminosity as a variable or as a constant ($I = 1.0$) value. It looks for the minimum of the function `align.pro` which is

$$stddev\left[(A - shiftf((I \cdot B), X, Y))^2\right] \tag{A.1}$$

where A and B are (a part of) the two input images, whereas x, y are the x and the y shift to be applied to img2 to match img1 and the term I takes into account the different illuminations of the two images.

Routine: `cam2_shift.pro` and `amoeba_comb.pro`

Inputs: ZIMPOL DRH output images FS1 and FS2

Steps:

1. flip cam1 image up-down and rotate cam2 image of 180°;
2. apply the amoeba method optimization;
3. shift cam2 and rescale its pixel values according to the results.

Prons: Very fast method that takes into account the whole image. Of course can be run also on the overscan-subtracted images.

Cons: Amoeba method results directly depends on the initial guesses, that have to be reasonable.

Results

Shifting results are listed in Tab. A.11. Methods 1, 2 and 3 are compatible, whereas method 4 and 5 give very different, self-consistent, results. Considering that these pre-processing input images are affected by the ZIMPOL internal dithering shift and that there are $\sim$ 20 pixels

Method	Input image	X	Y	stddev
1	FA	5.4000	-15.9000	3.0944
2	OBS284_0030	5.3000	-15.9000	4.0886
2	OBS284_0031	5.2000	-15.9000	4.5356
2	OBS284_0032	5.6000	-15.9000	4.0265
2	OBS284_0033	5.2000	-15.9000	3.4824
2	OBS284_0034	5.5000	-15.9000	3.7647
FA	5.3259	-15.8810	3.0937	
*4	OBS284_0030_OS	5.3000	4.3000	1.6791
4	OBS284_0031_OS	19.2000	18.4000	1.6930
4	OBS284_0032_OS	19.5000	-9.6000	1.3298
4	OBS284_0033_OS	-8.8000	18.3000	1.6683
4	OBS284_0034_OS	-8.5000	-9.7000	1.8963

Method	Input image	X	Y	$I = I_1/I_2$	fval
5	OBS284_0030_OS	5.2463	4.3525	1.0478	95.5480
5	OBS284_0031_OS	19.1215	-9.6156	1.0233	101.9969
5	OBS284_0032_OS	19.5367	18.3946	1.0241	47.8903
5	OBS284_0033_OS	-8.8904	-9.7385	1.0556	65.0090
5	OBS284_0034_OS	-8.5001	18.3339	1.0698	97.4719
5	OBS284_0030_OS	5.2066	4.3288	1.0000	—
5	OBS284_0031_OS	19.1607	-9.6545	1.0000	—
5	OBS284_0032_OS	19.5373	18.3897	1.0000	—
5	OBS284_0033_OS	-8.8580	-9.7214	1.0000	—
5	OBS284_0034_OS	-8.4617	18.2737	1.0000	—

Table A.11: In the first column I report the method used, the string in the second column refers to the input image used, column 3 and 4 report the x and y shift between cam1 and cam2. In the upper table, the last column report the standard deviation of the difference image between cam 1 and 2, while in the bottom table column 5 indicates the relative flux between cam 1 and 2 and the last column report the fval, which is amoeba output representing the goodness of the fit.

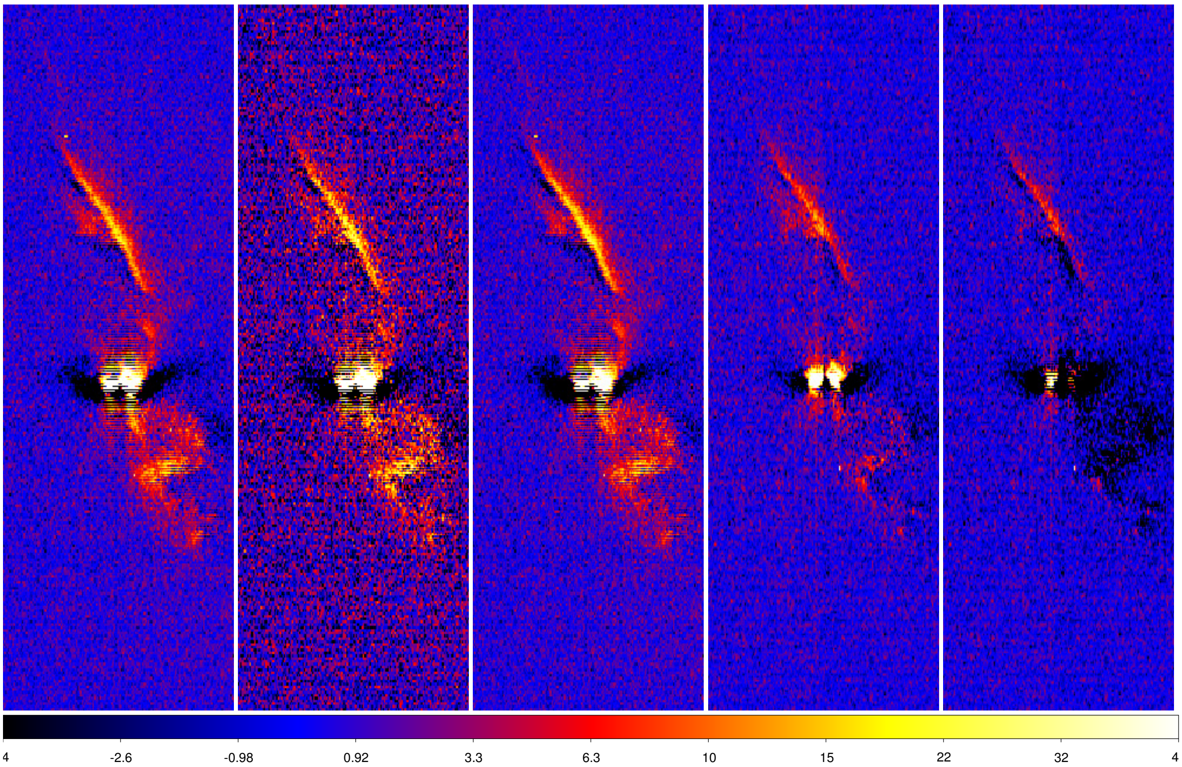

Figure A.5: Difference images obtained with the five different methods, from 1 to 5 form left to right. Images from OBS284_0030_OS were used for methods that implies only one image. Colours are in asinh scale to enhance the extended sources.

added along y-axis by the reading process, the results for the first three methods are therefore different from the results of the other two, but they are perfectly in agreement, when taking into account the dithering (Tab. A.4) and the y shift introduced by the mirrors. The shifts between the two cameras are less then 0.5 pixels and therefore are in agreement with those expected by the dithering.

The most critical points concerns the doubling of the row, that is the redistribution of the flux between open (even) and masked (odd) rows. The solution adopted in the DRH version 13.6 is not suitable because both it does not keep the total flux and treats each odd rows independently from the following row, producing rectangular pixels of 3.63 × 7.26 mas/pixel. The interpolation technique I introduced is based on the 4 nearest rows and is therefore more robust.

Another difference is that all these methods, except method 3, are based on the minimization of the residuals obtained with shifting the whole image and therefore both the stars and the extended regions contribute to the result. Conversely, in method 3 the shift is only guided by a 2D-Gaussian interpolation of the east source and the error is estimated in a small area around the star to avoid contaminations due to other sources. Another indicator of the alignment quality is the difference image obtained subtracting the shifted cam2 image to cam1 image. In Fig. A.5 I reported the difference image for method from 1 to 5: the images are striped, except for method 4 that uses the interpolation. This effect origins in the DRH routine, which substitutes covered rows simply duplicating each recorded row along y-axis as

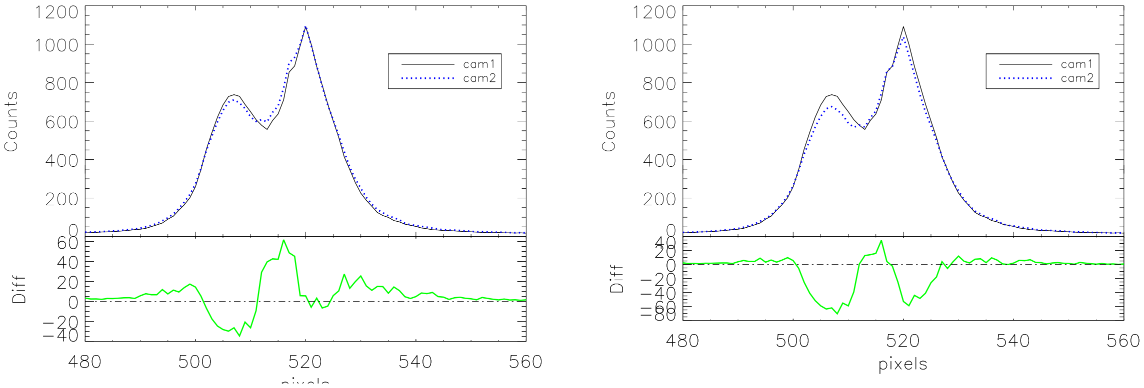

Figure A.6: Results for variable I (upper graph) and $I = 0$ (lower graph): Projection of the FfOS1 and FfOSs2 central lines using the median of 5 pixels. In the bottom pannel the difference between the two is enhanced.

described above. In method 4 , instead, I decided to double y dimension, e.g. the direction perpendicular to the masking stripes, using an interpolation based on consecutive recorded lines. Both these methods are not flux conservative. Moreover, in all these figures there is an unexpected feature near the two source positions: in the center we have a lot of light while in the wings the pixels values are negative.

We can therefore study the central 5 rows of cam1 and cam2 images FfOS1 and FfOSs2, make a median, and look for their difference, as shown in Fig. A.6. In Fig. A.5 the presence of stripes in the difference images of cam1 and cam2 is clear for most of the methods. To quantify this feature I proceed as follows:

1. find the position of the maximum in the image;
2. select a rectangular area (81x41 pixels) of the images, centered in the maximum, which includes both the two main sources
3. compose two images, one with only odd rows, the other one only with even rows.
4. make an histogram of both the images (red= even, blu= odd) and compare them.

The distribution of the pixel values can be easily described by Gaussian distributions: all the odd lines have in general higher values of those of the even rows. In Fig. A.7, the difference image between FA1 and FA2 applying method 1 is considered: the two pixels distributions present a difference of about 20% on the peak of the two Gaussians. Even if the FWHM is more or less the same (ΔFWHM=0.28 pixel),there is an excess of red pixels on the left and of blue ones on the right. As before, for image FS1_30-FS2_30 coming from method 2, the pixels distributions present a difference of 20% on the peak value, while the center and FWHM are more or less the same with Δc=0.67 pixel and ΔFWHM=0.21 pixel (Fig.A.8). In this case the use of only 1 image of the serie implies a wider FWHM (∼15.5 pixel instead of ∼8 pixel), as expected. The results of method 3 are in Fig.A.9: both the two Gaussian fits have a very wide FWHM (21.64 for the even rows, 21.71 for odd ones) and the relative shift is higher. This is because the best fit is evaluated in a small area that includes only the east source and not the extended features nor the west star. I noticed that the two peaks differs

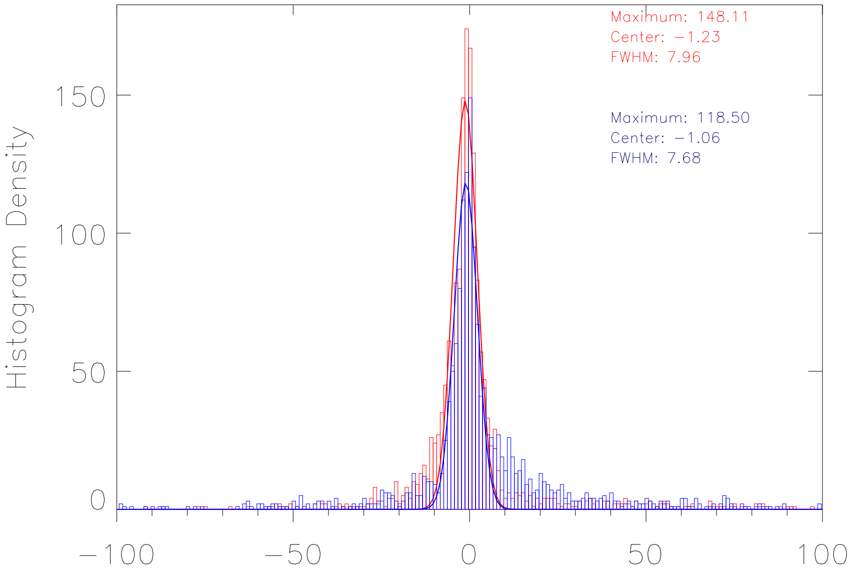

Figure A.7: histogram of odd and even rows of FA1+FA2 coming from method 1 based on ZIMPOL DRH combining all the RAqr sequence.

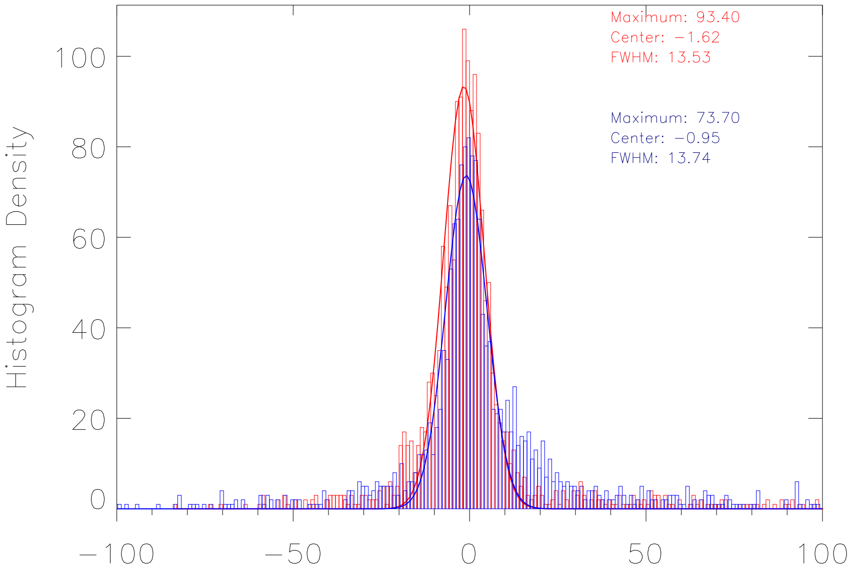

Figure A.8: histogram of odd and even rows of FS1_30+FS2_30 coming from method 2 based on ZIMPOL DRH intermediate output images: squared, preproc, dedithered images for single exposure.

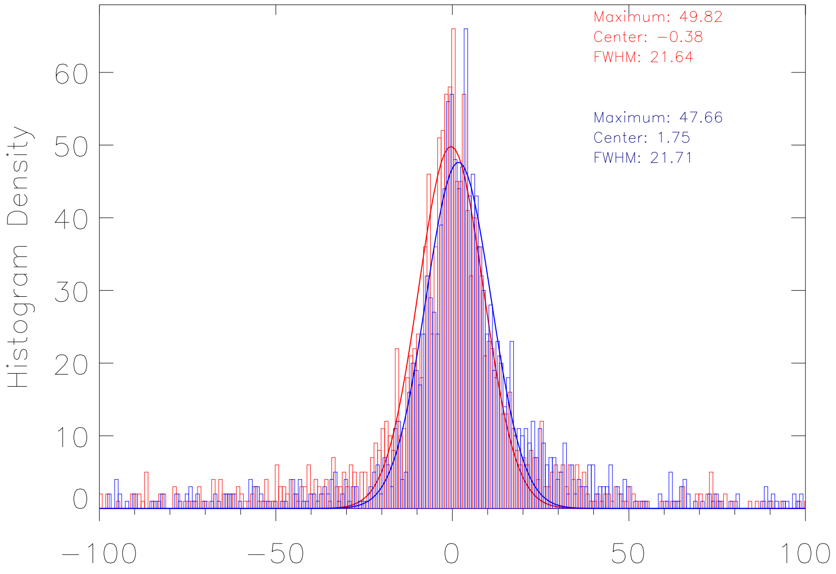

Figure A.9: histogram of odd and even rows of FA1 and FA2 coming from method 3 based on ZIMPOL DRH output images combining all the RAqr sequence.

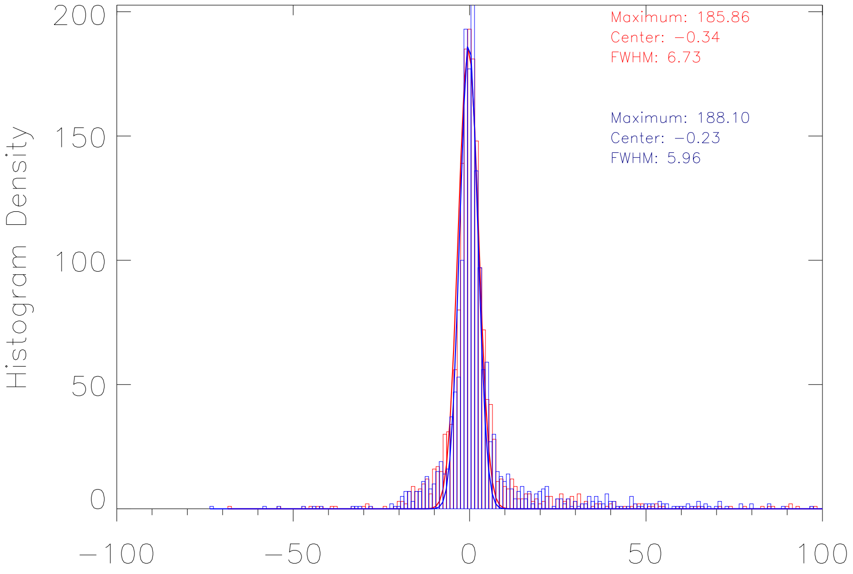

Figure A.10: histogram of odd and even rows of OS1_30+OS2_30 coming from method 4 based on ZIMPOL DRH intermediate images: rectangular, overscan subtraced images for single aperture.

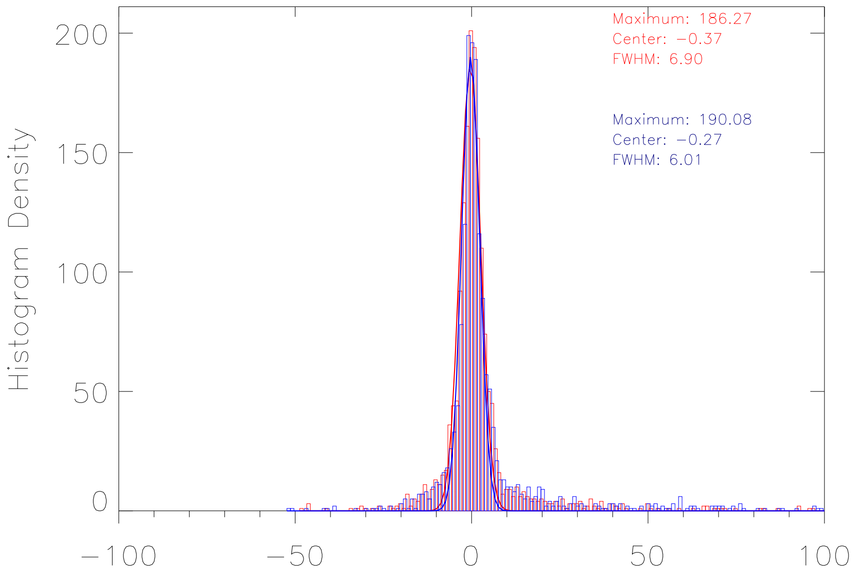

Figure A.11: histogram of odd and even rows of OS1_30+OS2_30 coming from method 5 based on ZIMPOL DRH intermediate images: rectangular, overscan subtraced images for single aperture.

by only 4.4%. The histogram relative to OS1_30-OS2_30 images aligned exploiting method 4 (Fig.A.10) seems to indicate that this solution is better then the previous: the two peaks differs only for less then 1.5%, the center is more or less the same and the FWHM is narrow (6 pixel). Applying method 5 to the same images (Fig. A.11), even and odd rows differs in intensity of about 2%.

Image quality

In this section I compared the quality of the different images and, therefore, the quality of some of the reduction steps. I used the methods described in Sec. A.1.2 to align the cam2 DRH output images to their respective cam 1 images. In Table A.12 I summarize all the

Input	m	Output	
FA1 FA2	1	FAs2	zpl_science_imaging_cam2_shifted.fits
FA1 FA2	3	FAgs2	cam2.fits
FS1 FS2	2	FSs2	zpl_science_imaging_cam2.fits_SPHERE_ZIMPOL_OBS♯♯♯_preproc_cam2_shifted.fits
OS1	dit	FfOS1	zpl_science_imaging_cam1.fits_SPHERE_ZIMPOL_OBS♯♯♯_os_preproc_cam1.fits.fits
OS2	dit	FfOS2	zpl_science_imaging_cam2.fits_SPHERE_ZIMPOL_OBS♯♯♯_os_preproc_cam2.fits.fits
FfOS1 FfOS2	4	FfOSs2	zpl_science_imaging_cam2.fits_SPHERE_ZIMPOL_OBS♯♯♯_os_preproc_cam2_shifted.fits

Table A.12: Input images for different methods (m) create new output images. Acronyms are indicated. OS1 and OS2 images were first corrected for dithering and then aligned using method 4.

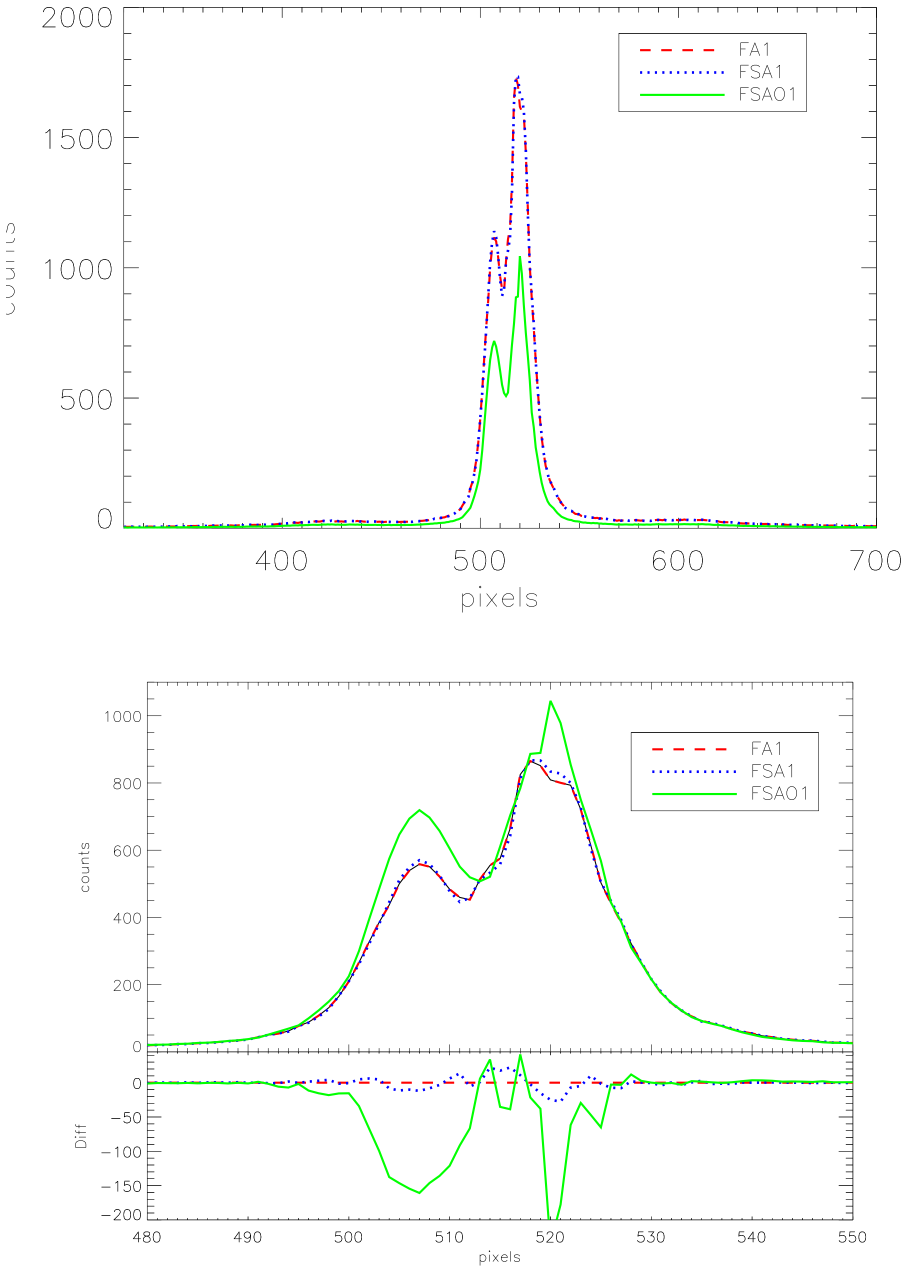

Figure A.12: *Top:* projection of the images using the median of 5 pixels. *Bottom:* a zoom of the central region.

Input	Output	
FS1 30-34	FSA1	z_s_i_cam1_ALL_S_Z_preproc_cam1.fits
FSs2 30-34	FSAs2	z_s_i_cam2_ALL_S_Z_preproc_cam2_shifted.fits
FfOS1 30-34	FSAO1	z_s_i_cam1_ALL_S_Z_OS_preproc_cam1.fits
FfOSs2 30-24	FSAOs2	z_s_i_cam2_ALL_S_Z_OS_preproc_cam2_shifted.fits

Table A.13: Acronyms for images obtained combining all frames of a single camera.

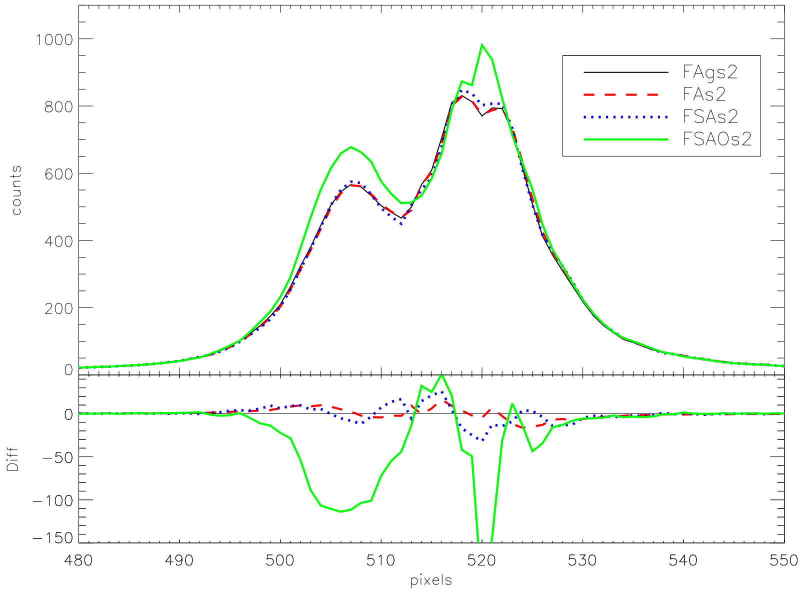

Figure A.13: *Top:* projection of the images using the median of 5 pixels. *Bottom:* a zoom of the central region.

Input	Output	
FA1 + FA2	FAB	
FS1 + FSs2	FSB	from 30 to 34
FfOS1 + FfOSs2	FSBfOS	from 30 to 34

Table A.14: Acronyms for images obtained combining each cam1 image with the respective cam2. I produced one FSB and one FSBfOS image for each exposure.

images I obtained. Images taken with camera 1 were never shifted except for the dithering: this correction on OS1 ensure that these images are aligned with those coming from other methods. I combined images from 30 to 34 for each algorithm as described in Table A.13. In order to match different images and to compare them with the original FA1 and FA2 images, I first tested if there are difference when combing images with the mean instead of the median of the pixel values. The effect is lower than 2%, therefore in the following I used the mean of all the images. FA1, FSA1 and FSAO1 are equivalent images obtained with different steps: they all are the combination of the 5 images of cam1. Equally, FAs2, FAgs2, FSAs2 and FSAOs2 are the combination of the 5 cam2 images, shifted exploiting method 4. I compared the flux and the S/N of these three (and four) equivalent images in order to underline their differences. In Fig. A.12 I compare the median pixel values of the central 5 rows of each image covering the two stars. When reproducing cover rows, the values of the open rows pixels diminish in order to maintain the total flux constant if using the interpolation method (method 4, in green in Fig. A.13), whereas the DRH doublets the rows. This explains the evident difference in flux of FSAO1. Therefore, in the zoom below, I halve all the values except for this latter. The flux distributions appear to be the same in the wings of all the images, but FSAO1 is brighter in the center of both the sources. Moreover, the two relative maxima observed in the western source have opposite relative flux in FA1 and FSA1 with respect to FSAO1.

I also combined all the 5 × 2 images together: every cam1 image was combined with its cam2 image as described in Table A.14. In the same way, all the FSB and the FSBfOS images were combined into FSAB and FSABfOS respectively. The comparison between these three equivalent images is shown in Fig. A.14

In Fig. A.15 the difference between images originating from the overscan-subtracted images (OS1 and OS2) is shown: images obtained combining all the 5 FfOS1 images of cam1, the respective 5 FfOSs2 for cam2 and this 10 frames all together. The agreement is quite good ($< 2\%$) except for the central few pixels, where it reaches $\sim 10\%$.

I then estimated the signal to noise distribution in the equivalent set of images for both cam1 and cam2: in Fig. A.16, I compared the S/N distribution in the images based on 100 5×5pixels apertures, with a noise sampling area of 45×45 pixels. I obtained that FSAO1 and FSAO2 are the best images in terms of signal to noise, whereas FSA1 and FSAs2 have, counts for counts, a lower S/N.

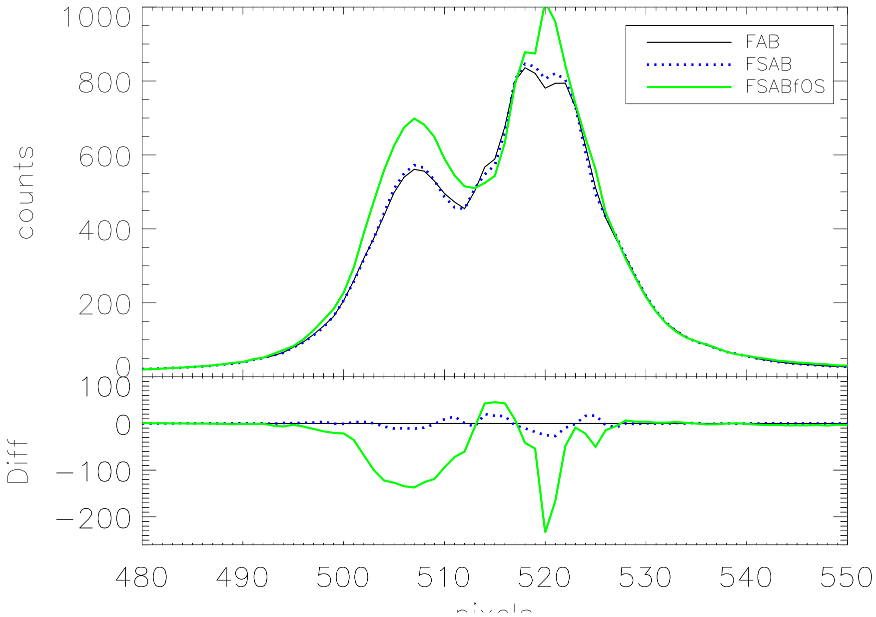

Figure A.14: Pixel values distribution in the center of the images that combine cam 1 and cam 2.

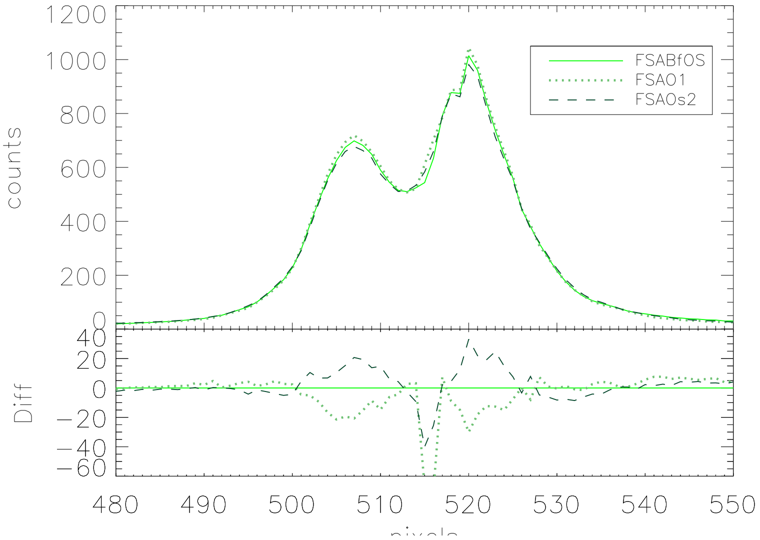

Figure A.15: using the median of 5 pixels. a zoom of the central region.

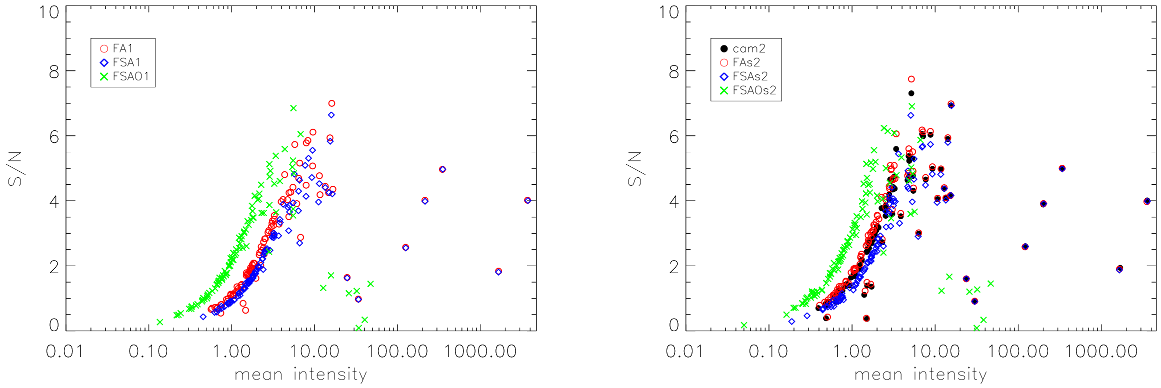

Figure A.16: S/N distribution in cam1 (left) and cam2 (right) equivalent images.

FILE	OPTI2	OPTI5	OPTI6	*X*	*Y*
TEC132_0001.fits	OPEN	B_Ha	B_Ha	8.5975	19.1715
TEC132_0002.fits	OPEN	CntHa	CntHa	6.7850	22.1822
TEC132_0003.fits	OPEN	B_Ha	CntHa	8.9317	21.8491
TEC132_0004.fits	OPEN	B_Ha	N_Ha	3.6552	23.2500
TEC132_0005.fits	OPEN	CntHa	B_Ha	6.4409	19.5370
TEC132_0006.fits	OPEN	CntHa	N_Ha	1.4970	23.6065
TEC134_0001.fits	OPEN	B_Ha	B_Ha	8.4037	19.2951
TEC134_0002.fits	OPEN	CntHa	CntHa	6.7850	22.1822
TEC134_0003.fits	OPEN	B_Ha	CntHa	8.7506	21.9130
TEC134_0004.fits	OPEN	B_Ha	N_Ha	3.4590	23.3517
TEC134_0005.fits	OPEN	CntHa	B_Ha	6.2329	19.6277
TEC134_0006.fits	OPEN	CntHa	N_Ha	1.3228	23.6939

Table A.15: Results of the gauss2dfit method for the first two OBs obtained on the 14-05-2015.

Tools for dual band imaging

The methods for cameras alignment described above aim to handle data obtained with the same filter in both the cameras (using only the common filter or the same filter in the two FW1 and FW2). Since they are all based on the minimization of the residual image, they cannot work when performing dual band imaging, if the two different filters in the two arms produce two different images.Indeed, applying the shift observed during Comm4 to the Cnt_Ha and B_Ha simultaneous images obtained in Comm3, the shift between the ghosts demonstrates that the two images are not well aligned. In the case of RAqr, it happens, for example, using the NB_Ha and CntHa filters simultaneously, where the two sources are resolved and not, respectively, as shown in Fig.A.1. In this case the center position needs to be known `a priori`.

In order to solve this issue, I planned some instrumental tests to measure the relative astrometric zero point in the two cameras: each filter introduces, indeed, a small image shift: I'll use the SPHERE internal artificial lamp to define the center of the image with different combination of H_α filters in all the tree wheels. The OB was run twice on May, 14th 2015

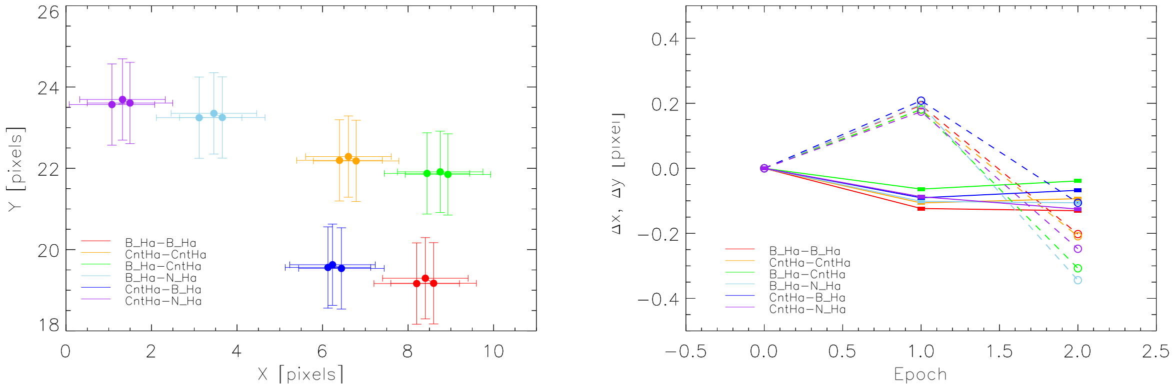

Figure A.17: Left: Relative shift between cam1 and cam2 in different epochs. Different colors refers to different filter combination as indicated in the legend, where the firs filter is in FW!, the second in FW2. Right: X (open circles) and Y (filled bars) time evolution.

(1 day-time and 1 night-time), and later on June, 5th 2015. The two cameras were aligned using method 3 because it does not require the two images to be the same. Even with a short exposure times, at least in some cases the center of the image is saturated, therefore I previously performed a Gaussian smooth (with a sampling area of 10 pixel) on the images, and then I exploited method 3 to infer the shift between the two cameras. Results are in Table A.15 and in Fig. A.17, were X and Y are defined as the shift to be applied to cam2. Even if the shift is well below 1 pixel, we notice that the direction of the shift is the same for different filter combination but differs from one epoch to the other. Several ingredients can contribute to this effect and the lack of points makes the understanding not straightforward. A deeper and constant monitoring of this effect, including other filters in this kind of technical observations, is needed to check if the instrument is really stable. The temperature can, indeed, impact on this as was observed by C. Ginsky (priv. com.). These three sequences were taken under quite similar temperature.

I can observe that the results for the two sequences are very close one to each other. The output images are well aligned.

Conclusions

Concluding, I found that:

- the best results comes from methods that use the interpolation technique to redistribute the flux in the cover rows. This method was later implemented in the `sz_pipeline`, the internal consortium ZIMPOL pipeline, that will be insert in a future DRH release;
- the two cameras are equally illuminated;
- the dithering works nominally;
- the combination of the dual band imaging is still an open question and the beam shift is under monitoring.

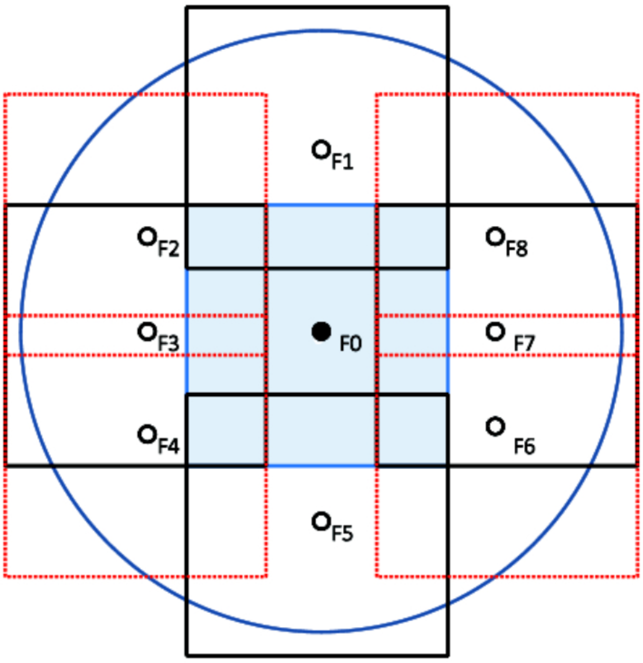

Figure A.18: With the use of the tip-tilt mirrors ZIMPOL can image an area of 8″radius (blue circle) adding together 9 different FoVs: the central one (F0, light blue area) and 8 off-axis fields (black and red squares).

The new reduction methods from preprocessed images was then modified as follows to take into account the advantages of the interpolation methods and the flux conservations:

1. extract right rows from left and right part of the CCD, and interpolate them in order to have squared images, using the interpolation and flux redistribution algorithm;
2. rotate and flip images;
3. correct cam1 for dithering and 21 pixel y-shift;
4. write FfOS1 and FfOS2;
5. align FfOS1 and FfOS2 using amoeba downhill method;
6. shift and multiply FfOS2 according to the previous results and write FfOSs2.

Another method that can be explored to better align the cameras can take advantage of the 4 ghosts that appear at $40\lambda/D$. This fake structures are created by the adaptive optics of the instrument and their position respect the central source is fixed. However, these spots are clearly visible and detectable only on no-coronagrahic observations of a very high S/N object.

A.2 Off-axis images

The off axis observation mode exploits the ZIMPOL tip-tilt mirrors to enlarge the Field of view up to 8.0″ from the star, as shown in Fig. A.18. This allows to have enough counts in the

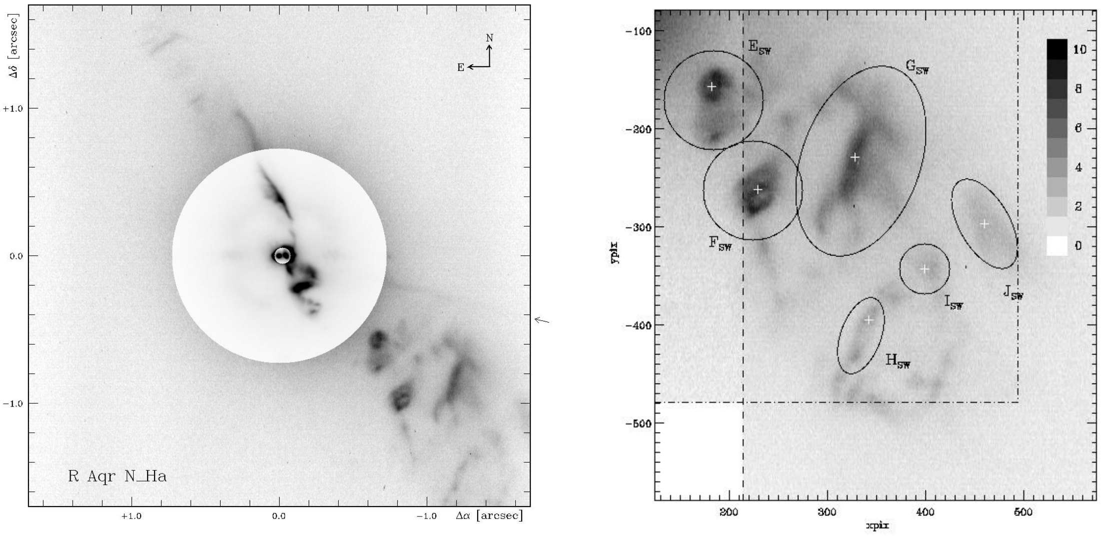

Figure A.19: Left: Map of the ZIMPOL $H_\alpha$line observation of R Aqr taken in the N_Ha common filter on Oct. 11th, 2014. The field is divided into three different gray scale regions ranging from 0 to 1000 ct $pix^{-1}frame^{-1}$ for the central binary, 0 to 100 for the inner jet region ($r < 0.72''$), and 0 to 10 for the outer jet region $r > 0.72''$. The red giant is at the zero point of the coordinate system. There is a small angle offset of 2°of the sky N orientation in a counter-clockwise direction with respect the (vertical) y-direction. A weak instrumental spike from a telescope spider is present at a position angle of about $-105°$ indicated by a small arrow outside the frame. Right: Images of the outer bubbles in the SW taken during the same night, with the same filter. The region on the right of the dashed line is from the off-axis field observation OBS284_0038 while the narrow section on the left is from the on-axis field observation OBS284_0034, which covers the region marked with the dashed dotted line.

outer part of the FoV avoiding the saturation effect of the central source, that is still beyond the coronagraph, and permitting the AO to close the loop on the source itself. `calibration grid`

A.2.1 Photometry

Comparing the photometry of the different fields of view is not straightforward. In the case of R Aqr, four off-axis field were observed: observations from OBS284_0035 to OBS284_0038 imaged the 02, 06, 04 and 08 field, respectively. Images were taken with the common Ha_NB filter with a 200s integration time each (see Tab.A.2), analysed with the SPHERE DRH and then aligned with the methods described above.

R Aqr circumstellar material forms several outspread structures, as shown in Fig A.19, that extend mainly in the SW direction, entering the F_{O2} field. The overlapping area between the central field and O2 consists of a $1''\times1.1''$, extending from $2.3''$ to $4''$ from the star, as shown in the right panel of Fig.A.19.

I studied this part of the circumstellar region with the aim of comparing the performances in these two ZIMPOL FoVs. I reduced this off-axis field with the same routines and method

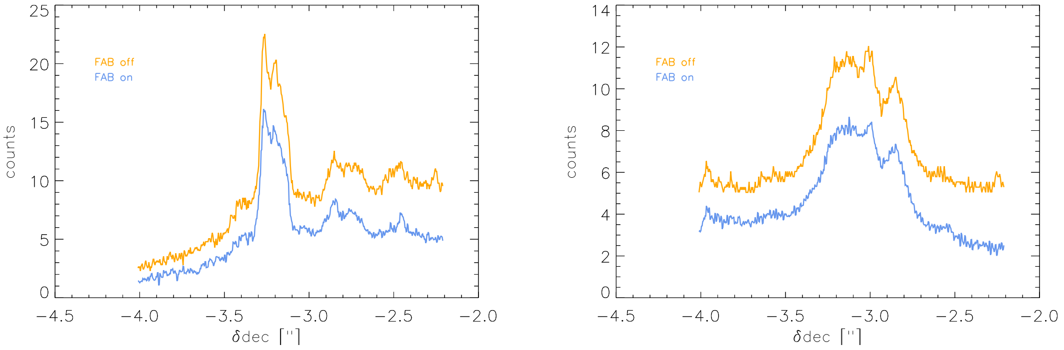

Figure A.20: Median counts profile of the F_{SW} bubble (left) and G_{SW} stripe (right) as a function of the declination, in the on-axis (light blue) and 02 off-axis (orange) fields FAB images.

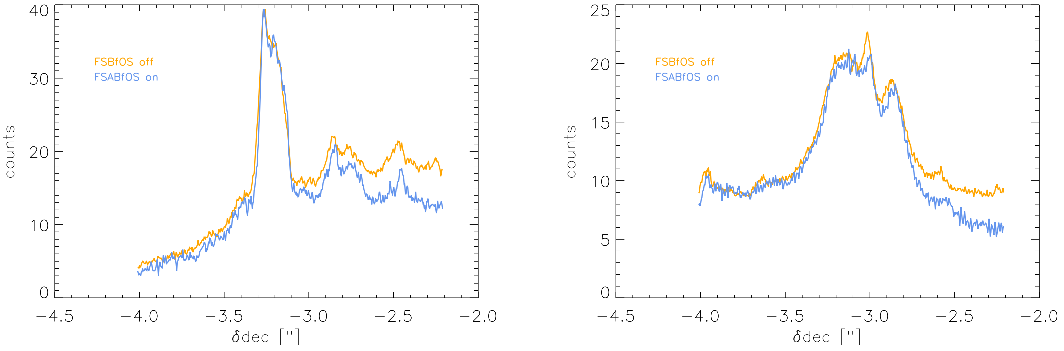

Figure A.21: Median counts profile of the F_{SW} bubble (left) and G_{SW} stripe (right) as a function of the declination, in the on-axis (light blue) and 02 off-axis (orange) fields FSABfOs images.

Figure	S/N
cam2	4.18169
FASs2	4.15215
FSAOs2	4.22260
FSABfOS	4.15960
FSAO1	3.75981
FSAOs2	4.02729

Table A.16: Signal to noise values in each images.

used for the central field (OBS284_0030-34 described above), and I found out that there are no additional bright clouds outside the 00 field. The two brightest features in the overlapping area are the F_{SW} bubble and the G_{SW} stripe (see Fig. A.19). I compared the flux in the FAB images of both the fields, focusing of these two bright structures. I recall that the total integration time is the same: the on-axis observation is composed of 5 exposures of $40s$ each, whereas the off-axis image is a single exposure of $200s$. In Fig.A.20 the off-axis field is brighter then the central one, with a ratio of about 1.7 in the case of the bubble and 1.5 for the stripe. The same algorithm applied to the FSABfOS images, obtained with the method 4 for doubling the line and aligning the cameras, gives the values shown in Fig.A.21: the counts in both the images are comparable. I derided that, in general, FAB images appear to be less illuminated with respect to the FSBfOS images. The same analysis on the other off-axis fields is not possible due to the lack of bright sources.

A.2.2 Off Axis field astrometry and derotation

In this section I'll study the alignment of the Cam1 and Cam2 images when using the tip tilt mirrors to image one of the off-axis fields. Since the final scientific aim was to image CT Cha b, I focused on the O_{F6} field and I exploited the FLAT obtained with the `V_CLC_MT_WF` mask, which includes a grid of dots useful for my purposes. The filter selected in both the two arms is B_Hα.

First of all I looked for the shift between cam1 and cam2 off-axis field: it is clear that there is also a rotation of the off axis field, one respect to the other one, as shown in Fig. A.22.

The rotation between the two cameras was determined exploiting IDL `polywarp.pro` and `poly_2d.pro` routines. These allowed me to create two matrices for the conversion, based on the 11 spots of the "astrometric grid" identified[1] in the calibration flat, and to apply them to the cam2 image. I obtained:

$$X_2 = (1.626 \pm 0.000) + (0.998 \pm 0.001)X_1 + (-0.023 \pm 0.025)Y_1 \quad (A.2)$$

$$Y_2 = (-20.804 \pm 0.000) + (0.023 \pm 0.000X_1 + (1.000 \pm 0.025)Y_1 \quad (A.3)$$

The rotation is therefore $\sim 1.520 \pm 1.409°$.

The result is in Fig. A.23: after the normalization and the subtraction of the two images,

---

[1] the pixel coordinates of the grid spots in each cam are obtained with the routine `rotation.pro` and are stored in `spot_grid_off.txt`.

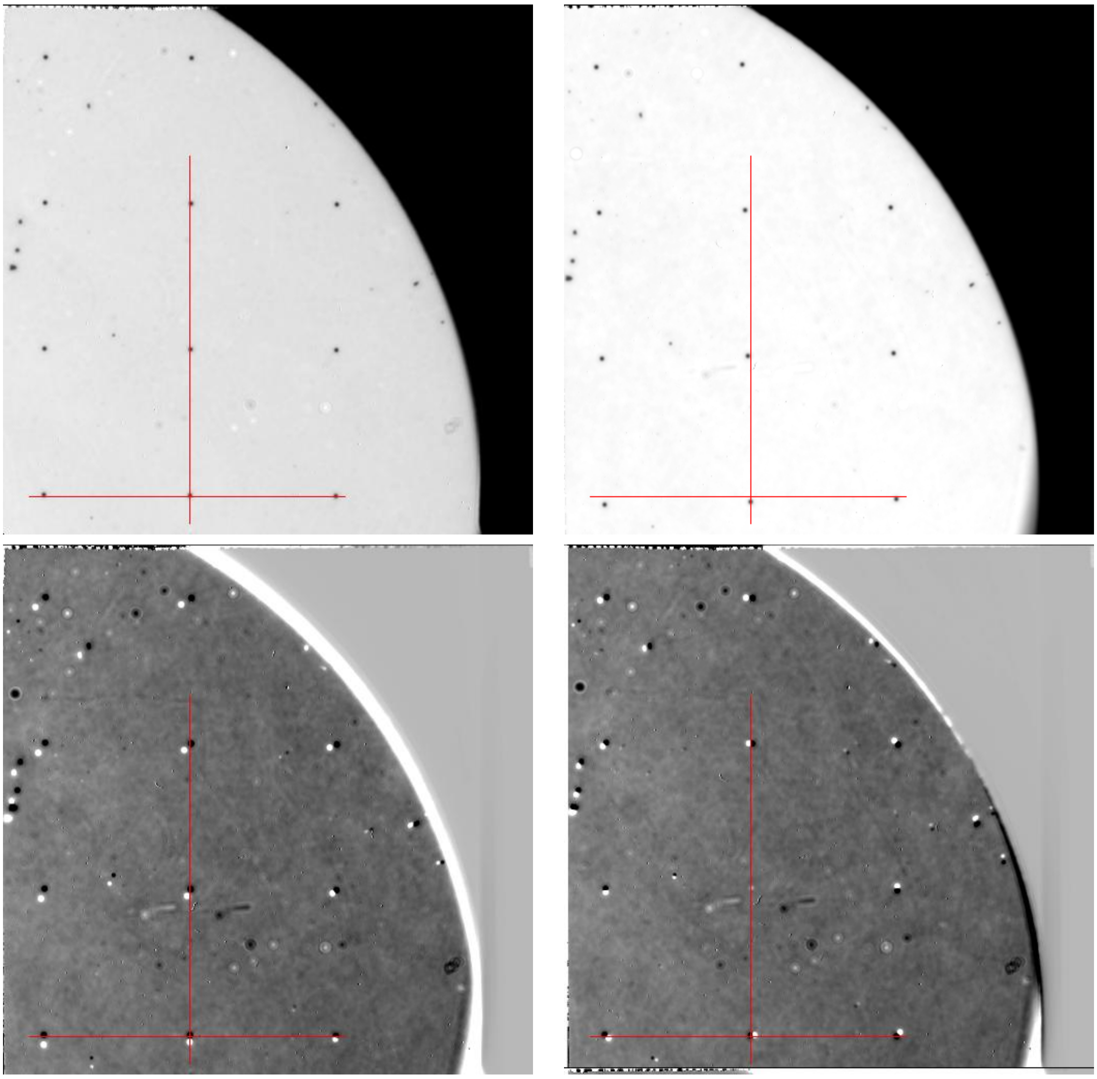

Figure A.22: *Top*: FA1 and FA2 images for the off-axis flat image. The two red lines are located an the same image positions and angles. *Bottom left*: the difference image between the two previous images, with no shift or normalization. *Bottom right*: difference between cam1 and the shifted cam2 image.

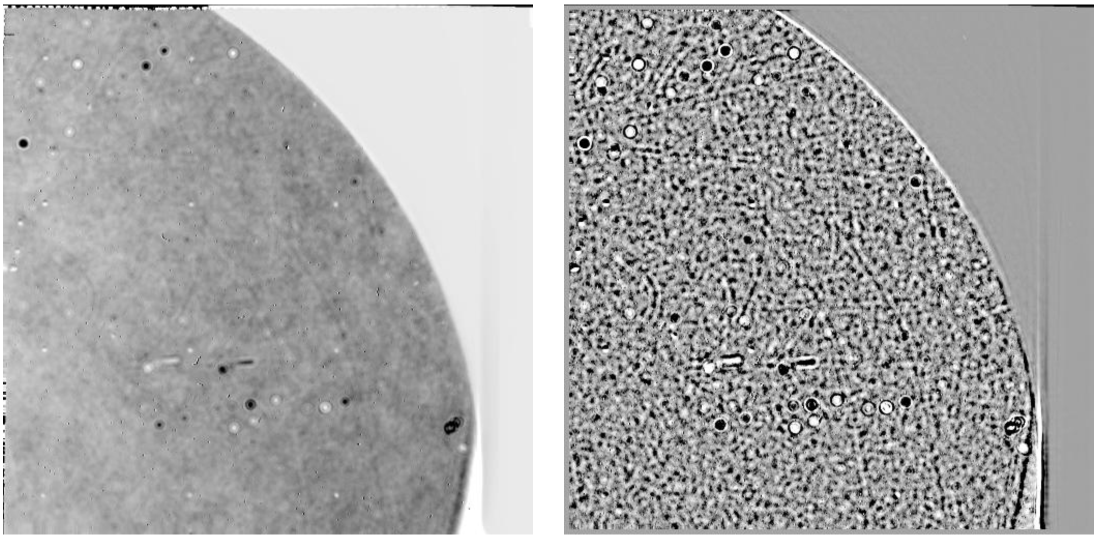

Figure A.23: Left: difference between cam1 and cam2 images, after applying the linear rotation to cam2. Right: the same, but with a normalization of the two cameras in order to take into account the different illumination of the spots and applying a local mean filter.

we can see that the left part of the cam 1 seems to be more illuminated than the cam2 (~ 300 count). After applying a spatial filter on the image, there are still some residuals of the spots, which seems to be non-axissimmetric, with a difference in flux of about 300 counts, whereas the stddev of the image is about 80 counts. There are also a lot of other spots and lines. Some of them have a dimension comparable with the spots of the grid, but they have a different origin. Others are smaller. There is also a replication of feature, like the "handle" shape in the middle, which appears twice also in cam 1 images.

The rotation of the off-axis field wrt the central field was not considered in this work.

Appendix B

Impact of Angular Differential Imaging on extended sources

B.1 Effects of angular differential imaging on circumstellar disk

The ADI technique was developed to enhance detection performances for faint point sources at close separation. It is well known that while enhancing detection limits, ADI somehow alter the position and especially the photometry of detected sources (self-subtraction effect). ADI also alter significantly extended sources around stars such as circumplanetary disks. A general description of the effects of ADI on circumstellar disk can be found, e.g., in Milli et al. (2012). Of course the effects are also related to the details of the procedures used and therefore, to infer the origin of these structures, I want to understand how our algorithm can modify the disk and stellar extended structures in general. In particular, our PCA applied simultaneously ADI and SDI to better take advantage of the use of IFS, while Milli et al. (2012) uses only monochromatic datasets and studies them with classical ADI and RDI (Marois et al. 2006), LOCI (Lafrenière et al. 2007), DLOCI (Pueyo et al. 2012) and a few variants of these methods. A few objects observed with SPHERE and then analysed with angular differential techniques, present both trailing and leading spiral like structures in which the pitch angle could vary by more than 180° as shown in Fig. B.1. In order to quantify the possible effects of the differential imaging on disk features, I took a star without disk, summed to it a fake

	HIP58465	HD100546
M_J	6.40	6.43
δ [°]	-57.2	-70.2
Obs. date	June, 2^{nd}	May, 29^{th}
IFS mode	YJ	YJ
DITs [sec]	64×64	$24 \times 16 \times 16$
rotation [°]	27.4	34.1
Seeing	1.2	1.0
Contrast	14.23	13.28

Table B.1: Comparison between HIP58465 and HD100546 observations.

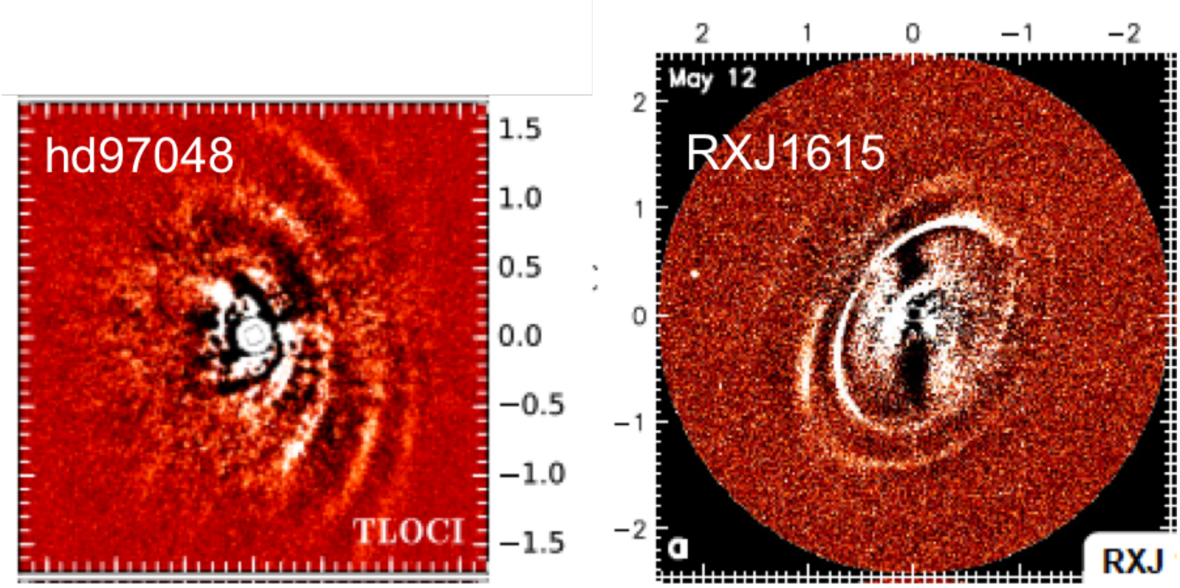

Figure B.1: Object observed with SPHERE that shows structure similar to HD100546.

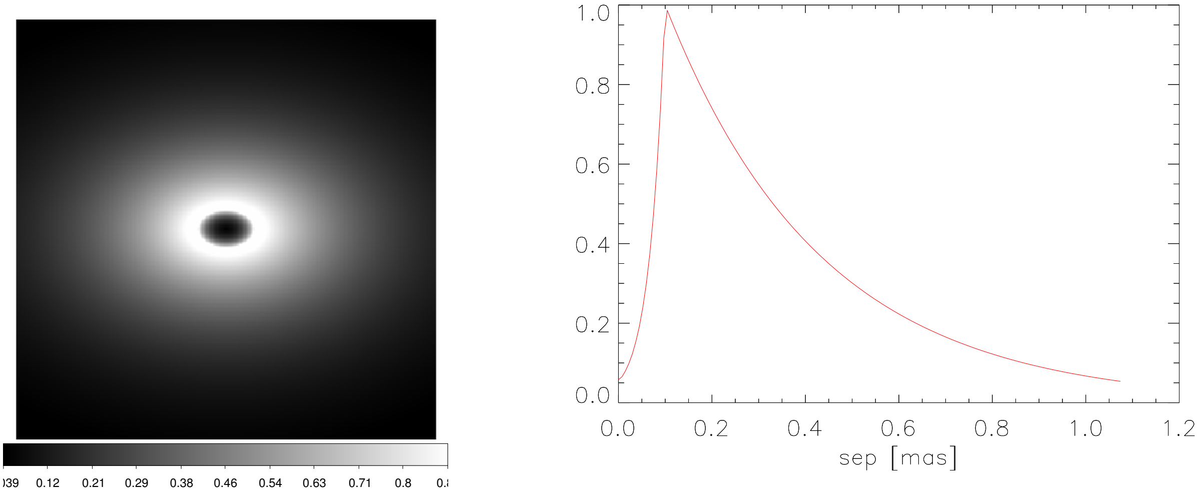

Figure B.2: Disk model image and it intensity profile along the semi major axis.

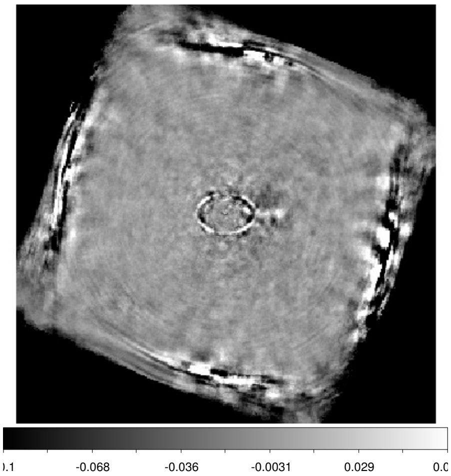

Figure B.3: Fake disk image after the PCA 50 modes.

disk, and then processed the images using the various algorithms. I selected the data from HIP58465 taken with VLT/SPHERE during the GTO on the 2^{nd} of June 2015. This stars is very similar to HD100546, which is my main scientific target, in terms of luminosity, as shown in Table B.1, but does not host any disk and was observed with the same SPHERE set-up. The noise regime for the two observations (HIP 58465 and HD 100564) are similar: in both cases IFS data are dominated by the thermal background of the instrument.

I built up a disk with parameters close to that found by Garufi et al. (2016) for HD100546 (see their Fig.2). The disk model is defined as:

$$I_{disk}(r) = \begin{cases} A \exp\left(\frac{r-r_0}{\sigma_1}\right) & \text{if } r > r_0 \\ A \exp\left(-\frac{r-r_0}{\sigma_2}\right) & \text{if } r < r_0 \end{cases} \tag{B.1}$$

where A=1, $r_0 = 0.15''$, $\sigma_1 = 0.05$ and $\sigma_2 = 0.5$. I then inclined the fake disk in order to obtain an eccentricity equal to 0.5 (that is similar to the case of HD 100546). The resulting disk model and its radial profile are in Fig.B.2. I did not convolve the disk with the instrumental profile before applying it to the star, because the short wavelengths of these observations make the convolution negligible. I added this model to the reference star 4D-datacube, applying the proper rotation angle and assuming a grey contrast between the star and the brightest part of the disk of 10^{-5}. I then run our PCA algorithm: the disk appears like a narrow ring, but the surface brightness varies with the angle (Fig. B.3). The darkest areas are those along the minor axis, as expected: the amplitude of the field rotation is low and the self-subtraction is significant. Moreover, it is known that ADI tends to under-subtract structures orthogonal to the radius, due to its principal components definition.

Then I added a perturbation of the disk model to get a spiral pattern:

$$I(r, \phi) = I_{disk}(r)\left[1 + f\cos(n\phi)\right] \tag{B.2}$$

where f is the peak to valley ratio of the spiral arms and n is the number of the arms. If I assume $r_0 = 0.12''$, $\sigma_1 = 0.02$ and $\sigma_2 = 0.05$ and a perturbation with $f = 0.2$ and $n = 4$. I obtained the model in Fig. B.4. I summed this model to the reference star datacube with a contrast equal to 10^{-5}. I also span a few variables combinations as described in Table B.2.

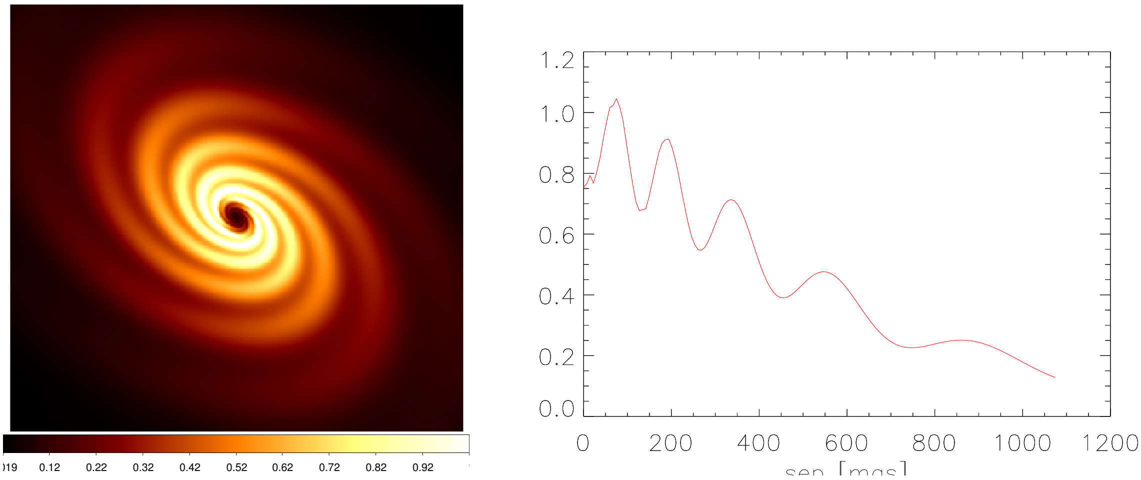

Figure B.4: The same disk as in Fig. B.2 with a spiral perturbation added. On the left disk image, on the right disk profile along the semi major axis.

Model	r_0["]	σ_1	σ_2	$\sharp$ arms	f	A	θ
spir4	0.12	0.02	0.05	4	0.05	4.e-5	45
spir6	0.12	0.02	0.05	4	0.2	1.e-5	45
spir7	0.12	0.05	0.25	4	0.2	1.e-5	45
spir8	0.12	0.05	0.5	4	0.2	1.e-5	45

Table B.2: For the most relevant models we report the number of arms, the peak to valley ratio of the spiral arms, the contrast of the model with respect to the star and the position angle of the disk semi major axis.

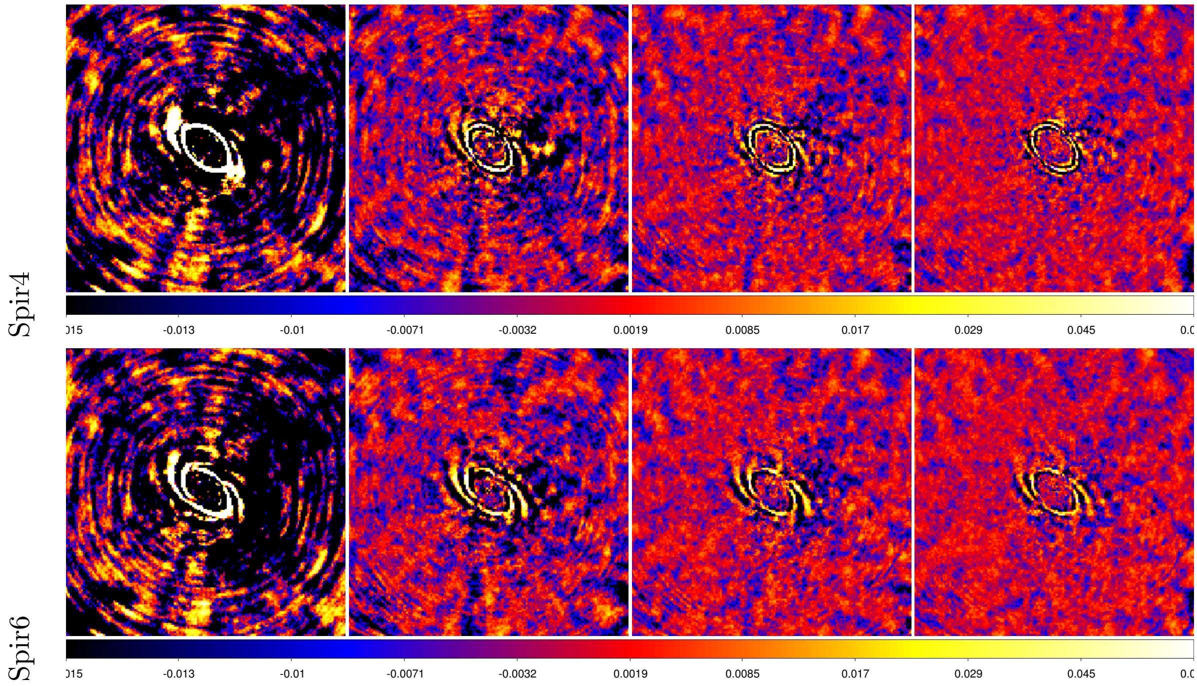

Figure B.5: The result of PCA on two different models. We used, from left to right, 10, 50, 100 and 150 modes.

The two most significant results are shown in Fig. B.5. The upper raw corresponds to spir4 model: there is an overall decreasing of the flux when using a higher number of principal components. The two spiral arms, clearly visible in the 10 components image, appear like a weak diffuse light running parallel to the disk in the 150 components image. In the bottom raw, the spir6 model has a higher f value that results in more tight spiral ones, the spiral arms are more defined and are visible also in the 150 components image.

To summarize:

- The PCA does not create new features of extended structures. It however increases the contrast between different areas.
- For this reason, homogeneous structures are more cancelled out then the peaked ones: this technique is more efficient for point-like structure with respect to extended disk.
- The effects of cancellation are larger where the structure is orthogonal to the radius of the PCA center. In the case of the disk, we have a minimum of signal along the two axis, mostly along the minor one.
- In general, the diffuse disk appears like a bright ring, located around the peak. In some cases, the PCA can split the brightest part of the disk into several concentric rings.
- In the case of spirals, they are strongly different. Weak and diffuse arms can become bright and thin after the PCA.

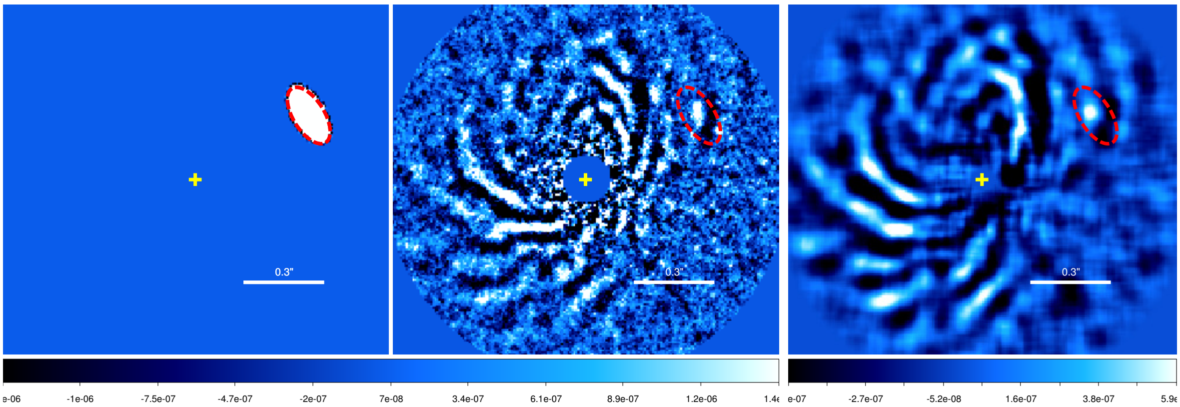

Figure B.6: left: image of the fake CPD we injected at all wavelength. Center: Results of the PCA on the datacube with the fake CPD disk injected. Right: the same as before after applying the smoothing. Color scales are in contrast. The red ellipse defines the original shape of the CPD. The yellow cross indicates the star position.

B.2 Effects of differential imaging and smoothing on a fake circumplanetary disk

In order to understand the effect of differential imaging and smoothing in the context of the short wavelength images of HD100546 planet b, I studied the impact of differential imaging and then smoothing on a fake spatially resolved circumplanetary disk (CPD)[1]. Like in the case of circumstellar disks, first of all I created a fake object that I injected in the data. In this case I used the IFS data of HD 100546 taken in YH mode on May 3^{rd}, 2015.

The left panel of Fig. B.6 shows the fake CPD image I injected in the data. This is simply a uniformly illuminated ellipse image, with local contrast equal to 10^{-5} with respect to the peak of the flux calibration at each wavelength. The ellipse I modelled is located at separation of 480 mas from the star, and at position angle of 300°, where there is not much disk signal in the IFS wavelength range, to minimize the interferences or superimpositions. The semimajor axis was initially set to 50 mas and the eccentricity is equal to 0.5. The ellipse is aligned tangentially with respect to the center of the image. The image is then smoothed with a Gaussian having $FWHM = 1\lambda/D$. This simulates the convolution with the instrumental profile. Monochromatic images were actually computed at all 39 wavelengths of IFS. This fake CPD was then summed to each individual frame of the 4-D datacube, according to rotation of each image, in the same way fake planets are usually injected, in order to monitor the attenuation due to the differential imaging methods. I noticed that this faint fake disk cannot be seen in the simple rotation and collapse of the datacube images.

The final differential image resulting from a 100 modes of ASDI PCA is shown in the central panel of Fig. B.6. The original size of the fake CPD in this image is circled in red. The original ellipse splits now into two blobs: the ADI process strongly attenuates the flat central part of the originally uniform disk, while having peaks closer to the edges of it. The separation between the two blobs is of about 35 mas, that is 1/3 of the original major axis of the disk. While visible, the blobs are not conspicuous and would not be noticed on the image. The right

---

[1] I call here an extended structure as seen in the HD 100546 image at the location of the planet b as a CPD although its extensions can be larger than the Hill radius of the planet

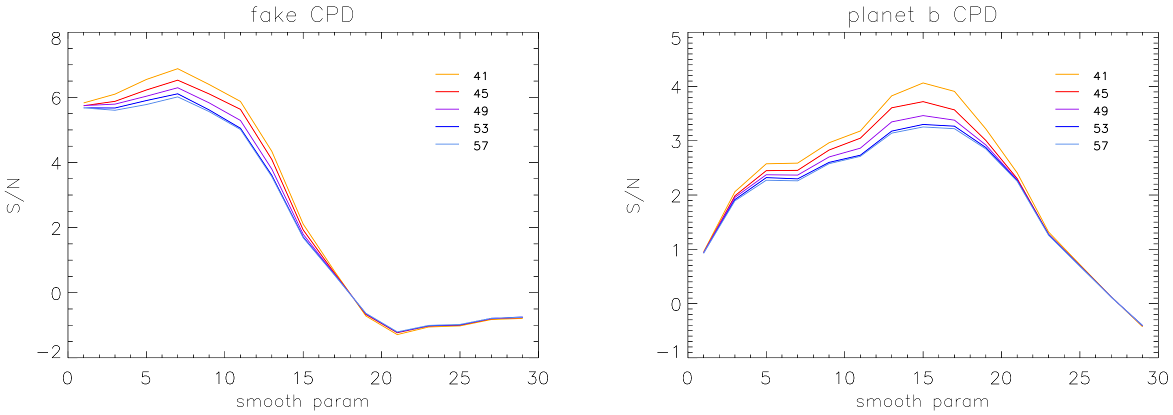

Figure B.7: Relation between the CPD S/N and the smooth parameter for different noise sample area (see the text).

a [mas]	b [mas]	s [pix]	S/N
50	25	7	6.8
75	37.5	11	6
100	50.	13	4.7
115	57.5	15	3.7
150	75	–	<1

Table B.3: Values for the CPD semi major axes, the smoothing parameter s that maximize the S/N and the value of S/N.

image of Fig. B.6 shows the result of smoothing the central image, exploiting IDL `smooth` procedure, with a parameter of 7 pixel: the fake CPD appears like a bright point source and its corresponding peak is among the brightest points in the image.
I then used four different sizes of the CPD to verify if there is a relation between the distance of the lobes generated by the PCA and the original CPD dimensions, and how this can impact on the smoothing technique. The first model pointed out, indeed, that a smoothing parameter of 7 pixels, roughly corresponding to the original size of the CPD, is the one which best shows it: with this value of the smoothing parameter I optimize signal-to-noise detection of this feature, that is, the CPD is much less prominent if I adopt a smaller or a larger value.

The signal is estimated as the peak value in an area centred where the object was injected. The dimension of this area was initially set to 3×3 pixels, located at the center of the fake CPD, but I discovered that since the signal is low (contrast of 10^{-5} in flux), the result has a low S/N and is therefore strongly dependent from the background. Therefore the sampling area was extended. The noise is estimated in an area in the SW region of our field of view, far from the brightest disk structures. The dimension of this area are variable but selected in order to avoid underestimation of the noise due to pixel-to-pixel cross-talk. I found that the value of smoothing that gives the highest S/N is independent from the sample noise area and that it correlates directly with the dimension of the injected fake CPD, as shown in Table B.3. An example of the S/N distribution as a function of the smooth parameter is in Fig. B.7, where different colors refers to a different side length for the noise sample area, as indicate in the legend using pixels unit. In the case of CPD with 150 mas of semi major axis,

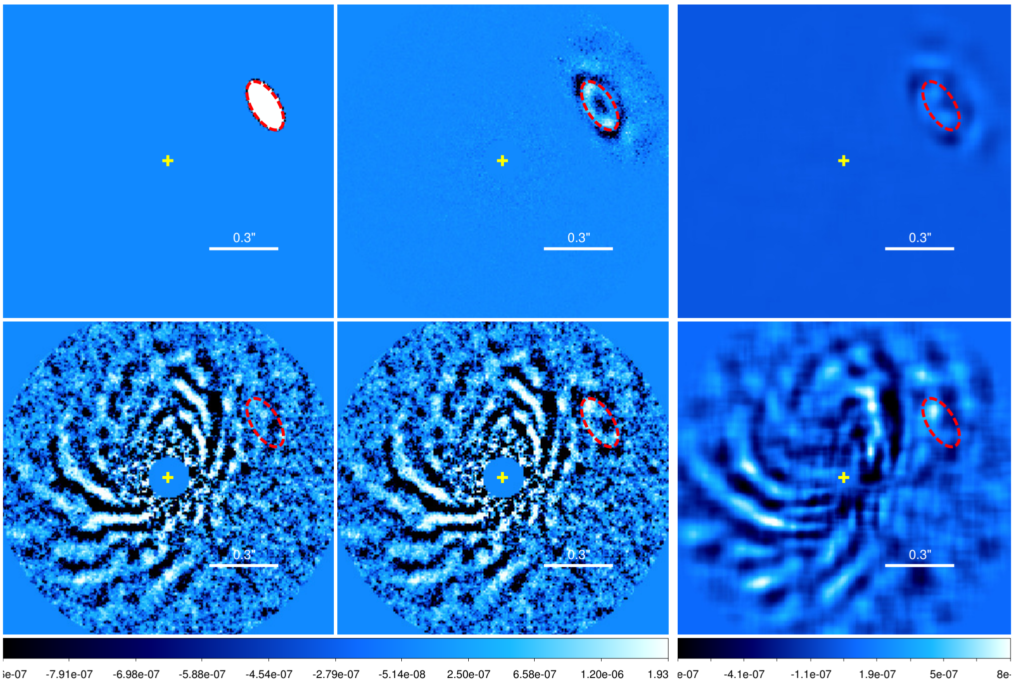

Figure B.8: On the top, images of the fake CPD, on the bottom images of HD100546 plus fake CPD. From left to right: the original image (injected disk model and processed HD100546), image obtained using 100 PCA modes, the same as before smoothed with the best smooth parameter.

the brightest signal of the fake CPD after applying the PCA exceed the dimension of out sample area. I conclude that the smoothing parameter that gives the highest S/N in the area of the disk corresponds to the real dimension of the fake CPD and therefore the smoothing technique can be used for infer the original size of the structure seen in ADI images. This is applied in Chapter 3.2 to the case of HD 100546.

B.3 Angular differential imaging on polarimetric data

Comparing the results I obtained with observations in classical imaging and observations in polarimetry, even if they cover the same wavelength range, is not straightforward. With this two different technique I could study the distribution of two different observables (the scattered light flux and its polarisation) that are complementary information for the study of circumstellar disk.

I tried to apply a pseudo-ADI on the polarimetric dataset with two methods. First, I realized that the ADI process is close to determining the second derivative along the azimuth (see Sec. B.1) and I therefore applied twice the azimuthal derivative to Q_ϕ images. What I get in the case of HD100546 IRDIS DPI J images is something like the two wings shape well detected in the SHINE dataset, as shown in Fig. B.9. The line running from NE to SW of the image correspond to a bad reflection of the light on one of the instruments spiders, that can happen at certain rotation angles in field stabilized observations (as those used for DPI). A more sophisticated approach uses the real parallactic angle values coming from the

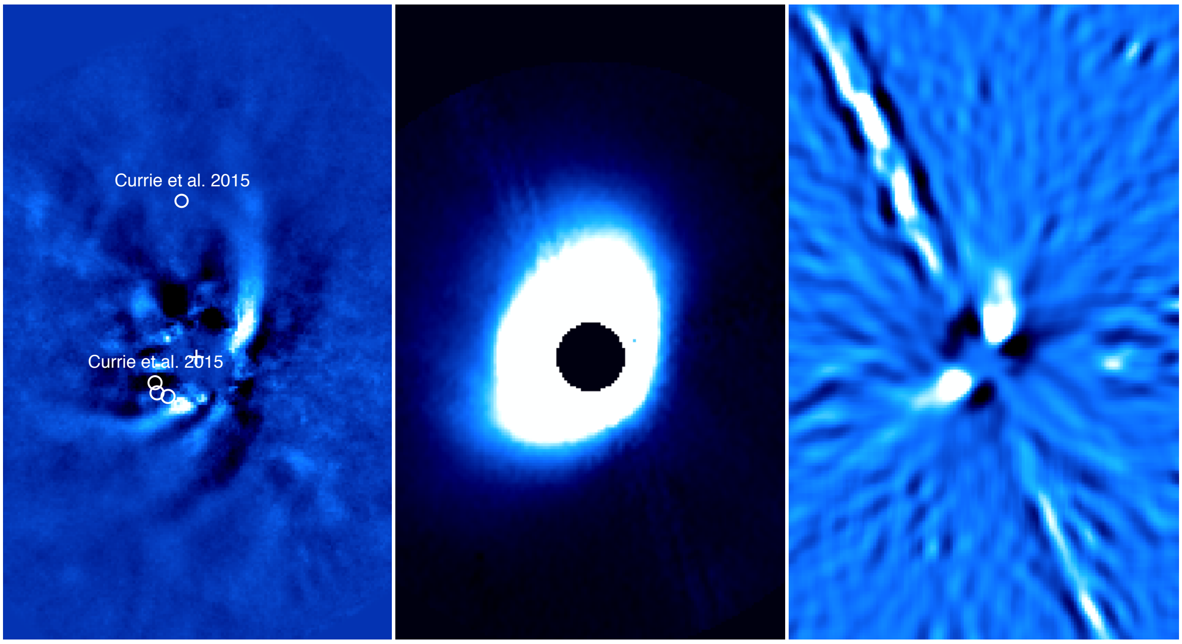

Figure B.9: Left: IFS image after sADI in J band (May2015), Center: IRDIS J Q_ϕ results from Christian Ginsky, Right: result of applying the second derivative to the central image. Different color scales are used.

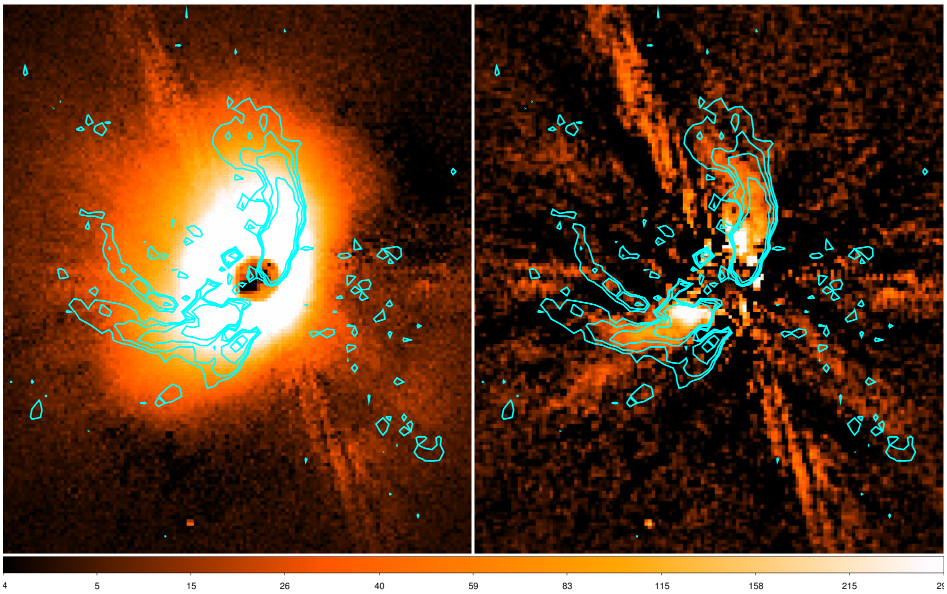

Figure B.10: IRDIS PDI J band Q_ϕ image (left) and the results of the simulated cADI analysis on this images. Overplotted in cyan the isophotes of IRDIS cADI H2 observations.

classical imaging sequence of the source to simulate a simple cADI analysis on the Q_ϕ DPI image: it first rotates it according to the opposite of the parallactic angles and then treats this new dataset as a normal one. The results for HD100546 IRDIS DPI J band image with the 31st May, 2016 rotation angles are shown in Fig. B.10. In this case, apart artefacts due to the residuals of the spiders, the two images are in good agreement.

Appendix C

Disk spectra

As described in Appendix B, ADI technique may strongly modify the light distribution of extended sources. This effect is also of great importance when extracting the disk spectra, that is not a straightforward operation. First of all, you need to define the disk itself, that is define which pixels in the scientific/target image can be assumed to correspond to disk structure. Then, the flux at different wavelengths should be derived. To this aim, I use the wavelength-collapsed RDI images of the disks, since this reduction is less aggressive than TLOCI or PCA. In this section I describe the procedure I developed to extract RDI 3-d datacubes of stars with prominent disks and used them to extract disk spectra. To this purpose I used stars observed with SPHERE/IFS in pupil stabilized mode.

Reference star identification

First of all you need to identify a reference star: same instrument set-up, close atmospheric conditions and the absence of disk or planets/background sources that can alter the photometry are the most important characteristics. It can be done by hand (e.g. searching for the object observed with same conditions, closest in time...), or dedicated observations of the reference star can be planned close to the scientific one.

However, an automatic best fit algorithm was developed to identify the best reference dataset among the SHINE survey for each scientific dataset. In this case, the criteria used to select the best match is the highest value of the correlation between the two images in the region between 20 and 80 pixels from center, that is approximately 0.15-$0.60''$. Two different kind of 3-d datacubes were considered for each star. The first one is simply obtained by rotating the individual images obtained at different epochs to the true north, and then making the median of these images. The second one is similar to the former one, save that a circular symmetric profile was subtracted from the individual images, this procedure being repeated at any wavelength. This circular symmetric profile was obtained by transforming the images into polar coordinates, slightly smoothing the transformed images along the azimuthal coordinate, and then taking the minimum of this smoothed image. This second procedure properly works only if, at each separation, there exists a region unaffected by the disk, otherwise there will be self subtraction.

These two different kinds of images were kept separate, so that the best matching image may be different in the two cases. At the end of the procedure, we found that the RDI images obtained using the PSF subtracted images provides better maps of the disks, so that we used this approach in the further analysis.

Reference star removal

The next step removes frame by frame the reference image from the scientific one. RDI 3-d images were obtained by subtracting to the 3-d IFS images of stars with prominent disks the best match among all observations acquired so far in the SHINE survey. Defining the target datacube as a function of the wavelength and rotation angle $dc_T(\lambda, \theta_T)$, and the same for the reference datacube $dc_R(\lambda, \theta_R)$, the algorithm matches each target frame with the reference one with the closest value of rotation angle, $min(\theta_T - \theta_R)$, that is obtained for $\theta_T i$ and $\theta_R j$ respectively. The final datacube is therefore:

$$dc'_T(\lambda, \theta_{T,i}) = dc_T(\lambda, \theta_{T,i}) - a(\lambda, \theta_{T'i}) \cdot dc_R(\lambda, \theta_{T,j})$$

where a is the rescaling factor defined in order to take into account the color difference between the target and the reference star:

$$a(\lambda, \theta_{T,i}) = \frac{median(dc_T(\lambda, \theta_{T,i}))}{median(dc_R(\lambda, \theta_{T,j}))}$$

Disk mapping

The third step of the procedure consists in generating a mask that selects the area of the image where there is signal from the disk. This can be done by putting some constraint on the minimum flux or some geometrical ones in order to remove contaminant sources or artefacts. In the automatic procedure, this was done by delimiting the image at 1.5 the standard deviation of the image over the ring between 20 and 70 pixels (0.15-0.52″); however, these extremes were modified in a few cases to better clean the selection of the disk pixels). The disk masks obtained in this way for a number of SPHERE targets are shown in Figure C.1.

Spectrum extraction

The last step is the extraction of the contrast spectrum of the disk. This is the total of the monochromatic images over the disk area divided by the total of the PSF of the star over an area having a radius of 1 λ/D. The contrast spectra (normalized at the value at 1.25 μm) are shown in Figure C.2.

We also extracted contrasts in magnitude within three spectral bands (Y: 1.00-1.10 μm; J: 1.20-1.30 μm; H: 1.50-1.65 μm). This allows to construct contrast colour-magnitude diagrams for the various disks. Values are in Table C.1. These contrast values often have quite large errors, with some very low value that is likely unreliable. There is however a clear range in intensity among disks, with some very bright one (RY Lup and T Cha). Taking into account these uncertainties, if we do not take into account debris disks (that is, HR4796A), results shows that there is a weak trend for brighter disks to be redder and faint disks bluer (Figure C.3). This suggests that a bluer colour signals the lack of contribution by large grains more than an excess of small ones. However, it might also indicate some contamination by stellar light at the shortest wavelengths.

Furthermore, disks seen at high inclination seem redder. This can be explained by a selective absorption of the shortest wavelength radiation. Within our small sample, edge-on disks look also brighter.

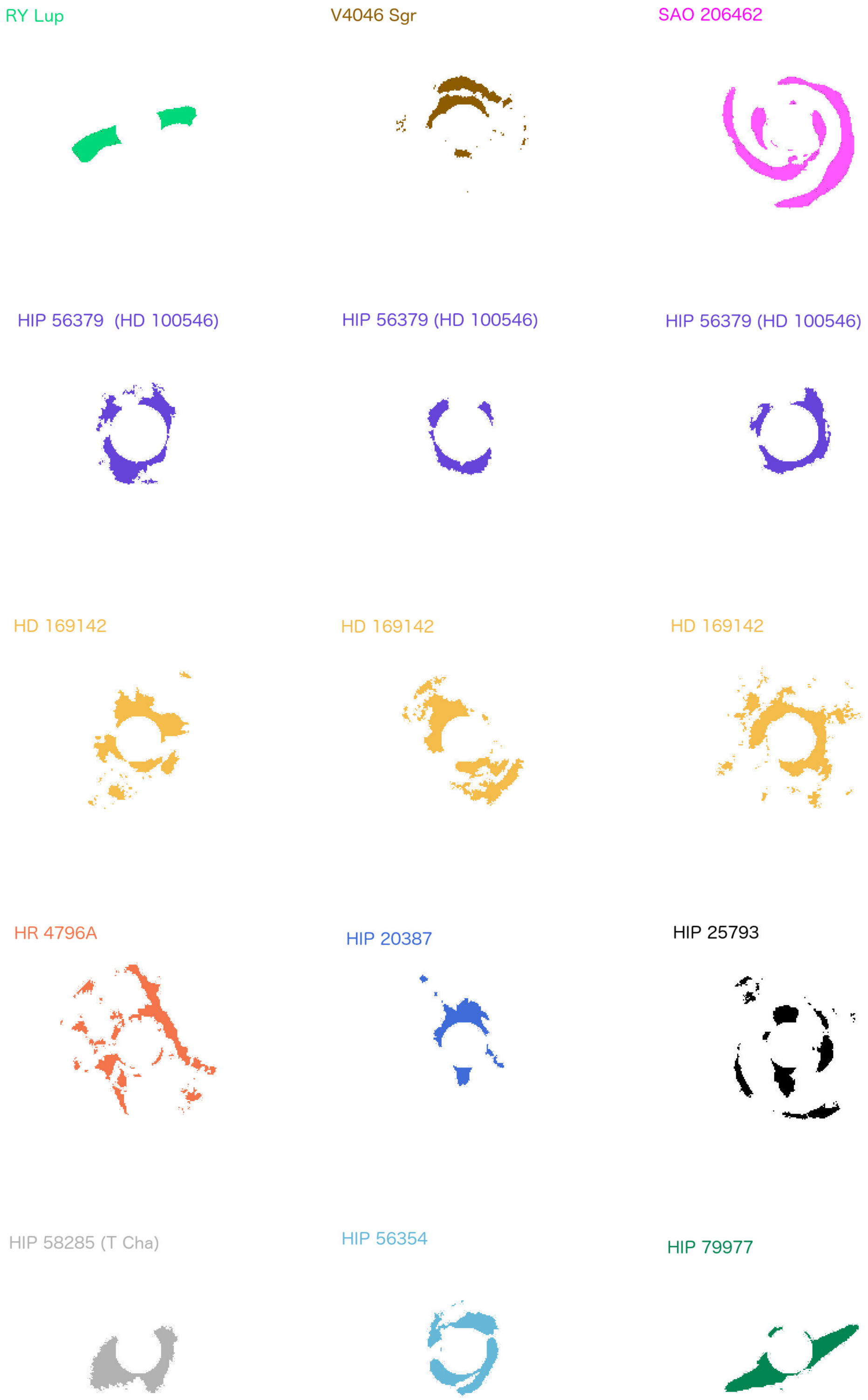

Figure C.1: Disk masks obtained with the automatic algorithm. For multiple observations, different masks were derived, as shown for HD 100564 (HIP 65379, second row) and HD 169142 (third row).

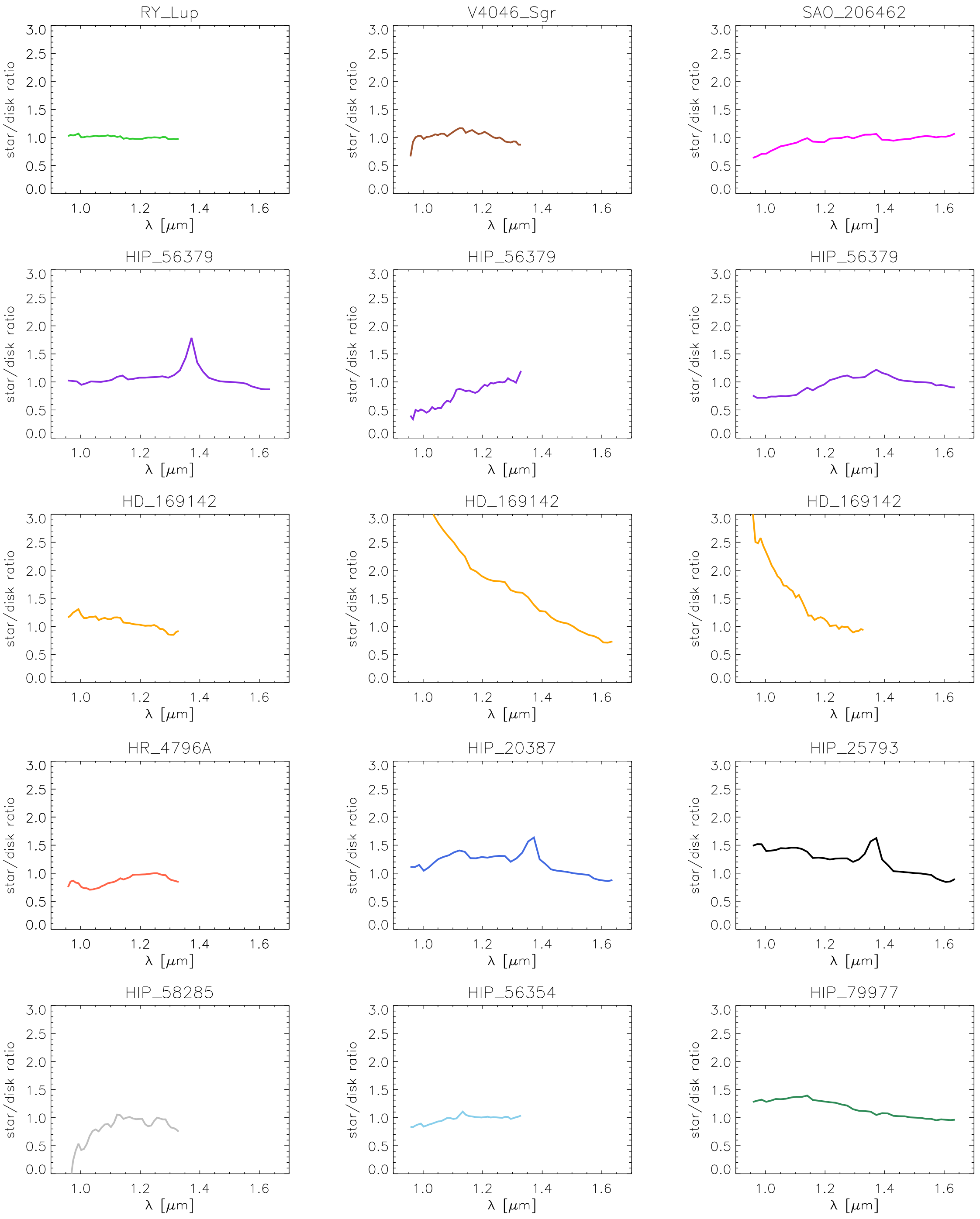

Figure C.2: Disk contrast spectra for a number of SPHERE targets. The spectra are normalized at 1.25 μm. Multiple observations for some targets are shown in separate plots.

Table C.1: Disk contrasts and their colours.

target	ΔJ	Y-J	J-H	Y-H
RY Lup	5.56	-0.028		
V4046 Sgr	8.00	-0.045		
SAO 206462	6.85	0.220	0.032	0.252
HIP 56379/2015-May	6.55	0.097	-0.166	-0.069
HIP 56379/2015-Jun	7.69	0.643		
HIP 56379/2016-May	7.09	0.405	0.129	0.276
HD 169142/June-2015	7.47	-0.213		
HD 169142/July-2015-3	7.36	-0.493	-0.704	-1,197
HD 169142/2016-Apr	9.70	-0.715		
HR 4796A	8.93	0.289		
HIP 20387	6.53	0.072	-0.351	-0.279
HIP 25793	7.13	-0.145	-0.326	-0.471
HIP 58285	5.66	0.315		
HIP 56354	6.07	0.095		
HIP 79977	7.19	-0.081	-0.254	-0.335

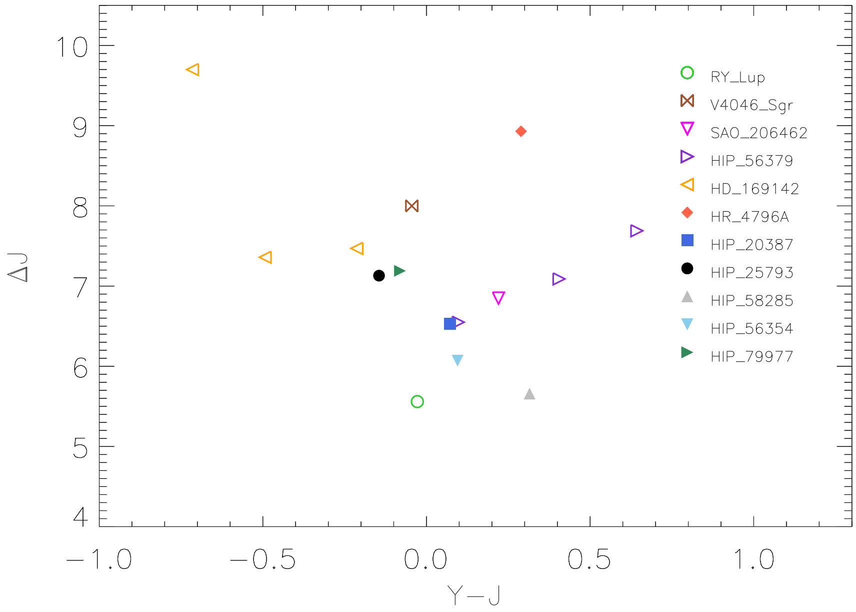

Figure C.3: Color magnitude diagram for the disks in the SHINE survey.

Bibliography

Adibekyan, V. 2017, ArXiv e-prints

Alcala, J. M., Covino, E., Franchini, M., et al. 1993, A&A, 272, 225

Alcalá, J. M., Manara, C. F., Natta, A., et al. 2017, A&A, 600, A20

Allard, F. 2014, in IAU Symposium, Vol. 299, Exploring the Formation and Evolution of Planetary Systems, ed. M. Booth, B. C. Matthews, & J. R. Graham, 271–272

Allard, F., Guillot, T., Ludwig, H.-G., et al. 2003, in IAU Symposium, Vol. 211, Brown Dwarfs, ed. E. Martín, 325

Allard, F., Hauschildt, P. H., Alexander, D. R., Tamanai, A., & Schweitzer, A. 2001, ApJ, 556, 357

Allard, F., Homeier, D., & Freytag, B. 2012, Philosophical Transactions of the Royal Society of London Series A, 370, 2765

Aller, K. M., Kraus, A. L., Liu, M. C., et al. 2013, ApJ, 773, 63

Allers, K. N. & Liu, M. C. 2013, ApJ, 772, 79

Alonso, A., Arribas, S., & Martinez-Roger, C. 1996, A&A, 313, 873

Alonso-Albi, T., Fuente, A., Bachiller, R., et al. 2009, A&A, 497, 117

Amara, A. & Quanz, S. P. 2012, MNRAS, 427, 948

Andrews, S. M., Rosenfeld, K. A., Wilner, D. J., & Bremer, M. 2011, ApJ, 742, L5

Antichi, J., Dohlen, K., Gratton, R. G., et al. 2009, ApJ, 695, 1042

Antoniucci, S., Podio, L., Nisini, B., et al. 2016, A&A, 593, L13

Ardila, D. R., Golimowski, D. A., Krist, J. E., et al. 2007, ApJ, 665, 512

Artigau, É., Gagné, J., Faherty, J., et al. 2015, ApJ, 806, 254

Augereau, J. C., Lagrange, A. M., Mouillet, D., & Ménard, F. 1999, A&A, 350, L51

Augereau, J. C., Lagrange, A. M., Mouillet, D., & Ménard, F. 2001, A&A, 365, 78

Avenhaus, H., Quanz, S. P., Meyer, M. R., et al. 2014, ApJ, 790, 56

Ayliffe, B. A. & Bate, M. R. 2009, MNRAS, 397, 657

Bachelet, E., Shin, I.-G., Han, C., et al. 2012, The Astrophysical Journal, 754, 73

Bailey, V., Meshkat, T., Reiter, M., et al. 2014, ApJ, 780, L4

Baliunas, S. L. & Vaughan, A. H. 1985, ARA&A, 23, 379

Baraffe, I., Chabrier, G., Barman, T. S., Allard, F., & Hauschildt, P. H. 2003, A&A, 402, 701

Baraffe, I., Homeier, D., Allard, F., & Chabrier, G. 2015, A&A, 577, A42

Barry, D. C. 1988, ApJ, 334, 436

Baruffolo, A., Bruno, P., Fantinel, D., et al. 2010, in Proc. SPIE, Vol. 7740, Software and Cyberinfrastructure for Astronomy, 77403J

Batalha, C., Lopes, D. F., & Batalha, N. M. 2001, ApJ, 548, 377

Baudino, J.-L., Bézard, B., Boccaletti, A., et al. 2015, A&A, 582, A83

Bazzon, A., Gisler, D., Roelfsema, R., et al. 2012, in Proc. SPIE, Vol. 8446, Ground-based and Airborne Instrumentation for Astronomy IV, 844693

Beaulieu, J.-P., Bennett, D. P., Batista, V., et al. 2016, ApJ, 824, 83

Béjar, V. J. S., Zapatero Osorio, M. R., Pérez-Garrido, A., et al. 2008, ApJ, 673, L185

Benisty, M., Malbet, F., Dougados, C., et al. 2010, A&A, 517, L3

Benisty, M., Stolker, T., Pohl, A., et al. 2017, A&A, 597, A42

Berton, A., Gratton, R. G., Feldt, M., et al. 2006, PASP, 118, 1144

Best, W. M. J., Liu, M. C., Magnier, E. A., et al. 2015, ApJ, 814, 118

Biller, B. A., Liu, M. C., Rice, K., et al. 2015, MNRAS, 450, 4446

Biller, B. A., Liu, M. C., Wahhaj, Z., et al. 2010, ApJ, 720, L82

Biller, B. A., Males, J., Rodigas, T., et al. 2014, ApJ, 792, L22

Boccaletti, A., Abe, L., Baudrand, J., et al. 2008, in Proc. SPIE, Vol. 7015, Adaptive Optics Systems, 70151B

Boccaletti, A., Pantin, E., Lagrange, A.-M., et al. 2013, A&A, 560, A20

Boccaletti, A. & the SPHERE consortium. in prep.

Böhm-Vitense, E. 2007, ApJ, 657, 486

Boisse, I., Bouchy, F., Hébrard, G., et al. 2011, A&A, 528, A4

Boisse, I., Moutou, C., Vidal-Madjar, A., et al. 2009, A&A, 495, 959

Bonavita, M., de Mooij, E. J. W., & Jayawardhana, R. 2013, PASP, 125, 849

Bonfanti, A., Ortolani, S., & Nascimbeni, V. 2016, A&A, 585, A5

Bonfanti, A., Ortolani, S., Piotto, G., & Nascimbeni, V. 2015, A&A, 575, A18

Bonnefoy, M., Chauvin, G., Dougados, C., et al. 2017, A&A, 597, A91

Bonnefoy, M., Marleau, G.-D., Galicher, R., et al. 2014, A&A, 567, L9

Bonnefoy, M., Zurlo, A., Baudino, J. L., et al. 2016, A&A, 587, A58

Boss, A. P. 1997, Science, 276, 1836

Bowler, B. P., Liu, M. C., Kraus, A. L., Mann, A. W., & Ireland, M. J. 2011, ApJ, 743, 148

Brittain, S. D., Carr, J. S., Najita, J. R., Quanz, S. P., & Meyer, M. R. 2014, ApJ, 791, 136

Brittain, S. D., Najita, J. R., Carr, J. S., et al. 2013, ApJ, 767, 159

Broeg, C., Schmidt, T. O. B., Guenther, E., et al. 2007, A&A, 468, 1039

Brown, J. M., Blake, G. A., Dullemond, C. P., et al. 2007, ApJ, 664, L107

Brown, T. M. 2001, ApJ, 553, 1006

Buenzli, E. & Schmid, H. M. 2009, A&A, 504, 259

Burgasser, A. J. 2014, in Astronomical Society of India Conference Series, Vol. 11, Astronomical Society of India Conference Series

Cameron, A. G. W. 1978, Moon and Planets, 18, 5

Campbell, B., Walker, G. A. H., & Yang, S. 1988, ApJ, 331, 902

Canovas, H., Min, M., Jeffers, S. V., Rodenhuis, M., & Keller, C. U. 2012, A&A, 543, A70

Canovas, H., Perez, S., Dougados, C., et al. 2015, A&A, 578, L1

Cardelli, J. A., Clayton, G. C., & Mathis, J. S. 1989, ApJ, 345, 245

Carolo, E. 2012, PhD thesis, University of Padua, Italy

Carolo, E., Desidera, S., Gratton, R., et al. 2014, A&A, 567, A48

Chabrier, G., Baraffe, I., Allard, F., & Hauschildt, P. 2000, ApJ, 542, 464

Charbonneau, P. & Steiner, O. 2012, Solar and Stellar Dynamos: Saas-Fee Advanced Course 39 Swiss Society for Astrophysics and Astronomy, Saas-Fee Advanced Course (Springer Berlin Heidelberg)

Chauvin, G., Desidera, S., Lagrange, A.-M., et al. 2017, ArXiv e-prints

Chauvin, G., Lagrange, A.-M., Bonavita, M., et al. 2010, A&A, 509, A52

Chauvin, G. & the SPHERE consortium. in prep., ApJ

Cheetham, A., Huélamo, N., Lacour, S., de Gregorio-Monsalvo, I., & Tuthill, P. 2015, MNRAS, 450, L1

Cieza, L. A., Olofsson, J., Harvey, P. M., et al. 2011, ApJ, 741, L25

Cincunegui, C., Díaz, R. F., & Mauas, P. J. D. 2007, A&A, 469, 309

Clampin, M., Krist, J. E., Ardila, D. R., et al. 2003, AJ, 126, 385

Claudi, R. U., Turatto, M., Gratton, R. G., et al. 2008, in Proc. SPIE, Vol. 7014, Ground-based and Airborne Instrumentation for Astronomy II, 70143E

Close, L. M., Follette, K. B., Males, J. R., et al. 2014, ApJ, 781, L30

Cotton, W. D., Mennesson, B., Diamond, P. J., et al. 2004, A&A, 414, 275

Crida, A., Morbidelli, A., & Masset, F. 2006, Icarus, 181, 587

Currie, T., Burrows, A., Girard, J. H., et al. 2014a, ApJ, 795, 133

Currie, T., Cloutier, R., Brittain, S., et al. 2015, ApJ, 814, L27

Currie, T., Daemgen, S., Debes, J., et al. 2014b, ApJ, 780, L30

Currie, T., Muto, T., Kudo, T., et al. 2014c, ApJ, 796, L30

Cutri, R. M., Skrutskie, M. F., van Dyk, S., et al. 2003, VizieR Online Data Catalog, 2246

de Boer, J., Salter, G., Benisty, M., et al. 2016, A&A, 595, A114

de Boer, J. & the SPHERE consortium. in prep., ApJ

De Rosa, R. J., Patience, J., Ward-Duong, K., et al. 2014, MNRAS, 445, 3694

Desidera, S., Carolo, E., Gratton, R., et al. 2011, A&A, 533, A90

Desidera, S., Gratton, R., Carolo, E., et al. 2012, A&A, 546, A108

Desidera, S., Gratton, R., Endl, M., et al. 2007, ArXiv e-prints

Desidera, S., Gratton, R. G., Lucatello, S., & Claudi, R. U. 2006a, A&A, 454, 581

Desidera, S., Gratton, R. G., Lucatello, S., Claudi, R. U., & Dall, T. H. 2006b, A&A, 454, 553

Desidera, S., Gratton, R. G., Scuderi, S., et al. 2004, A&A, 420, 683

Desort, M., Lagrange, A.-M., Galland, F., Udry, S., & Mayor, M. 2007, A&A, 473, 983

Dohlen, K., Langlois, M., Saisse, M., et al. 2008, in Proc. SPIE, Vol. 7014, Ground-based and Airborne Instrumentation for Astronomy II, 70143L

Dong, R., Fung, J., & Chiang, E. 2016, ApJ, 826, 75

Dong, R., Li, S., Chiang, E., & Li, H. 2017, ApJ, 843, 127

Dougherty, S. M., Bode, M. F., Lloyd, H. M., Davis, R. J., & Eyres, S. P. 1995, MNRAS, 272, 843

Dullemond, C. P. & Dominik, C. 2004, A&A, 421, 1075

Dullemond, C. P., Juhasz, A., Pohl, A., et al. 2012, RADMC-3D: A multi-purpose radiative transfer tool, Astrophysics Source Code Library

Dullemond, C. P. & Monnier, J. D. 2010, ARA&A, 48, 205

Dumusque, X., Lovis, C., Ségransan, D., et al. 2011, A&A, 535, A55

Endl, M., Kürster, M., & Els, S. 2000, A&A, 362, 585

Espaillat, C., Calvet, N., D'Alessio, P., et al. 2007, ApJ, 670, L135

Faherty, J. K., Rice, E. L., Cruz, K. L., Mamajek, E. E., & Núñez, A. 2013, AJ, 145, 2

Fang, M., van Boekel, R., Wang, W., et al. 2009, A&A, 504, 461

Feldt, M., Olofsson, J., Boccaletti, A., et al. 2017, A&A, 601, A7

Filippazzo, J. C., Rice, E. L., Faherty, J., et al. 2015, ApJ, 810, 158

Follette, K. B., Rameau, J., Dong, R., et al. 2017, AJ, 153, 264

Furlan, E., Luhman, K. L., Espaillat, C., et al. 2011, ApJS, 195, 3

Fusco, T., Petit, C., Rousset, G., et al. 2006, in Proc. SPIE, Vol. 6272, Society of Photo-Optical Instrumentation Engineers (SPIE) Conference Series, 62720K

Fusco, T., Rousset, G., Beuzit, J.-L., et al. 2005, in Proc. SPIE, Vol. 5903, Astronomical Adaptive Optics Systems and Applications II, ed. R. K. Tyson & M. Lloyd-Hart, 178–189

Fusco, T., Sauvage, J.-F., Petit, C., et al. 2014, in Proc. SPIE, Vol. 9148, Adaptive Optics Systems IV, 91481U

Gaia Collaboration, Brown, A. G. A., Vallenari, A., et al. 2016, ArXiv e-prints

Garufi, A., Meeus, G., Benisty, M., et al. 2017, A&A, 603, A21

Garufi, A., Quanz, S. P., Schmid, H. M., et al. 2016, A&A, 588, A8

Gaudi, B. S., Bennett, D. P., Udalski, A., et al. 2008, Science, 319, 927

Gauza, B., Béjar, V. J. S., Pérez-Garrido, A., et al. 2015, ApJ, 804, 96

Ginski, C., Schmidt, T. O. B., Mugrauer, M., et al. 2014, MNRAS, 444, 2280

Ginski, C., Stolker, T., Pinilla, P., et al. 2016, A&A, 595, A112

Ginski, C. & the SPHERE consortium. in prep.

Gisler, D., Schmid, H. M., Thalmann, C., et al. 2004, in Proc. SPIE, Vol. 5492, Ground-based Instrumentation for Astronomy, ed. A. F. M. Moorwood & M. Iye, 463–474

Gizis, J. E., Faherty, J. K., Liu, M. C., et al. 2012, AJ, 144, 94

Gomes da Silva, J., Santos, N. C., Boisse, I., Dumusque, X., & Lovis, C. 2014, A&A, 566, A66

Gomes da Silva, J., Santos, N. C., Bonfils, X., et al. 2011, A&A, 534, A30

Gräfe, C., Wolf, S., Roccatagliata, V., Sauter, J., & Ertel, S. 2011, A&A, 533, A89

Gratton, R., Desidera, S., & Claudi, R. 2009, MSAIt, 80, 312

Gratton, R. G., Bonanno, G., Bruno, P., et al. 2001, Experimental Astronomy, 12, 107

Gray, R. O., Corbally, C. J., Garrison, R. F., McFadden, M. T., & Robinson, P. E. 2003, AJ, 126, 2048

Gullbring, E., Hartmann, L., Briceño, C., & Calvet, N. 1998, ApJ, 492, 323

Guyon, O., Pluzhnik, E. A., Kuchner, M. J., Collins, B., & Ridgway, S. T. 2006, ApJS, 167, 81

Hartmann, L. & Kenyon, S. J. 1996, Annual Review of Astronomy and Astrophysics, 34, 207

Hartmann, L., Kenyon, S. J., Hewett, R., et al. 1989, ApJ, 338, 1001

Hatzes, A. P. & Cochran, W. D. 1993, ApJ, 413, 339

Henderson, C. B., Park, H., Sumi, T., et al. 2014, ApJ, 794, 71

Hennebelle, P. & Chabrier, G. 2011, ApJ, 743, L29

Herbig, G. H. 1977, ApJ, 214, 747

Herbig, G. H. 1980, IAU Circ., 3535

Herbst, W., Racine, R., & Warner, J. W. 1978, ApJ, 223, 471

Herczeg, G. J. & Hillenbrand, L. A. 2014, The Astrophysical Journal, 786, 97

Hinkley, S., Bowler, B. P., Vigan, A., et al. 2015, ApJ, 805, L10

Hinkley, S., Hillenbrand, L., Oppenheimer, B. R., et al. 2013, ApJ, 763, L9

Hollis, J. M., Boboltz, D. A., Pedelty, J. A., White, S. M., & Forster, J. R. 2001, ApJ, 559, L37

Hollis, J. M., Kafatos, M., Michalitsianos, A. G., & McAlister, H. A. 1985, ApJ, 289, 765

Hollis, J. M., Lyon, R. G., Dorband, J. E., & Feibelman, W. A. 1997, ApJ, 475, 231

Honda, M., Kudo, T., Takatsuki, S., et al. 2016, ApJ, 821, 2

Hu, J. Y., The, P. S., & de Winter, D. 1989, A&A, 208, 213

Huélamo, N., de Gregorio-Monsalvo, I., Macias, E., et al. 2015, A&A, 575, L5

Huélamo, N., Lacour, S., Tuthill, P., et al. 2011, A&A, 528, L7

Inoue, A. K., Honda, M., Nakamoto, T., & Oka, A. 2008, PASJ, 60, 557

Ireland, M. J., Kraus, A., Martinache, F., Law, N., & Hillenbrand, L. A. 2011, ApJ, 726, 113

Isaacson, H. & Fischer, D. 2010, ApJ, 725, 875

Isella, A., Chandler, C. J., Carpenter, J. M., Pérez, L. M., & Ricci, L. 2014, ApJ, 788, 129

Kafatos, M., Hollis, J. M., Yusef-Zadeh, F., Michalitsianos, A. G., & Elitzur, M. 1989, ApJ, 346, 991

Kaltenegger, L., Selsis, F., Fridlund, M., et al. 2010, Astrobiology, 10, 89

Kamohara, R., Bujarrabal, V., Honma, M., et al. 2010, A&A, 510, A69

Kellogg, E., Hollis, J. M., Pedelty, J., & Lyon, R. 2001, in Bulletin of the American Astronomical Society, Vol. 33, American Astronomical Society Meeting Abstracts #198, 818

Kraus, A. L. & Ireland, M. J. 2012, ApJ, 745, 5

Kuhn, J. R., Potter, D., & Parise, B. 2001, ApJ, 553, L189

Kürster, M., Endl, M., Rouesnel, F., et al. 2003, A&A, 403, 1077

Kurucz, R. L., Furenlid, I., Brault, J., & Testerman, L. 1984, Solar flux atlas from 296 to 1300 nm

Lachapelle, F.-R., Lafrenière, D., Gagné, J., et al. 2015, ApJ, 802, 61

Lafrenière, D., Jayawardhana, R., & van Kerkwijk, M. H. 2008, ApJ, 689, L153

Lafrenière, D., Marois, C., Doyon, R., Nadeau, D., & Artigau, É. 2007, ApJ, 660, 770

Lagrange, A.-M., Beuzit, J.-L., Chauvin, G., & Mouillet, D. 2008, in Proc. SPIE, Vol. 7015, Adaptive Optics Systems, 701503

Lagrange, A.-M., Langlois, M., Gratton, R., et al. 2016, A&A, 586, L8

Langlois, M., Dohlen, K., Vigan, A., et al. 2014, in Proc. SPIE, Vol. 9147, Ground-based and Airborne Instrumentation for Astronomy V, 91471R

Latham, D. W., Stefanik, R. P., Mazeh, T., Mayor, M., & Burki, G. 1989, Nature, 339, 38

Lavigne, J.-F., Doyon, R., Lafrenière, D., Marois, C., & Barman, T. 2009, The Astrophysical Journal, 704, 1098

Levenhagen, R. S. & Leister, N. V. 2006, MNRAS, 371, 252

Lew, B. W. P., Apai, D., Zhou, Y., et al. 2016, ApJ, 829, L32

Lin, D. N. C. & Papaloizou, J. 1979, MNRAS, 186, 799

Liu, M. C., Magnier, E. A., Deacon, N. R., et al. 2013, ApJ, 777, L20

Looper, D. L., Kirkpatrick, J. D., Cutri, R. M., et al. 2008, ApJ, 686, 528

Lovis, C., Dumusque, X., Santos, N. C., et al. 2011, ArXiv e-prints

Lubow, S. H. & Ida, S. 2010, Planet Migration, ed. S. Seager, 347–371

Lyot, B. 1939, MNRAS, 99, 580

Mace, G. N., Kirkpatrick, J. D., Cushing, M. C., et al. 2013, ApJS, 205, 6

MacGregor, M. A., Wilner, D. J., Czekala, I., et al. 2017, ApJ, 835, 17

Maire, A.-L., Bonnefoy, M., Ginski, C., et al. 2016a, A&A, 587, A56

Maire, A.-L., Langlois, M., Dohlen, K., et al. 2016b, in Proc. SPIE, Vol. 9908, Society of Photo-Optical Instrumentation Engineers (SPIE) Conference Series, 990834

Maire, A.-L., Stolker, T., Messina, S., et al. 2017, A&A, 601, A134

Mamajek, E. E. & Bell, C. P. M. 2014, MNRAS, 445, 2169

Mamajek, E. E. & Hillenbrand, L. A. 2008, ApJ, 687, 1264

Manjavacas, E., Bonnefoy, M., Schlieder, J. E., et al. 2014, A&A, 564, A55

Marley, M. S., Fortney, J. J., Hubickyj, O., Bodenheimer, P., & Lissauer, J. J. 2007, ApJ, 655, 541

Marois, C., Correia, C., Véran, J.-P., & Currie, T. 2014, in IAU Symposium, Vol. 299, Exploring the Formation and Evolution of Planetary Systems, ed. M. Booth, B. C. Matthews, & J. R. Graham, 48–49

Marois, C., Lafrenière, D., Doyon, R., Macintosh, B., & Nadeau, D. 2006, ApJ, 641, 556

Martin, R. G. & Lubow, S. H. 2011, ApJ, 740, L6

Martínez Fiorenzano, A. F., Gratton, R. G., Desidera, S., Cosentino, R., & Endl, M. 2005, A&A, 442, 775

Mayor, M. & Queloz, D. 1995, Nature, 378, 355

Mazoyer, J., Boccaletti, A., Choquet, É., et al. 2016, ApJ, 818, 150

McElwain, M. W., Metchev, S. A., Larkin, J. E., et al. 2007, ApJ, 656, 505

Mesa, D., Gratton, R., Zurlo, A., et al. 2015, A&A, 576, A121

Mesa, D., Vigan, A., D'Orazi, V., et al. 2016, A&A, 593, A119

Mesa, D., Zurlo, A., Milli, J., et al. 2017, MNRAS, 466, L118

Meunier, N. & Delfosse, X. 2009, A&A, 501, 1103

Meunier, N., Lagrange, A.-M., Mbemba Kabuiku, L., et al. 2017, A&A, 597, A52

Milli, J., Mouillet, D., Lagrange, A.-M., et al. 2012, A&A, 545, A111

Mizuno, H. 1980, Progress of Theoretical Physics, 64, 544

Mordasini, C. 2013, A&A, 558, A113

Mordasini, C., Alibert, Y., Benz, W., & Naef, D. 2008, in Astronomical Society of the Pacific Conference Series, Vol. 398, Extreme Solar Systems, ed. D. Fischer, F. A. Rasio, S. E. Thorsett, & A. Wolszczan, 235

Mouillet, D., Lagrange, A. M., Augereau, J. C., & Ménard, F. 2001, A&A, 372, L61

Mouillet, D., Lagrange, A.-M., Beuzit, J.-L., et al. 2002, in SF2A-2002: Semaine de l'Astrophysique Francaise, ed. F. Combes & D. Barret, 585

Murphy, S. J., Lawson, W. A., & Bessell, M. S. 2013, MNRAS, 435, 1325

Muterspaugh, M. W., Lane, B. F., Kulkarni, S. R., et al. 2010, AJ, 140, 1657

Natta, A., Meyer, M. R., & Beckwith, S. V. W. 2000, ApJ, 534, 838

Natta, A., Testi, L., Muzerolle, J., et al. 2004, A&A, 424, 603

Neuhäuser, R., Guenther, E. W., Wuchterl, G., et al. 2005, A&A, 435, L13

Neuhäuser, R., Mugrauer, M., Seifahrt, A., Schmidt, T. O. B., & Vogt, N. 2008, A&A, 484, 281

Nielsen, E. L., De Rosa, R. J., Rameau, J., et al. 2017, ArXiv e-prints

Noyes, R. W., Hartmann, L. W., Baliunas, S. L., Duncan, D. K., & Vaughan, A. H. 1984, ApJ, 279, 763

Oh, D., Hashimoto, J., Tamura, M., et al. 2016, PASJ, 68, L3

Oláh, K., Kolláth, Z., Granzer, T., et al. 2009, A&A, 501, 703

Olofsson, J., Benisty, M., Augereau, J.-C., et al. 2011, A&A, 528, L6

Olofsson, J., Benisty, M., Le Bouquin, J.-B., et al. 2013, A&A, 552, A4

Oppenheimer, B. R., Brenner, D., Hinkley, S., et al. 2008, ApJ, 679, 1574

Pace, G. 2013, A&A, 551, L8

Pace, G., Melendez, J., Pasquini, L., et al. 2009, A&A, 499, L9

Panić, O., Ratzka, T., Mulders, G. D., et al. 2014, A&A, 562, A101

Pantin, E., Waelkens, C., & Lagage, P. O. 2000, A&A, 361, L9

Paresce, F. & Hack, W. 1994, A&A, 287, 154

Pascucci, I., Testi, L., Herczeg, G. J., et al. 2016, ApJ, 831, 125

Patience, J., King, R. R., de Rosa, R. J., & Marois, C. 2010, A&A, 517, A76

Pavlov, A., Möller-Nilsson, O., Feldt, M., et al. 2008, in Proc. SPIE, Vol. 7019, Advanced Software and Control for Astronomy II, 701939

Perrin, M. D., Graham, J. R., Kalas, P., et al. 2004, in Proc. SPIE, Vol. 5490, Advancements in Adaptive Optics, ed. D. Bonaccini Calia, B. L. Ellerbroek, & R. Ragazzoni, 309–320

Perrot, C., Boccaletti, A., Pantin, E., et al. 2016, A&A, 590, L7

Perryman, M. A. C., Lindegren, L., Kovalevsky, J., et al. 1997, A&A, 323, L49

Petit, C., Sauvage, J.-F., Fusco, T., et al. 2014, in Proc. SPIE, Vol. 9148, Adaptive Optics Systems IV, 91480O

Pineda, J. E., Quanz, S. P., Meru, F., et al. 2014, ApJ, 788, L34

Pinilla, P., Birnstiel, T., & Walsh, C. 2015, A&A, 580, A105

Pohl, A., Sissa, E., Langlois, M., et al. 2017, ArXiv e-prints

Pollack, J. B., Hubickyj, O., Bodenheimer, P., et al. 1996, Icarus, 124, 62

Pueyo, L., Crepp, J. R., Vasisht, G., et al. 2012, ApJS, 199, 6

Quanz, S. P., Amara, A., Meyer, M. R., et al. 2015, ApJ, 807, 64

Quanz, S. P., Amara, A., Meyer, M. R., et al. 2013, ApJ, 766, L1

Quanz, S. P., Schmid, H. M., Geissler, K., et al. 2011, ApJ, 738, 23

Queloz, D., Henry, G. W., Sivan, J. P., et al. 2001, A&A, 379, 279

Quillen, A. C. & Trilling, D. E. 1998, ApJ, 508, 707

Racine, R., Walker, G. A. H., Nadeau, D., Doyon, R., & Marois, C. 1999, PASP, 111, 587

Ragland, S., Le Coroller, H., Pluzhnik, E., et al. 2008, ApJ, 679, 746

Rameau, J., Chauvin, G., Lagrange, A.-M., et al. 2013, ApJ, 772, L15

Rameau, J., Follette, K. B., Pueyo, L., et al. 2017, ArXiv e-prints

Reggiani, M., Quanz, S. P., Meyer, M. R., et al. 2014, ApJ, 792, L23

Rigliaco, E., Natta, A., Testi, L., et al. 2012, A&A, 548, A56

Robertson, P., Mahadevan, S., Endl, M., & Roy, A. 2014, Science, 345, 440

Robinson, R. D., Cram, L. E., & Giampapa, M. S. 1990, ApJS, 74, 891

Roelfsema, R., Bazzon, A., Schmid, H. M., et al. 2014, in Proc. SPIE, Vol. 9147, Ground-based and Airborne Instrumentation for Astronomy V, 91473W

Röser, S., Schilbach, E., Schwan, H., et al. 2008, A&A, 488, 401

Saar, S. H., Butler, R. P., & Marcy, G. W. 1998, ApJ, 498, L153

Saar, S. H. & Donahue, R. A. 1997, ApJ, 485, 319

Sahlmann, J. 2016, IAU Focus Meeting, 29, 217

Sahlmann, J., Lazorenko, P. F., Mérand, A., et al. 2013, in Proc. SPIE, Vol. 8864, Techniques and Instrumentation for Detection of Exoplanets VI, 88641B

Sahu, K. C., Bond, H. E., Anderson, J., & Dominik, M. 2014, ApJ, 782, 89

Sallum, S., Eisner, J. A., Close, L. M., et al. 2015a, ApJ, 801, 85

Sallum, S., Follette, K. B., Eisner, J. A., et al. 2015b, Nature, 527, 342

Samland, M., Mollière, P., Bonnefoy, M., et al. 2017, A&A, 603, A57

Santos, N. C., Gomes da Silva, J., Lovis, C., & Melo, C. 2010, A&A, 511, A54

Santos, N. C., Mayor, M., Naef, D., et al. 2000, A&A, 361, 265

Schlafly, E. F. & Finkbeiner, D. P. 2011, ApJ, 737, 103

Schlegel, D. J., Finkbeiner, D. P., & Davis, M. 1998, ApJ, 500, 525

Schmid, H. M., Bazzon, A., Milli, J., et al. 2017, A&A, 602, A53

Schmid, H. M., Beuzit, J.-L., Feldt, M., et al. 2006a, in IAU Colloq. 200: Direct Imaging of Exoplanets: Science Techniques, ed. C. Aime & F. Vakili, 165–170

Schmid, H.-M., Downing, M., Roelfsema, R., et al. 2012, in Proc. SPIE, Vol. 8446, Ground-based and Airborne Instrumentation for Astronomy IV, 84468Y

Schmid, H. M., Joos, F., & Tschan, D. 2006b, A&A, 452, 657

Seager, S., Whitney, B. A., & Sasselov, D. D. 2000, ApJ, 540, 504

Segura, A., Kasting, J. F., Meadows, V., et al. 2005, Astrobiology, 5, 706

Seifahrt, A., Neuhäuser, R., & Hauschildt, P. H. 2007, A&A, 463, 309

Shabram, M. & Boley, A. C. 2013, ApJ, 767, 63

Sharma, S., Bland-Hawthorn, J., Johnston, K. V., & Binney, J. 2011, ApJ, 730, 3

Simon, M., Dutrey, A., & Guilloteau, S. 2000, ApJ, 545, 1034

Simpson, E. K., Baliunas, S. L., Henry, G. W., & Watson, C. A. 2010, MNRAS, 408, 1666

Sissa, E., Gratton, R., Desidera, S., et al. 2016, A&A, 596, A76

Sissa, E. & the SPHERE consortium. in prep.

Skumanich, A. 1972, ApJ, 171, 565

Soderblom, D. R., Stauffer, J. R., Hudon, J. D., & Jones, B. F. 1993, ApJS, 85, 315

Solf, J. & Ulrich, H. 1985, A&A, 148, 274

Soummer, R. 2005, ApJ, 618, L161

Soummer, R., Aime, C., & Falloon, P. E. 2003, A&A, 397, 1161

Soummer, R., Pueyo, L., & Larkin, J. 2012, ApJ, 755, L28

Sparks, W. B. & Ford, H. C. 2002, ApJ, 578, 543

Stam, D. M., de Rooij, W. A., Cornet, G., & Hovenier, J. W. 2006, A&A, 452, 669

Stam, D. M., Hovenier, J. W., & Waters, L. B. F. M. 2004, A&A, 428, 663

Strassmeier, K., Washuettl, A., Granzer, T., Scheck, M., & Weber, M. 2000, A&AS, 142, 275

Strassmeier, K. G., Fekel, F. C., Bopp, B. W., Dempsey, R. C., & Henry, G. W. 1990, ApJS, 72, 191

Struve, O. 1952, The Observatory, 72, 199

Szeifert, T., Hubrig, S., Schöller, M., et al. 2010, A&A, 509, L7

Tachihara, K., Dobashi, K., Mizuno, A., Ogawa, H., & Fukui, Y. 1996, PASJ, 48, 489

Tetzlaff, N., Neuhäuser, R., & Hohle, M. M. 2011, MNRAS, 410, 190

Thalmann, C., Janson, M., Garufi, A., et al. 2016, ApJ, 828, L17

Thalmann, C., Mulders, G. D., Hodapp, K., et al. 2014, A&A, 566, A51

Thalmann, C., Mulders, G. D., Janson, M., et al. 2015, ApJ, 808, L41

Thalmann, C., Schmid, H. M., Boccaletti, A., et al. 2008, in Proc. SPIE, Vol. 7014, Ground-based and Airborne Instrumentation for Astronomy II, 70143F

Thatte, N., Abuter, R., Tecza, M., et al. 2007, MNRAS, 378, 1229

Tody, D. 1993, in Astronomical Society of the Pacific Conference Series, Vol. 52, Astronomical Data Analysis Software and Systems II, ed. R. J. Hanisch, R. J. V. Brissenden, & J. Barnes, 173

Torres, C. A. O., Quast, G. R., Melo, C. H. F., & Sterzik, M. F. 2008, Young Nearby Loose Associations, ed. B. Reipurth, 757

Valenti, J. A. & Fischer, D. A. 2005, ApJS, 159, 141

van Boekel, R., Henning, T., Menu, J., et al. 2017, ApJ, 837, 132

van der Plas, G., van den Ancker, M. E., Acke, B., et al. 2009, A&A, 500, 1137

Vassallo, D. 2014, Master's thesis, Universita' degli Studi di Bologna, Italy

Vaughan, A. H. & Preston, G. W. 1980, PASP, 92, 385

Vigan, A., Bonnefoy, M., Ginski, C., et al. 2016, A&A, 587, A55

Vigan, A., Gry, C., Salter, G., et al. 2015, MNRAS, 454, 129

Vigan, A., Langlois, M., Moutou, C., & Dohlen, K. 2008, A&A, 489, 1345

Vigan, A., Moutou, C., Langlois, M., et al. 2010, MNRAS, 407, 71

Vigan, A., Patience, J., Marois, C., et al. 2012, A&A, 544, A9

Voges, W., Aschenbach, B., Boller, T., et al. 1999, A&A, 349, 389

Voges, W., Aschenbach, B., Boller, T., et al. 2000, IAU Circ., 7432, 1

Wallerstein, G. & Greenstein, J. L. 1980, PASP, 92, 275

Walsh, C., Juhász, A., Pinilla, P., et al. 2014, ApJ, 791, L6

Whelan, E. T., Dougados, C., Perrin, M. D., et al. 2010, ApJ, 720, L119

Wright, C. M., Maddison, S. T., Wilner, D. J., et al. 2015, MNRAS, 453, 414

Wright, C. O., Egan, M. P., Kraemer, K. E., & Price, S. D. 2003, AJ, 125, 359

Wright, J. T., Marcy, G. W., Butler, R. P., & Vogt, S. S. 2004, ApJS, 152, 261

Wu, Y.-L., Close, L. M., Males, J. R., et al. 2015, ApJ, 801, 4

Wu, Y.-L., Sheehan, P. D., Males, J. R., et al. 2017, ApJ, 836, 223

Wyatt, M. C. 2008, ARA&A, 46, 339

Wyatt, M. C., Panić, O., Kennedy, G. M., & Matrà, L. 2015, Ap&SS, 357, 103

Yorke, H. W. & Bodenheimer, P. 1999, ApJ, 525, 330

Zechmeister, M. & Kürster, M. 2009, A&A, 496, 577

Zhao, J. K., Oswalt, T. D., Rudkin, M., Zhao, G., & Chen, Y. Q. 2011, AJ, 141, 107

Zhao-Geisler, R., Quirrenbach, A., Köhler, R., & Lopez, B. 2012, A&A, 545, A56

Zhou, Y., Herczeg, G. J., Kraus, A. L., Metchev, S., & Cruz, K. L. 2014, The Astrophysical Journal Letters, 783, L17

Zurlo, A., Vigan, A., Galicher, R., et al. 2016, A&A, 587, A57

Zurlo, A., Vigan, A., Mesa, D., et al. 2014, A&A, 572, A85